Understanding and Treating *Mycobacterium tuberculosis* Infection: A Multi-Scale Modeling Approach

by

Nicholas Anthony Cilfone

A dissertation submitted in partial fulfillment
of the requirements for the degree of
Doctor of Philosophy
(Chemical Engineering)
in the University of Michigan
2014

Doctoral Committee:

Professor Jennifer J. Linderman, Chair
Professor Denise E. Kirschner
Endowed Professor Steven L. Kunkel
Assistant Professor Greg M. Thurber

To my family

Acknowledgements

I would first like to thank my advisor Professor Jennifer Linderman for her guidance throughout my studies. Her willingness to let me find my own way has allowed me to become the researcher that I am today. Her ability to balance both academic excellence and commitment to her family is a testament to her character. She will always be an inspiration to me. I am thankful that I got the opportunity to have her as my mentor. I would also like to thank Professor Denise Kirschner for shaping me as a researcher. Although it was never official, she was certainly my co-advisor throughout my studies. She was never afraid to take a hard edge with me, which I will always be grateful of. She will continue to serve as an inspiration for her collaborative spirit and ability to bring cross-discipline researchers together. I would like to thank the collaborators who made this work possible: Joanne Flynn and her group at University of Pittsburgh and Veronique Dartois and her group at Rutgers University. I would also like to thank my committee members past and present for their help and guidance: Steve Kunkel, Greg Thurber, and Lola Adefeso-Eniola.

Thanks to both the Linderman and Kirschner research groups for their help and friendship over the past 5 years: Mohammad Fallahi-Sichani, Paul Wolberg, Lad Dombrowski, Hayley Warsinski, Chang Gong, Cordelia Ziraldo, Mohammad El-Kebir, Joe Waliga, Madhuresh Sumit, and Danielle Trakimas. In particular, thanks to Cory Perry for being patient while I learned C++. Thanks to Simeone Marino for all the helpful

discussions about sensitivity analysis along with conversations about proper futbol. Thanks to Laura Chang for always being willing to converse about anything and for keeping our office lively. Thanks to Elsje Pienaar for her collaborative effort on everything related to model calibration and antibiotics.

Thanks to both my family and friends for always being supportive of me. Specifically, thanks to Jacob Dickinson and Alex Thompson for being the greatest friends I could imagine and for living with me for 3 years. Our friendships will go well beyond what we've done here. Thanks to my brothers, Marc and Chris, for always being my brothers. No matter what transpired and how many times I didn't call back, you both were always there to keep me going. Thanks to Ashley for being the sister that I never had. To my parents, I would never have made it this far without you. Thank you for letting me be different growing up. You always supported my love for science and did everything you could to foster that love. Lastly, thanks to Alissa Kerner for being incredible. There is not enough space to describe what she has done for me. To her, "Things are never quite as scary when you've got a best friend."

Table of Contents

List of Figures

List of Tables

List of Appendices

Abstract

Tuberculosis (TB), caused by the pathogen *Mycobacterium tuberculosis* (*Mtb*), remains a significant burden on global health. Central to both host immune responses and antibiotic treatment are structures known as granulomas. In this dissertation we used computational and experimental approaches at a single granuloma level to understand how immune responses to *Mtb* contribute to both bacterial control and persistence. In addition, we predicted the dynamics of antibiotics in granulomas and designed improved treatment strategies.

We built a hybrid multi-scale model of *Mtb* infection that integrates the cytokines tumor necrosis factor-α (TNF) and interleukin-10 (IL-10). We predicted that a balance of TNF and IL-10 is essential to infection control with minimal host-induced tissue damage. We extended our description of TNF and IL-10 to include simplified models of intracellular signaling driving macrophage polarization, which suggests that the temporal dynamics of macrophage polarization in granulomas are predictive of granuloma outcome. Next, we focused on determining the role of IL-10 in controlling antimicrobial activity. We predicted a transient role for IL-10 in controlling a trade-off between early host immunity antimicrobial responses and tissue damage. This trade-off determines sterilization of granulomas. Lastly, using an experimental model of granuloma formation, we measured significant gradients of TNF in granulomas.

We developed a pharmacokinetic and pharmacodynamic model of oral dosing of rifampin and isoniazid used to treat *Mtb* and incorporated it into our computational model. We predicted that oral antibiotic strategies fail due to sub-optimal exposure in granulomas, which leads to bacterial regrowth between doses. We extended our platform to include a description of inhaled formulations dosed to the lungs with reduced frequencies. We predicted that dosing every two-weeks with an inhaled formulation of isoniazid is feasible with increased sterilization capabilities and reduced toxicity, while an inhaled formulation of rifampin has equivalent sterilization capabilities, but early associated toxicity and infeasible carrier loadings.

The keys to understanding immune responses and successful antibiotic treatment of TB lie in the dynamics at the site of infection. Our results help identify the roles of cytokines during *Mtb* infection, provide new possibilities for immune related therapies, and guide design of better antibiotic strategies.

Chapter 1

Introduction

1.1 Motivation

Tuberculosis (TB) remains a global concern, causing an estimated 1.3 million deaths and an estimated 8.6 million new cases diagnosed in 2013 (1). Upon infection with *Mycobacterium tuberculosis (Mtb)*, approximately 10-15% of individuals develop active TB disease, where the immune response is unable to control infection and without treatment death commonly occurs (1–4). A larger portion of individuals (~85-90%) develop latent TB, where the immune response is able to control infection but unable to successfully clear the pathogen. These individuals show no outward signs of infection and are non-infectious. Estimates indicate that near one-third of the world's population is latently infected (2–7). Reactivation of TB, i.e. transitioning from the latent state to active disease, occurs at a rate of ~ 10% per year per individual and can be attributed in part to aging, treatment with anti-inflammatory drugs, or due to HIV co-infection (5, 8, 9).

Upon infection with *Mtb* multiple dynamic structures known as granulomas form in the host's lungs and other tissues (e.g. lymph nodes) (4, 7, 10–12). Granulomas form in both latently and actively infected individuals. Granulomas are the site of both bacterial persistence and host immune response, functioning to physically contain and immunologically restrain pathogen outgrowth (12). Therefore, control of bacteria in granulomas is likely critical to preventing infection progression. Granulomas that are

unable to sterilize a large fraction of the bacterial population can seed new granulomas and may lead to pathologies like TB pneumonia (7, 13–16). Successful control of bacteria in granulomas relies on many coordinated host immune responses including secretion of cytokines (effector molecules that direct the immune response), cellular trafficking, and cellular activation (4, 7, 17–22).

Individuals with active *Mtb* infection require antibiotic treatment, necessitating a minimum six-month regimen of daily dosing using four orally dosed drugs (1, 2). Latently infected individuals are also treated with antibiotics, to reduce their chance of reactivation, but regimens are shorter (three to six months) and only require a single antibiotic (1). In contrast, most other bacterial infections are successfully treated within a few weeks using mono-therapies (2). This complex and lengthy treatment regime leads to issues of compliance and chronic toxicity and causes many patients to interrupt treatment before complete bacterial sterilization. In addition, multi-drug resistant TB (MDR-TB) is becoming more prevalent and requires even longer treatment durations (18-24 months) with antibiotics that are more toxic and less effective at killing bacteria (1, 2, 7, 23, 24).

Although TB has been studied for several decades, we still lack a fundamental understanding of the immune response to *Mtb* and a basic knowledge of antibiotic distribution and efficacy at the site of infection. Direct measurement of antibiotics at the site of infection in human and animal models of TB are only recently being reported (2, 25, 26). Therefore many basic questions still surround *Mtb* infection: What immunological responses cause some individuals to develop active TB and a larger portion to develop latent TB? What are the underlying immunological mechanisms that lead to effective pathogen control? Why are current antibiotic regimens ineffective? Can

more effective antibiotic therapies be developed that alleviate compliance and toxicity issues? In this dissertation, we utilize computational and experimental approaches to address key aspects of these questions.

1.2 Fundamentals of *Mycobacterium tuberculosis* Infection and Granuloma Formation

Infection occurs upon inhalation of *Mtb.* Alveolar macrophages phagocytose the bacteria and migrate across the epithelium and into the lung parenchyma. Intracellular *Mtb* are able to avoid phago-lysosomal fusion, allowing intracellular replication and eventual cellular lysis (3, 4, 7, 15, 18, 21, 27–29). These extracellular bacteria infect nearby macrophages, leading to secretion of signaling molecules (chemokines and cytokines). Secretion of signaling molecules recruits more monocytes from the blood to the infection site forming the beginnings of a granuloma (7). A large fraction of the initial cells recruited to the site of infection are neutrophils which phagocytose *Mtb*, yet their role in controlling infection during the initial stages of the immune response remains to be determined (7, 21, 30–32). After ~12-21 days, dendritic cells carrying *Mtb* antigens traffic to nearby draining lymph nodes (Fig. 1.1), and prime the adaptive immune response (21, 27). Once primed, the cells making up the adaptive immune response, mainly T cells and B cells, traffic to granulomas via chemotactic signals. Once the cells of the adaptive immune response arrive at the infection site T cells help contribute to antimicrobial processes through mechanisms such as cellular-mediated killing and induction of macrophage activation (Fig. 1.1) (7, 33).

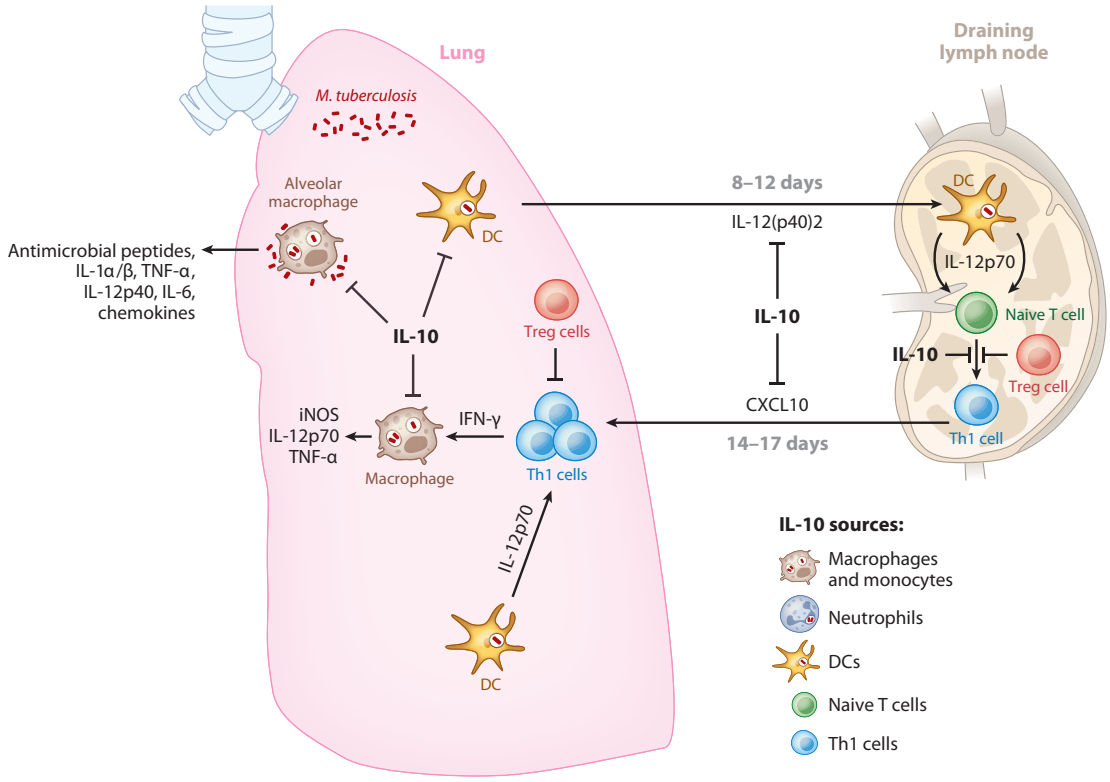

Figure 1.1 Regulation of the immune response to *Mtb* infection by IL-10
Following phagocytosis, bacteria begin replicating inside macrophages. Infected macrophages produce chemokines and cytokines and recruit more macrophages to the site of infection. Dendritic cells (DC) traffic to the nearest draining lymph node to prime the adaptive immune response which consists of many subsets of T cells. These cells traffic back to the site of infection and promote antimicrobial responses, secreting cytokines such as interferon-γ (IFN-γ). Many cells produce IL-10 in granulomas, including infected macrophages, neutrophils, and T cells. IL-10 functions to limit macrophage antimicrobial responses and regulate the production of chemokines and cytokines. Adapted with permission from (7).

The formation and organization of a granuloma, shown in Fig. 1.2, is the pathological hallmark of *Mtb* infection. Granulomas function as both the bacterial niche for pathogen growth and an immune microenvironment for antimicrobial function (7, 21). Granulomas have a distinct spatial and cellular organization including a core of bacteria, infected macrophages, and neutrophils surrounded by an inner shell of resting and activated macrophages, followed by a mixed outer region of T cells, B cells, and macrophages (Fig. 1.2). Recent evidence has revealed that each individual bacterium deposited in the alveolar space leads to the formation of a distinct granuloma (16, 34).

Granulomas form during both active and latent infection (6). In a non-human primate model of TB there are limited differences between granulomas in active and latent classified monkeys. Both classifications display similar measurements of colony forming units (CFU) per granuloma and antimicrobial responses (16). The only significant difference between clinical classifications is the number of total granulomas per host (16). Humans and non-human primates display a broad spectrum of granuloma pathologies including caseous, necrotizing, cellular, calcified, and fibrotic granulomas (3, 21). It is still not well understood if granulomas are host-protective structures or if they promote bacterial persistence and pathology (7, 21). Most likely granulomas in different stages of infection and pathology cover a broad spectrum of host-protective or pathogenic characterization (4, 7). An important goal in understanding TB is determining the characteristics and mechanisms of the immune response in granulomas that function to properly control infection in comparison with granulomas that fail to exert long-term control over the bacteria (4, 7, 21).

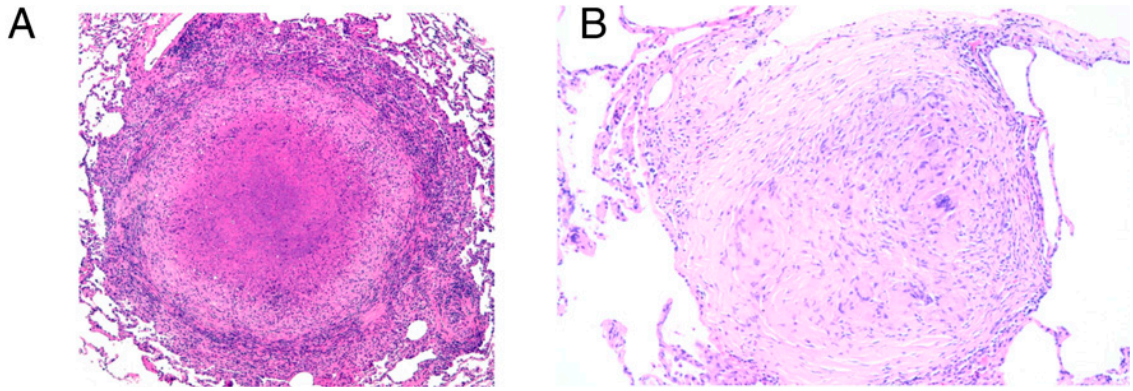

Figure 1.2 Granulomas from the non-human primate model of infection display different pathologies (A) Caseous granuloma with a necrotic center surrounded by macrophages and a peripheral region of lymphocytes (B) Healing granuloma characterized by a central regions undergoing fibrous transformation. Adapted with permission from (35).

1.2.1 Important Cells and Molecules During Infection

Formation of a granuloma relies on coordinated immune processes including cellular recruitment, cellular activation, antimicrobial function, and production of molecular mediators known as cytokines and chemokines (4, 5, 20, 36–40). Chemokines such as CCL2 and CCL5, secreted by infected and activated macrophages, are critical to recruiting T cells to the site of infection (19, 29, 39, 41–45). In human, non-human primate, and murine models of TB, the CD4+ T cell response is necessary for effective control of bacteria in granulomas (46, 47). The primary effector function of antigen-specific CD4+ T cells is the production of interferon-γ (IFN-γ), which is a necessary signal for activation of macrophages (7, 21, 22, 41, 47). Another CD4+ T cell effector function that may be necessary is the ability to induce apoptosis of infected macrophages through the Fas/Fas-ligand pathway (48, 49). CD8+ T cells contribute to control of infection through cytotoxic functions such as perforin/granzyme based killing mechanisms (50). Additionally, both CD4+ and CD8+ T cells derived from granulomas have the capability to produce cytokines (47, 51). However, there is evidence that only a small fraction of T cells in granulomas actually produce cytokines during infection (personal communication – Joanne Flynn).

Cytokines are key molecular mediators of the immune response and influence the behavior and fate of many immune cells and processes during *Mtb* infection. The pro-inflammatory cytokine tumor necrosis factor-α (TNF) is a critical component for infection control, while interleukin-10 (IL-10) functions as an anti-inflammatory cytokine and has been correlated with worsened infection outcome in both a clinical and experimental setting (30, 31, 52–55). A balance of these pro- and anti-inflammatory

mediators is thought to be central to granuloma function and infection control, but the complexity of the immune response and limitations of experimental models has constrained our understanding (7, 21, 52, 56–60).

1.2.2 Tumor Necrosis Factor-α (TNF)

TNF is produced by NFκB activated macrophages, *Mtb* infected macrophages, and both CD4+ and CD8+ T cells in response to infection (Fig. 1.1) (38, 61). During infection, TNF controls many bactericidal and immune responses. Classical macrophage activation occurs through TNF induction of the NFκB pathway, in conjunction with IFN-γ and the STAT1 pathway (20, 62–66). TNF influences recruitment of cells to the site of infection and induces the production of chemokines from macrophages (e.g. CCL2, CCL5) (67). TNF signaling can also result in cellular apoptosis through caspase-mediated pathways (66, 68). TNF abrogation during *Mtb* infection, through either genetic knockouts or antibody-based depletion, demonstrates its critical nature to formation, function, and maintenance of granulomas (9, 36–38, 69–72). In murine models granulomas form improperly and are largely unstructured, while latently infected non-human primates treated with anti-TNF molecules have increased bacterial burdens (9, 36–38, 69–72). Additionally, TNF antagonists, such as those used to treat rheumatoid arthritis increase the incidence of TB reactivation in humans (73, 74). As the immune response to *Mtb* is highly complex and contains many TNF-related mechanisms, the function of TNF in a granuloma is still being elucidated.

1.2.3 Interleukin-10 (IL-10)

IL-10 is produced by a spectrum of immune cells during *Mtb* infection, including many macrophage and T-cell subsets (Fig. 1.1) (7, 52). IL-10 functions by inhibiting cytokine/chemokine production, preventing cellular apoptosis/necrosis, and reducing macrophage activation (75–78). The classical source of IL-10 during *Mtb* infection is the macrophage (21). Activated macrophage derived IL-10 is thought to control excess cellular activation and limit host-induced tissue damage (57, 75, 79, 80). Infection of macrophages with *Mtb* induces significant IL-10 production due to interaction of toll-like receptors and pattern-recognition receptors with *Mtb*-derived molecules (7, 13, 55, 81–84). Different strains of *Mtb* have been shown to induce greater production of IL-10 upon infection and may be linked to pathogen virulence (7). Recent evidence has pointed to neutrophils as a significant source of IL-10 (Fig. 1.1), but their contribution to overall IL-10 production in granulomas and effects on infection outcome are still poorly characterized (30, 85, 86). Additionally, many T cell subsets, including CD4+, CD8+, and regulatory T cells can also produce large quantities of IL-10 (Fig. 1.1) which may contribute to overall control of the host immune response (87–92).

The role of IL-10 during *Mtb* infection is still not well understood, in part due to the spectrum of cellular sources. It is thought that IL-10 contributes to pathogen persistence by diminishing the strength of the antimicrobial immune response to *Mtb* in order to prevent excess lung damage and pathology (7, 52, 57, 93). Studies of IL-10 genetic knockouts in murine models of TB have been difficult to interpret. Early studies demonstrated no difference in bacterial load, while more recent reports have shown increased inflammatory responses and reduced bacterial burdens in both lungs and spleen

(7, 94, 95). Additionally, some reports indicated reduction in bacterial load was associated with increased inflammation and tissue pathology (93).

A central feature of many granulomas is an acellular caseous necrotic core, which may provide a route to airway erosion and fibrosis (4, 43). Both anti-microbial and pathogenic mechanisms contribute to caseous necrosis, and IL-10 may be critical in regulating acceptable levels of caseous necrosis and subsequent host damage. During *Mtb* infection IL-10 limits macrophage apoptosis/necrosis but how inhibition of these mechanisms prevents tissue damage is still unclear (43, 59, 78, 96–105). The spectrum of cellular sources, numerous functions, and granuloma complexity has limited our ability understand the role of IL-10 during *Mtb* infection (Fig. 1.1). Furthermore, measuring the spatiotemporal dynamics of IL-10 during granuloma formation and function in a relevant animal model is very difficult. Additional challenges arise when attempting to experimentally dissect how the dynamics of two cytokines with opposing functions, TNF and IL-10, could control bacterial levels in a granuloma (7, 21, 52).

1.2.4 The Spectrum of Macrophage Polarization

In recent years, the complexity of macrophage differentiation and activation in response to different stimuli has been a subject of active study. Macrophages have been classified into to two characteristic populations, known as polarization states (Fig. 1.3) (21, 64, 106). M1 (or classically activated) macrophages display a pro-inflammatory phenotype, expressing high levels of pro-inflammatory cytokines (e.g. TNF), high production of reactive nitrogen and oxygen species, and strong antimicrobial capabilities (64, 106, 107). M2 (or alternatively activated) macrophages display an anti-inflammatory

phenotype, expressing high levels of anti-inflammatory cytokines (e.g. IL-10), promoting wound healing and tissue remodeling, and reduced bactericidal action (79, 108, 109).

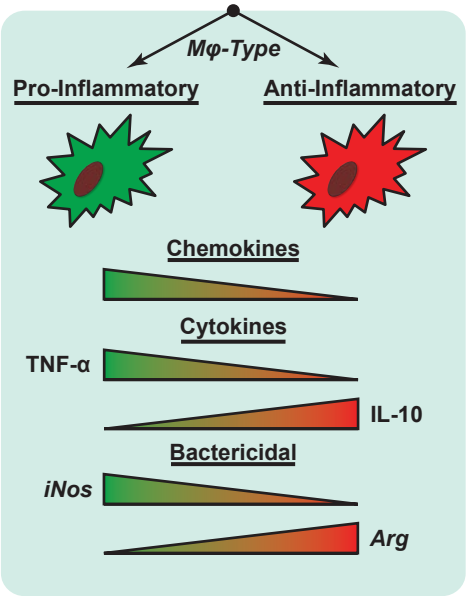

Figure 1.3 Diagram demonstrating the spectrum of macrophage polarization and related effector functions
As macrophages are polarized towards a pro-inflammatory (M1) state they demonstrate increased production of TNF and chemokines, reduced production of IL-10, and increased bactericidal function. As macrophages are polarized towards an anti-inflammatory (M) state they demonstrate increased production of IL-10, reduced production of TNF and chemokines, and reduced bactericidal function.

Many cell types participate in the immune response to *Mtb*, but the macrophage is the primary cell type and functions to control inflammation, contribute to antimicrobial processes, and harbor the pathogen (21, 110). Although macrophages are a significant fraction of the cells in granulomas, the spectrum of macrophage activation states in the context of *Mtb* infection is still not well understood. Animal models of TB suggest that different macrophage polarization states can control granuloma pathology through induction of pro- and anti-inflammatory responses (111). M1 macrophages are thought to be associated with the primary antimicrobial response during the early stages of infection, while M2 macrophages are thought to control late stage inflammation to prevent excess

pathology (21). In a non-human primate model of infection, multiple granuloma types displayed a characteristic spatial separation between M1 and M2 macrophage, with M1-like macrophages closer to the center of the structure and M2-like macrophages mainly in the peripheral regions (111).

TNF and IFN-γ stimulation and signaling through NFκB and STAT1 pathways respectively, leads to M1 macrophage polarization (106, 112). Conversely, stimulation of macrophages with IL-10, along with other cytokines, leads to STAT3 signaling which causes M2 polarization (106, 109). In the context of granuloma formation and function in response to *Mtb*, the temporal dynamics of macrophage polarization due to cytokine stimulation and their contribution to infection are not understood. How macrophages polarize over the course of infection, spatially organize, and control outcome presents a significant challenge that cannot currently be determined using experimental methods.

1.3 Antibiotic Treatment of TB

Treatment of antibiotic susceptible TB requires a minimum of 6 months of combination therapy with rifampicin (RIF), isoniazid (INH), pyrazinamide (PZA), and ethambutol (ETH) (1, 2). The number of different antibiotics and prolonged treatment length leads to poor patient compliance and increased frequency of withdrawal from treatment (2, 25, 35, 113). This can cause treatment failure, infection relapse, and emergence of antibiotic resistant bacterial populations (2, 24). Therefore, availability of shorter and more effective treatment regimens could have a large impact on the global disease burden of TB.

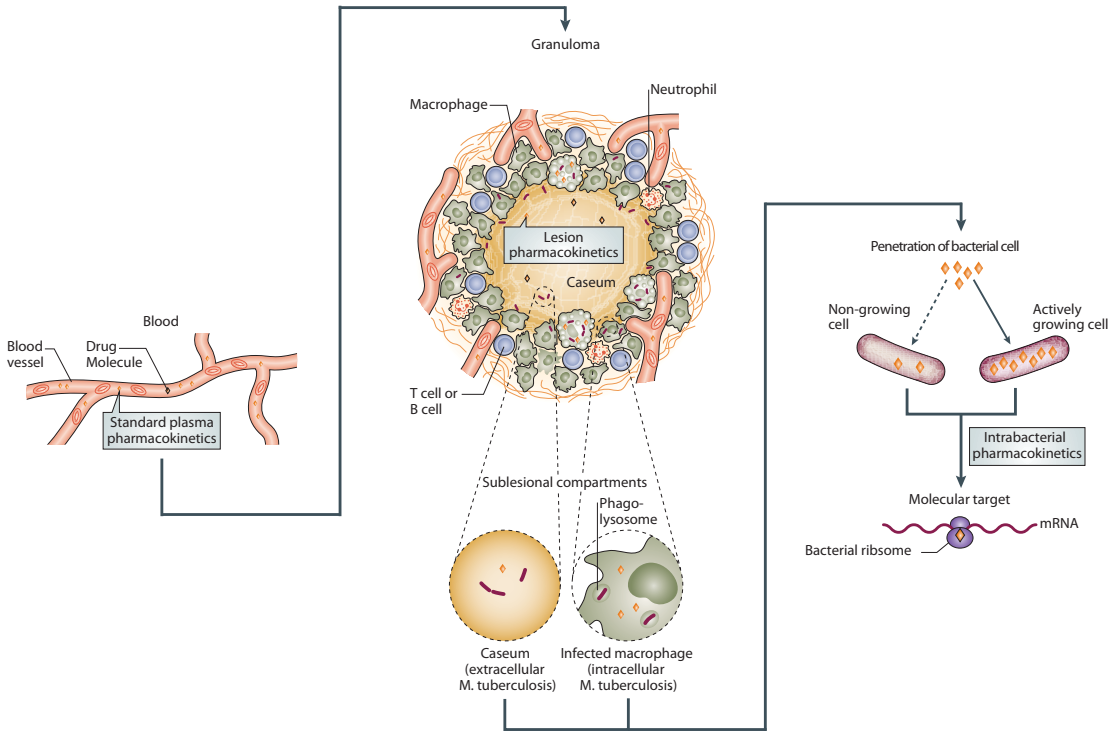

Figure 1.4 The path of antibiotics from the blood to the site of action during *Mtb* infection
From systemic circulation antibiotics enter the lung tissue and must penetrate the densely packed granuloma. Antibiotics accumulate in immune cells and are metabolized. Antibiotics must permeate far enough into the granuloma to reach distinct populations of bacteria (extracellular or intracellular) residing near the center of the lesion. Furthermore, the antibiotics must cross the bacterial cell wall to reach their intended molecular target. Adapted with permission from (2).

Optimization of the current treatment duration and the use of polypharmacy were established using empirical processes based on 40 years of patient trials (113). Consequently, there has been limited rational design and optimization of dosing strategies, along with a striking lack of knowledge as to how antibiotics distribute from systemic circulation to the site of infection (Fig. 1.4) (2, 113). We are only beginning to understand how each antibiotic differentially distributes from the plasma into granulomas (2, 25, 26). Two of the first line drugs, RIF and INH exhibit significantly lower antibiotic concentrations in granulomas than in plasma, while moxifloxacin accumulates in both lung tissue and granulomas relative to plasma (2, 25). Further complications arise when

attempting to understand the effects of these unique antibiotic distributions in granulomas (Fig. 1.4). The heterogeneity in spatial organization of bacterial populations, replication state of bacteria, and vascular supply all contribute to the efficacy of antibiotics at the site of infection (2). It is likely that a combination of these factors contributes to the lengthy antibiotic course required for treatment. Direct measurement of antibiotic gradients and their underlying dynamics at the site of infection in animal models of TB is very difficult. MALDI-mass-spec-imaging is emerging as the most promising technique, yet it is invasive and is limited to non-temporal studies (2, 26).

Despite the primary importance of antibiotic concentrations at the site of infection, many animal pharmacodynamics studies still rely on comparing plasma concentrations of antibiotics to minimum-inhibitory concentrations (MIC) determined in broth culture (113). This has lead to poor predictive indices of antibiotic efficacy, such as exposure after a single dose. We are beginning to learn that common 'rules-of-thumb', such as assuming drug equilibration between plasma and all granulomas, cannot be used to assess the efficacy of antibiotics for the treatment of TB (2, 113). In addition, comparison of antibiotic regimens using different doses or dose frequencies in a clinical setting is rare. Only a limited number of trials can be completed due to patient availability, along with many ethical concerns associated with standard of care (114). New antibiotic regimens that take into account a basic understanding of differential distribution into tissues and granulomas in order to optimally penetrate granulomas could help reduce failed treatments and increase the sterilizing capabilities of existing antibiotics. Measurements of differential distributions in experimental systems are difficult to carry out and have limited temporal resolution due the sheer sample size that

would be required. In addition, an experimental technique to track both the temporal dynamics of antibiotics and bacterial load simultaneously at the single granuloma level does not exist. Therefore, we need novel tools that can accurately replicate the dynamics of antibiotic treatment in granulomas over long timescales in order to better understand how temporal dynamics of antibiotics contributes to treatment outcome.

1.4 Inhaled Delivery of Antibiotics

Orally dosed antibiotics must navigate a significant number of transport hurdles in order to reach *Mtb* in granulomas (Fig. 1.4). Delivery of antibiotics via an inhaled route may overcome many limitations of oral dosing for treatment of TB by providing: direct dosing to the disease site, reduced systemic toxicity and clearance, and improved patient compliance with reduced dosing frequency (115–118). Aerosolized drugs have been successfully used for many years to treat diseases such as cystic fibrosis, asthma, and many other respiratory infections (116). However, development of inhaled formulations of antibiotics for the treatment of TB is still a relatively new field (116).

A fabricated carrier loaded with one or more antibiotics is dosed into the lungs (Fig. 1.5) through an aerosol delivery system (e.g. nebulizer) (116, 118). Based on physical characteristics, carriers settle in different regions of the lungs (119, 120). Once deposited, carriers are taken up by alveolar macrophages and lung endothelial cells, and release the loaded antibiotic based on tunable physio-chemical properties (Fig. 1.5) (115, 117). An inhaled dose should elevate antibiotic concentrations in the lungs and will avoid first-pass metabolism (121). This could expose *Mtb* in granulomas to significantly higher antibiotic concentrations compared to oral dosing.

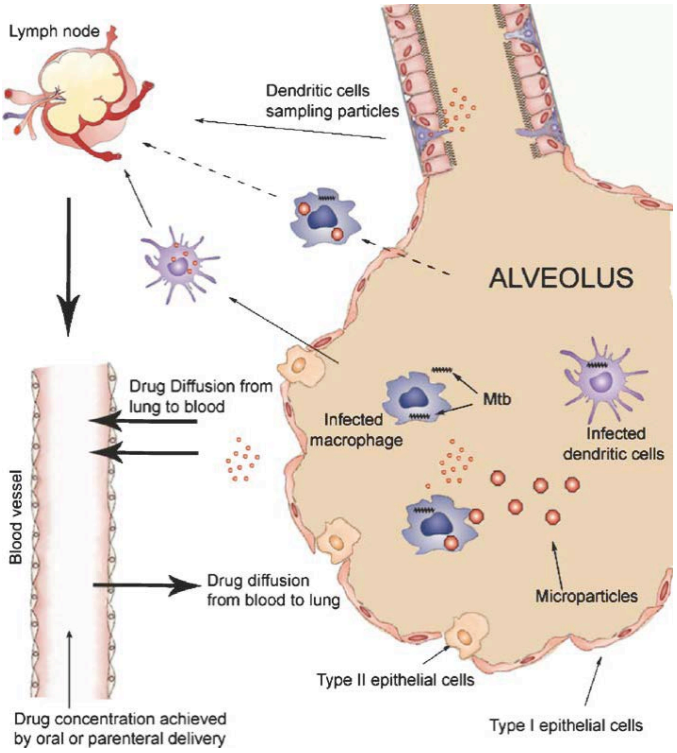

Figure 1.5 Comparison of inhaled and oral administration routes
Inhaled formulations deposit in the alveolus after dosing and are taken up by healthy and infected macrophages. Inhaled formulations release antibiotics into the lung and thus antibiotics diffuse from the lung tissue and drain into blood vessels. As oral administration relies on antibiotics reaching systemic circulation the antibiotics diffuse from the blood vessels into the lung tissue. Adapted with permission from (116).

In an *in vitro* setting, antibiotic carriers are rapidly phagocytosed by infected macrophages, elevating intracellular concentrations and improving sterilization capabilities (122–127). However, *in vitro* studies poorly reflect the structural organization and heterogeneity of granulomas (3). In a guinea pig model of TB, inhaled PLGA carriers co-loaded with RIF and INH had similar sterilizing capabilities as 45 daily oral doses of antibiotics (117, 128). A single dose of an inhaled formulation of INH to healthy non-human primates demonstrated a 2-fold higher AUC/MIC index measured from plasma, compared to oral doses (129). An inhaled formulation of capreomycin was well-tolerated

in the lungs of healthy humans, but measured plasma concentrations were above MICs only for the highest dose (300 mg) and for less than 4 hours (130). To rationally design inhaled formulations it is necessary to understand the contributions of pharmacokinetics, pharmacodynamics, and behavior at the site of infection. Measuring and understanding these dynamics in clinically relevant models (e.g. non-human primates) is difficult and costly. Thus, new approaches are needed to quickly assess the efficacy and dynamics of inhaled formulations for the treatment of TB in order to considerably reduce development time of new treatments.

1.5 Models of TB

1.5.1 Experimental Models of TB

Early stage human clinical samples of granulomas are rarely available. Bronchoalveolar lavage (BAL) fluid can be collected from patients, but it only represents a sample of the epithelial lining fluid and not what is occurring granulomas (32, 51). Similarly, blood can be drawn from patients in an attempt to measure biomarkers of infection, such as T cell phenotypes (131–133). There is limited evidence that the blood accurately reflects the infection environment and to date no good biomarkers correlating with *Mtb* infection control have been discovered (133).

Therefore, we have relied on animal models to contribute much to our understanding of the immunology and pathology of TB (3, 116, 134). Murine models are the most commonly used animal models for the study of TB, as they are cost-effective and have a wide variety of available reagents. Murine models are the most useful for studying the immunological response to chronic *Mtb* infection (3). However, the

granulomas that form in response to infection are very different than those in humans. The well-circumscribed cuff of lymphocytes surrounding an inner core of macrophages found in humans does not exist in murine models. Instead, murine granulomas are unorganized structures containing a mix of macrophages and lymphocytes (3, 7). Human granulomas develop much different pathology during the later stages of infection, such as necrosis, fibrosis, and calcification, which murine granulomas do not form (3, 135). In addition, the murine model has no latent state of infection, observed in the majority of human infections. *Mtb* replicate freely during the first ~4 weeks of infection in the murine model, and upon the onset of adaptive immunity the bacterial load remains stable for many months (17, 68, 136). This chronic state of elevated bacterial load leads to disease progression and eventual morbidity (3). In comparison, the bacterial load in humans is reduced to very low levels after the onset of the adaptive immune response (136). There are also murine models that use *Mtb*-derived antigen instead of live bacteria to quickly and cheaply study the immune response during TB (72, 137, 138). These models use bacterial antigens conjugated to inert beads which induce a granuloma-like structure to form in the lungs after ~2 weeks in sensitized mice. These *Mtb* antigen-display models elicit a highly Th-1 polarized response with dendritic cells and macrophages coalescing near the beads (137–139).

Other animal models are used to study infection such as guinea pigs and zebrafish. *Mycobacterium marinum* is a genetic relative of *Mtb* that infects fish and other ecotherms (140, 141). In response to M. marinum, zerbrafish develop organized granulomas that are necroctic and progressive. The main advantage of zebrafish models of infection is that the host is transparent in its early life allowing the early immune

response to be studied temporally (140). Guinea pig models of TB are progressive, similar to the murine model, yet are able to better recapitulate the granuloma organization observed in humans (3, 142, 143). Guinea pigs are highly susceptible to *Mtb* infection and thus they represent a good model of an unsuccessful host immune response (3). This makes guinea pig models a good model for testing vaccines, as a successful vaccine must protect against *Mtb* in the most unsuccessful of host responses (3, 144).

Non-human primates (NHPs) have re-emerged as the best pathological representation of human TB. Given a low infectious dose of *Mtb,* NHPs develop both 'active' and 'latent' classifications of disease similar to what is observed in humans (14, 16, 18, 135). Furthermore, the spectrum and heterogeneity of granuloma pathologies (caseous, fibrotic, necrotic, etc.) seen in humans is well-represented within the same animal (18, 135). Similar to infection in humans, bacteria replicate freely until the onset of the adaptive immune response wherein the bacterial load drops significantly to very low levels (16). In lesions from NHPs with either active or latent infection, the killing capacity of the immune response is similar at the individual granuloma scale, with a significant number of sterile granulomas (a granuloma with no detectable bacteria) existing in both outcomes (16). This heterogeneity between granulomas makes it difficult to identify predictors of disease outcome, but is critical to recapitulating the immune response observed in humans. Yet, there are significant drawbacks to the NHP model: reagents are not as readily available, animal rights concerns, the animals require BSL-3 facilities, and there are significant upfront and maintenance costs.

No animal model is able to fully represent the diversity and heterogeneity of human granulomas and human disease. In addition, the pharmacokinetics and metabolism

of antibiotics vary significantly between different species (145, 146). The choice of which model system to use relies heavily on what facet of *Mtb* infection is to be studied along with two practical factors, cost and availability of reagents.

1.5.2 Computational Models of Mtb Infection and Treatment

Biological processes act over multiple spatial (molecular, cellular, tissue) and temporal scales (seconds, minutes, hours) with constant cross talk between scales (147, 148). For instance, it is difficult to understand how changes to cytokine concentrations, like IL-10, can manifest itself across spatiotemporal scales and control infection outcome in an experimental model. Computational models can help to understand and translate the wealth of experimentally generated data by creating a multi-scale realization of systems level behavior of the immune response to *Mtb* infection (9, 36, 37, 57, 58, 71, 80, 149–153). Furthermore, computational models of TB can be used for *in silico* experiments, such as predicting new mechanisms or discovering new drug targets, which may not feasible in current experimental models of TB.

Differential equation models are deterministic models that describe species of interest as a continuous variable that is a function of space, time, or both. Once parameter values are fit to experimental data or estimated from literature, differential equation models can be quickly solved and used to easily explore the dynamics of infection over long time scales (58, 80). These types of models have been used to understand the roles of cytokines (such as TNF, IL-10, and IFN-γ) in granulomas, the role of T cell priming and trafficking to granulomas, and macrophage polarization during *Mtb* infection (58, 72,

80, 152). However, it is difficult to replicate the spatial heterogeneity of granulomas, the stochastic nature of infection, and differential outcomes using a deterministic model.

In addition to modeling *Mtb* infection, differential equations have been used to model the pharmacokinetics (PK) of antibiotics for the treatment of TB (25, 154–156). Pharmacokinetics refers to the prediction of the time varying concentrations of a substance in a living system (146). Typically, a compartment represents each organ or lumped-versions of organs and flow of antibiotics in and out of each compartment is assumed to be first order. By simple antibiotic mass balance a differential equation model of each compartment is constructed (146). Data from the plasma of patients or animals is used to fit model parameters. The calibrated PK model is then used to predict antibiotic efficacy or to examine overall drug distribution. These types of models have been used for studies such as: understanding the PKs of RIF and how it may contribute to development of resistance; understanding the distribution of RIF and INH from the plasma to the lungs and finally to granulomas (25, 154). However, classical PK models to study the efficacy of antibiotics during *Mtb* infection use very simple descriptions of the granuloma or bacteria. These models assume a well-mixed granuloma compartment with no heterogeneity in bacterial replication states or spatial distributions (25, 154, 155, 157–160). Further work is needed to accurately link PK models of antibiotic distribution with heterogeneous models of granulomas to enable prediction of the effects of drug dynamics, bacterial populations, and bacterial distributions on treatment efficacy.

Agent-based models (ABMs), sometimes referred to as individual-based models, are stochastic models that utilize discrete entities known as agents (161–163). Each agent is autonomous and behaves based on the set of rules, interactions, and states given to it.

Since each agent acts as an individual entity, spatial and temporal heterogeneity arises naturally in the model (161, 162). In addition, an environment containing soluble molecules is modeled using differential equation models of diffusion and reaction (37, 151, 164, 165). Agents interact with the environment, which can influence decisions and behavior. An advantage of ABMs is their ability to generate complex system-level emergent behavior from the simple rule-based descriptions of each individual (149, 161, 163). ABMs have been used to describe the immune response to *Mtb*, leading to emergent formation of a granuloma after infecting a single macrophage (37, 151). An advantage of ABMs is that both infection dynamics and the immune response (various immune cells and cytokines, e.g. macrophages, T cells, TNF, and IL-10) can be easily tracked in space and time, unlike experimental systems. ABMs of *Mtb* infection predicted the influence of the timing of the adaptive immune response and importance of TNF in controlling infection outcome (37, 151).

Interactions of cells and their environment are fundamental mechanisms on which biological systems are built, with constant exchange of information between the two (147, 148). Recently, ABMs have been linked to differential equation models that describe the single-cell level receptor-ligand trafficking and intracellular signaling events of cytokines (9, 36, 57, 71). Inclusion of these dynamics creates multi-scale ABMs that better describe the influence of extracellular mediators and processes on biological behavior across spatiotemporal scales. This allows agents in an ABM to interact with the environment in more detail by binding soluble ligands to cell-associated receptors, and initiating various signaling pathways (36, 57, 71). ABMs of *Mtb* infection were linked to single-cell level models of TNF receptor-ligand trafficking dynamics and used to predict

the importance of TNF receptor internalization on controlling bacterial levels and inflammation (36). An additional model of NFκB signaling was added to the model of TNF receptor-ligand trafficking dynamics and used to predict the effects of mRNA stability on bacterial levels and inflammation (71). However, the effects of IL-10 and its receptor-ligand trafficking dynamics on TNF availability, macrophage polarization, and infection outcome still need to be elucidated since they can have significant impacts on the antimicrobial response.

1.6 Dissertation Overview

The goal of this dissertation is two-fold. First, we use computational and experimental models of *Mtb* infection to understand how the pro-inflammatory cytokine TNF and the anti-inflammatory cytokine IL-10 functionally co-exist in granulomas. We determine that a balance of TNF and IL-10 can control the trade-off between inflammation and tissue damage. We investigate the role of a balance of TNF and IL-10 on shaping macrophage polarization in granulomas. We also examine how IL-10 can influence bacterial sterilization at the single granuloma level.

Second, we use computational techniques to understand antibiotic treatment of *Mtb* infection at the single granuloma level. We investigate the value of inhaled formulations of antibiotics, in comparison with current orally dosed regimens, to improve antibiotic distribution and treatment efficacy.

These two broad goals are covered in four sections:

1.6.1 Aim 1: Development of a Computationally Efficient Hybrid Multi-Scale Agent-Based Model of TB Infection

Previously developed hybrid multi-scale agent-based models of *Mtb* infection have provided valuable insights and predictions of important mechanisms and possible therapeutic targets (9, 36, 37, 71, 151, 152). Yet, as more processes are modeled, computational tractability of models significantly decreases. In order to include new processes of interest (e.g. IL-10 and antibiotics) while maintaining computational tractability, we explore ways to improve computational speed. We implement three different numerical algorithms for solving soluble molecule diffusion and two numerical algorithms for solving individual agent receptor-ligand and intracellular signaling processes. Additionally, we demonstrate the concept of tuneable resolution and its ability to significantly reduce model complexity (150). We show when implementation of particular numerical algorithms can significantly reduce computational times. The development of efficient hybrid multi-scale agent-based models is discussed in Chapter 2.

1.6.2 Aim 2: Identifying the Roles of TNF and IL-10 During Granuloma Formation Using Multi-Scale Computational Modeling

Several studies have suggested that a balance of TNF and IL-10 could be a crucial mediator between controlling bacterial growth while simultaneously preventing host induced tissue damage (6, 52, 54, 60, 87). However, there are many unanswered questions surrounding TNF and IL-10 in the context of *Mtb* infection: What molecular scale processes control the concentrations of TNF and IL-10? Does a balance of TNF and IL-10 promote granulomas to contain bacteria? How do TNF and IL-10 control

macrophage polarization during granuloma formation? What role does IL-10 play in determining granuloma sterilization or bacterial persistence? We address the complex and multi-scale effects of TNF and IL-10 during *Mtb* infection by developing a model that integrates both TNF and IL-10 single-cell level receptor-ligand dynamics. We subsequently extend the model by describing the intracellular signaling pathways associated with TNF and IL-10 (NFκB and STAT3). Using these models we predict the impact of a balance of TNF and IL-10 related-processes on infection control, granuloma outcome, inflammation, and macrophage polarization (57). Model development and analyses are discussed in Chapter 3, 4, and 5.

1.6.3 Aim 3: Understanding and Improving the Efficacy of Antibiotics in Granulomas During TB Infection

We expand our multi-scale agent-based model by incorporating pharmacokinetic (PK) and pharmacodynamic (PD) models of RIF and INH. This model allows us to elucidate the spatial and temporal dynamics of antibiotic treatment at the site of *Mtb* infection that cannot be explored in experimental systems. We develop a model of inhaled formulations of antibiotics using carrier encapsulation properties to control antibiotic availability in granulomas. Using these models we demonstrate the failure of oral dosing to sterilize bacteria due to sub-optimal exposure and bacterial re-growth. Additionally, we predict novel inhaled formulations of RIF and INH that can reduce dosing frequency and improve sterilizing capabilities. Model development and analyses are discussed in Chapter 6 and Appendix C.

1.6.4 Aim 4: Measuring TNF Concentration Gradients in TB Granulomas

Previous computational studies have identified that concentration gradients of TNF controls differential regulation of cellular activation and apoptosis processes in granulomas (9, 72). However, little experimental work has been dedicated to measuring gradients of cytokines in granulomas even though they could be an essential feature of the immune response to infection. Using a simple experimental system of murine granuloma formation we measure spatial gradients of TNF in *ex vivo* lung samples. We create a methodology for reconstructing soluble gradients based on data collected using flow cytometry and fluorescence microscopy and an idealized representation of TNF receptor-ligand trafficking. The development of the experimental method and proof-of-concept results are demonstrated in Chapter 7.

1.7 References

1. *Global Tuberculosis Report 2013*,. World Health Organization, Geneva ; :1–145.

2. Dartois, V. 2014. The path of anti-tuberculosis drugs: from blood to lesions to mycobacterial cells. *Nat. Rev. Microbiol.* 12: 159–167.

3. Flynn, J. L. 2006. Lessons from experimental Mycobacterium tuberculosis infections. *Microbes Infect.* 8: 1179–88.

4. Flynn, J. L., and J. Chan. 2001. Immunology of tuberculosis. *Annu. Rev. Immunol.* 19: 93–129.

5. Lin, P. L., and J. L. Flynn. 2010. Understanding latent tuberculosis: a moving target. *J. Immunol.* 185: 15–22.

6. Gideon, H. P., and J. L. Flynn. 2011. Latent tuberculosis: what the host “sees”? *Immunol. Res.* 50: 202–12.

7. O’Garra, A., P. S. Redford, F. W. McNab, C. I. Bloom, R. J. Wilkinson, and M. P. R. Berry. 2013. The immune response in tuberculosis. *Annu. Rev. Immunol.* 31: 475–527.

8. Flynn, J. L. 2004. Immunology of tuberculosis and implications in vaccine development. *Tuberculosis* 84: 93–101.

9. Fallahi-Sichani, M., J. L. Flynn, J. J. Linderman, and D. E. Kirschner. 2012. Differential risk of tuberculosis reactivation among anti-TNF therapies is due to drug binding kinetics and permeability. *J. Immunol.* 188: 3169–78.

10. Ehlers, S., and U. E. Schaible. 2012. The granuloma in tuberculosis: dynamics of a host-pathogen collusion. *Front. Immunol.* 3: 411.

11. Davis, J. M., and L. Ramakrishnan. 2008. "The very pulse of the machine": the tuberculous granuloma in motion. *Immunity* 28: 146–8.

12. Ramakrishnan, L. 2012. Revisiting the role of the granuloma in tuberculosis. *Nat. Rev. Immunol.* 12: 352–66.

13. Ordway, D., M. Henao-Tamayo, M. Harton, G. Palanisamy, J. Troudt, C. Shanley, R. J. Basaraba, and I. M. Orme. 2007. The hypervirulent Mycobacterium tuberculosis strain HN878 induces a potent TH1 response followed by rapid down-regulation. *J. Immunol.* 179: 522–31.

14. Lin, P. L., T. Coleman, J. P. J. Carney, B. J. Lopresti, J. Tomko, D. Fillmore, V. Dartois, C. Scanga, L. J. Frye, C. Janssen, E. Klein, C. E. Barry, and J. L. Flynn. 2013. Radiologic responses in cynomolgous macaques for assessing tuberculosis chemotherapy regimens. *Antimicrob. Agents Chemother.* .

15. Cooper, A. M. 2009. Cell-mediated immune responses in tuberculosis. *Annu. Rev. Immunol.* 27: 393–422.

16. Lin, P. L., C. B. Ford, M. T. Coleman, A. J. Myers, R. Gawande, T. Ioerger, J. Sacchettini, S. M. Fortune, and J. L. Flynn. 2014. Sterilization of granulomas is common in active and latent tuberculosis despite within-host variability in bacterial killing. *Nat. Med.* 20: 75–9.

17. Mohan, V. P., C. A. Scanga, K. Yu, H. M. Scott, K. E. Tanaka, E. Tsang, M. M. Tsai, J. L. Flynn, and J. Chan. 2001. Effects of tumor necrosis factor alpha on host immune response in chronic persistent tuberculosis: possible role for limiting pathology. *Infect. Immun.* 69: 1847–55.

18. Lin, P. L., S. Pawar, A. Myers, A. Pegu, C. Fuhrman, T. a Reinhart, S. V Capuano, E. Klein, and J. L. Flynn. 2006. Early events in Mycobacterium tuberculosis infection in cynomolgus macaques. *Infect. Immun.* 74: 3790–803.

19. Algood, H. M. S., and J. L. Flynn. 2004. CCR5-deficient mice control Mycobacterium tuberculosis infection despite increased pulmonary lymphocytic infiltration. *J. Immunol.* 173: 3287–96.

20. Algood, H. M. S., P. L. Lin, D. Yankura, A. Jones, J. Chan, and J. L. Flynn. 2004. TNF influences chemokine expression of macrophages in vitro and that of CD11b+ cells in vivo during Mycobacterium tuberculosis infection. *J. Immunol.* 172: 6846–57.

21. Flynn, J. L., J. Chan, and P. L. Lin. 2011. Macrophages and control of granulomatous inflammation in tuberculosis. *Mucosal Immunol.* 4: 271–8.

22. Flynn, J. L., J. Chan, K. J. Triebold, D. K. Dalton, T. a Stewart, and B. R. Bloom. 1993. An essential role for interferon gamma in resistance to Mycobacterium tuberculosis infection. *J. Exp. Med.* 178: 2249–54.

23. Russell, D. G., C. E. Barry, and J. L. Flynn. 2010. Tuberculosis: what we don't know can, and does, hurt us. *Science* 328: 852–6.

24. Duncan, K., and C. E. Barry. 2004. Prospects for new antitubercular drugs. *Curr. Opin. Microbiol.* 7: 460–5.

25. Kjellsson, M. C., L. E. Via, A. Goh, D. Weiner, K. M. Low, S. Kern, G. Pillai, C. E. Barry, and V. Dartois. 2012. Pharmacokinetic evaluation of the penetration of antituberculosis agents in rabbit pulmonary lesions. *Antimicrob. Agents Chemother.* 56: 446–57.

26. Prideaux, B., V. Dartois, D. Staab, D. M. Weiner, A. Goh, L. E. Via, C. E. Barry, and M. Stoeckli. 2011. High-sensitivity MALDI-MRM-MS imaging of moxifloxacin distribution in tuberculosis-infected rabbit lungs and granulomatous lesions. *Anal. Chem.* 83: 2112–8.

27. Grosset, J. 2003. Mycobacterium tuberculosis in the extracellular compartment: an underestimated adversary. *Antimicrob. Agents Chemother.* 47: 833–6.

28. Cooper, A. M., and E. Torrado. 2012. Protection versus pathology in tuberculosis: recent insights. *Curr. Opin. Immunol.* 24: 431–7.

29. Cambier, C. J., K. K. Takaki, R. P. Larson, R. E. Hernandez, D. M. Tobin, K. B. Urdahl, C. L. Cosma, and L. Ramakrishnan. 2013. Mycobacteria manipulate macrophage recruitment through coordinated use of membrane lipids. *Nature* .

30. Doz, E., R. Lombard, F. Carreras, D. Buzoni-Gatel, and N. Winter. 2013. Mycobacteria-infected dendritic cells attract neutrophils that produce IL-10 and specifically shut down Th17 CD4 T cells through their IL-10 receptor. *J. Immunol.* 191: 3818–26.

31. Blomgran, R., and J. D. Ernst. 2011. Lung Neutrophils Facilitate Activation of Naive Antigen-Specific CD4+ T Cells during Mycobacterium tuberculosis Infection. *J. Immunol.* 186: 7110–9.

32. Eum, S.-Y., J.-H. Kong, M.-S. Hong, Y.-J. Lee, J.-H. Kim, S.-H. Hwang, S.-N. Cho, L. E. Via, and C. E. Barry. 2010. Neutrophils are the predominant infected phagocytic cells in the airways of patients with active pulmonary TB. *Chest* 137: 122–8.

33. Ito, T., J. M. Connett, S. L. Kunkel, and A. Matsukawa. 2013. The linkage of innate and adaptive immune response during granulomatous development. *Front. Immunol.* 4: 10.

34. Ford, C. B., P. L. Lin, M. R. Chase, R. R. Shah, O. Iartchouk, J. Galagan, N. Mohaideen, T. R. Ioerger, J. C. Sacchettini, M. Lipsitch, J. L. Flynn, and S. M. Fortune. 2011. Use of whole genome sequencing to estimate the mutation rate of Mycobacterium tuberculosis during latent infection. *Nat. Genet.* 43: 482–6.

35. Lin, P. L., V. Dartois, P. J. Johnston, C. Janssen, L. Via, M. B. Goodwin, E. Klein, C. E. Barry, and J. L. Flynn. 2012. Metronidazole prevents reactivation of latent Mycobacterium tuberculosis infection in macaques. *Proc. Natl. Acad. Sci. U. S. A.* 109: 14188–93.

36. Fallahi-Sichani, M., M. El-Kebir, S. Marino, D. E. Kirschner, and J. J. Linderman. 2011. Multiscale computational modeling reveals a critical role for TNF-α receptor 1 dynamics in tuberculosis granuloma formation. *J. Immunol.* 186: 3472–83.

37. Ray, J. C. J., J. L. Flynn, and D. E. Kirschner. 2009. Synergy between individual TNF-dependent functions determines granuloma performance for controlling Mycobacterium tuberculosis infection. *J. Immunol.* 182: 3706–17.

38. Flynn, J. L., M. M. Goldstein, J. Chan, K. J. Triebold, K. Pfeffer, C. J. Lowenstein, R. Schreiber, T. W. Mak, and B. R. Bloom. 1995. Tumor necrosis factor-alpha is required in the protective immune response against Mycobacterium tuberculosis in mice. *Immunity* 2: 561–72.

39. Egen, J. G., A. G. Rothfuchs, C. G. Feng, N. Winter, A. Sher, and R. N. Germain. 2008. Macrophage and T cell dynamics during the development and disintegration of mycobacterial granulomas. *Immunity* 28: 271–84.

40. Davis, J. M., and L. Ramakrishnan. 2009. The role of the granuloma in expansion and dissemination of early tuberculous infection. *Cell* 136: 37–49.

41. Cooper, A. M., and S. a Khader. 2008. The role of cytokines in the initiation, expansion, and control of cellular immunity to tuberculosis. *Immunol. Rev.* 226: 191–204.

42. Sierra-Filardi, E., C. Nieto, A. Domínguez-Soto, R. Barroso, P. Sánchez-Mateos, A. Puig-Kroger, M. López-Bravo, J. Joven, C. Ardavín, J. L. Rodríguez-Fernández, C. Sánchez-Torres, M. Mellado, and A. L. Corbí. 2014. CCL2 Shapes Macrophage Polarization by GM-CSF and M-CSF: Identification of CCL2/CCR2-Dependent Gene Expression Profile. *J. Immunol.* .

43. Saunders, B. M., and W. J. Britton. 2007. Life and death in the granuloma: immunopathology of tuberculosis. *Immunol. Cell Biol.* 85: 103–11.

44. Vesosky, B., E. K. Rottinghaus, P. Stromberg, J. Turner, and G. Beamer. 2010. CCL5 participates in early protection against Mycobacterium tuberculosis. *J. Leukoc. Biol.* 87: 1153–65.

45. Ansari, a. W., A. Kamarulzaman, and R. E. Schmidt. 2013. Multifaceted Impact of Host C-C Chemokine CCL2 in the Immuno-Pathogenesis of HIV-1/M. tuberculosis Co-Infection. *Front. Immunol.* 4: 312.

46. Yao, S., D. Huang, C. Y. Chen, L. Halliday, R. C. Wang, and Z. W. Chen. 2014. CD4+ T Cells Contain Early Extrapulmonary Tuberculosis (TB) Dissemination and Rapid TB Progression and Sustain Multieffector Functions of CD8+ T and CD3- Lymphocytes: Mechanisms of CD4+ T Cell Immunity. *J. Immunol.* .

47. Green, A. M., R. Difazio, and J. L. Flynn. 2013. IFN-γ from CD4 T cells is essential for host survival and enhances CD8 T cell function during Mycobacterium tuberculosis infection. *J. Immunol.* 190: 270–7.

48. Torrado, E., and A. M. Cooper. 2011. What do we really know about how CD4 T cells control Mycobacterium tuberculosis? *PLoS Pathog.* 7: e1002196.

49. Gallegos, A. M., J. W. J. van Heijst, M. Samstein, X. Su, E. G. Pamer, and M. S. Glickman. 2011. A gamma interferon independent mechanism of CD4 T cell mediated control of M. tuberculosis infection in vivo. *PLoS Pathog.* 7: e1002052.

50. Stegelmann, F., M. Bastian, K. Swoboda, R. Bhat, V. Kiessler, a. M. Krensky, M. Roellinghoff, R. L. Modlin, and S. Stenger. 2005. Coordinate Expression of CC Chemokine Ligand 5, Granulysin, and Perforin in CD8+ T Cells Provides a Host Defense Mechanism against Mycobacterium tuberculosis. *J. Immunol.* 175: 7474–7483.

51. Gerosa, F., C. Nisii, S. Righetti, R. Micciolo, M. Marchesini, A. Cazzadori, and G. Trinchieri. 1999. CD4(+) T cell clones producing both interferon-gamma and interleukin-10 predominate in bronchoalveolar lavages of active pulmonary tuberculosis patients. *Clin. Immunol.* 92: 224–34.

52. Redford, P., P. Murray, and A. O'Garra. 2011. The role of IL-10 in immune regulation during M. tuberculosis infection. *Mucosal Immunol.* 4: 1–10.

53. Bouabe, H., Y. Liu, M. Moser, M. R. Bösl, and J. Heesemann. 2011. Novel Highly Sensitive IL-10-{beta}-Lactamase Reporter Mouse Reveals Cells of the Innate Immune System as a Substantial Source of IL-10 In Vivo. *J. Immunol.* 187: 3165–76.

54. Duell, B. L., C. K. Tan, A. J. Carey, F. Wu, A. W. Cripps, and G. C. Ulett. 2012. Recent insights into microbial triggers of interleukin-10 production in the host and the impact on infectious disease pathogenesis. *FEMS Immunol. Med. Microbiol.* .

55. Cyktor, J. C., and J. Turner. 2011. Interleukin-10 and immunity against prokaryotic and eukaryotic intracellular pathogens. *Infect. Immun.* 79: 2964–73.

56. Torrado, E., and A. M. Cooper. 2013. Cytokines in the balance of protection and pathology during mycobacterial infections. *Adv. Exp. Med. Biol.* 783: 121–40.

57. Cilfone, N. A., C. R. Perry, D. E. Kirschner, and J. J. Linderman. 2013. Multi-Scale Modeling Predicts a Balance of Tumor Necrosis Factor-α and Interleukin-10 Controls the Granuloma Environment during Mycobacterium tuberculosis Infection. *PLoS One* 8: e68680.

58. Marino, S., A. Myers, J. L. Flynn, and D. E. Kirschner. 2010. TNF and IL-10 are major factors in modulation of the phagocytic cell environment in lung and lymph node in tuberculosis: a next-generation two-compartmental model. *J. Theor. Biol.* 265: 586–98.

59. Rojas, M., M. Olivier, P. Gros, L. F. Barrera, and L. F. García. 1999. TNF-alpha and IL-10 modulate the induction of apoptosis by virulent Mycobacterium tuberculosis in murine macrophages. *J. Immunol.* 162: 6122–31.

60. Saraiva, M., and A. O'Garra. 2010. The regulation of IL-10 production by immune cells. *Nat. Rev. Immunol.* 10: 170–181.

61. Saunders, B. M., H. Briscoe, and W. J. Britton. 2004. T cell-derived tumour necrosis factor is essential, but not sufficient, for protection against Mycobacterium tuberculosis infection. *Clin. Exp. Immunol.* 137: 279–87.

62. Harris, J., J. C. Hope, and J. Keane. 2008. Tumor necrosis factor blockers influence macrophage responses to Mycobacterium tuberculosis. *J. Infect. Dis.* 198: 1842–50.

63. Gutierrez, M. G., B. B. Mishra, L. Jordao, E. Elliott, E. Anes, and G. Griffiths. 2008. NF-kappa B activation controls phagolysosome fusion-mediated killing of mycobacteria by macrophages. *J. Immunol.* 181: 2651–63.

64. Mosser, D. M., and J. P. Edwards. 2008. Exploring the full spectrum of macrophage activation. *Nat. Rev. Immunol.* 8: 958–69.

65. Tay, S., J. J. Hughey, T. K. Lee, T. Lipniacki, S. R. Quake, and M. W. Covert. 2010. Single-cell NF-kappaB dynamics reveal digital activation and analogue information processing. *Nature* 466: 267–71.

66. Wajant, H., K. Pfizenmaier, and P. Scheurich. 2003. Tumor necrosis factor signaling. *Cell Death Differ.* 10: 45–65.

67. Zhou, Z., M. C. Connell, and D. J. MacEwan. 2007. TNFR1-induced NF-kappaB, but not ERK, p38MAPK or JNK activation, mediates TNF-induced ICAM-1 and VCAM-1 expression on endothelial cells. *Cell. Signal.* 19: 1238–48.

68. Keane, J., B. Shurtleff, and H. Kornfeld. 2002. TNF-dependent BALB/c murine macrophage apoptosis following Mycobacterium tuberculosis infection inhibits bacillary growth in an IFN-gamma independent manner. *Tuberculosis (Edinb).* 82: 55–61.

69. Chakravarty, S. D., G. Zhu, M. C. Tsai, V. P. Mohan, S. Marino, D. E. Kirschner, L. Huang, J. Flynn, and J. Chan. 2008. Tumor necrosis factor blockade in chronic murine tuberculosis enhances granulomatous inflammation and disorganizes granulomas in the lungs. *Infect. Immun.* 76: 916–26.

70. Lin, P. L., A. Myers, L. Smith, C. Bigbee, M. Bigbee, C. Fuhrman, H. Grieser, I. Chiosea, N. N. Voitenek, S. V Capuano, E. Klein, and J. L. Flynn. 2010. Tumor necrosis factor neutralization results in disseminated disease in acute and latent Mycobacterium tuberculosis infection with normal granuloma structure in a cynomolgus macaque model. *Arthritis Rheum.* 62: 340–50.

71. Fallahi-Sichani, M., D. E. Kirschner, and J. J. Linderman. 2012. NF-κB Signaling Dynamics Play a Key Role in Infection Control in Tuberculosis. *Front. Physiol.* 3: 170.

72. Fallahi-Sichani, M., M. a Schaller, D. E. Kirschner, S. L. Kunkel, and J. J. Linderman. 2010. Identification of key processes that control tumor necrosis factor availability in a tuberculosis granuloma. *PLoS Comput. Biol.* 6: e1000778.

73. Wallis, R. S. 2009. Infectious complications of tumor necrosis factor blockade. *Curr. Opin. Infect. Dis.* 22: 403–9.

74. Wallis, R. S. 2008. Tumour necrosis factor antagonists: structure, function, and tuberculosis risks. *Lancet Infect. Dis.* 8: 601–11.

75. Ouyang, W., S. Rutz, N. K. Crellin, P. a Valdez, and S. G. Hymowitz. 2011. Regulation and functions of the IL-10 family of cytokines in inflammation and disease. *Annu. Rev. Immunol.* 29: 71–109.

76. Moore, K. W., R. de Waal Malefyt, R. L. Coffman, and A. O'Garra. 2001. Interleukin-10 and the interleukin-10 receptor. *Annu. Rev. Immunol.* 1: 683–765.

77. Bogdan, C., Y. Vodovotz, and C. Nathan. 1991. Macrophage Deactivation by Interleukin 10. *J. Exp. Med.* 174.

78. Balcewicz-Sablinska, M., H. Gan, and H. G. Remold. 1999. Interleukin 10 produced by macrophages inoculated with Mycobacterium avium attenuates mycobacteria-induced apoptosis by reduction of TNF-α activity. *J. Infect. Dis.* 180: 1230–1237.

79. Gordon, S. 2003. Alternative activation of macrophages. *Nat. Rev. Immunol.* 3: 23–35.

80. Wigginton, J. E., and D. Kirschner. 2001. A model to predict cell-mediated immune regulatory mechanisms during human infection with Mycobacterium tuberculosis. *J. Immunol.* 166: 1951–67.

81. Manca, C., L. Tsenova, C. E. Barry, A. Bergtold, S. Freeman, P. a Haslett, J. M. Musser, V. H. Freedman, and G. Kaplan. 1999. Mycobacterium tuberculosis CDC1551 induces a more vigorous host response in vivo and in vitro, but is not more virulent than other clinical isolates. *J. Immunol.* 162: 6740–6.

82. Portevin, D., S. Gagneux, I. Comas, and D. C.-3048359 Young. 2011. Human macrophage responses to clinical isolates from the Mycobacterium tuberculosis complex discriminate between ancient and modern lineages. *PLoS Pathog* 7: e1001307 ST – Human macrophage responses to clini.

83. Newton, S. M., R. J. Smith, K. A. Wilkinson, M. P. Nicol, N. J. Garton, K. J. Staples, G. R. Stewart, J. R. Wain, A. R. Martineau, S. Fandrich, T. Smallie, B. Foxwell, A. Al-Obaidi, J. Shafi, K. Rajakumar, B. Kampmann, P. W. Andrew, L. Ziegler-Heitbrock, M. R. Barer, and R. J. Wilkinson. 2006. A deletion defining a common Asian lineage of Mycobacterium tuberculosis associates with immune subversion. *Proc. Natl. Acad. Sci. U. S. A.* 103: 15594–8.

84. Nair, S., P. a Ramaswamy, S. Ghosh, D. C. Joshi, N. Pathak, I. Siddiqui, P. Sharma, S. E. Hasnain, S. C. Mande, and S. Mukhopadhyay. 2009. The PPE18 of Mycobacterium tuberculosis interacts with TLR2 and activates IL-10 induction in macrophage. *J. Immunol.* 183: 6269–81.

85. Bru, A., and P.-J. Cardona. 2010. Mathematical modeling of tuberculosis bacillary counts and cellular populations in the organs of infected mice. *PLoS One* 5: e12985.

86. Marzo, E., C. Vilaplana, G. Tapia, J. Diaz, V. Garcia, and P.-J. Cardona. 2014. Damaging role of neutrophilic infiltration in a mouse model of progressive tuberculosis. *Tuberculosis (Edinb).* 94: 55–64.

87. O'Garra, A., P. Vieira, P. Vieira, and A. E. Goldfeld. 2004. IL-10–producing and naturally occurring CD4+ Tregs: limiting collateral damage. *J. Clin. Invest.* 114: 1–7.

88. Yssel, H., R. De Waal Malefyt, M. G. Roncarolo, J. S. Abrams, R. Lahesmaa, H. Spits, and J. E. de Vries. 1992. IL-10 is produced by subsets of human CD4+ T cell clones and peripheral blood T cells. *J. Immunol.* 149: 2378–84.

89. Madura Larsen, J., C. S. Benn, Y. Fillie, D. van der Kleij, P. Aaby, and M. Yazdanbakhsh. 2007. BCG stimulated dendritic cells induce an interleukin-10 producing

T-cell population with no T helper 1 or T helper 2 bias in vitro. *Immunology* 121: 276–82.

90. Scott-Browne, J. P., S. Shafiani, G. Tucker-Heard, K. Ishida-Tsubota, J. D. Fontenot, A. Y. Rudensky, M. J. Bevan, and K. B. Urdahl. 2007. Expansion and function of Foxp3-expressing T regulatory cells during tuberculosis. *J. Exp. Med.* 204: 2159–69.

91. Roncarolo, M. G., M. Battaglia, R. Bacchetta, K. Fleischhauer, and M. K. Levings. 2006. Interleukin-10-secreting type 1 regulatory T cells in rodents and humans. *Immunol. Rev.* 212: 28–50.

92. Ribeiro-Rodrigues, R., T. Resende Co, R. Rojas, Z. Toossi, R. Dietze, W. H. Boom, E. Maciel, and C. S. Hirsch. 2006. A role for CD4+CD25+ T cells in regulation of the immune response during human tuberculosis. *Clin. Exp. Immunol.* 144: 25–34.

93. Higgins, D. M., J. Sanchez-Campillo, A. G. Rosas-Taraco, E. J. Lee, I. M. Orme, and M. Gonzalez-Juarrero. 2009. Lack of IL-10 alters inflammatory and immune responses during pulmonary Mycobacterium tuberculosis infection. *Tuberculosis (Edinb).* 89: 149–57.

94. Cyktor, J. C., B. Carruthers, R. a Kominsky, G. L. Beamer, P. Stromberg, and J. Turner. 2013. IL-10 inhibits mature fibrotic granuloma formation during Mycobacterium tuberculosis infection. *J. Immunol.* 190: 2778–90.

95. Pitt, J. M., E. Stavropoulos, P. S. Redford, A. M. Beebe, G. J. Bancroft, D. B. Young, and A. O'Garra. 2012. Blockade of IL-10 signaling during bacillus Calmette-Guérin vaccination enhances and sustains Th1, Th17, and innate lymphoid IFN-γ and IL-17 responses and increases protection to Mycobacterium tuberculosis infection. *J. Immunol.* 189: 4079–87.

96. Keane, J., H. G. Remold, and H. Kornfeld. 2000. Virulent Mycobacterium tuberculosis strains evade apoptosis of infected alveolar macrophages. *J. Immunol.* 164: 2016–20.

97. Majno, G., and I. Joris. 1995. Apoptosis, oncosis, and necrosis. An overview of cell death. *Am. J. Pathol.* 146: 3–15.

98. Fayyazi, a, B. Eichmeyer, a Soruri, S. Schweyer, J. Herms, P. Schwarz, and H. J. Radzun. 2000. Apoptosis of macrophages and T cells in tuberculosis associated caseous necrosis. *J. Pathol.* 191: 417–25.

99. Laskin, D. L., and K. J. Pendino. 1995. Macrophages and inflammatory mediators in tissue injury. *Annu. Rev. Pharmacol. Toxicol.* 35: 655–77.

100. Kaufmann, S. H. E., and A. Dorhoi. 2013. Inflammation in tuberculosis: interactions, imbalances and interventions. *Curr. Opin. Immunol.* 25: 441–9.

101. Casadevall, A., and L. Pirofski. 2003. The damage-response framework of microbial pathogenesis. *Nat. Rev. Microbiol.* 1: 17–24.

102. Balcewicz-Sablinska, M. K., J. Keane, H. Kornfeld, and H. G. Remold. 1998. Pathogenic Mycobacterium tuberculosis evades apoptosis of host macrophages by release of TNF-R2, resulting in inactivation of TNF-alpha. *J. Immunol.* 161: 2636–41.

103. Zhang, D.-W., J. Shao, J. Lin, N. Zhang, B.-J. Lu, S.-C. Lin, M.-Q. Dong, and J. Han. 2009. RIP3, an energy metabolism regulator that switches TNF-induced cell death from apoptosis to necrosis. *Science* 325: 332–6.

104. He, S., L. Wang, L. Miao, T. Wang, F. Du, L. Zhao, and X. Wang. 2009. Receptor interacting protein kinase-3 determines cellular necrotic response to TNF-alpha. *Cell* 137: 1100–11.

105. Roca, F. J., and L. Ramakrishnan. 2013. TNF Dually Mediates Resistance and Susceptibility to Mycobacteria via Mitochondrial Reactive Oxygen Species. *Cell* 1–14.

106. Mantovani, A., A. Sica, S. Sozzani, P. Allavena, A. Vecchi, and M. Locati. 2004. The chemokine system in diverse forms of macrophage activation and polarization. *Trends Immunol.* 25: 677–86.

107. Biswas, S. K., and A. Mantovani. 2010. Macrophage plasticity and interaction with lymphocyte subsets: cancer as a paradigm. *Nat. Immunol.* 11: 889–96.

108. Martinez, F. O., L. Helming, and S. Gordon. 2009. Alternative activation of macrophages: an immunologic functional perspective. *Annu. Rev. Immunol.* 27: 451–83.

109. Gordon, S., and P. R. Taylor. 2005. Monocyte and macrophage heterogeneity. *Nat. Rev. Immunol.* 5: 953–64.

110. Rubin, E. J. 2009. The granuloma in tuberculosis--friend or foe? *N. Engl. J. Med.* 360: 2471–3.

111. Mattila, J. T., O. O. Ojo, D. Kepka-Lenhart, S. Marino, J. H. Kim, S. Y. Eum, L. E. Via, C. E. Barry, E. Klein, D. E. Kirschner, S. M. Morris, P. L. Lin, and J. L. Flynn. 2013. Microenvironments in tuberculous granulomas are delineated by distinct populations of macrophage subsets and expression of nitric oxide synthase and arginase isoforms. *J. Immunol.* 191: 773–84.

112. Qin, H., A. T. Holdbrooks, Y. Liu, S. L. Reynolds, L. L. Yanagisawa, and E. N. Benveniste. 2012. SOCS3 Deficiency Promotes M1 Macrophage Polarization and Inflammation. *J. Immunol.* 189: 3439–48.

113. Dartois, V., and C. E. Barry. 2013. A medicinal chemists' guide to the unique difficulties of lead optimization for tuberculosis. *Bioorg. Med. Chem. Lett.* 23: 4741–50.

114. Dooley, K. E., E. E. Bliven-Sizemore, M. Weiner, Y. Lu, E. L. Nuermberger, W. C. Hubbard, E. J. Fuchs, M. T. Melia, W. J. Burman, and S. E. Dorman. 2012. Safety and pharmacokinetics of escalating daily doses of the antituberculosis drug rifapentine in healthy volunteers. *Clin. Pharmacol. Ther.* 91: 881–8.

115. Misra, A., A. J. Hickey, C. Rossi, G. Borchard, H. Terada, K. Makino, P. B. Fourie, and P. Colombo. 2011. Inhaled drug therapy for treatment of tuberculosis. *Tuberculosis (Edinb).* 91: 71–81.

116. Muttil, P., C. Wang, and A. J. Hickey. 2009. Inhaled drug delivery for tuberculosis therapy. *Pharm. Res.* 26: 2401–16.

117. Griffiths, G., B. Nyström, S. B. Sable, and G. K. Khuller. 2010. Nanobead-based interventions for the treatment and prevention of tuberculosis. *Nat. Rev. Microbiol.* 8: 827–34.

118. Sosnik, A., A. M. Carcaboso, R. J. Glisoni, M. a Moretton, and D. a Chiappetta. 2010. New old challenges in tuberculosis: potentially effective nanotechnologies in drug delivery. *Adv. Drug Deliv. Rev.* 62: 547–59.

119. Andrade, F., M. Videira, D. Ferreira, A. Sosnik, and B. Sarmento. 2013. Nanotechnology and pulmonary delivery to overcome resistance in infectious diseases. *Adv. Drug Deliv. Rev.* .

120. Hirota, K., T. Kawamoto, T. Nakajima, K. Makino, and H. Terada. 2013. Distribution and deposition of respirable PLGA microspheres in lung alveoli. *Colloids Surf. B. Biointerfaces* 105: 92–7.

121. Mitchison, D. a, and P. B. Fourie. 2010. The near future: improving the activity of rifamycins and pyrazinamide. *Tuberculosis (Edinb).* 90: 177–81.

122. Verma, R. K., J. Kaur, K. Kumar, A. B. Yadav, and A. Misra. 2008. Intracellular time course, pharmacokinetics, and biodistribution of isoniazid and rifabutin following pulmonary delivery of inhalable microparticles to mice. *Antimicrob. Agents Chemother.* 52: 3195–201.

123. Hirota, K., T. Hasegawa, H. Hinata, F. Ito, H. Inagawa, C. Kochi, G.-I. Soma, K. Makino, and H. Terada. 2007. Optimum conditions for efficient phagocytosis of rifampicin-loaded PLGA microspheres by alveolar macrophages. *J. Control. Release* 119: 69–76.

124. Parikh, R., S. Dalwadi, P. Aboti, and L. Patel. 2014. Inhaled microparticles of antitubercular antibiotic for in vitro and in vivo alveolar macrophage targeting and activation of phagocytosis. *J. Antibiot. (Tokyo).* 1–8.

125. Yoshida, A., M. Matumoto, H. Hshizume, Y. Oba, T. Tomishige, H. Inagawa, C. Kohchi, M. Hino, F. Ito, K. Tomoda, T. Nakajima, K. Makino, H. Terada, H. Hori, and G.-I. Soma. 2006. Selective delivery of rifampicin incorporated into poly(DL-lactic-co-glycolic) acid microspheres after phagocytotic uptake by alveolar macrophages, and the killing effect against intracellular Mycobacterium bovis Calmette-Guérin. *Microbes Infect.* 8: 2484–91.

126. Zhou, H., Y. Zhang, D. L. Biggs, M. C. Manning, T. W. Randolph, U. Christians, B. M. Hybertson, and K. Ng. 2005. Microparticle-based lung delivery of INH decreases INH metabolism and targets alveolar macrophages. *J. Control. Release* 107: 288–99.

127. Makino, K., T. Nakajima, M. Shikamura, F. Ito, S. Ando, C. Kochi, H. Inagawa, G.-I. Soma, and H. Terada. 2004. Efficient intracellular delivery of rifampicin to alveolar macrophages using rifampicin-loaded PLGA microspheres: effects of molecular weight and composition of PLGA on release of rifampicin. *Colloids Surf. B. Biointerfaces* 36: 35–42.

128. Sharma, A., S. Sharma, and G. K. Khuller. 2004. Lectin-functionalized poly (lactide-co-glycolide) nanoparticles as oral/aerosolized antitubercular drug carriers for treatment of tuberculosis. *J. Antimicrob. Chemother.* 54: 761–6.

129. Kumar Verma, R., J. K. Mukker, R. S. P. Singh, K. Kumar, P. R. P. Verma, and A. Misra. 2012. Partial biodistribution and pharmacokinetics of isoniazid and rifabutin following pulmonary delivery of inhalable microparticles to rhesus macaques. *Mol. Pharm.* 9: 1011–6.

130. Dharmadhikari, A. S., M. Kabadi, B. Gerety, A. J. Hickey, P. B. Fourie, and E. Nardell. 2013. Phase I, single-dose, dose-escalating study of inhaled dry powder capreomycin: a new approach to therapy of drug-resistant tuberculosis. *Antimicrob. Agents Chemother.* 57: 2613–9.

131. Walzl, G., K. Ronacher, W. Hanekom, T. J. Scriba, and A. Zumla. 2011. Immunological biomarkers of tuberculosis. *Nat. Rev. Immunol.* 11: 343–54.

132. Jamil, B., F. Shahid, Z. Hasan, N. Nasir, T. Razzaki, G. Dawood, and R. Hussain. 2007. Interferon gamma/IL10 ratio defines the disease severity in pulmonary and extra pulmonary tuberculosis. *Tuberculosis (Edinb).* 87: 279–87.

133. Nunes-Alves, C., M. G. Booty, S. M. Carpenter, P. Jayaraman, A. C. Rothchild, and S. M. Behar. 2014. In search of a new paradigm for protective immunity to TB. *Nat. Rev. Microbiol.* 12: 289–99.

134. Dannenberg, A. M. 1989. Immune mechanisms in the pathogenesis of pulmonary tuberculosis. *Rev. Infect. Dis.* 11 Suppl 2: S369–78.

135. Lin, P. L., M. Rodgers, L. Smith, M. Bigbee, A. Myers, C. Bigbee, I. Chiosea, S. V Capuano, C. Fuhrman, E. Klein, and J. L. Flynn. 2009. Quantitative comparison of active and latent tuberculosis in the cynomolgus macaque model. *Infect. Immun.* 77: 4631–42.

136. Tsai, M. C., S. Chakravarty, G. Zhu, J. Xu, K. Tanaka, C. Koch, J. Tufariello, J. Flynn, and J. Chan. 2006. Characterization of the tuberculous granuloma in murine and human lungs: cellular composition and relative tissue oxygen tension. *Cell. Microbiol.* 8: 218–32.

137. Chensue, S. W., K. Warmington, J. Ruth, P. Lincoln, M. C. Kuo, and S. L. Kunkel. 1994. Cytokine responses during mycobacterial and schistosomal antigen-induced pulmonary granuloma formation. Production of Th1 and Th2 cytokines and relative contribution of tumor necrosis factor. *Am. J. Pathol.* 145: 1105–13.

138. Chensue, S. W., K. Warmington, J. H. Ruth, N. Lukacs, and S. L. Kunkel. 1997. Mycobacterial and schistosomal antigen-elicited granuloma formation in IFN-gamma and IL-4 knockout mice: analysis of local and regional cytokine and chemokine networks. *J. Immunol.* 159: 3565–73.

139. Qiu, B., K. A. Frait, F. Reich, E. Komuniecki, and S. W. Chensue. 2001. Chemokine expression dynamics in mycobacterial (type-1) and schistosomal (type-2) antigen-elicited pulmonary granuloma formation. *Am. J. Pathol.* 158: 1503–15.

140. Ramakrishnan, L. 2013. *The New Paradigm of Immunity to Tuberculosis*, (M. Divangahi, ed). Springer New York, New York, NY ; :251–266.

141. Cosma, C. L., O. Humbert, D. R. Sherman, and L. Ramakrishnan. 2008. Trafficking of superinfecting Mycobacterium organisms into established granulomas occurs in mammals and is independent of the Erp and ESX-1 mycobacterial virulence loci. *J. Infect. Dis.* 198: 1851–5.

142. Ly, L. H., M. I. Russell, and D. N. McMurray. 2007. Microdissection of the cytokine milieu of pulmonary granulomas from tuberculous guinea pigs. *Cell. Microbiol.* 9: 1127–36.

143. Shang, S., M. Harton, M. H. Tamayo, C. Shanley, G. S. Palanisamy, M. Caraway, E. D. Chan, R. J. Basaraba, I. M. Orme, and D. J. Ordway. 2011. Increased Foxp3 expression in guinea pigs infected with W-Beijing strains of M. tuberculosis. *Tuberculosis (Edinb).* 91: 378–85.

144. Kramp, J. C., D. N. McMurray, C. Formichella, and A. Jeevan. 2011. The in vivo immunomodulatory effect of recombinant tumour necrosis factor-alpha in guinea pigs vaccinated with Mycobacterium bovis bacille Calmette-Guérin. *Clin. Exp. Immunol.* 165: 110–20.

145. Akabane, T., K. Tabata, K. Kadono, S. Sakuda, S. Terashita, and T. Teramura. 2010. A comparison of pharmacokinetics between humans and monkeys. *Drug Metab. Dispos.* 38: 308–16.

146. Gerlowski, L. E., and R. K. Jain. 1983. Physiologically based pharmacokinetic modeling: principles and applications. *J. Pharm. Sci.* 72: 1103–27.

147. Southern, J., J. Pitt-Francis, J. Whiteley, D. Stokeley, H. Kobashi, R. Nobes, Y. Kadooka, and D. Gavaghan. 2008. Multi-scale computational modelling in biology and physiology. *Prog. Biophys. Mol. Biol.* 96: 60–89.

148. Dada, J. O., and P. Mendes. 2011. Multi-scale modelling and simulation in systems biology. *Integr. Biol. (Camb).* 3: 86–96.

149. Walpole, J., J. a Papin, and S. M. Peirce. 2013. Multiscale Computational Models of Complex Biological Systems. *Annu. Rev. Biomed. Eng.* 137–154.

150. Linderman, J. J., C. A. Hunt, S. Marino, M. Fallahi-Sichani, and D. Kirschner. 2014. Tuneable resolution as an approach to study multi-scale, multi-organ models in systems biology. *WIRES Syst. Biol. Med.* In Press.

151. Segovia-Juarez, J. L., S. Ganguli, and D. Kirschner. 2004. Identifying control mechanisms of granuloma formation during M. tuberculosis infection using an agent-based model. *J. Theor. Biol.* 231: 357–76.

152. Marino, S., M. El-Kebir, and D. Kirschner. 2011. A hybrid multi-compartment model of granuloma formation and T cell priming in tuberculosis. *J. Theor. Biol.* 280: 50–62.

153. Marino, S., D. Sud, H. Plessner, P. L. Lin, J. Chan, J. L. Flynn, and D. E. Kirschner. 2007. Differences in reactivation of tuberculosis induced from anti-TNF treatments are based on bioavailability in granulomatous tissue. *PLoS Comput. Biol.* 3: 1909–24.

154. Goutelle, S., L. Bourguignon, P. H. Maire, M. Van Guilder, J. E. Conte, and R. W. Jelliffe. 2009. Population modeling and Monte Carlo simulation study of the pharmacokinetics and antituberculosis pharmacodynamics of rifampin in lungs. *Antimicrob. Agents Chemother.* 53: 2974–81.

155. Wilkins, J. J., R. M. Savic, M. O. Karlsson, G. Langdon, H. McIlleron, G. Pillai, P. J. Smith, and U. S. H. Simonsson. 2008. Population pharmacokinetics of rifampin in pulmonary tuberculosis patients, including a semimechanistic model to describe variable absorption. *Antimicrob. Agents Chemother.* 52: 2138–48.

156. Ankomah, P., and B. R. Levin. 2012. Two-drug antimicrobial chemotherapy: a mathematical model and experiments with Mycobacterium marinum. *PLoS Pathog.* 8: e1002487.

157. Goutelle, S., L. Bourguignon, R. W. Jelliffe, J. E. Conte, and P. Maire. 2011. Mathematical modeling of pulmonary tuberculosis therapy: Insights from a prototype model with rifampin. *J. Theor. Biol.* 282: 80–92.

158. Peloquin, C. A., G. S. Jaresko, C. L. Yong, A. C. Keung, A. E. Bulpitt, and R. W. Jelliffe. 1997. Population pharmacokinetic modeling of isoniazid, rifampin, and pyrazinamide. *Antimicrob. Agents Chemother.* 41: 2670–9.

159. Wilkins, J. J., G. Langdon, and H. Mcilleron. 2011. Variability in the population pharmacokinetics of isoniazid in South African tuberculosis patients *. *Current* .

160. Davies, G. R., and E. L. Nuermberger. 2008. Pharmacokinetics and pharmacodynamics in the development of anti-tuberculosis drugs. *Tuberculosis (Edinb).* 88 Suppl 1: S65–74.

161. An, G., Q. Mi, J. Dutta-Moscato, and Y. Vodovotz. 2009. Agent-based models in translational systems biology. *Wiley Interdiscip. Rev. Syst. Biol. Med.* 1: 159–71.

162. Hunt, C. A., R. C. Kennedy, S. H. J. Kim, and G. E. P. Ropella. 2013. Agent-based modeling: a systematic assessment of use cases and requirements for enhancing pharmaceutical research and development productivity. *Wiley Interdiscip. Rev. Syst. Biol. Med.* 5: 461–80.

163. Bauer, A. L., C. a. a. A. Beauchemin, and A. S. Perelson. 2009. Agent-based modeling of host-pathogen systems: The successes and challenges. *Inf. Sci. (Ny).* 179: 1379–1389.

164. Ziraldo, C., Q. Mi, G. An, and Y. Vodovotz. 2013. Computational Modeling of Inflammation and Wound Healing. *Adv. wound care* 2: 527–537.

165. Wang, J., L. Zhang, C. Jing, G. Ye, H. Wu, H. Miao, Y. Wu, and X. Zhou. 2013. Multi-scale agent-based modeling on melanoma and its related angiogenesis analysis. *Theor. Biol. Med. Model.* 10: 41.

Chapter 2

Efficient Numerical Implementation of Hybrid Multi-Scale Agent-Based Models to Describe Biological Systems

The work in Chapter 2 was submitted as: Cilfone, N.A., Kirschner, D.E., Linderman, J.J. Efficient numerical implementation of hybrid multi-scale agent-based models to describe biological systems. (2014).

2.1 Introduction

Computational models are used in systems biology for understanding, predicting, and translating a wealth of experimentally generated data into a realization of systems behavior. Multi-scale computational models in particular have provided valuable insights and predictions for application to areas as diverse as infectious disease, inflammation, cancer, stem-cell differentiation, angiogenesis, and disease treatment (1–11). A defining feature of multi-scale computational models is a description of biological mechanisms that operate over different spatiotemporal scales (5, 12–15). When building multi-scale models four different areas must be considered (Figure 2.1): (1) *constructing* models – how to create a mathematical formulation that is able to recapitulate the dynamics of a biological system at an individual scale, (2) *linking* models – how to join individual scale models to allow for exchange of information, (3) *solving* models – determining the most efficient way to solve the underlying mathematics, and (4) *analyzing* models – how to

make and understand model predictions. In this Chapter, we focus on methods to link individual scale models and efficiently solve the resulting multi-scale model (Figure 2.1).

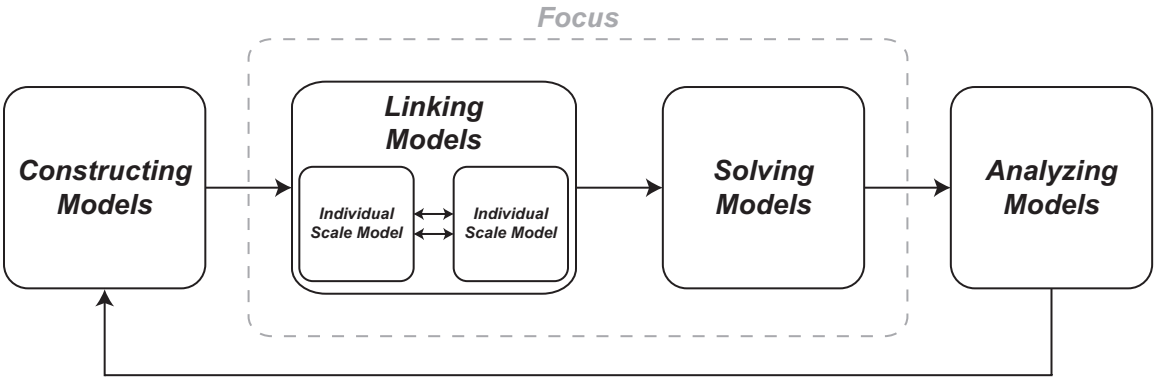

Figure 2.1 Considerations for building multi-scale models
(1) Constructing models: how to create mathematical formulations that accurately represent individual scale dynamics of a biological system, (2) Linking models: how to connect mathematical formulations of individual scale models to create multi-scale models, (3) Solving models: implementing efficient methods to solve multi-scale models, and (4) Analyzing models: Understanding and translating model predictions. Model analysis commonly leads back to model construction in order to include new biological mechanisms of interest. In this work, we focus on how to link individual scale models and efficiently solve the resultant multi-scale model.

We typically link descriptions of biological phenomena operating at an individual scale together to form a multi-scale model (5). One approach to linking individual scale models, referred to as hierarchical linking, is to solve the lowest scale (i.e. the smallest length or time scale) model to completion and subsequently feed the output, for example in the form of an initial condition or parameter value, to the model at the next higher scale (5, 16, 17). However, this type of linking methodology is inappropriate when information across scales needs to be continually exchanged and in both directions. For instance, vascular endothelial growth factor (VEGF) can induce an endothelial cell to divide which may elongate a blood vessel in a new direction. The new endothelial cells will produce more VEGF, leading to cellular movement and continued growth of the blood vessel in the new direction (6, 18). Without exchange of information in both directions (molecular to cellular and cellular to molecular), sprouting of new blood

vessels would likely not occur. The nature of biological systems, with constant exchange of information across scales, necessitates multi-scale models that mimic this dynamic exchange of information (5, 16, 17). The resulting multi-scale model is more complex than the individual-scale parts, making it more computationally difficult to solve. Therefore, efficient methodologies to link and solve multi-scale models are necessary. Models that combine aspects of both continuous and discrete model constructs are commonly referred to as *hybrid* models. We focus our discussion on hybrid multi-scale agent-based models where an agent-based model (discrete), is informed by differential equation models (continuum) operating at a different scale (Figure 2.2).

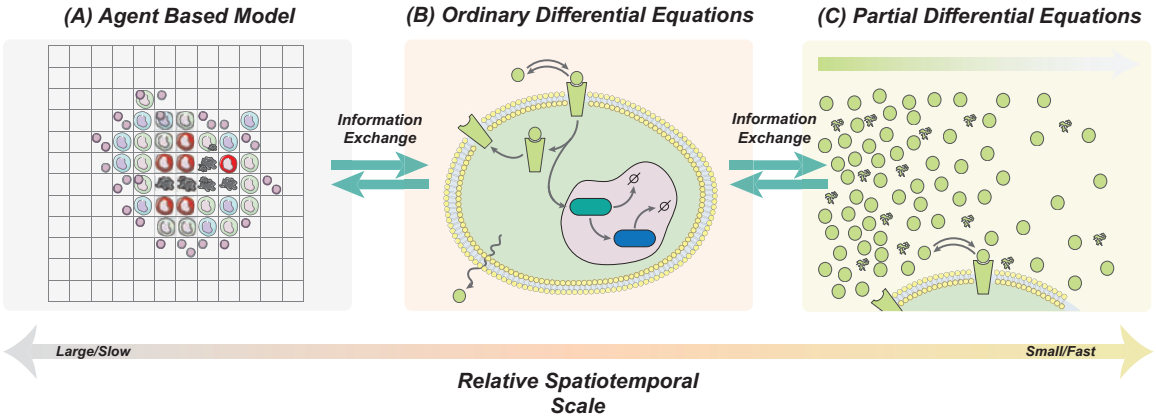

Figure 2.2 Mathematical representations of biological processes acting across different spatiotemporal scales
How individual scale models are combined with exchange of information across scales. (1) An agent-based model (ABM) represents tissue and cellular scales (e.g. cell activation states). (2) Ordinary differential equation models represent molecular scale behaviors associated with cells (e.g. receptor-ligand trafficking and intracellular signaling). (3) Partial differential equation models represent molecular scale behaviors of the environment (e.g. soluble molecule diffusion). Together these integrated individual scale models form the basis of a hybrid multi-scale agent-based model.

Agent-based models (ABMs, sometimes called individual based models – IBMs) are stochastic, discrete models that utilize individual entities known as *agents*, here representing individual biological cells (Figure 2.2). Each agent is autonomous and behaves based on decisions from the set of rules, interactions, and states given to it,

leading to heterogeneity between agents. ABMs can generate complex system-level emergent behavior from simple rule-based descriptions of each individual (4, 5, 14, 19). Agents receive inputs from the environment, influencing their decision making, and can also have the ability to alter their environment. Hybrid ABMs arise when continuum models are used to describe part of the overall system, such as the environment and parts of the agent decision-making processes (8, 14, 15, 20). A hybrid ABM is also termed multi-scale when a portion of the model, such as the continuum models, is describing behaviors at a different spatiotemporal scale than the ABM (Figure 2.2).

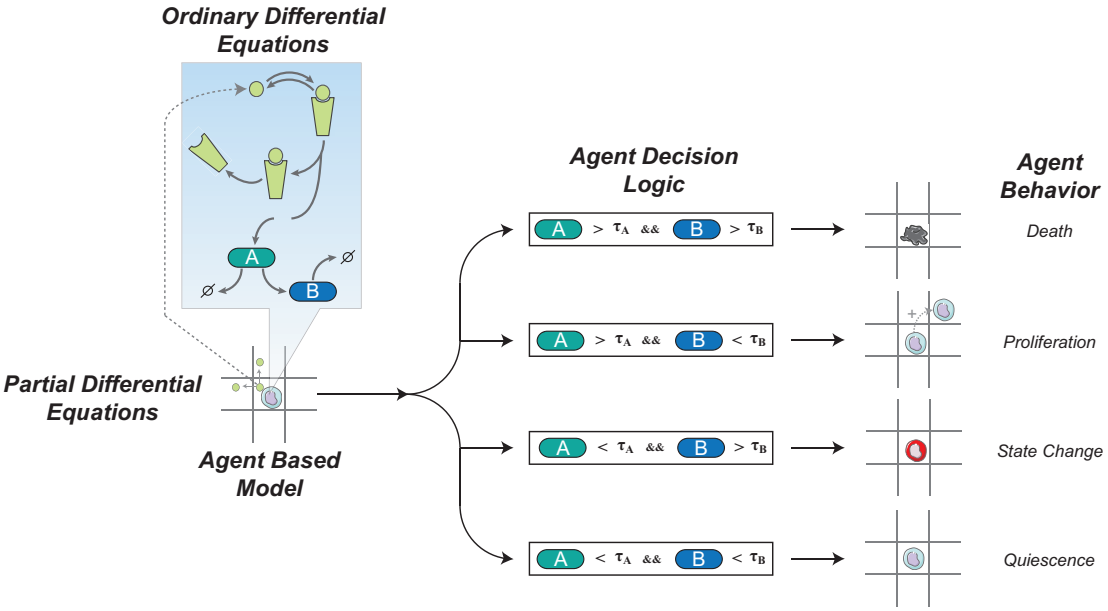

Figure 2.3 Example of how information is exchanged across scales in a hybrid multi-scale agent-based model
Soluble molecules in the environment (with diffusion and degradation described using partial differential equations) interact with agents through agent-associated reactions (ordinary differential equations). Based on relative levels of agent-associated species (species A, *green* and species B, *blue*) agents make different decisions: (1) if both species A and B are above specified thresholds the agent will die, (2) if only species A (*green*) is above the specified threshold the agent will proliferate, (3) if only species B (*blue*) is above the specified threshold the agent will change state, (4) if both species A and B are below specified thresholds the agent will be quiescent. Agent decision logic using thresholds is only one example of how agent-associated reactions can be linked to various dynamics. Other examples include Poisson processes of agent-associated quantities and rate of change of agent-associated species (9, 14, 33). Figure style adapted from (14).

We focus on the use of continuum models to describe the dynamics of the environment and agent-associated reactions influencing agent decision-making processes that occur at a smaller spatial and faster time scale than the ABM (Figure 2.2, Figure 2.3). These hybrid multi-scale ABMs use a temporally separated approach in which the continuum models are solved using conventional numerical methods on a faster time scale than the ABM; syncing between scales is required to reconcile information exchange (21, 22). While many platforms exist for developing ABMs (e.g. NetLogo, Repast, Swarm, SPARK, CHASTE, MASON, and FLAME (11, 22–27)), we have found the flexibility of an in-house platform necessary to link and solve hybrid multi-scale ABMs. We review methods for linking individual scale ABMs to differential equation models and efficient implementations of numerical solvers that allows constant exchange of information across models. We then briefly illustrate the applicability of hybrid multi-scale agent based models in describing various biological systems and demonstrate relative computational speeds using the hybrid multi-scale model of *Mycobacterium tuberculosis* infection presented in detail in Chapters 3, 4, 5, 6, and Appendix C.

2.2 Examples of Hybrid Multi-Scale ABMs

Hybrid multi-scale ABMs (Figure 2.2) are being used to describe many biological systems (1–11). To orient the reader, we briefly describe three such systems:

2.2.1 Epithelial Restitution

The wound healing response of damaged epithelial cells involves restitution (resealing the epithelial layer), proliferation, and differentiation (28). The cytokines

transforming-growth-factor-β (TGF-β) and epidermal growth factor (EGF) are necessary for beginning restitution processes, diffusing through the extracellular matrix (Figure 2.2C), binding to TGF-β and EGF receptors on endothelial cells, and signaling through SMAD and ERK pathways (Figure 2.2B) (28). In the ABM, endothelial cells are represented as individual agents (Figure 2.2A) whose behavior, such as migration and adherence, depends on SMAD and ERK signaling (Figure 2.3). At the tissue scale, the reconnection of damaged epithelium (restitution) with healthy endothelial is critical to wound healing and constitutes much of the early wound healing response to damaged tissue. This hybrid multi-scale ABMs qualitatively matches temporal experimental data and predicts the importance of environmental interactions on the dynamics of epithelial restitution.

2.2.2 Growth Patterns of Brain Tumors

The expression of EGF receptors in brain tumors is associated with rapid growth and invasion. Yet, in growing tumors, cells only display a single phenotype of either migration or proliferation. Transforming-growth-factor-α (TGF-α) diffuses within the extracellular environment (Figure 2.2C) and binds and dimerizes with EGF receptors, initiating downstream signaling through PLCγ (Figure 2.2B). These downstream signaling processes mediate the phenotype of a tumor cell (Figure 2.3). In the ABM, tumor cells are represented as individual agents (Figure 2.2A) with both proliferative and migratory potentials determined by levels of PLCγ and bound EGFR (Figure 2.3). The proliferative and migratory nature of tumor cells leads to tumor growth and expansion (29–31). These hybrid multi-scale ABMs of tumor growth have shown that increased

EGF receptor density correlates with tumor expansion based on early phenotypic switching driven by TGF-α autocrine signaling (29–31).

2.2.3 Immune Response to Mycobacterium tuberculosis

During *M. tuberculosis* infection the immune system relies on a variety of cells and molecules to coordinate an effective immune response (9, 11, 32–35). Two soluble molecules of interest are the pro-inflammatory cytokine tumor necrosis factor-α (TNF-α) and the anti-inflammatory cytokine interleukin-10 (IL-10). These cytokines diffuse through the lung tissue (Figure 2.2C), bind to cell-associated receptors (TNFR1, TNFR2, and IL-10R), and signal through pathways such as NFκB and STAT3 (Figure 2.2B). Macrophages and T cells are key immune cells, modeled as agents (Figure 2.2A), with many states (e.g. resting, activated, deactivated) and functions (e.g. bactericidal ability) driven by levels of NFκB and STAT3 (Figure 2.3). Control of infection relies on the formation of an organized structure of immune cells, known as a granuloma, and its function over the long timescale of infection. Hybrid multi-scale ABMs of *M. tuberculosis* infection are able to reproduce the emergent phenomenon of granuloma formation and have demonstrated a critical balance between TNF-α and IL-10 in controlling granuloma function (see Chapters 3, 4, and 5) (9, 11, 33). In addition, treatment of infection with antibiotics is critical to pathogen removal during *M. tuberculosis* infection (see Chapters 6 and Appendix C). The effects of two first-line antibiotics, rifampicin (RIF) and isoniazid (INH) on bacterial burden have been simulated in a hybrid multi-scale ABM (Pienaar et al. submitted). Antibiotics diffuse through the lung environment (Figure 2.2C), are taken up by immune cells (Figure 2.2A), and are

able to kill bacteria. This hybrid multi-scale ABM (from Chapters 3, 4, 5, 6, and Appendix C) will be used to demonstrate relative computational speeds in later sections.

2.3 Basics Concepts For Hybrid Multi-Scale ABMs

2.3.1 Mathematical Framework and Linking

We describe the elements of a 2-dimensional hybrid multi-scale ABM (Figure 2.2), but the framework presented is easily adapted to any dimensionality required. An ABM describes relevant biological cells as individual agents. Each agent (A) has an associated state (V) and position (x, y) that can change with time. Examples of agent states include activated, proliferating, infected, and cancerous. Changes in state are based on a set of stochastic agent rules and interactions, but are also influenced by quantities included in differential equation models of the environment. The construction of an ABM is beyond the scope of this Chapter but is well-described in the literature (18, 19, 23, 25, 28, 36–40).

Agents have a set of agent-associated reactions that are occurring in each individual agent:

$$For\ Each\ A(x,y,V): \frac{dY_r}{dt} = f(L, Y_1, Y_2, \dots, Y_R) + \beta_r \qquad r = 1, 2, \dots, R \qquad (Eqn.\ 2.1)$$

Eqn. 2.1 represents the agent-associated reactions (R total reactions), where Y_r is an agent-associated species, t is time, L is a soluble molecule, and β_r are parameters independent of t and Y_r. Multiple soluble molecules can be included, although in our examples we will only include one for simplicity. The agent-associated reactions describe reactions occurring in agents, such as a cell-cycle proteins controlling proliferation or actin remodeling controlling cellular movement (41, 42). More common is a description

of receptor-ligand binding and trafficking and ensuing intracellular signaling processes as in the three examples given above (33, 43–46). These reactions are typically based on mass-action kinetics (47). A simple example of receptor-ligand binding, trafficking, and intracellular signaling reactions for a single agent are given in Table 2.1.

Table 2.1 Example of Agent-Associated Reactions: Receptor-Ligand Binding, Trafficking, and Intracellular Signaling

Description	Equation
Soluble Molecule – $[L]$ (M)	$\frac{d[L]}{dt} = (\rho/N_{AV})\left(k_{synth} - k_f[L][Y_1] + k_r[Y_2]\right)$
Free Molecule – $[Y_1]$ (#/cell)	$\frac{d[Y_1]}{dt} = -k_f[L][Y_1] + k_r[Y_2] + k_{rec}[Y_3]$
Bound Receptor – $[Y_2]$ (#/cell)	$\frac{d[Y_2]}{dt} = k_f[L][Y_1] - k_r[Y_2] - k_{int}[Y_2]$
Internalized Receptor – $[Y_3]$ (#/cell)	$\frac{d[Y_3]}{dt} = k_{int}[Y_2] - k_{rec}[Y_3]$
Signaling Molecule – $[Y_4]$ (#/cell)	$\frac{d[Y_4]}{dt} = k_{sig}[Y_3] - k_{dec}[Y_4]$
Response Factor – $[Y_5]$ (#/cell)	$\frac{d[Y_5]}{dt} = k_{resp}[Y_4] - k_d[Y_5]$

k_f – association rate constant (1/M*s), k_r – dissociation rate constant (1/s), k_{int} – internalization rate constant (1/s), k_{rec} – recycling rate constant (1/s), k_{synth} – synthesis rate constant (#/cell*s), k_{sig} – signaling rate constant (1/s), k_{dec} – signal decay rate constant (1/s), k_{resp} – signal response rate constant (1/s), k_d – response decay rate constant (1/s), ρ (cells/L), N_{AV} – Avogadro's constant (#/mol)

Soluble molecules (L) diffuse and degrade in the environment and agent-associated reactions are dependent upon the local concentration of these soluble molecules (Eqn. 2.1). The linked mathematical representation is a diffusion-reaction equation:

$$\frac{\partial L(x,y,t)}{\partial t} = D\nabla^2 L(x,y,t) - k_{deg}L(x,y,t) + \sum_{A(x,y,V)} \left(f(L, Y_1, Y_2, \dots, Y_R) + \beta_r\right) \qquad (Eqn.\ 2.2)$$

where t is time, D is the isotropic diffusion coefficient, k_{deg} is the extracellular degradation rate constant, and $f(L, Y_1, Y_2, \dots, Y_R) + \beta_r$ is from the set of agent-associated reactions (47, 48). This mathematical formulation allows each agent to interact with soluble molecules in the environment through agent-associated species unique to each agent $A(x,y,V)$. This allows for the dynamic exchange of information between differential

equation models and the ABM, as Eqn. 2.1 and Eqn. 2.2 are dependent upon both agents and soluble molecules. Agents are moving, interacting, and changing state in the ABM with a simultaneous and direct interface with extracellular soluble molecules that are diffusing in the environment. Changes to soluble molecules concentrations in the environment factor into the agent decision-making processes, while changes in agent-associated reactions influence agent states (Figure 2.3).

2.3.2 Operator Splitting

The numerical solution of Eqn. 2.2 as written is difficult and would require significant computational power due to equation assembly and the different timescales present in the equation. We can use temporal operator splitting to decouple Eqn. 2.2 into a simpler and more tractable system (8, 49–53). Here, we split Eqn. 2.2 into three equations: (1) soluble molecule diffusion (operator Θ_1), (2) agent-associated reactions (operator Θ_2), and (3) soluble molecule degradation (operator Θ_3). Therefore, Eqn. 2.2 becomes:

$$\frac{\partial L(x,y,t)}{\partial t} = D\nabla^2 L(x,y,t) = \Theta_1 \qquad (Eqn.\ 2.3)$$

$$For\ Each\ A(x,y,V): \frac{dY_r}{dt} = f(L, Y_1, Y_2, \dots, Y_R) + \beta_r = \Theta_2 \qquad r = 1, 2, \dots, R \qquad (Eqn.\ 2.4)$$

$$\frac{\partial L(x,y,t)}{\partial t} = -k_{deg} L(x,y,t) = \Theta_3 \qquad (Eqn.\ 2.5)$$

This reduces the problem to solving a partial differential equation (PDE) (Eqn. 2.3), a set of non-linear ordinary differential equations (ODEs) for each agent (Eqn. 2.4), and a simple linear first order ODE (Eqn. 2.5). Eqn. 2.5 has an analytical solution:

$$L(x,y,t) = L(x,y,t_0)e^{-k_{deg}t} \qquad (Eqn.\ 2.6)$$

The remaining equations, Eqn. 2.3 and Eqn. 2.4 (such as those shown in Table 2.1), can now be solved using existing numerical methods and discrete time steps. The overall numerical approximation to Eqn. 2.2 is then obtained by mathematically combining the solution to each individual equation (Eqn. 2.3, 2.4, and 2.5) using a splitting methodology. The splitting method determines the accuracy of the overall solution and also determines relative time steps used for the individual equations.

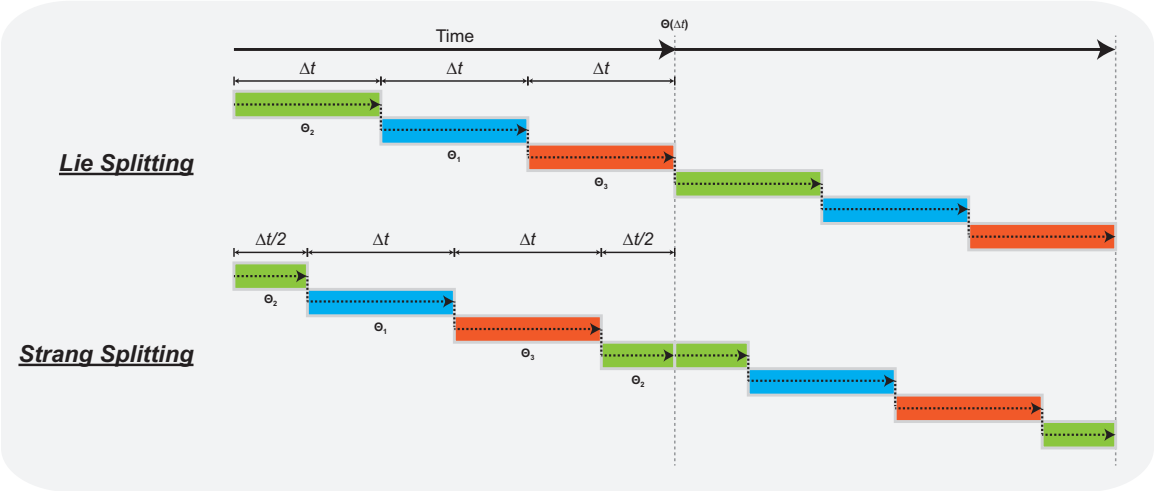

Figure 2.4 Operator splitting algorithms
The top panel represents Lie Splitting where each operator (Θ_1, Θ_2, and Θ_3) is advanced in time one after the other. The bottom panel represents Strang splitting where one operator (Θ_2) is advanced halfway in time, followed by the other operators being advanced all the way in time (Θ_1 and Θ_3), then the first operator (Θ_2) is advanced another half-step in time.

Lie splitting (also known as first-order splitting) is the most commonly used method in multi-scale ABMs. As shown in Figure 2.4, the solution to each individual equation is estimated in sequence using the same time step (Δt), with the solution of each operator as the input to the next operator (8, 9, 51):

$$\Theta_1(\Delta t) \rightarrow \Theta_2(\Delta t) \rightarrow \Theta_3(\Delta t) \approx \Theta(\Delta t) \qquad (Eqn.\ 2.7)$$

Lie splitting has first order accuracy with solution error due to splitting of Eqn. 2.2 being proportional to the discrete time step O(Δt) (8, 9, 51).

A simple improvement over Lie splitting is Strang splitting (Eqns. 2.8-2.9), shown in Figure 2.4, which is second order accurate O(Δt^2) (52):

$$\Theta_2\left(\frac{\Delta t}{2}\right) \rightarrow \left(\Theta_1(\Delta t) \rightarrow \Theta_3(\Delta t)\right) \rightarrow \Theta_2\left(\frac{\Delta t}{2}\right) \approx \Theta(\Delta t) \qquad (Eqn.\ 2.8)$$

$$\Theta_2\left(\frac{\Delta t}{2}\right) \rightarrow \Theta_4(\Delta t) \rightarrow \Theta_2\left(\frac{\Delta t}{2}\right) \approx \Theta(\Delta t) \qquad (Eqn.\ 2.9)$$

The most computationally intensive operator is solved using the full time step (Δt), while the less computationally intensive operator is solved using a half time step ($\Delta t/2$). With three operators, two are grouped together (in this case Θ_1 and Θ_3) and the splitting method is used on the combined operator (Θ_1 and Θ_3). The splitting between the Θ_1 and Θ_3 operators remains Lie splitting. We group the diffusion operator (Θ_1) and the degradation operator (Θ_3) together in all further sections and refer to the combined operator as Θ_4. We advocate the use of Strang splitting as the increased accuracy provides increased flexibility in choosing appropriate time steps. We base all further analysis on implementation of Strang splitting.

While operator splitting makes Eqn. 2.2 easier to solve, if too large of a time step (Δt) is chosen, one is essentially considering the system to be mathematically decoupled. This can lead to non-phenomenological behavior of the system. Additional operator splitting techniques have been developed and include higher order methods such as Yoshida splitting (4th and 6th order), Kahan splitting, and Zassenhaus products (54–57). Although the accuracy of the splitting method increases with these methods, additional function evaluations (some requiring steps backwards in time) make them more complicated approaches.

2.3.3 Model Layers and Discretization

Hybrid multi-scale ABMs are implemented using multiple super-imposed layers of information (8). We follow this methodology and describe two layers: an *environment layer* and an *agent layer*. The environment layer holds information for each soluble molecule (L) and is discretized into grid points of uniform spacing, Δx and Δy (Figure 2.5). The discretized grid is described using lattice parameters; i increases in the x-dimension and j increases in the y-dimension. Thus the local soluble molecule concentration is given by $L_{i,j}$. The agent layer, also a discretized grid, holds positional information of the agents, providing a framework for agent movement, behavior, and interaction. Agents in the agent layer interact with the environment layer at their corresponding positions. We prefer to maintain the same discretization size for both agent and environment layer, due to the simplicity in mapping between the two layers. Different discretization sizes of the environment and agent layers (Δx, Δy) have been used in the context of a hybrid multi-scale ABM but require interpolation between agent and environment layers (8).

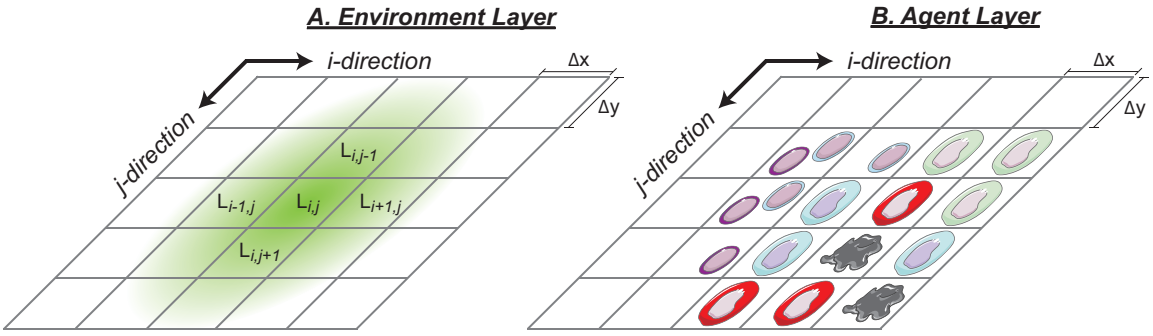

Figure 2.5 Model layers and discretization
Implementation of multiple layers holding different types of information discretized into grid of spacing Δx and Δy represented by i,j coordinates. (A) The environment layer represents the extracellular space of the hybrid agent-based model and holds soluble molecule concentrations. (B) The agent layer holds positional information of agents. Agents in the agent layer interact with the environment layer at their corresponding positions.

2.3.4 Tuneable Resolution

As more agent-associated reactions and species are included in Eqn. 2.4 (see Table 2.1), the computational cost of solving the equations grows. Each additional reaction or species must be solved for every agent in the system; in published models the number of agents ranges from a few hundred to as many as 100,000. Tuneable resolution is an approach that advocates reducing the complexity of a system by 'coarse-graining' a detailed model (or aspects of that model) to save computational resources while preserving key mechanisms and behaviors (see Chapter 6 and Appendix C) (46). For instance, an initial and fairly simple or 'coarse-grained' model is developed and the computational cost associated with solving the model is acceptable. Spurred by more biological data or additional questions, a more detailed or 'fine-grained' model containing many more agent-associated reactions is formulated, but it requires significant computational resources to solve. For subsequent biological questions, however, all of the detail of this 'fine-grained' model may not be needed. The goal is to use the 'fine-grained' model to build a better 'coarse-grained' model that estimates key mechanisms and behaviors from the 'fine-grained' model while simultaneously alleviating computational burdens (and facilitating model sharing and analysis). For example, it may be reasonable to assume pseudo steady-state for some agent-associated reactions or to use an apparent rate constant (k_{app}) to approximate a set of reactions; sensitivity analysis and consideration of time scales may aid in these decisions (Pienaar et al. submitted) (46, 58, 59).

2.4 Numerical Methods for PDE Sub-Models

We review three numerical methods for solving the two-dimensional form of Eqn. 2.3 in Cartesian coordinates.

$$\frac{\partial L(x,y,t)}{\partial t} = D\left(\frac{\partial^2 L(x,y,t)}{\partial x^2} + \frac{\partial^2 L(x,y,t)}{\partial y^2}\right) \qquad (Eqn.\ 2.10)$$

2.4.1 Forward-Time Central-Space Method

The simplest and most frequently used numerical method for solving the diffusion equation is the forward-time central-space (FTCS) approximation (8, 9, 60). FTCS is an explicit method that uses a first order forward approximation of the time derivative and a second order central difference approximation of the spatial derivatives (Eqn. 2.11) (60, 61).

$$\frac{L_{i,j}^{t+\Delta t} - L_{i,j}^{t}}{\Delta t} = D\left(\frac{L_{i+1,j}^{t} - L_{i,j}^{t} + L_{i-1,j}^{t} - L_{i,j}^{t}}{\Delta x^2} + \frac{L_{i,j+1}^{t} - L_{i,j}^{t} + L_{i,j-1}^{t} - L_{i,j}^{t}}{\Delta y^2}\right) \qquad (Eqn.\ 2.11)$$

Thus, at each lattice coordinate (i,j) the concentration at the next time step ($t+\Delta t$) can be directly calculated from concentrations at the current time step (t). This requires the discretized grid concentrations ($L_{i,j}$) in the environment layer to be stored for both the current time point (t) and the next time point ($t+\Delta t$). Insulating boundary conditions are applied by ensuring the flux across the boundary is zero by setting the appropriate concentration difference to zero (e.g. for the $i = 0$ boundary $L_{i-1,j} - L_{i,j}$ would be set to zero). Dirichlet boundary conditions are applied by setting the appropriate concentration (e.g. for the $i = 0$ boundary $L_{i-1,j}$ could be set to zero).

The FTCS method is O(Δt) accurate in time and O(Δx^2, Δy^2) in space, while the computational cost is O(n^2) per time step. The FTCS method is numerically stable only if the following criterion is met:

$$D\Delta t\left(\frac{1}{\Delta x^2}+\frac{1}{\Delta y^2}\right)\leq\frac{1}{2} \qquad (Eqn.\ 2.12)$$

2.4.2 Alternating-Direction Explicit Method

The alternating-direction explicit (ADE) numerical method is an extension of the FTCS method built upon the Peaceman-Rachford alternating direction concept (60, 62). Let both $u_{i,j}$ and $v_{i,j}$ be finite difference approximations of the soluble molecule concentration, $L(x,y,t)$, in Eqn. 2.13 and Eqn. 2.14 defined below:

$$\frac{u_{i,j}^{t+\Delta t}-u_{i,j}^{t}}{\Delta t}=D\left(\frac{u_{i+1,j}^{t}-u_{i,j}^{t}+u_{i-1,j}^{t+\Delta t}-u_{i,j}^{t+\Delta t}}{\Delta x^2}+\frac{u_{i,j+1}^{t}-u_{i,j}^{t}+u_{i,j-1}^{t+\Delta t}-u_{i,j}^{t+\Delta t}}{\Delta y^2}\right) \qquad (Eqn.\ 2.13)$$

$$\frac{v_{i,j}^{t+\Delta t}-v_{i,j}^{t}}{\Delta t}=D\left(\frac{v_{i+1,j}^{t+\Delta t}-v_{i,j}^{t+\Delta t}++v_{i-1,j}^{t}-v_{i,j}^{t}}{\Delta x^2}+\frac{v_{i,j+1}^{t+\Delta t}-v_{i,j}^{t+\Delta t}+v_{i,j-1}^{t}-v_{i,j}^{t}}{\Delta y^2}\right) \qquad (Eqn.\ 2.14)$$

In the case of u, iteration proceeds in both the forward i and j directions. Thus, the values in Eqn. 2.13 of $u_{i-1,j}^{t+\Delta t}$ and $u_{i,j-1}^{t+\Delta t}$ are known from previous calculations when iterating forward through the grid. In the case of v, iteration proceeds in the reverse i and j directions (i.e. iterating backwards through the grid). Thus, the values in Eqn. 2.14 at $v_{i+1,j}^{t+\Delta t}$ and $v_{i,j+1}^{t+\Delta t}$ are known from previous calculations when iterating backwards through the grid. Boundary conditions are set in the same manner as the FTCS method. The soluble molecule concentration at the next time point, $L_{i,j}^{t+\Delta t}$, is given by:

$$L_{i,j}^{t+\Delta t}=\frac{v_{i,j}^{t+\Delta t}+u_{i,j}^{t+\Delta t}}{2} \qquad (Eqn.\ 2.15)$$

The ADE method requires values to be stored for $u_{i,j}$, $v_{i,j}$, and $L_{i,j}$ for both the current time point (t) and the next time point ($t+\Delta t$) in the environment layer.

The ADE method is O(Δt^2) accurate in time and O(Δx^2, Δy^2) in space, i.e. it is more accurate than the FTCS method, but the computational cost remains O(n^2) per time step. Furthermore, the ADE method is an explicit method that is unconditionally numerically stable (typically seen with implicit methods), which does not place a restriction on Δt (60). Thus, Δt can be chosen based solely on the accuracy of the solution needed. A maximum Δt of approximately 4-6 times the Δt predicted by the conditional stability criterion of the FTCS method (Eqn. 2.12) can be used for the ADE method while maintaining acceptable accuracy (11, 60).

2.4.3 Spectral Methods – Discrete Sine and Cosine Transforms

Spectral methods solve PDEs by assuming the solution is a sum of basis functions and choosing basis coefficients in order to best satisfy the solution (63–65). Spectral methods reduce PDEs to ODEs, greatly diminishing the difficulty of computation. In practice, solution of the diffusion equation with spectral methods is fairly straightforward (66). First, Eqn. 2.10 is discretized in the same manner as the FTCS method except that the time derivative is left in continuous form:

$$\frac{\partial L}{\partial t} = D\left(\frac{L^t_{i+1,j} - L^t_{i,j} + L^t_{i-1,j} - L^t_{i,j}}{\Delta x^2} + \frac{L^t_{i,j+1} - L^t_{i,j} + L^t_{i,j-1} - L^t_{i,j}}{\Delta y^2}\right) \qquad (Eqn.\ 2.16)$$

The two-dimensional discrete sine transform (DST) and discrete cosine transform (DCT) are defined as:

$$L^t_{i,j} = \sum_{k=0}^{M-1}\sum_{l=0}^{N-1} \overline{A}_{k,l} \sin\left(\frac{\pi}{M+1}(k+1)(i+1)\right)\sin\left(\frac{\pi}{N+1}(l+1)(j+1)\right) \quad (Eqn.\ 2.17)$$

$$L_{i,j}^{t} = \sum_{k=0}^{M-1}\sum_{l=0}^{N-1} \overline{A}_{k,l} \cos\left(\frac{\pi}{M-1}(k)(i)\right)\cos\left(\frac{\pi}{N-1}(l)(j)\right) \qquad (Eqn.\ 2.18)$$

Where k and l are the spectrally transformed i and j discretization, M and N are the lengths of k and l, and $\bar{A}_{k,l}$ are the spectral coefficients. The DST is an even-valued function at k = -1, k = M, l = -1, and l = N which naturally applies a Dirichlet boundary condition (constant zero concentration). The DCT is an odd-valued function at k = -1, k = M, l = -1, and l = N which naturally applies a Neumann boundary condition (insulating).

We apply the appropriate transform (depending on the appropriate boundary condition for the physical situation) to each term in Eqn. 2.16 (64). After simplifying the resulting equation with common trigonometric identities, the equation is now an ODE:

$$\frac{\partial \overline{A}_{k,l}}{\partial t} = -P_{i,j}\overline{A}_{k,l} \qquad (Eqn.\ 2.19)$$

with solution:

$$\overline{A}_{k,l}^{t+\Delta t} = \overline{A}_{k,l}^{t} e^{-P_{i,j}\Delta t} \qquad (Eqn.\ 2.20)$$

In the case of the DST:

$$P_{i,j} = \frac{2D}{\Delta x \Delta y}\left\{2 - \left(\cos\left(\frac{\pi(i+1)}{M+1}\right) + \cos\left(\frac{\pi(j+1)}{N+1}\right)\right)\right\} \qquad (Eqn.\ 2.21)$$

and in the case of the DCT:

$$P_{i,j} = \frac{2D}{\Delta x \Delta y}\left\{2 - \left(\cos\left(\frac{\pi(i)}{M-1}\right) + \cos\left(\frac{\pi(j)}{N-1}\right)\right)\right\} \qquad (Eqn.\ 2.22)$$

$P_{i,j}$ is invariant and can be calculated from the discretization of the simulation space and the diffusion coefficient of the soluble molecule. If the spectral coefficients $\bar{A}_{k,l}$ at the current time point (t) can be determined then the spectral coefficients at the next time point ($t+\Delta t$) are given by Eqn. 2.20. Therefore, the solution has advanced forward in time

in the spectral space. If the spectral coefficients at the next time point ($t+\Delta t$) can be converted back into soluble molecule concentrations ($L_{i,j}$) then the diffusion equation has been advanced in time.

Techniques for calculating discrete spectral coefficients from values on a discretized grid (known as the forward transform) and the inverse (known as the inverse transform) have been well studied over the past half-century (67). Currently, the best available algorithm is the Fast Fourier Transform (FFT) which can compute transforms in O(*n log n*) time (64, 68). The FFTw (www.fftw.org) library provides a simple C++ interface for computing spectral coefficients and their inverses. Thus, an implementation for solving the diffusion equation using spectral methods is as follows:

1. Use Eqn. 2.21 or Eqn. 2.22 to calculate a propagator matrix ($M_{i,j}$) defined as:

   $$M_{i,j} = e^{-P_{i,j}\Delta t} \qquad (Eqn.\ 2.23)$$

   This only needs to be done once, as these coefficients are invariant.

2. Compute the spectral coefficients using the forward DCT or DST from the FFTw library for the current soluble molecule concentration field.

   $$\overline{A}_{k,l}^{t} = DCT\left(L_{i,j}\right) \text{ or } DST\left(L_{i,j}\right) \qquad (Eqn.\ 2.24)$$

3. Multiply the spectral coefficients by the propagator matrix ($M_{i,j}$).

   $$\overline{A}_{k,l}^{t+\Delta t} = \overline{A}_{k,l}^{t} M_{i,j} \qquad (Eqn.\ 2.25)$$

4. Compute the soluble molecule concentration at the next time point ($t+\Delta t$) from the spectral coefficients by using the iDCT or tDST from the FFTw library.

   $$L_{i,j}^{t+\Delta t} = iDCT\left(\overline{A}_{k,l}^{t+\Delta t}\right) \text{ or } iDST\left(\overline{A}_{k,l}^{t+\Delta t}\right) \qquad (Eqn.\ 2.26)$$

5. Repeat 2-4 for the next soluble molecule diffusion time step.

Spectral methods require the soluble molecule concentrations to be stored at (t) and ($t+\Delta t$) in the environment layer. The accuracy of spectral methods is difficult to relate to O notation. It has been demonstrated that the method is 'spectrally accurate', where errors tend to decay exponentially leading to much greater accuracy than purely finite difference methods (63–65). Similarly, stability requirements are typically determined by examining the solution with different combinations of time step and discretization size (64, 65). Using FFTw algorithms the computational cost is O($n \log n$) per time step with an associated cost of O(n^3) per time step for a simple i,j matrix multiplication of the propagator matrix and spectral coefficients. The matrix multiplication cost could be reduced using optimized routines such as the Strassen Algorithm, but in the scope of an entire hybrid multi-scale ABM the reduction in computational cost would be minimal (69).

One drawback of spectral methods is that the algorithm has difficulty handling discontinuities or shock-like behaviors in input matrices. Spectral methods produce artifacts (or aliasing) at jump discontinuities, known as the 'Gibb's Phenomenon', since the algorithm attempts to map continuous periodic functions to finite square functions (63, 64, 70). Agents modify concentrations in the environment in hybrid multi-scale ABMs, for example by secretion or uptake of soluble molecules, and therefore the input concentration field into the spectral method can be fairly discontinuous. A technique known as smoothing (or anti-aliasing) is applied to alleviate these issues (71). The most common smoothing method is the '2/3' rule, yet its computational cost can be large (71). We have implemented a simpler smoothing method in hybrid multi-scale ABMs by using the FTCS method presented above. We take between 2 and 5 FTCS algorithm steps

before solving the diffusion equation using spectral methods. Thus, an implementation of a 'smoothed' spectral method is as follows:

1. Use Eqn. 2.11 to solve soluble molecule diffusion using the FTCS method. Use a time step that satisfies Eqn. 2.12. Repeat 2-6 times.
2. Solve soluble molecule diffusion using the spectral method presented above, typically using time steps 25-50 times larger than the smoother time step.

2.4.4 Other Available Numerical Methods

Implicit and semi-implicit algorithms have also been used in hybrid multi-scale ABMs due to their stability characteristics (2, 13, 51, 72–74). While increased stability allows for large time steps, the need to assemble and determine a Jacobian matrix and the use of linear algebra solvers for systems of equations can be a complex task. Many libraries are available (e.g. LAPACK, LINPACK, PETSc, and GSL), yet adapting existing code to libraries can cause difficulties. The ease of implementation of explicit schemes with the FFTw library has led us away from implicit methods. Other recent advancements in solving PDEs are the multigrid and discrete wavelet transform methods. The multigrid method has been demonstrated in the context of hybrid multi-scale ABMs (27, 73, 75). Implementation of the algorithm without libraries could be challenging, as available libraries (PETSc, Dune, Trilinos, FETK) may be difficult to interface with existing code. The discrete wavelet transform (DWT) captures information in both the frequency and time domain, unlike the DCT and DST which capture only frequency information (76). Thus, the DWT can handle local discontinuities better than spectral methods while still using similar methods to compute wavelet coefficients at an O (*n log*

n) or even O(*n*) computational cost. DWTs are still relatively new and have yet to be applied in the context of a hybrid multi-scale ABM. Additionally, only limited libraries exist which presents a barrier to efficient usage. We are currently evaluating the possible benefits of both the multigrid and DWT algorithms in the context of solving soluble molecule diffusion in hybrid multi-scale ABMs.

2.5 Numerical Methods for ODE Sub-Models

Eqn. 2.4 is a description of any agent-associated reactions and must be solved for each agent in the simulation. For ease of explanation we present the numerical methods in the context of a single agent in vector notation (Eqn. 2.27).

$$\frac{d\vec{Y}}{dt} = f\left(L, \vec{Y}\right) + \vec{\beta} \qquad (Eqn.\ 2.27)$$

2.5.1 Forward Euler

The simplest and easiest algorithm to implement is the forward Euler (FE) method. Using a forward finite difference estimation of the first order derivative in Eqn. 2.27 and rearranging leads to:

$$\vec{Y}(t + \Delta t) = \vec{Y}(t) + \left(\frac{d\vec{Y}(t)}{dt}\right)\Delta t \qquad (Eqn.\ 2.28)$$

FE requires only the concentrations of each species at the current time point (*t*) to be known and an estimate of the derivative at the current time point (Eqn. 2.28). FE is O(*Δt*) accurate in time and its computational cost is O(*n*) per time step. The FE method is conditionally stable and is numerically unstable for stiff equations and large time steps. The criteria for numerical stability of the solution of a set of linear ODEs is given by:

$$|1 + \lambda\Delta t| < 1 \qquad (Eqn.\,2.29)$$

where λ is the set of eigenvalues for the system (77). For non-linear systems of ODEs (as in Table 2.1) the equations can be linearized and the behavior of the linearized system analyzed for stability, giving an approximate local stability criteria for the non-linear system (78). In practice this can be difficult for large systems of ODEs, and hence the stability limit for a particular set of ODEs is typically determined by trial-and-error (79). Numerical stability requirements of the FE method in no way guarantee accuracy of the solution.

2.5.2 4th Order Runge-Kutta

Runge-Kutta methods use higher-order terms from the Taylor-series expansion of the first derivative. The higher order terms are evaluated at distinct points and subsequently combined to give a better approximation to the first derivative (61, 77). Most common is the 4th order Runge-Kutta (RK4) formulation given by:

$$\vec{Y}(t + \Delta t) = \vec{Y}(t) + \frac{1}{6}(c_1 + 2c_2 + 2c_3 + c_4) \qquad (Eqn.\,2.30)$$

where

$$c_1 = \left(\frac{d\vec{Y}(t)}{dt}\right)\Delta t \qquad (Eqn.\,2.31)$$

$$c_2 = \left(\frac{d\left(\vec{Y}(t) + \frac{1}{2}c_1\right)}{dt}\right)\Delta t \qquad (Eqn.\,2.32)$$

$$c_3 = \left(\frac{d\left(\vec{Y}(t) + \frac{1}{2}c_2\right)}{dt}\right)\Delta t \qquad (Eqn.\,2.33)$$

$$c_4 = \left(\frac{d\left(\vec{Y}(t) + c_3\right)}{dt}\right)\Delta t \qquad (Eqn.\,2.34)$$

RK4 requires only the concentrations of each species at the current time point (t) to be known along with four estimates of the derivative (Eqn. 2.30). The RK4 method is $O(\Delta t^4)$ accurate in time, a significant improvement on the FE method. Its computational cost remains $O(n)$ per time step. RK4 is also a conditionally stable method. The criteria for numerical stability of linear ODEs is shown below, where λ is the set of eigenvalues for the system (78):

$$(1 + \lambda\Delta t) + \frac{1}{2}(\lambda\Delta t)^2 + \frac{1}{6}(\lambda\Delta t)^3 + \frac{1}{24}(\lambda\Delta t)^4 < 1 \qquad (Eqn.\ 2.35)$$

As mentioned above, biological systems are in general non-linear; therefore in practice the stability limit is again determined by trial-and-error.

2.5.3 Other Available Numerical Methods

A simple extension of the RK4 method is an adaptive step size Runge-Kutta method, known as RK4-5 (13, 61, 80, 81). This method determines the necessary time step for a given accuracy on-the-fly based on estimates of local error by calculating both the 4th order and 5th order Runge-Kutta solutions. The additional computational cost in calculating both 4th and 5th order solutions, estimating error, and determining the correct time step could be outweighed by significantly larger time steps. Implicit algorithms for solving ODEs can also be used (2, 51, 53, 73, 74, 82, 83). Similar to PDE algorithms, implicit algorithms require determining a Jacobian matrix and implementation of linear algebra solvers. Considering the large number of agents per simulation (anywhere from 100s to 100,000s), assembly and solution using can be an overwhelming task. Recently, some have suggested the use of in situ adaptive tabulation (ISAT) to minimize the number of numerical method calls (22, 84–88). ISAT functions by tabulating existing

solutions and determining appropriate regions of solution space where use of existing solutions or simple interpolation can accurately represent the solution without ever calling the numerical method (84, 85). ISAT has not been demonstrated in the context of hybrid multi-scale ABMs but the theoretical reduction in computational cost is enticing. Lastly, many external programs and frameworks exist for solving systems of ODEs that could be linked to a hybrid multi-scale ABM such as MATLAB, COPASI, and CVODE (5, 22, 40, 89, 90). In our experience linking external programs to existing code can be difficult and may confer a large computational cost associated with module communication.

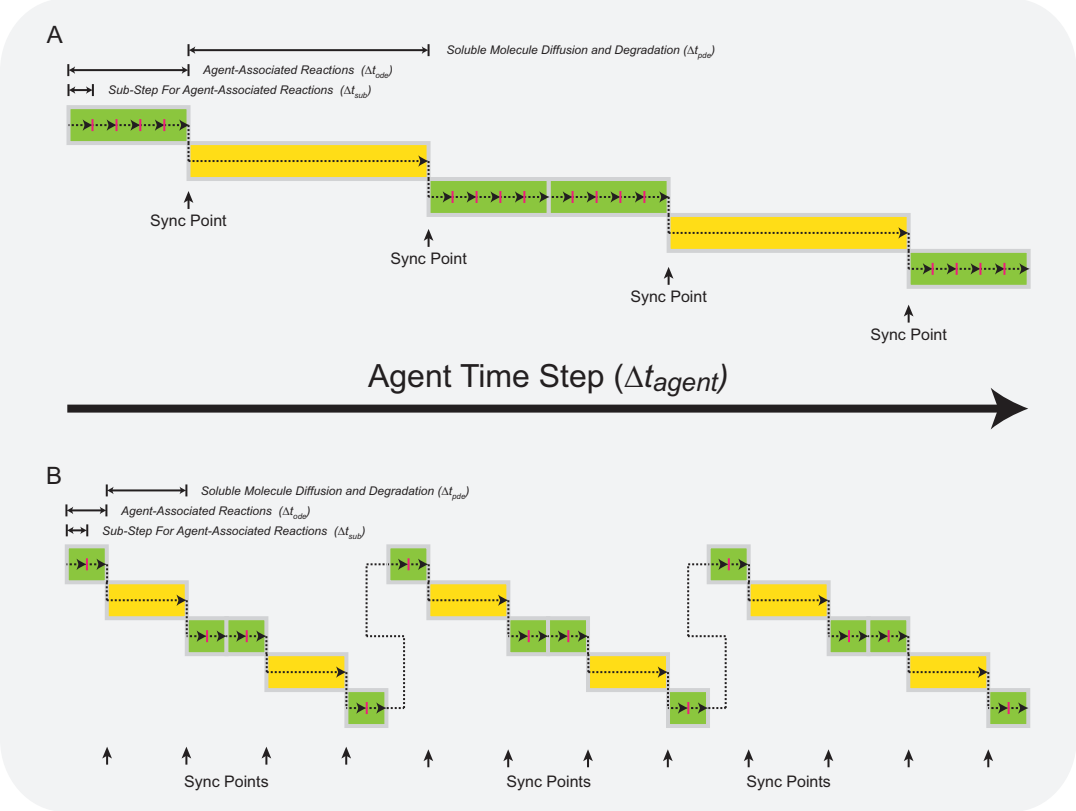

Figure 2.6 Syncing time steps across hybrid multi-scale agent-based models
Example of two different combinations of time steps for soluble molecule diffusion and agent-associated reactions. (A) A large time step for soluble molecule diffusion requires few sync points with the agent-associated reactions. (B) A small time step for soluble molecule diffusion requires a significant number of sync points with the agent-associated reactions.

2.6 Syncing Numerical Methods in Hybrid Multi-Scale ABMs

It is critical to maintain *sync points* where differing time steps used to solve the PDEs, ODEs, and ABM are reconciled, thus linking the mathematics, exchanging information across scales, and allowing the model to correctly proceed forward in time. A challenge of hybrid multi-scale ABMs is to determine the largest time step for each numerical method that maintains easily identifiable sync points. For instance, a numerical method that solves soluble molecule diffusion with a large time step requires fewer sync points with the agent-associated reactions (Figure 2.6A) than a numerical method that solves soluble molecule diffusion with a smaller time steps (Figure 2.6B). A simple procedure for determining time steps that maintain sync points is given below. We assume Strang splitting and a previously determined time step for the agent-based model, Δt_{agent}:

1. Estimate the maximum time step to solve the soluble molecule diffusion and degradation (Θ_4) for the chosen numerical method. A good starting point for all numerical methods is Eqn. 2.12. Reduce the estimated time step to a number divisible by Δt_{agent} for syncing and set this value as Δt_{pde}.
2. Estimate the maximum time step, Δt_{ode}, to solve the ODE model of agent-associated reactions (Θ_2) for the chosen numerical method. This can be accomplished by linearizing the equations and using Eqn. 2.29 or Eqn. 2.35 or by using trial-and-error in a 'test-bed' environment such as a standalone implementation of the numerical method in C++ or MATLAB (The Mathworks Inc. – Natick, MA). Frequently, the maximal time step for numerical accuracy and stability will be significantly smaller than $\Delta t_{pde}/2$. Choose Δt_{ode} such that stability

and accuracy requirements are satisfied. Additionally reduce Δt_{ode} to a number that is evenly divisible by $\Delta t_{pde}/2$ for syncing.

3. Using the estimated time steps (Δt_{agent}, Δt_{pde}, and Δt_{ode}) solve the hybrid ABM.
4. Reduce all time steps by a factor of 2 and re-solve the system.
5. Compare the model solutions. If the solutions are inconsistent the time steps are too large. Reduce all time steps (Δt_{pde} and Δt_{ode}) and re-verify that each is able to 'sync'. Repeat steps 3-5 until the model solutions are within the desired tolerance.

A full hybrid multi-scale ABM algorithm is shown in Figure 2.7 and includes: (1) the agent time step, Δt_{agent} (agents move, change state, etc.), (2) the ODE time step, Δt_{ode} (agent-associated reactions), and (3) the PDE time step, Δt_{pde} (diffusion and degradation).

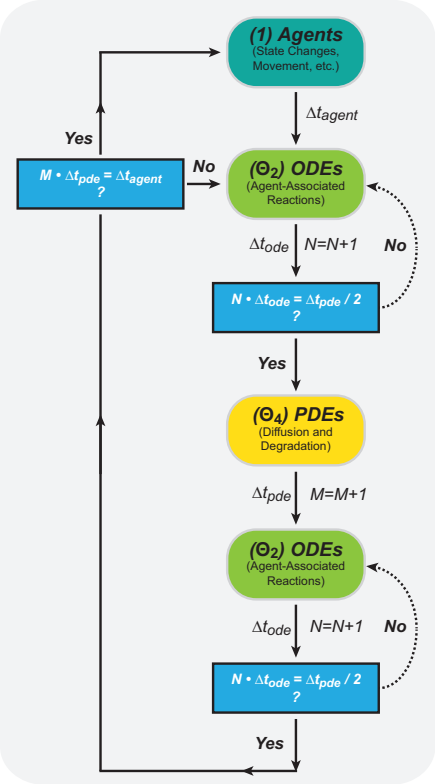

Figure 2.7 Diagram of a solution algorithm for a hybrid multi-scale agent-based
(1) Update agents (movement, states, proliferation, etc). (2) Solve a single time step (Δt_{ode}) for agent-associated reactions (Θ_2). Increment a counter N. If the total time step ($N \times \Delta t_{ode}$) is equal to ($\Delta t_{pde}/2$) then move on to soluble molecule diffusion and degradation. If not, take another single time step for agent-associated reactions (Θ_2) and check again. (3) Solve a single time step (Δt_{pde}) for soluble molecule diffusion

and degradation. Increment a counter M. (4) Solve a single time step (Δt_{ode}) for agent-associated reactions (Θ_2). Increment a counter N. If the total time step ($N \times \Delta t_{ode}$) is equal to ($\Delta t_{pde}/2$) move on to the final check. If not, take another single time step for agent-associated reactions (Θ_2) and check again. (5) If the total time step ($M \times \Delta t_{pde}$) is equal to (Δt_{agent}) then a full time step has been completed. Continue by updating agents as indicated in (1). If not, continue solving with step (2).

2.7 Comparison of Computational Speeds using an Example Hybrid Multi-Scale ABM

Choosing numerical methods that maintain computational tractability of a hybrid multi-scale ABM is essential. Considerations affecting the choice of numerical methods include: number of agents, number of agent-associated reactions, and model dimensionality (i.e. 2D or 3D). In addition, uncertainty and sensitivity analysis is commonly used to understand how variations in parameter values affect model results, which necessitates large numbers of model simulations (~10^3) (91). In practice, hybrid multi-scale ABMs that require over a day to run severely limits the usefulness of modeling efforts.

As an example of the application of numerical methods described above, we ran several comparison simulations with our hybrid multi-scale ABM of *M. tuberculosis* infection discussed in Chapters 3, 4, 5, 6, and Appendix C (9, 11, 33) (Pienaar et al. submitted). In these models the discretization size (Δx, Δy) of the environment and agent layers is 20 μm. In Scenario 1, we simulate 100 days of the immune response following an initial infection with *M. tuberculosis*. Diffusion and degradation of three soluble molecules (two cytokines and one chemokine) are tracked, and thirteen agent-associated differential equations describe receptor-ligand binding, trafficking and signaling of TNF and IL-10 (see Chapter 3 for full details) (11). Soluble molecule diffusivities are ~10^{-8} cm^2/sec for cytokines and chemokines. In Scenario 2, we simulate 50 days of the immune

response following an initial infection with *M. tuberculosis* plus an additional 50 days of antibiotic treatment (see Appendix C for full details) (Pienaar et al. submitted). Diffusion and degradation of five soluble molecules (two cytokines, one chemokine, and two antibiotics) are tracked, and thirteen agent-associated differential equations describe receptor-ligand binding, trafficking and signaling of TNF and IL-10. In addition, the model in Scenario 2 tracks the anti-microbial response of antibiotics against bacteria. Soluble molecule diffusivities for molecules such as antibiotics are between 10^{-6} and 10^{-7} cm^2/sec. As antibiotics diffuse much faster through tissue than cytokines and chemokines, there are additional restrictions on time steps used in numerical methods that must be considered. In both Scenario 1 and 2, we also employed a tuneable resolution approach (assuming pseudo steady state for multiple reactions and using apparent rate constants) to reduce the thirteen agent-associated differential equations to two agent-associated differential equations (Pienaar et al. submitted).

We show relative computational speeds for both a 100x100 (4 mm^2) and 200x200 (16 mm^2) simulation grid. For the larger grid, the number of calculations is increased due to ~2-fold more agents and 4-fold more simulation space. For Scenarios 1 and 2, we ran combinations of each numerical method described above. In addition, we demonstrate reductions in computational burdens based on a tuneable resolution approach. Table 2.2 and Table 2.3 depict fold-changes in computational speed normalized to the slowest value for the specific grid size (higher values indicate shorter computation times). Model runs were carried out on the Flux computing cluster available from Advanced Research Computing at the University of Michigan, Ann Arbor.

Table 2.2 Relative computational speeds for Scenario 1

	100 × 100 Simulation Grid ~5,000 Agents			200 × 200 Simulation Grid ~10,000 Agents		
	ODE Numerical Method			***ODE Numerical Method***		
PDE Numerical Method	**FE (Δt = 0.6s)**	**RK4 (Δt = 6s)**	**TR (Δt = 6s)**	**FE (Δt = 0.6s)**	**RK4 (Δt = 6s)**	**TR (Δt = 6s)**
FTCS (Δt = 6s)	1.0	2.3	4.6	1.0	2.6	5.4
ADE (Δt = 30s)	1.8	4.3	12.8	1.2	3.9	7.7
SM (Δt = 120s)	1.8	5.5	22.7	1.2	5.2	23.6

FTCS – Forward Time Central Space, ADE – Alternating Direction Explicit, SM – Spectral Method, FE – Forward Euler, RK4 – Runge-Kutta 4th Order, TR – Tuneable Resolution
N=3 for all simulations. 100×100 – Relative Speed of 1.0 corresponds to 7589 s of simulation time, 200×200 – Relative Speed of 1.0 corresponds to 46907 s of simulation time

Table 2.3 Relative computational speeds for Scenario 2

	100 × 100 Simulation Grid ~5,000 Agents						200 × 200 Simulation Grid ~10,000 Agents					
	ODE Numerical Method						***ODE Numerical Method***					
PDE Numerical Method	**FE**		**RK4**		**TR**		**FE**		**RK4**		**TR**	
FTCS	(0.6/0.6)	1.4	(0.6/0.6)	1.0	(0.6/0.6)	1.5	(0.6/0.6)	1.4	(0.6/0.6)	1.0	(0.6/0.6)	1.2
ADE	(3.0/0.6)	2.8	(3.0/3.0)	3.2	(3.0/3.0)	3.6	(3.0/0.6)	3.1	(3.0/3.0)	4.0	(3.0/3.0)	4.9
SM	(60/0.6)	6.8	(60/6.0)	15.8	(60/6.0)	43.8	(60/0.6)	8.3	(60/6.0)	26.3	(60/6.0)	63.5

(xx/xx) → (Soluble Molecule Diffusion Time Step / Agent-Associated Reactions Time Step)
FTCS – Forward Time Central Space, ADE – Alternating Direction Explicit, SM – Spectral Method, FE – Forward Euler, RK4 – Runge-Kutta 4th Order, TR – Tuneable Resolution
N=3 for all simulations. 100×100 – Relative Speed of 1.0 corresponds to 26968 s of simulation time, 200×200 – Relative Speed of 1.0 corresponds to 259150 s of simulation time

Our results in Table 2.2 and Table 2.3 demonstrate that implementation of appropriate numerical methods and time steps can dramatically improve overall computational speed in hybrid multi-scale ABMs. Moving to more sophisticated numerical methods for solution both ODEs and PDEs increases computational speed by up to 5-fold. The benefits of a tuneable resolution approach are easily observed, with a further 2-fold to 5-fold increase in the computational speed beyond increases due to choice of numerical method (Table 2.2 and Table 2.3). Although Scenario 1 does benefit from spectral methods, the diffusion time step cannot be increased (beyond 120 seconds) as the mathematics begin to decouple at larger time step (see Operator Splitting section). The diffusion time steps in Scenario 2 are restricted to smaller values as the antibiotics

diffuse much faster than cytokines and chemokines in the environment. With these restrictions on diffusion time steps, decoupling is less of a concern in Scenario 2 and spectral methods are more advantageous than in Scenario 1. In both scenarios a combination of tuneable resolution and spectral methods increases computational speeds more than 20-fold.

There are caveats to implementation of faster and more efficient numerical algorithms in the context of hybrid multi-scale ABM. Increasing the efficiency of solving one operator (Eqn. 2.3-2.5) is eventually limited by the efficiency of solving a different operator. For instance, implementing a spectral-based algorithm for solving the diffusion operator is of limited benefit if the agent-associated reactions (ODEs) are solved using a Forward Euler-based methodology (Table 2.2). Thus, improvements in one operator must also be thought of in the context of another operator, leading to a constant cycle of re-evaluation and implementation of numerical solvers.

Another critical aspect of solving hybrid multi-scale ABMs is the importance of correctly choosing algorithms with compatible time steps. The benefit of implementing a different numerical algorithm can be hindered if the algorithm cannot take sufficiently large time steps due to limitations of another numerical algorithm. For instance, in Scenario 2 a Runge-Kutta 4^{th} order based algorithm to solve the agent-associated reactions could theoretically use time steps upwards of 5-10 seconds. However, due to faster tissue diffusivity values of antibiotics (~10-fold higher than cytokines and chemokines) a Forward-Time Central Space based algorithm, along with operator splitting, limits use of a larger time step (Table 2.3).

Lastly, it is important to understand the computational costs associated with expanding the size of a model. On average, transitioning from a 100x100 to a 200x200 simulation grid reduces the computational speed ~7-fold. We have also expanded the example hybrid multi-scale ABM to 3-dimensions (100x100 to 100x100x100), which reduced the reduced the computational speed ~42-fold. Without a priori knowledge of these factors that contribute to computational costs, hybrid multi-scale ABMs may become too bulky or inefficient to provide novel insights into complex biological systems.

2.8 Discussion

Multi-scale models aim to replicate fundamental behaviors of biological systems, with constant exchange of information across scales, in order to better understand and predict system behavior as a whole. Coupling individual scale models, such as an agent-based model and differential equation models, to allow for the exchange of information is typically accomplished by linking the mathematical formulations at each scale. Thus, tools to link individual scale models and efficient methods of solving the subsequent models are important to advance the use of hybrid multi-scale ABMs in generating new biological knowledge from the wealth of available data.

In this Chapter, we describe the general framework for linking ABMs and differential equation models and solving the resulting hybrid multi-scale model, including layers, discretization, and operator splitting. The framework is extendable to different levels of model detail and adaptable to the focus and needs of the problem (e.g. inclusion of antibiotic treatment in an infection model, or moving from two to three dimensions).

We review three numerical algorithms for solving soluble molecule diffusion and two numerical algorithms for solving individual agent-associated reactions. Additionally, we demonstrate the merits of a tuneable resolution approach to reduce the complexity of a system and limit computational cost (46). We anticipate that future versions of current ABM platforms and languages, such as NetLogo or SPARK, will build on hybrid model concepts and include a framework to allow for exchange of information across individual scale models. This would allow a less knowledgeable user to easily develop a hybrid multi-scale ABM and prevent the need for many users to 're-invent the wheel' in order to link individual scale models.

We demonstrate how an appropriate choice of numerical algorithms and time steps can improve the computational tractability and efficiency of a hybrid multi-scale ABM. The most important factors in choosing these algorithms are: (1) familiarity with the underlying mathematics, (2) an understanding of relative process rates, and (3) computational time and power available. If unfamiliar with numerical methods, it is easier to implement an algorithm built around simple mathematical concepts, such as FTCS for solving soluble molecule diffusion, than to start with a more mathematically sophisticated algorithm. As the user becomes comfortable with a simple implementation, more complex algorithms tend to build on simpler concepts in an incremental fashion. Second, it is necessary to have a basic understanding of relative rates (e.g. rates of diffusion compared to rates of agent-associated reactions) in order to determine whether solution of a hybrid multi-scale ABM will benefit from a particular numerical algorithm. For instance, a small molecule drug diffuses through tissue much faster than a soluble protein molecule (such as a cytokine) so implementing a method that solves the agent-

associated reactions with a time step larger than the time step required for solving diffusion of the drug through tissue has limited benefits as the diffusive rate restricts the overall time step (Table 2.3). Lastly, it is important to know the computational power available and computational time needed for each model, as new numerical methods can have diminishing returns. For instance, running sensitivity analysis requires a large number of model simulations. Therefore, implementing a new numerical method in a model will have more benefits in this instance compared to individual model runs.

Multi-scale models are becoming a more prevalent tool to understand systems-level biological phenomena. As multi-scale efforts continue to expand in scope, it is important to have a rational understanding of the underlying mathematical framework and numerical methods available to solve them. We demonstrate a framework and suggest tools that allow for efficient implementation of hybrid multi-scale ABMs to help guide the choice and development of both new model creation and existing platforms.

2.9 References

1. Hunt, C. A., R. C. Kennedy, S. H. J. Kim, and G. E. P. Ropella. 2013. Agent-based modeling: a systematic assessment of use cases and requirements for enhancing pharmaceutical research and development productivity. *Wiley Interdiscip. Rev. Syst. Biol. Med.* 5: 461–80.

2. Materi, W., and D. S. Wishart. 2007. Computational systems biology in drug discovery and development: methods and applications. *Drug Discov. Today* 12: 295–303.

3. Wang, J., L. Zhang, C. Jing, G. Ye, H. Wu, H. Miao, Y. Wu, and X. Zhou. 2013. Multi-scale agent-based modeling on melanoma and its related angiogenesis analysis. *Theor. Biol. Med. Model.* 10: 41.

4. An, G., Q. Mi, J. Dutta-Moscato, and Y. Vodovotz. 2009. Agent-based models in translational systems biology. *Wiley Interdiscip. Rev. Syst. Biol. Med.* 1: 159–71.

5. Walpole, J., J. a Papin, and S. M. Peirce. 2013. Multiscale Computational Models of Complex Biological Systems. *Annu. Rev. Biomed. Eng.* 137–154.

6. Qutub, A. A., F. Mac Gabhann, E. D. Karagiannis, P. Vempati, and A. S. Popel. 2009. Multiscale models of angiogenesis. *IEEE Eng. Med. Biol. Mag.* 28: 14–31.

7. Deisboeck, T. S., Z. Wang, P. Macklin, and V. Cristini. 2011. Multiscale cancer modeling. *Annu. Rev. Biomed. Eng.* 13: 127–55.

8. Guo, Z., P. M. a Sloot, and J. C. Tay. 2008. A hybrid agent-based approach for modeling microbiological systems. *J. Theor. Biol.* 255: 163–75.

9. Fallahi-Sichani, M., M. El-Kebir, S. Marino, D. E. Kirschner, and J. J. Linderman. 2011. Multiscale computational modeling reveals a critical role for TNF-α receptor 1 dynamics in tuberculosis granuloma formation. *J. Immunol.* 186: 3472–83.

10. Fallahi-Sichani, M., J. L. Flynn, J. J. Linderman, and D. E. Kirschner. 2012. Differential risk of tuberculosis reactivation among anti-TNF therapies is due to drug binding kinetics and permeability. *J. Immunol.* 188: 3169–78.

11. Cilfone, N. A., C. R. Perry, D. E. Kirschner, and J. J. Linderman. 2013. Multi-Scale Modeling Predicts a Balance of Tumor Necrosis Factor-α and Interleukin-10 Controls the Granuloma Environment during Mycobacterium tuberculosis Infection. *PLoS One* 8: e68680.

12. Sloot, P. M. a, and A. G. Hoekstra. 2010. Multi-scale modelling in computational biomedicine. *Brief. Bioinform.* 11: 142–52.

13. Southern, J., J. Pitt-Francis, J. Whiteley, D. Stokeley, H. Kobashi, R. Nobes, Y. Kadooka, and D. Gavaghan. 2008. Multi-scale computational modelling in biology and physiology. *Prog. Biophys. Mol. Biol.* 96: 60–89.

14. Wang, Z., J. D. Butner, R. Kerketta, V. Cristini, and T. S. Deisboeck. 2014. Simulating Cancer Growth with Multiscale Agent-Based Modeling. *Semin. Cancer Biol.* 1–9.

15. 2007. *Single-Cell-Based Models in Biology and Medicine*, (A. R. A. Anderson, M. A. J. Chaplain, and K. A. Rejniak, eds). Birkhäuser Basel, Basel.

16. Coveney, P. V, and P. W. Fowler. 2005. Modelling biological complexity: a physical scientist's perspective. *J. R. Soc. Interface* 2: 267–80.

17. Kirschner, D. E., S. T. Chang, T. W. Riggs, N. Perry, and J. J. Linderman. 2007. Toward a multiscale model of antigen presentation in immunity. *Immunol. Rev.* 216: 93–118.

18. Qutub, A. a, and A. S. Popel. 2009. Elongation, proliferation & migration differentiate endothelial cell phenotypes and determine capillary sprouting. *BMC Syst. Biol.* 3: 13.

19. Bauer, A. L., C. a. a. A. Beauchemin, and A. S. Perelson. 2009. Agent-based modeling of host-pathogen systems: The successes and challenges. *Inf. Sci. (Ny).* 179: 1379–1389.

20. Krinner, A., I. Roeder, M. Loeffler, and M. Scholz. 2013. Merging concepts - coupling an agent-based model of hematopoietic stem cells with an ODE model of granulopoiesis. *BMC Syst. Biol.* 7: 117.

21. Walker, D. C., and J. Southgate. 2009. The virtual cell--a candidate co-ordinator for "middle-out" modelling of biological systems. *Brief. Bioinform.* 10: 450–61.

22. Dada, J. O., and P. Mendes. 2011. Multi-scale modelling and simulation in systems biology. *Integr. Biol. (Camb).* 3: 86–96.

23. Figueredo, G. P., T. V Joshi, J. M. Osborne, H. M. Byrne, and M. R. Owen. 2013. On-lattice agent-based simulation of populations of cells within the open-source Chaste framework. *Interface Focus* 3: 20120081.

24. Bailey, A. M., M. B. Lawrence, H. Shang, A. J. Katz, and S. M. Peirce. 2009. Agent-based model of therapeutic adipose-derived stromal cell trafficking during ischemia predicts ability to roll on P-selectin. *PLoS Comput. Biol.* 5: e1000294.

25. Santoni, D., M. Pedicini, and F. Castiglione. 2008. Implementation of a regulatory gene network to simulate the TH1/2 differentiation in an agent-based model of hypersensitivity reactions. *Bioinformatics* 24: 1374–80.

26. Angermann, B. R., F. Klauschen, A. D. Garcia, T. Prustel, F. Zhang, R. N. Germain, and M. Meier-Schellersheim. 2012. Computational modeling of cellular signaling processes embedded into dynamic spatial contexts. *Nat. Methods* 9: 283–9.

27. Kaul, H., Z. Cui, and Y. Ventikos. 2013. A multi-paradigm modeling framework to simulate dynamic reciprocity in a bioreactor. *PLoS One* 8: e59671.

28. Stern, J. R., S. Christley, O. Zaborina, J. C. Alverdy, and G. An. 2012. Integration of TGF-β- and EGFR-based signaling pathways using an agent-based model of epithelial restitution. *Wound Repair Regen.* 20: 862–71.

29. Athale, C. a, and T. S. Deisboeck. 2006. The effects of EGF-receptor density on multiscale tumor growth patterns. *J. Theor. Biol.* 238: 771–9.

30. Athale, C., Y. Mansury, and T. S. Deisboeck. 2005. Simulating the impact of a molecular “decision-process” on cellular phenotype and multicellular patterns in brain tumors. *J. Theor. Biol.* 233: 469–81.

31. Wang, Z., V. Bordas, J. Sagotsky, and T. S. Deisboeck. 2012. Identifying therapeutic targets in a combined EGFR-TGFβR signalling cascade using a multiscale agent-based cancer model. *Math. Med. Biol.* 29: 95–108.

32. Ray, J. C. J., J. L. Flynn, and D. E. Kirschner. 2009. Synergy between individual TNF-dependent functions determines granuloma performance for controlling Mycobacterium tuberculosis infection. *J. Immunol.* 182: 3706–17.

33. Fallahi-Sichani, M., D. E. Kirschner, and J. J. Linderman. 2012. NF-κB Signaling Dynamics Play a Key Role in Infection Control in Tuberculosis. *Front. Physiol.* 3: 170.

34. Flynn, J. L., and J. Chan. 2001. Immunology of tuberculosis. *Annu. Rev. Immunol.* 19: 93–129.

35. Marino, S., J. J. Linderman, and D. E. Kirschner. 2011. A multifaceted approach to modeling the immune response in tuberculosis. *Wiley Interdiscip. Rev. Syst. Biol. Med.* 3: 479–89.

36. Christley, S., and G. An. 2013. Agent-Based Modeling in Translational Systems Biology. In *Complex Systems and Computational Biology Approaches to Acute Inflammation SE - 3* Y. Vodovotz, and G. An, eds. Springer New York, New York, NY. 29–49.

37. Rapin, N., O. Lund, M. Bernaschi, and F. Castiglione. 2010. Computational immunology meets bioinformatics: the use of prediction tools for molecular binding in the simulation of the immune system. *PLoS One* 5: e9862.

38. Segovia-Juarez, J. L., S. Ganguli, and D. Kirschner. 2004. Identifying control mechanisms of granuloma formation during M. tuberculosis infection using an agent-based model. *J. Theor. Biol.* 231: 357–76.

39. Gong, C., J. T. Mattila, M. Miller, J. L. Flynn, J. J. Linderman, and D. Kirschner. 2013. Predicting lymph node output efficiency using systems biology. *J. Theor. Biol.* 335C: 169–184.

40. Adra, S., T. Sun, S. MacNeil, M. Holcombe, and R. Smallwood. 2010. Development of a three dimensional multiscale computational model of the human epidermis. *PLoS One* 5: e8511.

41. Alarcón, T., H. M. Byrne, and P. K. Maini. 2004. Towards whole-organ modelling of tumour growth. *Prog. Biophys. Mol. Biol.* 85: 451–72.

42. Wolff, K., C. Barrett-Freeman, M. R. Evans, a B. Goryachev, and D. Marenduzzo. 2014. Modelling the effect of myosin X motors on filopodia growth. *Phys. Biol.* 11: 016005.

43. Basak, S., M. Behar, and A. Hoffmann. 2012. Lessons from mathematically modeling the NF-κB pathway. *Immunol. Rev.* 246: 221–38.

44. Tay, S., J. J. Hughey, T. K. Lee, T. Lipniacki, S. R. Quake, and M. W. Covert. 2010. Single-cell NF-kappaB dynamics reveal digital activation and analogue information processing. *Nature* 466: 267–71.

45. Braun, D. a, M. Fribourg, and S. C. Sealfon. 2013. Cytokine Response Is Determined by Duration of Receptor and Signal Transducers and Activators of Transcription 3 (STAT3) Activation. *J. Biol. Chem.* 288: 2986–93.

46. Linderman, J. J., C. A. Hunt, S. Marino, M. Fallahi-Sichani, and D. Kirschner. 2014. Tuneable resolution as an approach to study multi-scale, multi-organ models in systems biology. *WIRES Syst. Biol. Med.* In Press.

47. Lauffenburger, D. A., and J. J. Linderman. 1993. Receptors: Models For Binding, Trafficking, and Signaling. In Oxford University Press, New York.

48. Bird, R. B., W. E. Stewart, and E. N. Lightfoot. 1994. *Transport Phenomena*,. John Wiley & Sons, New York.

49. Lucas, T. A. 2008. Operator Splitting for an Immunology Model Using Reaction-Diffusion Equations with Stochastic Source Terms. *SIAM J. Numer. Anal.* 46: 3113–3135.

50. Sundnes, J., G. T. Lines, and A. Tveito. 2005. An operator splitting method for solving the bidomain equations coupled to a volume conductor model for the torso. *Math. Biosci.* 194: 233–48.

51. Mitha, F., T. a Lucas, F. Feng, T. B. Kepler, and C. Chan. 2008. The Multiscale Systems Immunology project: software for cell-based immunological simulation. *Source Code Biol. Med.* 3: 6.

52. Strang, G. 1968. On the Construction and Comparison of Difference Schemes. *SIAM J. Numer. Anal.* 5: 506–517.

53. Choi, T., M. R. Maurya, D. M. Tartakovsky, and S. Subramaniam. 2012. Stochastic operator-splitting method for reaction-diffusion systems. *J. Chem. Phys.* 137: 184102.

54. Karlsen, K. H., K. –. Lie, J. . Natvig, H. . Nordhaug, and H. . Dahle. 2001. Operator Splitting Methods for Systems of Convection–Diffusion Equations: Nonlinear Error Mechanisms and Correction Strategies. *J. Comput. Phys.* 173: 636–663.

55. Yoshida, H. 1990. Construction of higher order symplectic integrators. *Phys. Lett. A* 150: 262–268.

56. Csomós, P., I. Faragó, and Á. Havasi. 2005. Weighted sequential splittings and their analysis. *Comput. Math. with Appl.* 50: 1017–1031.

57. Geiser, J., G. Tanoğlu, and N. Gücüyenen. 2011. Higher order operator splitting methods via Zassenhaus product formula: Theory and applications. *Comput. Math. with Appl.* 62: 1994–2015.

58. Gong, C., J. J. Linderman, and D. Kirschner. 2014. Harnessing the Heterogeneity of T Cell Differentiation Fate to Fine-Tune Generation of Effector and Memory T Cells. *Front. Immunol.* 5: 1–15.

59. Marino, S., M. El-Kebir, and D. Kirschner. 2011. A hybrid multi-compartment model of granuloma formation and T cell priming in tuberculosis. *J. Theor. Biol.* 280: 50–62.

60. Barakat, H. Z., and J. A. Clark. 1966. On the Solution of the Diffusion Equations by Numerical Methods. *J. Heat Transfer* 88: 421.

61. Press, W. H. 2002. *Numerical Recipes in C++: the art of scientific computing*, 2nd ed. Cambridge University Press, Cambridge, UK.

62. Peaceman, D. W., and H. H. Rachford, Jr. 1955. The Numerical Solution of Parabolic and Elliptic Differential Equations. *J. Soc. Ind. Appl. Math.* 3: 28–41.

63. Trefethen, L. N. 1996. *Finite Difference and Spectral Methods for Ordinary and Partial Differential Equations*,. Unpublished Text.

64. Costa, B. 2004. Spectral Methods for Partial Differential Equations. 6.

65. Fornberg, B. 1996. A practical guide to pseudospectral methods. x, 231 p.

66. Mugler, D. H., and R. A. Scott. 1988. Fast fourier transform method for partial differential equations, case study: The 2-D diffusion equation. *Comput. Math. with Appl.* 16: 221–228.

67. Duhamel, P., and M. Vetterli. 1990. Fast fourier transforms: A tutorial review and a state of the art. *Signal Processing* 19: 259–299.

68. Frigo, M., and S. G. Johnson. 2005. The Design and Implementation of FFTW3. *Proc. IEEE* 93: 216–231.

69. Strassen, V. 1969. Gaussian elimination is not optimal. *Numer. Math.* 13: 354–356.

70. Gottlieb, D., and C.-W. Shu. 1997. On the Gibbs Phenomenon and Its Resolution. *SIAM Rev.* 39: 644–668.

71. Hou, T. Y., and R. Li. 2007. Computing nearly singular solutions using pseudo-spectral methods. *J. Comput. Phys.* 226: 379–397.

72. Zhang, L., B. Jiang, Y. Wu, C. Strouthos, P. Z. Sun, J. Su, and X. Zhou. 2011. *Developing a multiscale, multi-resolution agent-based brain tumor model by graphics processing units.*,. ; :46.

73. Wise, S. M., J. S. Lowengrub, and V. Cristini. 2011. An Adaptive Multigrid Algorithm for Simulating Solid Tumor Growth Using Mixture Models. *Math. Comput. Model.* 53: 1–20.

74. Frieboes, H. B., J. S. Lowengrub, S. Wise, X. Zheng, P. Macklin, E. L. Bearer, and V. Cristini. 2007. Computer simulation of glioma growth and morphology. *Neuroimage* 37 Suppl 1: S59–70.

75. Wise, S., J. Kim, and J. Lowengrub. 2007. Solving the regularized, strongly anisotropic Cahn–Hilliard equation by an adaptive nonlinear multigrid method. *J. Comput. Phys.* 226: 414–446.

76. Daubechies, I. 1990. The wavelet transform, time-frequency localization and signal analysis. *IEEE Trans. Inf. Theory* 36: 961–1005.

77. Riley, K. F., M. P. Hobson, and S. J. Bence. 2002. *Mathematical Methods for Physics and Engineering: A Comprehensive Guide*,. Cambridge University Press.

78. LeVeque, R. J. 2007. *Finite Difference Methods for Ordinary and Partial Differential Equations: Steady-state and Time-Dependent Problems*,. Society for Industrial and Applied Mathematics (SIAM, 3600 Market Street, Floor 6, Philadelphia, PA 19104).

79. Rao, S., A. van der Schaft, K. van Eunen, B. M. Bakker, and B. Jayawardhana. 2014. A Model Reduction Method for Biochemical Reaction Networks. *BMC Syst. Biol.* 8: 52.

80. Stefanini, M. O., F. T. H. Wu, F. Mac Gabhann, and A. S. Popel. 2009. The Presence of VEGF Receptors on the Luminal Surface of Endothelial Cells Affects VEGF Distribution and VEGF Signaling. *PLoS Comput. Biol.* 5.

81. Zingg, D. W., and T. T. Chisholm. 1999. Runge–Kutta methods for linear ordinary differential equations. *Appl. Numer. Math.* 31: 227–238.

82. Palsson, S., T. P. Hickling, E. L. Bradshaw-Pierce, M. Zager, K. Jooss, P. J. O'Brien, M. E. Spilker, B. O. Palsson, P. Vicini, and P. J. O Brien. 2013. The development of a fully-integrated immune response model (FIRM) simulator of the immune response through integration of multiple subset models. *BMC Syst. Biol.* 7: 95.

83. Heidlauf, T., and O. Röhrle. 2013. Modeling the Chemoelectromechanical Behavior of Skeletal Muscle Using the Parallel Open-Source Software Library OpenCMISS. *Comput. Math. Methods Med.* 2013: 517287.

84. Singer, M., S. Pope, and H. Najm. 2006. Modeling unsteady reacting flow with operator splitting and ISAT. *Combust. Flame* 147: 150–162.

85. Pope, S. B. 1997. Computationally efficient implementation of combustion chemistry using in situ adaptive tabulation. *Combust. Theory Model.* 1: 41–63.

86. Hedengren, J. D., and T. F. Edgar. 2005. Order reduction of large scale DAE models. *Comput. Chem. Eng.* 29: 2069–2077.

87. Hedengren, J. D., and T. F. Edgar. 2005. In Situ Adaptive Tabulation for Real-Time Control. *Ind. Eng. Chem. Res.* 44: 2716–2724.

88. Chakrabarti, A., S. Verbridge, A. D. Stroock, C. Fischbach, and J. D. Varner. 2012. Multiscale models of breast cancer progression. *Ann. Biomed. Eng.* 40: 2488–500.

89. Sun, T., S. Adra, R. Smallwood, M. Holcombe, and S. MacNeil. 2009. Exploring hypotheses of the actions of TGF-beta1 in epidermal wound healing using a 3D computational multiscale model of the human epidermis. *PLoS One* 4: e8515.

90. Holcombe, M., S. Adra, M. Bicak, S. Chin, S. Coakley, A. I. Graham, J. Green, C. Greenough, D. Jackson, M. Kiran, S. MacNeil, A. Maleki-Dizaji, P. McMinn, M. Pogson, R. Poole, E. Qwarnstrom, F. Ratnieks, M. D. Rolfe, R. Smallwood, T. Sun, and D. Worth. 2012. Modelling complex biological systems using an agent-based approach. *Integr. Biol. (Camb).* 4: 53–64.

91. Marino, S., I. B. Hogue, C. J. Ray, and D. E. Kirschner. 2008. A methodology for performing global uncertainty and sensitivity analysis in systems biology. *J. Theor. Biol.* 254: 178–96.

Chapter 3

Multi-Scale Modeling Predicts a Balance of Tumor Necrosis Factor-α and Interleukin-10 Controls the Granuloma Environment During *Mycobacterium tuberculosis* Infection.

The work in Chapter 3 has been published as: Cilfone, N. A., Perry, C. R., Kirschner, D. E., Linderman, J. J. Multi-Scale Modeling Predicts a Balance of Tumor Necrosis Factor-α and Interleukin-10 Controls the Granuloma Environment during *Mycobacterium tuberculosis* Infection. *PLoS One* **8,** e68680 (2013).

3.1 Introduction

Tuberculosis (TB) is an infectious disease caused by the pathogen *Mycobacterium tuberculosis (Mtb)*. Approximately one-third of the world's population is infected with *Mtb*, with 2-3 million deaths and an estimated 10 million new clinical cases each year (1, 2). Upon infection with *Mtb*, 5-10% of individuals develop active pulmonary TB, while about 90% develop a state of chronic infection, known as latent pulmonary TB, showing no clinical signs of disease (3–5).

Granulomas are structures which form in the lungs as a result of the immune response to inhaled *Mtb*. Granulomas serve as the central site of host-pathogen interaction during *Mtb* infection, with a host typically developing several granulomas based on the number of inhaled bacteria (4, 6). During latent pulmonary TB, granulomas

are able to control *Mtb* but not completely eradicate the bacteria, while during active pulmonary TB *Mtb* growth is unrestrained in a portion of granulomas. The host factors that control the outcome of infection, in particular the formation and function of a granuloma, are not well understood and thus are difficult to use as therapeutic targets.

Granulomas have a distinct cellular and spatial organization that creates a unique immune microenvironment in attempt to control infection. Bacteria and infected macrophages are found in the center of the structure and are surrounded by a region of mainly resting and activated macrophages (immune cells that phagocytose foreign material) followed by an outer cuff comprised predominantly of T cells (white blood cells that participate in cell-mediated immunity) (7–12). Formation of a granuloma relies on coordinated immunological processes that include recruitment of immune cells to sites of infection, activation of macrophages, and production of particular molecular mediators known as cytokines (4, 13–19). Cytokines direct immune responses by influencing the fate and behavior of many immune cells. A pro-inflammatory cytokine, tumor necrosis factor-α (TNF-α), and an anti-inflammatory cytokine, interleukin-10 (IL-10), are hypothesized to be central to granuloma formation and function, but understanding the importance of each cytokine is complicated by the myriad of cellular and signaling processes acting across multiple spatial (tissue, cellular, molecular) and temporal (seconds to years) scales (Figure 3.1) (20–25).

IL-10 is a pleiotropic anti-inflammatory cytokine that is produced by immune cells (including both adaptive and innate immune cells) and regulates a variety of immune processes in response to pathogens (20, 22, 23, 25–32). During infection with *Mtb*, IL-10 is primarily produced by infected and non-infected macrophages, with smaller

quantities arising from regulatory T cells (20, 23, 25, 33). Production of IL-10 from other T cell sources, including subsets of CD4+ and CD8+ T cells, is still fairly uncharacterized (20, 34). IL-10 plays at least three major roles during *Mtb* infection (Figure 3.1): (1.) IL-10 inhibits the production of TNF-α through modulation of STAT3 transcription factors during TNF-α mRNA transcription (35–44), (2.) IL-10 inhibits the production of chemokines by immune cells, resulting in indirect regulation of cellular recruitment to the site of infection (45–48), and (3.) IL-10 works in concert with other regulatory mechanisms, such as CTLA-4 and transforming growth factor-β, in order to suppress cellular function, e.g. down regulation of activated macrophages (22, 23, 28, 49–51).

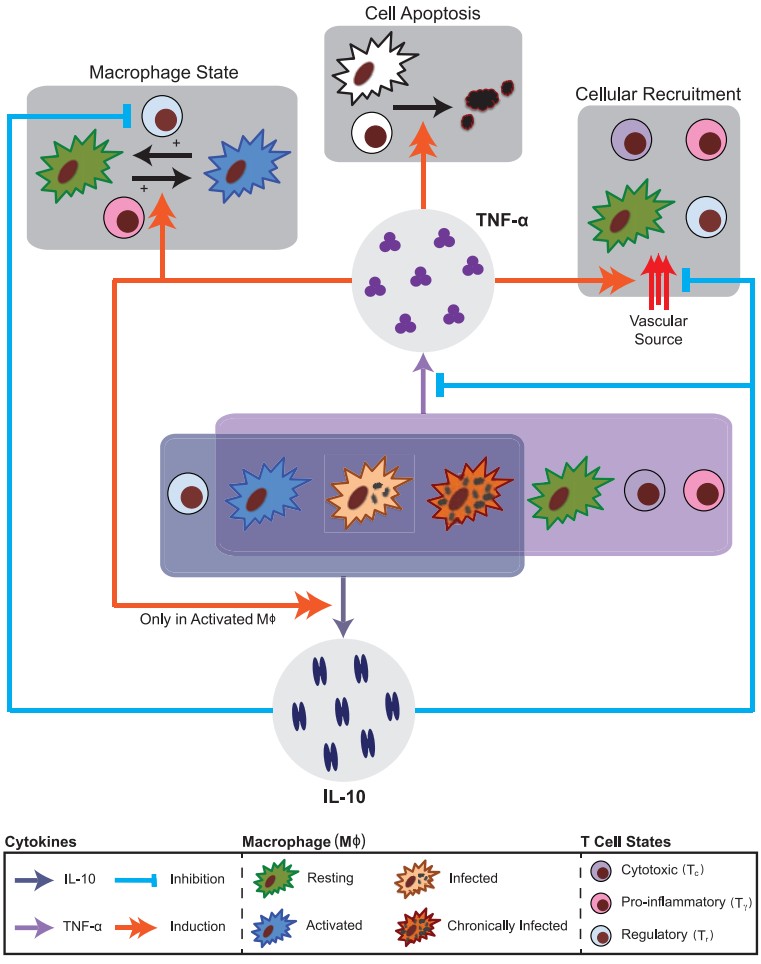

Figure 3.1 Schematic diagram of TNF-α and IL-10 mechanisms included in *GranSim*
Regulatory T cells, activated macrophages, infected macrophages, and chronically infected macrophages are able to produce IL-10. IL-10 inhibits the production of TNF-α in all cell types. IL-10 indirectly prevents the recruitment of immune cells to the site of infection by inhibiting chemokine production. IL-10 limits the secondary regulatory mechanism (cell-cell contact, TGF-β, and other regulatory mechanisms) down regulation of activated macrophages by regulatory T cells. Activated macrophages, infected macrophages, chronically infected macrophages, resting macrophages (STAT1 or NFκB activated), cytotoxic T cells, and pro-inflammatory T cells are able to produce TNF-α. TNF-α directly induces recruitment of immune cells to the site of infection (lung). TNF-α induces production of IL-10 in activated macrophages, which represents the pro/anti inflammatory plasticity of activated macrophages. TNF-α, along with interferon-γ derived from pro-inflammatory T cells, induces activation of resting macrophages or it can induce the caspase-mediated apoptosis pathway found in all cell types.

Patients with pulmonary TB show elevated levels of IL-10 in lungs, serum, sputum, and bronchoalveolar lavage (BAL) fluid, suggesting a role for IL-10 in preventing control of *Mtb* infection. Genetic studies in humans suggest a correlation between *IL-10* gene polymorphisms and an increase in *Mtb* susceptibility (20). In *IL-10*$^{-/-}$ mice there are reports of enhanced, normal, or poorer control of *Mtb* infection (52–62). Differing genetic backgrounds of the *IL-10*$^{-/-}$ mice and differences between mouse models and human infection make these data difficult to interpret. Computational models of *Mtb* infection predict a role for IL-10 in achieving latency with limited tissue damage and in helping balance the major macrophage phenotypes present in granulomas (63, 64). Finally, in studies of other granulomatous diseases, such as *Leishmania major*, *IL-10*$^{-/-}$ mice display severe host damage while IL-10 overexpressing cells show increased recovery from toxic-shock like conditions (26).

TNF-α is a pro-inflammatory cytokine produced by infected and non-infected macrophages, CD4+ T cells, and CD8+ T cells in response to *Mtb* infection (17, 65). TNF-α mediates multiple immune and bactericidal responses during *Mtb* infection (Figure 3.1): (1.) TNF-α, in conjunction with interferon-γ from CD4+ T cells, activates resting macrophages through the NFκB signaling axis (15, 66–70), (2.) TNF-α promotes

cellular recruitment, both directly and indirectly, by inducing expression of chemokines in macrophages and directly influencing the recruitment of cells from vascular sources (71), (3.) TNF-α controls caspase-mediated apoptosis of cells (70, 72), (4.) TNF-α can alter the activated macrophage phenotype, thus causing activated macrophages to produce IL-10 (73–75). Studies in both animal and computational models have shown that TNF-α and its controlling processes are critical to the formation and function of granulomas. Removal of TNF-α during *Mtb* infection leads to a range of outcomes, such as unstructured granulomas, and large increases in total bacterial burden (13, 14, 17, 76–80). Furthermore, patients receiving TNF-α antagonists to treat inflammatory diseases such as rheumatoid arthritis show increased incidence of TB reactivation (81, 82).

Taken together, these studies highlight the role of TNF-α as an important initiator of inflammatory and bactericidal processes and IL-10 as an inhibitor of activation and a potential contributor to chronic infection. Several studies have suggested that a balance of TNF-α and IL-10 may be necessary for controlling infection while at the same time preventing severe host tissue damage during *Mtb* infection (5, 20–22, 25). Yet, the complexity of the immune response to *Mtb* (Figure 3.1) makes it difficult to address this hypothesis using traditional experimental systems.

In this Chapter we address the complex and multi-scale effects of TNF-α and IL-10 during *Mtb* infection using a systems biology approach. Building on our previous work (13), we develop a multi-scale computational model of *Mtb* infection that integrates both TNF-α and IL-10 experimental data, including single-cell level receptor-ligand dynamics. We then ask: What molecular scale processes control the concentrations of TNF-α and IL-10? Do TNF-α and IL-10 processes also affect infection outcomes? Does

a balance of TNF-α and IL-10 concentrations exist in those granulomas that are able to contain bacteria? Our computational model allows us to explore the dynamics of pro- and anti-inflammatory cytokines across multiple spatial (molecular, cellular, and tissue level) and temporal scales and determine their effects on control of *Mtb* infection.

3.2 Materials and Methods

3.2.1 Multi-Scale Hybrid Agent-Based Model Overview

We constructed a multi-scale computational model of lung granuloma formation and function during *Mtb* infection (Figure A.1 in Appendix A). We describe immune processes over three biological scales: tissue, cellular, and molecular. Tissue and cellular scale events are described with a next-generation two-dimensional agent-based model (ABM) that uses a set of rules and interactions to describe the stochastic behavior of discrete immune cells in the lung (GranSim) (13, 14). The molecular scale model is composed of three sub-models, each described by systems of differential equations, and is linked to the tissue and cellular scale (83, 84): (1) Single-cell level TNF-α and IL-10 secretion and receptor-ligand dynamics are described by ordinary differential equations (ODEs), (2) diffusion of TNF-α, IL-10, and chemokines are described by partial differential equations (PDEs), and (3) degradation of TNF-α, IL-10, and chemokines are described by ODEs. Chemokine (consisting of CCL2, CCL5, and CXCL9/10/11) receptor-ligand dynamics, which are not the focus of the current Chapter, are excluded from the model. Figure 3.2 shows the tissue, cellular, and molecular scale models and how they are interconnected to form our multi-scale hybrid agent-based model of the immune response to *Mtb* infection.

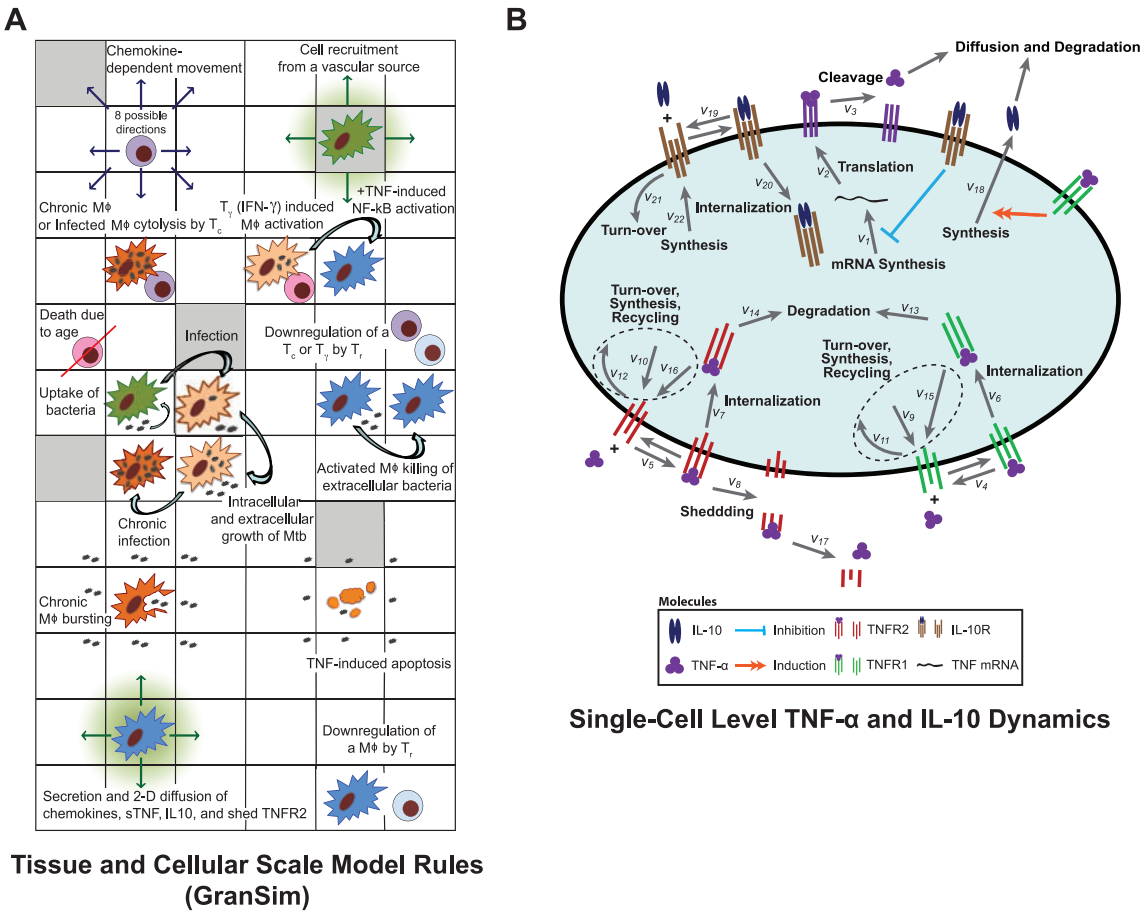

Figure 3.2 Schematic representation of the hybrid multi-scale ABM of the immune response to *Mtb*
A. An overview of GranSim with a sub-section of model rules shown that represents known immune cell behaviors and interactions (Adapted from (13)). A full list of rules is available in Appendix A B. Schematic representation of single cell-level TNF-α and IL-10 binding and trafficking reactions. Model equations are shown in Table A.1 in Appendix A and Table A.2 in Appendix A.

3.2.2 Tissue and Cellular Scale Model (GranSim)

3.2.2.1 Immune Cells and Bacilli

We include both macrophages (Mϕs) and T cells as distinct agents in our model. These agents have multiple states including: regulatory T cell (T_r), cytotoxic T cell (T_c), pro-inflammatory T cell (T_γ), resting macrophage (resting Mϕ), infected macrophage (infected Mϕ), chronically infected macrophage (chronic Mϕ), and activated macrophage (activated Mϕ) (Figure 3.2A) (14). Other cell types, e.g. neutrophils, B cells and foamy

macrophages, may play a role during *Mtb* infection but are not included in the model due to insufficient evidence as to their function during infection (4). The model can be easily adapted to include these cell types once more data become available. *Mtb* reside in Mϕs but can also exist in the extracellular space of the lung and in areas of hypoxia/caseation (4). We track three bacterial populations as continuous variables in each Mϕ agent or in the extracellular space: intracellular bacteria (B_{int}), extracellular bacteria (B_{ext}), and bacteria in hypoxic/caseated areas (B_{cas}).

3.2.2.2 ABM Rules and Interactions

Figure 3.2A shows a representative selection of rules and interactions used to describe the tissue and cellular scale dynamics in the model. The simulation environment consists of 20x20μm micro-compartments in which agents and bacteria can reside. A full description of rules and interactions is available in Appendix A. Briefly, rules and interactions describe chemotaxis, intracellular and extracellular growth of *Mtb*, phagocytosis of bacteria by Mϕs, T cell killing, interferon-γ induced STAT1 activation of resting Mϕs by T_γ, deactivation of immune cells by T_r, secretion of chemokines, and development of caseated areas. We updated many agent rules and interactions from our prior generation ABM to reflect additional experimental data including: infected Mϕs that transition to activated Mϕs kill B_{int} at the same rate that activated Mϕs kill B_{ext} (85, 86), resting Mϕs that are partially activated (NFκB or STAT1 positive) kill extracellular bacteria at an increased rate (4, 85, 86), partially activated resting Mϕs express STAT1 or NFκB activation for a limited timeframe to better describe the need for re-stimulation (69), T cell killing through Fas/FasL or cytotoxic mechanisms occurs in the Moore

neighborhood, hypoxic bacterial growth of B_{ext} is scaled based on the number of caseated compartments in the Moore neighborhood (87), and B_{cas} die with a specified death rate and probability (87).

3.2.2.3 Cell Recruitment

Recruitment of immune cells to the site of infection has been suggested to be highly correlated with control of *Mtb* (88, 89). We updated our previous cell recruitment algorithm by adding chemokine- and cytokine-dependent recruitment rates of immune cells to the infection site (Figure A.2 in Appendix A). This is consistent with observed dose-dependent migration rates of immune cells in response to chemokines (88, 90). We recruit resting Mϕs and T cells (T_γ, T_c, and T_r) from vascular sources randomly distributed across the simulation environment. The recruitment rate at each vascular source is dependent upon the concentrations of CCL2, CCL5, CXCL9, and TNF-α in the specified micro-compartment. Recruitment rates for each molecule are modeled using a concentration threshold and Michaelis-Menton kinetics. The overall recruitment rate for each agent is the summation of the contribution by CCL2, CCL5, CXCL9, and TNF-α and is scaled by a maximum probability of recruitment, which turns the continuous recruitment rate into a stochastic event. The probability functions for recruitment of resting Mϕs, T_γ, T_c, and T_r are given in Appendix A and values of recruitment parameters are given in Table A.3 in Appendix A.

3.2.3 Molecular Scale Model

3.2.3.1 IL-10 and IL-10 Receptor-Ligand Dynamics

We developed a model of IL-10 receptor-ligand dynamics based on experimental data (Figure 3.2B). We assume that IL-10 is synthesized by infected Mϕs, chronic Mϕs, activated Mϕs, and T_r and released directly into the extracellular environment (25, 26, 34, 50, 91–95). IL-10 exists in the extracellular space as a non-covalently bonded dimer where it can bind to cell-surface IL-10R1 and IL-10R2 (96, 97). Signaling occurs through association of bound IL-10R1 with the IL-10R2 subunit. IL-10R1 is the high affinity receptor compared to IL-10R2, which mainly exists as a signaling subunit to bound IL-10R1 (26). For simplicity, we include only a general IL-10R that represents both IL-10R1 and IL-10R2 (98, 99). IL-10R is synthesized by cells and is removed from the membrane by turnover (100). Bound IL-10R can be internalized followed by degradation or recycling to the surface (101). These processes are modeled by mass-action kinetics as shown in Table A.1 in Appendix A and Table A.2 in Appendix A; definitions and values of rate constants are defined in Table A.4 in Appendix A.

3.2.3.2 TNF-α and TNF-α Receptor-Ligand Dynamics

TNF-α and TNF-α receptor-ligand dynamics events are illustrated in Figure 3.2B. The equations describing these events were modified from earlier work in order to accommodate IL-10 receptor-ligand dynamics as discussed above (13, 79, 80). TNF-α mRNA is transcribed and subsequently translated into its membrane bound form, mTNF, by NFκB-activated resting Mϕs, infected Mϕs, chronic Mϕs, activated Mϕs, T_γ, and T_c. mTNF is cleaved from the membrane into its soluble form (sTNF), by the

metalloproteinase TACE. sTNF can reversibly bind to the two receptors, TNFR1 and TNFR2. TNFR1 and TNFR2 are synthesized by the cell and are removed from the membrane by turnover. Bound TNFR1 and TNFR2 can be internalized and then degraded or recycled to the surface in their unbound state. sTNF bound to TNFR2 may be shed to the extracellular space where it can dissociate. These processes are modeled by mass-action kinetics as shown in Table A.1 in Appendix A and Table A.2 in Appendix A; definitions and values of rate constants are defined in Table A.4 in Appendix A.

3.2.3.3 Linking TNF-α and IL-10 Receptor-Ligand Dynamics

TNF-α and IL-10 receptor-ligand dynamics are linked in two ways (Figure 3.2B): bound IL-10R inhibits TNF-α mRNA transcription and bound TNFR1 can induce synthesis of IL-10 in activated Mϕs (35, 73). Inhibition of TNF-α mRNA transcription shows rapid switch-like behavior, and we modeled this process with a three-parameter logistic function (35):

$$k_{mRNA-Mod} = k_{mRNA}\left(\beta + \frac{1-\beta}{1+e^{\frac{[IL10\cdot IL10R]-\gamma_I}{\delta_I}}}\right) \qquad (Eqn.\ 3.1)$$

We captured the ability of bound TNFR1 to induce synthesis of IL-10 in activated Mϕs with Michaelis-Menton type kinetics, which roughly approximates the mechanisms influencing the plasticity of activated Mϕs to produce IL-10 at lower (classically activated Mϕs) or higher (alternatively activated Mϕs) rates (modeled in detail in Chapter 4) (73–75, 102, 103).

$$k_{synthMacAct-Mod} = k_{synthMacAct}\left(\frac{[sTNF\cdot TNFR1]}{[sTNF\cdot TNFR1]+h_{synthMacAct}}\right) \qquad (Eqn.\ 3.2)$$

Parameter values and definitions are found in Table A.4 in Appendix A. Other molecular scale mechanisms of IL-10 inhibition of TNF-α processes, such as inhibition of TACE activity, can be included in future models as more data become available (37, 104, 105).

3.2.3.4 Diffusion of Soluble Molecules

Diffusion of soluble TNF-α, IL-10, and chemokines is described by the two-dimensional diffusion equation:

$$\frac{\partial C}{\partial t} = D\left(\frac{\partial^2 C}{\partial x^2} + \frac{\partial^2 C}{\partial y^2}\right) \qquad (Eqn.\ 3.4)$$

We track soluble CCL2, CCL5, CXCL9, TNF-α, IL-10, and shed bound TNFR2 as continuous species that can diffuse in the lung environment. We use the alternating-direction explicit (ADE) method for discretizing the environment and solving the diffusion equation (see Chapter 2) (106). This method is unconditionally stable, allowing us to use a solver time step five times larger than in previous work, simultaneously increasing computational performance and solution accuracy (Appendix A).

3.2.3.5 Degradation of Soluble Molecules

Degradation of soluble CCL2, CCL5, CXCL9, TNF-α, IL-10, and shed bound TNFR2 is described by:

$$\frac{\partial C}{\partial t} = -k_{\text{deg}} C \qquad (Eqn.\ 3.5)$$

In order to increase the accuracy of the degradation calculation and to prevent unnecessary computational burden, we calculate degradation using the analytical solution to Eq. 5 (see Chapter 2) (Appendix A).

3.2.4 Linking the Molecular Scale Model to the Tissue and Cellular Scale Model

Molecular scale dynamics involving TNF-α are linked to the tissue and cellular scale model (GranSim) (Figure 3.2) through cell recruitment (discussed above), NFκB activation of Mϕ, and caspase induced cell apoptosis. We describe TNF-α induced NFκB activation of each Mϕ and TNF-α induced apoptosis of cells as Poisson processes with a probability of occurrence determined by a rate constant, threshold value, and a saturation value (see Appendix A for equations and Table A.5 in Appendix A for parameter definitions and values). TNF-α induced NFκB activation of Mϕ is dependent on the concentration of bound TNFR1 per cell, while TNF-α induced apoptosis is dependent on the concentration of internalized bound TNFR1 per cell (13, 79). Molecular scale dynamics involving IL-10 are linked to GranSim through chemokine down regulation and compensation of alternative suppressive functions. IL-10 inhibits the production of chemokines by Mϕs; we use a simple threshold relationship in which the synthesis of chemokines is reduced by half once the number of bound IL-10R is above the specified threshold (45–48). The probability of alternative suppressive functions of T_r occurring is linearly dependent on the ratio described by:

$$\frac{[TNF \cdot TNFR1]}{[TNF \cdot TNFR1] + [IL10 \cdot IL10R]} \qquad (Eqn.\ 3.6)$$

This simulates the dependence of other regulatory mechanisms on IL-10 that are not the focus of this Chapter (22, 23, 28, 49–51).

3.2.5 Parameter Estimation and Model Validation

We estimate model parameter values using experimental data where available and previous modeling studies (13, 14, 63). When data are unavailable we use uncertainty and sensitivity analyses to explore the parameter space to match observed qualitative behavior (see below) (107). Cell-specific TNF-α receptor-ligand dynamics model parameters are estimated from literature as previously described (13, 79, 80). We updated parameter estimates for rate constants, concentration thresholds, and saturation concentrations of TNF-α induced Poisson processes (69). Parameters for the updated cell recruitment algorithm were estimated using uncertainty and sensitivity analyses and validated by comparing total T cells numbers against non-human primate estimates (108).

IL-10 receptor-ligand dynamics model parameters are estimated based on experimental data. The synthesis rate constant of IL-10 by infected Mϕs is estimated using *in vitro* kinetic IL-10 ELISA data from both human monocyte-derived Mϕs and a THP-1 cell line infected with *Mtb* strain H37Rv (92, 95). The synthesis rate constant of IL-10 by activated Mϕ is estimated using *in vitro* kinetic IL-10 ELISA data from M-CSF activated human monocyte-derived Mϕs and single-time point IL-10 ELISA data from interferon-γ activated murine Mϕ (91, 103). The half-saturation of IL-10 induction by bound TNFR1 in activated Mϕs is estimated using uncertainty and sensitivity analysis such that on average synthesis rates of IL-10 fall into above estimated ranges. Synthesis of IL-10 by T_r is estimated using *in vitro* kinetic IL-10 ELISA data from both human and mouse purified T cells (34, 93, 94). The three parameters describing inhibition of TNF-α mRNA synthesis by bound IL-10R (Eq. 1), are estimated from *in vitro* human monocyte-derived Mϕs stimulated with *Mycobacterium avium* (cultured with and without an anti-

IL-10 antibody) or stimulated with lipopolysaccharide (36, 37). Data on the peak, timing, and shape of soluble TNF-α concentration data were used to estimate parameters describing TNF mRNA synthesis (See Figure A.4 in Appendix A). A complete list of IL-10 and TNF-α receptor-ligand dynamics parameters along with all other model parameters are found in Table A.3 in Appendix A, Table A.4 in Appendix A, and Table A.5 in Appendix A.

Using methods described above we determine a baseline set of parameters, referred to as the *baseline containment parameter set*, which results in robust control of *Mtb* infection with structures similar to granulomas observed in humans and non-human primates. We validate and test our baseline containment parameter set using multiple experimentally verified scenarios to ensure it can describe the immune response to *Mtb* infection. For example, we perform virtual deletion simulations that mimic experimental studies of gene knockouts by setting the relevant model parameters (probabilities and rate constants) to zero from the beginning of a simulation. Virtual deletion experiments are carried out for interferon-γ, TNF-α, and T cells for model validation, while IL-10 deletion experiments are predictions of the model. We compare our predicted simulations with corresponding data from human, mouse, and non-human primate studies.

3.2.6 Model Outputs and Analysis Metrics

We consider multiple model outputs relevant to granuloma formation and function during *Mtb* infection. At the cellular scale, we measure numbers of immune cells, frequency of T cell killing, caseated areas, and rates of cellular recruitment. At the molecular scale, we track average concentrations of TNF-α and IL-10 in the granuloma

along with number of TNF-α induced processes. Specifically, we measure the number of resting Mϕs that undergo TNF-α induced apoptosis as a metric of healthy tissue damage, the number of activated Mϕ as a metric of bactericidal activation levels, and total bacterial load (the sum of B_{int} and B_{ext}) as a metric of infection status. Simulation results are organized by infection outcome, which includes bacterial containment (stable total bacterial load of ~10^3), clearance (total bacterial load of zero), and unresolved clearance (total bacterial load of zero with non-steady state numbers of activated Mϕs), and data is shown for only the dominant outcome. This allows us to use common statistical techniques to analyze the results. Further explanation and non-dominant outcome data is provided in Appendix A.

We hypothesize that a beneficial outcome for the host corresponds to a low total bacterial load, low tissue damage (induced by apoptosis), and sufficient immune activation. Thus, we combine the three metrics – total bacterial load, healthy tissue damage, and Mϕ activation levels – together into a single metric we define as the *host-pathogen index (H.P.I.)*.

$$H.P.I = \frac{B_{Tot} + \frac{1}{M\varphi_{Activated}} + M\varphi_{\mathrm{Re}sting}^{Apoptosis}}{3 * H.P.I._{Max}} \qquad (Eqn.\ 3.7)$$

H.P.I. is an evenly weighted average of the total bacterial load, the number of apoptotic resting Mϕs, and the inverse of the number of activated Mϕs, normalized between zero and one. The inverse of the number of activated Mϕs is used so that low values for all metrics correspond to beneficial behavior.

To simplify the presentation of the influence of molecular scale TNF-α and IL-10 related parameters we divide them into three groups for each molecule: (1) parameters

that are part of the synthesis pathway are organized into the *synthesis group*, (2) parameters that control the spatial aspects are organized into the *spatial group*, and (3) parameters that control binding and signaling are organized into the *signaling group*. Table A.4 in Appendix A and Table A.5 in Appendix A describe each parameter and group.

3.2.7 Uncertainty and Sensitivity Analysis

Uncertainty and sensitivity analyses are used to identify model parameters that have a significant effect on model output. Latin hypercube sampling (LHS) is a straightforward and computationally effective method for simultaneously varying multiple parameters and sampling the parameter space (107). Partial rank correlation coefficients (PRCCs) are used to quantify the effects of varying each parameter on non-linear model outputs, indicating model sensitivity to specific parameters. A PRCC value of -1 is a perfect negative correlation while a PRCC value of +1 represents a perfect positive correlation. PRCC values are differentiated with a student t-test to assess significance. In this Chapter, we use the LHS algorithm to generate 250 unique parameter sets, which are simulated in replication 4 times and the average of the outputs are used to calculate PRCC values. This number of simulations indicates a PRCC value of above 0.24 or below -0.24 is considered to be highly significant with a p value < 0.001 (107). We separate the molecular scale TNF-α and IL-10 model parameters from GranSim model parameters when carrying out LHS in order to better understand how each scale affects the others (intra vs. inter-scale effects).

3.2.8 Model Implementation

A two-dimensional 100x100 lattice of micro-compartments represents a 2x2mm section of lung tissue. Initial conditions include pre-seeded resting Mϕ in the lung environment and placing an infected Mϕ at the center of the grid (6). We use zero concentration boundary conditions for diffusion of soluble molecules on all four of the grid edges. Granulomas are typically separated from one another and tissue concentrations of chemokines and cytokines are typically negligible in normal lung tissue (6). We use torodial boundary conditions for agent movement on the lattice. The rules and interactions of the ABM are solved on a 10 min time step (28,800 agent time steps for 200 days of simulation). Diffusion and degradation of soluble molecules are updated on a 30 second time step. TNF-α and IL10 receptor-ligand dynamics ODEs are solved for each agent using a Runge-Kutta 4^{th} order numerical solver with a time-step of 6 seconds.

Our model was constructed using the C++ programming language in conjunction with Boost libraries (distributed under the Boost Software License – available at www.boost.org). The Qt framework (open-source, distributed under GPL – available at qt.digia.com) was used to build the graphical user interface (GUI), which allows us to visualize, track, and plot different facets of our simulated granulomas in real-time. The model can be used with or without GUI visualization and is cross-platform (Mac, Linux, Windows). Simulations were performed on the Nyx/Flux computing cluster available at the Center for Advanced Computing at the University of Michigan and post-processing for visualization was carried out on non-cluster resources, which included multi-core desktops and laptops.

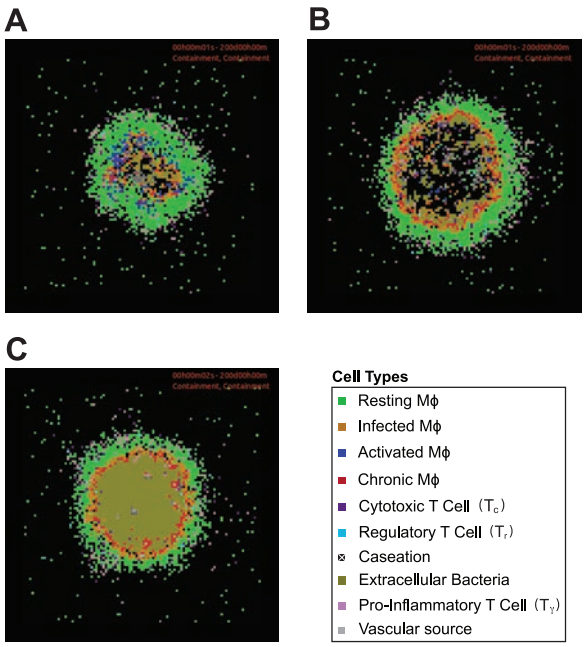

Figure 3.3 Model validation of simulated granulomas at 200 days post-infection
A. Simulation using baseline containment parameter set. B. Simulation using TNF-α knockout parameter set (baseline containment parameter set but with $k_{RNA\_Mac} = 0$ and $k_{RNA\_Tcell} = 0$). C. Interferon-γ knockout parameter set (baseline containment parameter set $P_{STAT1} = 0$). Cell types are as follows: resting macrophages (resting Mϕ), infected macrophages (infected Mϕ), chronically infected macrophage (chronic Mϕ), activated macrophage (activated Mϕ), pro-inflammatory T cell (T_γ), cytotoxic T cell (T_c), regulatory T cell (T_r), and extracellular bacteria (B_{ext}). Agent and bacteria colors are shown in the included legend. These same colors are used for subsequent images. Model parameters are given in Table A.3 in Appendix A, Table A.4 in Appendix A, and Table A.5 in Appendix A. For full length time-lapse simulations please see http://malthus.med.micro.umich.edu/lab/movies/TNF-IL10.

3.3 Results

3.3.1 Simulated Granulomas Display Infection Outcomes Comparable to Experimental Models

We first test whether our multi-scale computational model can recapitulate known features of the immune response to *Mtb* infection. Using estimation methods described above, we identify a *baseline containment parameter set* (Table A.4 in Appendix A and Table A.5 in Appendix A) that leads to robust control of *Mtb* infection over 200 days post-infection, including a stable total bacterial load of ~10^3 and organized granulomas comparable to histological observations in humans and non-human primates (7–10).

Simulated granulomas (Figure 3.3A) contain a core of infected Mϕs, chronic Mϕs, B_{ext} and areas of caseation that are surrounded primarily by resting Mϕs and activated Mϕs, and a peripheral region consisting mainly of T_c, T_γ, and T_r. About 15% of simulations using the baseline containment parameter set lead to granulomas that are able to clear all bacteria. This occurs when infected Mϕs and chronic Mϕs are killed through TNF-α induced apoptosis or T cell mediated killing at the initial stages of simulated infection. Data suggest that some individuals do not become infected when exposed to *Mtb*, consistent with our simulations that result in clearance before a granuloma begins to form (16). By varying model parameters in the baseline containment parameter set our model is also able to predict different granuloma outcomes, as observed in non-human primate models, including primarily clearance or uncontrolled growth of bacteria (16).

We further validate our model by performing virtual deletion experiments (see Materials and Methods) for TNF-α ($k_{RNA\_Mac} = 0$ and $k_{RNA\_Tcell} = 0$) and interferon-γ ($P_{STAT1} = 0$). These lead to an increased total bacterial load including increased B_{ext} in the interior of larger and more irregular shaped granulomas (Fig. 3B-C). TNF-α and interferon-γ are important initiators of inflammatory and bactericidal processes during *Mtb* infection (4). Virtual deletions of TNF-α or interferon-γ are unable to control disease progression due to a lack of Mϕ activation and bactericidal activity, consistent with experimental data (16, 17). These results also agree with our previous computational studies using models that did not include molecular level dynamics for IL-10 (13, 14).

3.3.2 IL-10 is Necessary to Control Inflammatory Processes and Tissue Damage During Mtb Infection

To explore the role of IL-10 during *Mtb* infection, we probe both the formation and function of granulomas when IL-10 is absent. We perform a virtual deletion experiment by setting IL-10 synthesis parameters to zero in the baseline containment parameter set ($k_{synthMacAct} = 0$, $k_{synthMacInf} = 0$, and $k_{synthTcell} = 0$), thus generating the *IL-10 knockout parameter set*. Figure 3.4 shows the average total bacterial load, number of activated Mϕs, apoptosis of resting Mϕs, and average tissue TNF-α concentration for simulations using either the baseline containment parameter set or the IL-10 knockout parameter set.

IL-10 knockout (*IL-10*$^{-/-}$) granulomas have similar total bacterial loads compared to baseline containment granulomas, but with elevated numbers of activated Mϕs, increased apoptosis of resting Mϕs, increased cellular infiltration rates (not shown), and increased average tissue TNF-α concentrations (Figure 3.4C-F). *IL-10*$^{-/-}$ granulomas contain large clusters of activated Mϕs in the periphery of the structure indicating that they fail to maintain proper levels of immune cell activation (Figure 3.4A-B). *IL-10*$^{-/-}$ granulomas show an increased probability of clearing *Mtb*, with ~40% of simulations clearing bacteria compared to ~15% of simulations with the baseline containment parameter set. However, the increase in clearance outcomes is also associated with large clusters of activated Mϕs and increased apoptosis of resting Mϕs that persists beyond clearance of bacteria (see Table A.10 in Appendix A). The excessive influx of inflammatory cells, in both *IL-10*$^{-/-}$ containment and clearance outcomes, is directly due to the lack of IL-10, which controls multiple inflammatory processes through multiple

mechanisms (Figure 3.1). Thus, our model suggests that IL-10 is necessary during *Mtb* infection to modulate activation levels and restrict apoptosis of resting Mϕs (a measurement of tissue damage), which is consistent with earlier modeling studies (63, 64). These results also suggest that variable outcomes reported from experimental *IL-10*$^{-/-}$ studies may be due to the large amount of variability in infection outcome, small sample sizes, and differences between animal models (52–62).

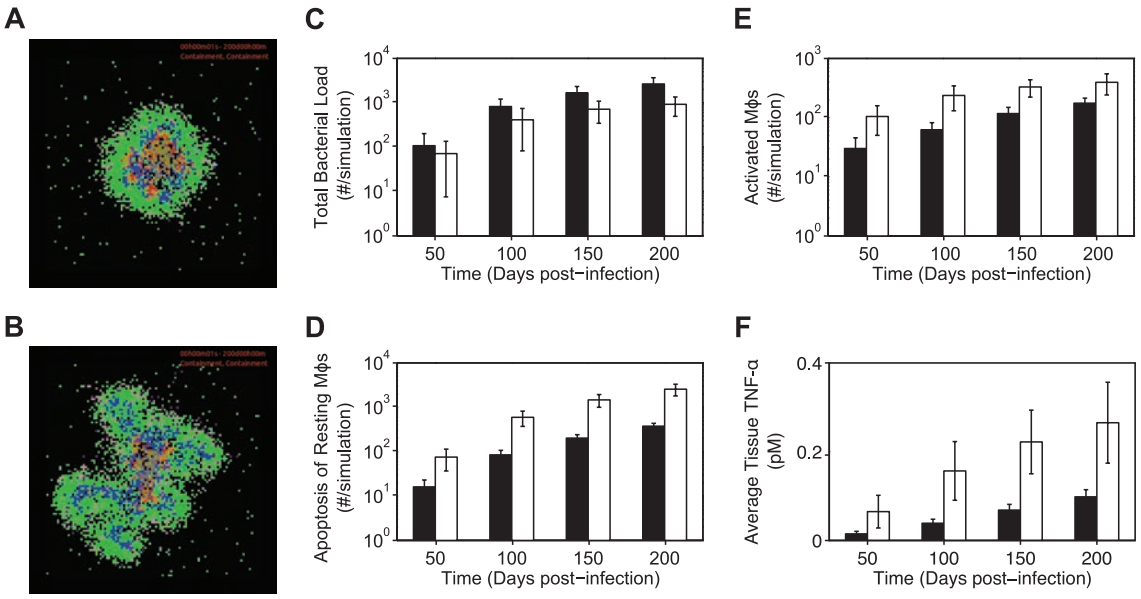

Figure 3.4 Time course simulation results for baseline and IL-10 knockout scenarios
Simulation using baseline containment parameter set at 200 days post-infection. B. Simulation using the IL-10 knockout parameter set at 200 days post-infection. Agents and bacteria colors are as in Figure 3.3. C-F. Simulation results at 50, 100, 150 and 200 days post-infection using the baseline containment parameter set (black bars) and the IL-10 knockout parameter set (white bars). The few simulations that lead to clearance of *Mtb* in a granuloma are not shown here (see Table A.10 in Appendix A). C. Total bacterial load. D. Number of activated Mϕ. E. Number of apoptotic resting Mϕ. F. Average tissue concentration of TNF-α (pM). For full length time-lapse simulations please see http://malthus.med.micro.umich.edu/lab/movies/TNF-IL10.

3.3.3 Granuloma Outcomes Are Sensitive to Multiple TNF-α and IL-10 Processes that Control Average Concentrations in a Granuloma

We now predict which biological processes are controlling concentrations of TNF-α and IL-10 in a granuloma during *Mtb* infection. We analyze the impact of TNF-α

and IL-10 molecular scale processes on granuloma outcomes using sensitivity analyses and group important parameters together based on the relevant processes they describe. Table 3.1 lists model parameters that are significantly correlated with key features of the granuloma: total bacterial load, average tissue concentration of TNF-α, average tissue concentration of IL-10, and granuloma size (see also Table A.11 in Appendix A and S12 in Appendix A). These important TNF-α and IL-10 parameters fall into three groups (as defined in Materials and Methods): (1) the *synthesis group*, (2) the *spatial group*, and (3) the *signaling group*. Processes described by the parameters in these three groups shape the concentrations of TNF-α and IL-10 in a granuloma environment and thus in turn control granuloma outcome (Figure 3.5). We now focus our analyses on the effects of manipulating parameters in each of the three groups on granuloma formation and function.

Table 3.1 Molecular Scale TNF-α and IL-10 Parameters Significantly Correlated With Selected Model Outputs At 200 Days Post-Infection

			Selected Model Outputs†			
Parameter Group	**Parameter**	**Parameter Description**	**Bacterial Load***	**Avg. Tissue TNF-α**	**Avg. Tissue IL-10**	**Gran Size**
TNF-α Synthesis	$k_{SynthMac}$	Minimum TNF-α mRNA synthesis rate of macrophages	--	+		
	k_{RNA_Mac}	Basal TNF-α mRNA synthesis rate of macrophages	---	+++		
TNF-α Signaling	K_{d1}	Equilibrium dissociation constant of sTNF/TNFR1	+++			
	k_{on1}	sTNF/TNFR1 association rate constant	---			
	k_{int1}	TNFR1 internalization rate constant	+++	---	---	---
	k_{t2}	TNFR2 turn-over rate constant	-			
	$TNFR1_{Mac}$	TNFR1 density on the surface of macrophages	---	---		-
	τ_{apop}	Internalized sTNF/TNFR1 threshold for TNF-induced apoptosis	++			
	τ_{NFkB}	Cell surface sTNF/TNFR1 threshold for TNF-induced NFκB activation		--	--	-
	k_{NFkB}	Rate constant for TNF-induced NFκB activation in macrophages	---			
TNF-α Spatial	D_{TNF}	Diffusion coefficient of sTNF		+++	++	+++
	k_{deg}	sTNF degradation rate constant	++	---	-	
IL-10 Synthesis	$k_{SynthMacAct}$	Full synthesis rate of IL-10 by activated macrophages	+++	---		-
IL-10 Signaling	K_d	Equilibrium dissociation constant of IL-10/IL-10R	--			
	k_{on}	IL-10/IL-10R association rate constant	+++	---	---	
	k_{int}	IL-10R internalization rate constant	---	+++	+	
	$IL10R_{Mac}$	IL-10R density on the surface of macrophages	+++	---	---	
IL-10 Spatial	k_{deg}	Soluble IL-10 degradation rate constant	-	++	--	

Significant PRCC values are as follows: -/+ 0.001 < p < 0.01 --/++ 0.0001 < p < 0.001 ---/+++ p < 0.0001

* Bacterial load incorporates PRCC values for IntMtb, ExtMtb, and TotMtb

† Detailed sensitivity analysis is presented in Table A.11 in Appendix A and A.12 in Appendix A

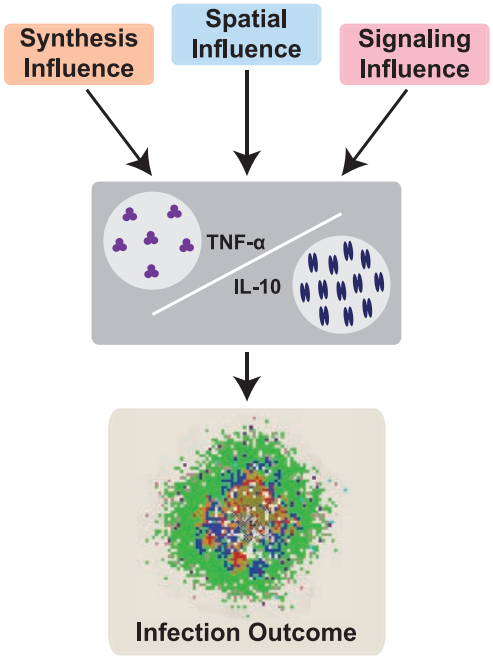

Figure 3.5 Three main processes influence the concentrations of TNF-α and IL-10 and control infection outcome
Model parameters that are relevant to TNF-α or IL-10 synthesis (synthesis influence), that control the spatial distribution of TNF-α or IL-10 (spatial influence), and that control the binding and signaling of TNF-α or IL-10 (signaling influence). These three parameter groups control the concentrations of TNF-α and IL-10 in the granuloma environment and thus in turn directly control infection outcome. Parameter groups are described in Table A.4 in Appendix A and Table A.5 in Appendix A.

3.3.4 Synthesis Rates of TNF-α and IL-10 Have Opposing Effects on Bacterial Control and Tissue Damage

We first analyze the effects of parameters in the synthesis group on a granuloma environment. Sensitivity analysis (Table 3.1) indicates that the basal rate of TNF-α mRNA synthesis by Mϕs correlates negatively with total bacterial load and positively with average tissue TNF-α concentration, while the IL-10 synthesis rate for activated Mϕs correlates positively with total bacterial load and negatively with average tissue TNF-α concentration. Thus, TNF-α and IL-10 synthesis group parameters have a

significant impact on their concentrations in a granuloma environment.

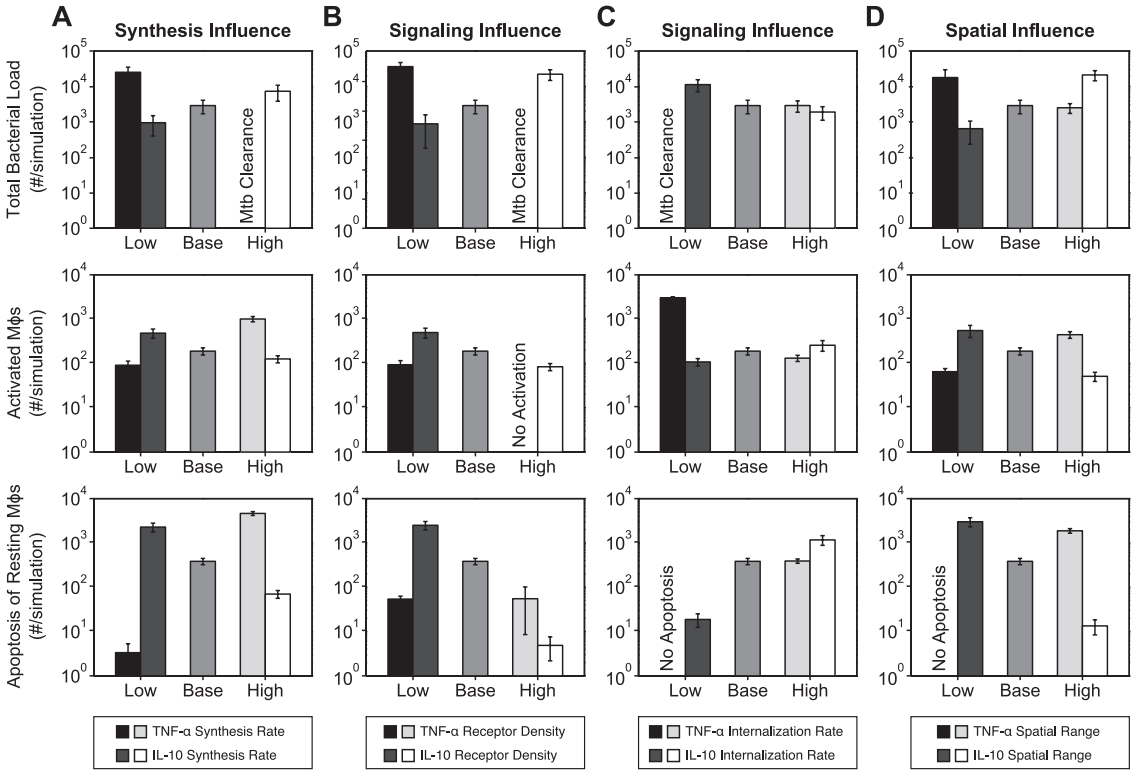

Figure 3.6 Simulation results showing the effects of varying each influence in a granuloma environment

Simulation results from 30 replications showing the effects of varying each of the three influences: the synthesis influence, signaling influence, and spatial influence (Figure 3.5; Table A.4 and Table A.5 in Appendix A). Results using the baseline containment parameter set, labeled 'base', are included for comparison (parameter values in Table A.4 in Appendix A and Table A.5 in Appendix A). A. Effects of mRNA synthesis rate of TNF-α by Mϕ ('Low' $k_{RNA\_Mac} = 0.5$ #/cell*s, 'High' $k_{RNA\_Mac} = 3.0$ #/cell*s) and synthesis rate of IL-10 by activated Mϕ ('Low' $k_{synthMacAct} = 0.1$ #/cell*s, 'High' $k_{synthMacAct} = 1.0$ #/cell*s). B. Effect of TNFR1 receptor density on Mϕ ('Low' $TNFR1_{mac} = 500$, 'High' $TNFR1_{mac} = 5000$) and IL-10R receptor density on Mϕ ('Low' $IL10R_{mac} = 500$, 'High' $IL10R_{mac} = 5000$). C. Effect of bound TNFR1 internalization rate constant ('Low' $k_{int1} = 10^{-4}$ s^{-1}, 'High' $k_{int1} = 10^{-3}$ s^{-1}) and bound IL-10R internalization rate constant ('Low' $k_{int} = 10^{-4}$ s^{-1}, 'High' $k_{int} = 10^{-3}$ s^{-1}). D. Effect of spatial range of TNF-α ('Low' $D_{TNF} = 1 \times 10^{-8}$ cm^2/s $k_{deg} = 2.3 \times 10^{-2}$ s^{-1}, 'High' $D_{TNF} = 9 \times 10^{-8}$ cm^2/s $k_{deg} = 5 \times 10^{-5}$ s^{-1}) and spatial range of IL-10 ('Low' $D_{IL10} = 1 \times 10^{-8}$ cm^2/s $k_{deg} = 1.6 \times 10^{-2}$ s^{-1}, 'High' $D_{IL10} = 8 \times 10^{-8}$ cm^2/s $k_{deg} = 1.8 \times 10^{-6}$ s^{-1}). Low indicates a lower value than baseline while high indicates a higher value than baseline.

We manipulate the synthesis rates of TNF-α mRNA by Mϕs and the synthesis of IL-10 by activated Mϕs to both high and low values. Figure 3.6A shows the results of these manipulations on average total bacterial load, number of activated Mϕs, and apoptosis of resting Mϕs (see also Table A.9 in Appendix A). Low rates of TNF-α

mRNA synthesis and high rates of IL-10 synthesis show increased bacterial loads with lower levels of activated Mϕs and less apoptosis of resting Mϕs. Conversely, high rates of TNF-α mRNA synthesis and low rates of IL-10 synthesis display clearance or reduced bacterial loads with increased levels of activated Mϕs, but at the cost of increased apoptosis of resting Mϕs. Thus, the rates of synthesis of TNF-α mRNA and IL-10 have opposing effects on controlling bacterial load and on preventing tissue damage in the host. Using moderate synthesis rates for TNF-α and IL-10 (as reflected in our baseline containment parameter set) results in bacterial containment with limited host-mediated tissue damage in a granuloma.

3.3.5 Signaling Parameters Establish the Best Response to TNF-α and IL-10 Concentrations that Regulates Apoptosis and Activation of Macrophages

Next we explore the effects of parameters in the signaling group on granuloma formation and function to understand how signaling parameters control the response to concentrations of TNF-α and IL-10 in a granuloma environment (Figure 3.5). Sensitivity analysis (Table 3.1) reveals that the internalization rate constants of bound TNFR1 and bound IL10R1 and the average densities of TNFR1 and IL-10R1 on Mϕ are significantly correlated with total bacterial load and average tissue concentrations of TNF-α and IL-10 (see also Table A.6 in Appendix A and Table A.8 in Appendix A). Hence, we analyze the effects of changing *two* signaling parameters, for both TNF-α and IL-10, on average total bacterial load, number of activated Mϕs, and apoptosis of resting Mϕs.

Figure 3.6B shows simulation results for manipulations of TNFR1 density and IL-10R density on the surface of Mϕs (see also Table A.6 in Appendix A). Low TNFR1

densities lead to increased bacterial loads, lower levels of activated Mϕs and less apoptosis of resting Mϕs by preventing Mϕs from responding to the concentration of TNF-α in a granuloma environment. The benefit in reducing TNF-α induced apoptosis is outweighed by the decrease in TNF-α induced NFκB activation. High TNFR1 densities lead to bacterial clearance with limited activated Mϕs and low apoptosis of resting Mϕs. Increased TNFR1 density promotes the ability of infected Mϕs to respond to the concentration of TNF-α, which leads to early activation and apoptosis of infected cells and encourages bacterial clearance. We observe lower total bacterial numbers with higher levels of activated Mϕs and increased apoptosis of resting Mϕs at low IL-10R densities, resulting from the decreased response of immune cells to IL-10 concentrations. The reduced response decreases the likelihood of initiating the IL-10 inhibition cascade and limits TNF-α production and its induced processes. High IL-10R densities promote inhibitory signaling, leading to an increased bacterial load with less activated Mϕs and limited apoptosis of resting Mϕs.

Next, we manipulate the internalization rate constants of bound TNFR1 and bound IL-10R (Figure 3.6C, see also Table A.8 in Appendix A). Low internalization rates of bound TNFR1 cause bacterial clearance with no apoptosis of resting Mϕs, but with uncontrolled numbers of activated Mϕs since low internalization rates favor NFκB induction over apoptosis as the response to TNF-α concentrations (67, 78). High internalization rates of bound TNFR1 have limited effects on total bacterial load and apoptosis of resting Mϕs with only a slight decrease in number of activated Mϕs. Lowering the internalization rate of bound IL10R leads to an increased bacterial load, decreased apoptosis of resting Mϕs, and no change in activated Mϕs, while increasing the

internalization rate only increases apoptosis of resting Mϕs with no changes in total bacterial load or activated Mϕs. These results suggest that the internalization rate of bound IL-10R is preventing apoptosis of resting Mϕs at the cost of bacteria load. Taken together, these results suggest that the parameters in the signaling group are establishing the most beneficial response to the concentrations of TNF-α and IL-10, which is critical to the control of the immune response occurring in a granuloma.

3.3.6 TNF-α and IL-10 Spatial Parameters Focus Bactericidal Processes in Infected Regions of Granulomas and Limit Healthy Tissue Damage in Non-Infected Regions

Lastly, we explore the effects of parameters in the spatial group on granuloma formation and function (Figure 3.5). Sensitivity analysis (Table 3.1) demonstrates that diffusivity of TNF-α and degradation rates of TNF-α and IL-10 correlate with average tissue concentrations of TNF-α and IL-10 and total bacteria load (see also Table A.11 in Appendix A and S12 in Appendix A). These results highlight that the spatial distributions of TNF-α and IL-10 are important for granuloma function. To probe the role of the spatial distribution of cytokines, we simultaneously manipulate the diffusivity (D) and degradation rate (k_{deg}) of TNF-α or IL-10 in order to extend or contract the spatial range (L) of each molecule, as estimated by (109) (see also Figure A.3 in Appendix A):

$$L = \sqrt{D/k_{deg}} \qquad (Eqn.\ 3.8)$$

Figure 3.6D shows the effects of altering the spatial range of TNF-α and IL-10 on average total bacterial load, number of activated Mϕs, and apoptosis of resting Mϕs (see also Table A.7 in Appendix A).

Reduced TNF-α spatial ranges lead to an increased total bacterial load with a decrease in activated Mϕs and limited apoptosis of resting Mϕs. Increased TNF-α spatial ranges cause no change in total bacterial load, small changes in activated Mϕs and significant increases in apoptosis of resting Mϕs. These results suggest that if the spatial range of TNF-α is large, the response of resting Mϕs in the periphery of granulomas shifts from NFκB activation to apoptosis. Similarly, if the spatial range of TNF-α is insufficient, apoptosis of infected Mϕ in the core of the granuloma is limited. Reduced IL-10 spatial ranges result in a decreased total bacterial load with a slight increase in activated Mϕs and a significant increase in apoptosis of resting Mϕs. Increased IL-10 spatial ranges result in an increased total bacterial load with a decrease in activated Mϕs and a decrease in apoptosis of resting Mϕs. In contrast to the situation for TNF-α, these results suggest that a large spatial range of IL-10 inhibits apoptosis of resting Mϕs in peripheral granuloma regions, but at the cost of limited Mϕ activation. Yet, too small of an IL-10 spatial range cannot control TNF-α induced processes in the entire granuloma environment. Overall, our simulations demonstrate that spatial distributions of concentrations of TNF-α and IL-10 during *Mtb* infection are essential to maintaining effective levels of inflammation within regions containing bacteria, but limiting inflammatory processes in the outer regions of the granuloma that contain few, if any, bacteria.

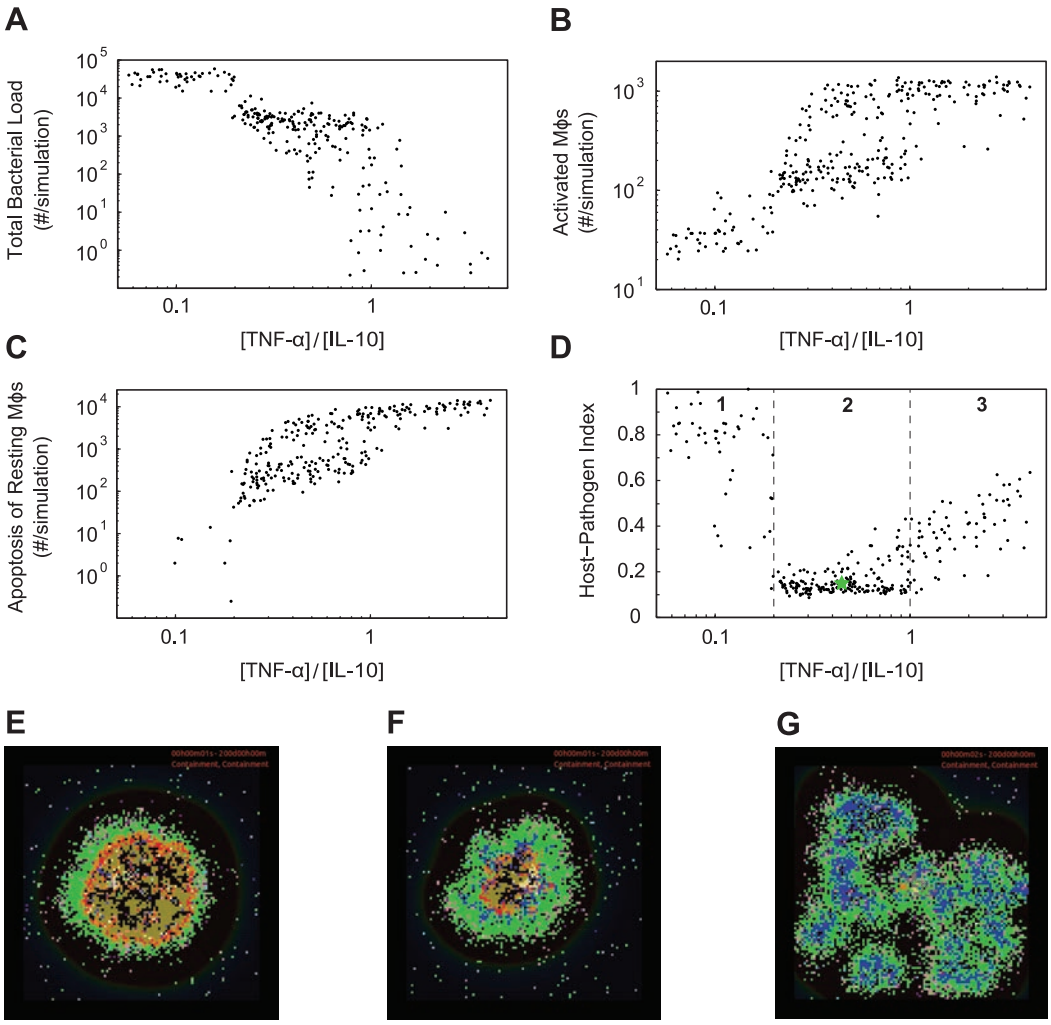

Figure 3.7 Altering the ratio of [TNF-α]/[IL-10] in a granuloma environment
Simulation results at 200 days post-infection showing the effects of altering the ratio of average tissue concentrations of TNF-α to IL-10 in the granuloma environment ([TNF-α]/[IL-10]). A total of 296 simulations (4 replications) were performed yielding various values of [TNF-α]/[IL-10]. Comparison of the ratio of concentrations of TNF-α to IL-10 with: A. B. C. Total bacterial load, number of activated Mϕ, and number of apoptotic resting Mϕ as a function of [TNF-α]/[IL-10]. D. Host-Pathogen Index (H.P.I), a metric that combines the three previous measures as a function of [TNF-α]/[IL-10]. The green star is the average simulation result for the baseline containment parameter set. E-G. Representative granuloma snapshots at 200 days post-infection for each of the regions (1, 2, and 3) defined in Figure 3.7D. For full length time-lapse simulations please see http://malthus.med.micro.umich.edu/lab/movies/TNF-IL10.

3.3.7 A Balance of TNF-α and IL-10 Concentrations Promotes an Environment That Contains Bacterial Growth with Minimal Tissue Damage

We have shown that three parameter groups are critical to controlling the average tissue concentrations of TNF-α and IL-10 and the subsequent responses necessary for granuloma function. Is there a balance of TNF-α and IL-10 concentrations that promotes strong immune cell activation, control of *Mtb* infection, and minimal host-induced tissue damage? To answer this question, we modulate concentrations of TNF-α and IL-10 available in a granuloma by simultaneously varying the synthesis of TNF-α mRNA by Mϕs and the synthesis of IL-10 by activated Mϕs. Each combination of parameters yields ratios of average tissue concentrations ([TNF-α]/[IL-10]), which we plot against representative model outputs of total bacterial load, number of activated Mϕs, and apoptosis of resting Mϕs at 200 days post-infection (Figure 3.7A-C).

When [TNF-α]/[IL-10] is less than ~0.2 the immune response to *Mtb* in a granuloma is dulled, with low levels of activated Mϕs and increased total bacterial loads, but with low apoptosis of resting Mϕs. These granulomas are unable to contain the growth of *Mtb* and generally show larger lesion sizes and higher levels of B_{ext} (Figure 3.7E). Conversely, when [TNF-α]/[IL-10] is greater than ~1.0, the immune response to *Mtb* infection in a granuloma is hyper-inflammatory, with high levels of apoptosis of resting Mϕs, high levels of activated Mϕs, and a low total bacterial load. This response causes significant tissue damage, while at the same time reducing bacterial loads and promoting clearance of bacteria. Granulomas that do achieve clearance of *Mtb* continue to activate Mϕs, recruit T cells, and cause healthy cell death well beyond the removal of the pathogen, due to the lack of anti-inflammatory mediators (Figure 3.7G). When [TNF-

α]/[IL-10] is between ~0.2 and ~1.0 simulations indicate that the granuloma response is balanced, with intermediate values of total bacterial load, low apoptosis of resting Mϕs and sufficient numbers of activated Mϕs (Figure 3.7F).

We calculate the H.P.I (defined in Materials and Methods) to provide a measure of overall granuloma function at different values of [TNF-α]/[IL-10] (Figure 3.7D). We devised this metric to incorporate the three measures just examined above - total bacterial load, apoptosis of resting Mϕs (tissue damage), and activated Mϕs (immune cell activation levels). Three general behaviors occur, and are indicated by regions 1, 2, and 3 in Figure 3.7D. Region 1, where the granuloma environment is dominated by IL-10, includes granulomas that display uncontrolled growth of *Mtb*, little to no Mϕ activation and no apoptosis of resting Mϕs (Figure 3.7E). In this region, the H.P.I is between ~0.30 – 1.0. Region 2, where the granuloma environment is slightly IL-10 biased, includes granulomas that contain growth of *Mtb* with suitable levels of Mϕ activation, low levels of apoptosis of resting Mϕs, and a calculated H.P.I between ~0.1 – 0.30 (Figure 3.7F). Region 3, with the TNF-α concentration dominating the granuloma environment, includes granulomas that contain or clear *Mtb* with uncontrolled Mϕ activation, high levels of apoptosis of resting Mϕs, and a calculated H.P.I. falling between ~0.3 – 0.6 (Figure 3.7G). We see similar results for the balance of TNF-α and IL-10 in a granuloma at all time points beyond ~75 days post-infection (data not shown). Our results demonstrate that a balance of concentrations of TNF-α and IL-10 promotes pathogen control while simultaneously preventing severe host tissue damage in a stable granuloma.

3.4 Discussion

Granulomas are dynamic microenvironments consisting of an array of immune cells and cytokines. The time scale of persistent infection (typically years) coupled with the complexity of this environment, all contained within host lung tissue, limits experimental approaches to decipher many features of granulomas. To understand the opposing roles and impacts of TNF-α and IL-10 in granuloma formation and function across multiple spatial and temporal scales we use a systems biology approach. We extend our previous multi-scale hybrid agent-based model of *Mtb* infection by integrating TNF-α and IL-10 single-cell level receptor-ligand dynamics. We use our model to predict the impact of these dynamics on the longer-term and larger-scale cellular and tissue immune responses to *Mtb*.

We show that IL-10 is necessary to control activation levels and to prevent tissue damage in a granuloma. Simulations also predict that three groups of TNF-α and IL-10 parameters, representing processes relevant to cytokine synthesis, signaling, and spatial distribution, control concentrations of TNF-α and IL-10 in a granuloma environment and eventually determine infection outcome, at the tissue scale, over the long-term (Figure 3.5). We demonstrate that each parameter group is balancing a trade-off between host-induced tissue damage and bactericidal processes through various TNF-α and IL-10 mechanisms.

Spatial localization of TNF-α and IL-10 is important in focusing bactericidal and inflammatory activities in a granuloma (Figure 3.6D and Figure A.3 in Appendix A). In the core of the granuloma (where infected cells reside) bactericidal and inflammatory processes are necessary, while in the peripheral regions of the granuloma (where non-

infected cells reside) cell death must be prevented through regulatory mechanisms. A balance of resting and infected Mϕ activation with restricted apoptosis of uninfected Mϕs is needed to contain bacterial growth with limited tissue damage. Both experimental and computational evidence point to the ability of immune cells to respond to different concentrations (across orders of magnitude) of TNF-α, via either NFκB activation or caspase-induced apoptosis, and IL-10, via anti-inflammatory or developmental transcription factors (13, 69, 80, 110). Together with earlier studies on granuloma formation, this suggests the spatial organization of immune cells within a granuloma, where infected Mϕs and *Mtb* reside in the center of the structure, is ideal for optimal control of bacteria (9, 80, 111).

We demonstrate for the first time that a balance of TNF-α and IL-10 concentrations is essential to mediate between *Mtb* infection control and prevention of host-induced tissue damage (Figure 3.7). Our results predict that granulomas with biased anti-inflammatory environments, having higher average concentrations of IL-10 than TNF-α, promote containment of bacteria and prevention of host tissue damage instead of bacterial clearance with high levels of healthy tissue damage. Shaler et al. (53) found that granuloma cells adopted a selectively suppressive phenotype when compared to airway lumen cells and proposed that granulomas may be immunosuppressive in nature. In contrast with the classical idea that granulomas function to wall off bacteria from its surroundings, granulomas may instead function as a niche that allows the survival of bacteria (11, 53). What is still not understood is whether the nature of the granuloma environment arises due to the host-response or due to an immune-evasive mechanism of *Mtb* in order to support bacterial persistence, since hyper-virulent strains of *Mtb* can

induce increased IL-10 production from macrophages (112). A biased anti-inflammatory granuloma environment may have evolved over many generations from continued evolution of the host immune response and *Mtb* (20, 22). During long-term containment, bacterial growth is restricted but are able persist in the host almost indefinitely, while the host shows no adverse signs of infection with limited host tissue damage. Thus, an anti-inflammatory biased granuloma that promotes containment may be the best outcome for both the host and the bacteria once infection has persisted past the initial stages of the immune response. The balance of TNF-α and IL-10 concentrations in a granuloma presents a possible new avenue for treatment strategies. Granulomas that are 'out of balance' may need addition of antibodies or exogenous cytokines in order to shift from poorer outcomes and towards containment outcomes.

The simulations analyzed here focused on relatively mature granulomas. Strategies to treat early developing and less mature granulomas may differ, although the likelihood of detection and of infection at such an early stage (within weeks of infection) in a clinical setting is small. Anti-IL-10 and anti-IL-10R antibodies used *in-vivo* in the context of *Mtb* infection can result in increased bacterial control (22, 54). Conversely, transgenic mice that overexpress IL-10 are more susceptible to *Mtb* infection and have an increased chance of reactivation (55). However, since containment of bacteria appears to be an optimal outcome for both the host and the pathogen, it is still unclear how to treat these granulomas. We also note that there are other cytokines and immune cells, for example TGF-β and neutrophils, that may influence the immune response to *Mtb* (4). Future studies could incorporate the dynamics of additional cytokines and immune cell

types into an ABM to determine the effects of this complex milieu of cytokines interacting during *Mtb* infection.

Our modeling approach in this Chapter represents a critical step towards fully understanding the roles of TNF-α and IL-10 and their effects on long-term *Mtb* infection outcome. In addition, the hybrid agent-based model platform we developed will allow us to rapidly explore new treatment strategies (such as immunomodulation) to affect the immune response to *Mtb*, narrowing the large design space for future experiments.

3.5 References

1. Comas, I., and S. Gagneux. 2009. The past and future of tuberculosis research. *PLoS Pathog.* 5: e1000600.

2. Daley, C. L. 2010. Update in tuberculosis 2009. *Am. J. Respir. Crit. Care Med.* 181: 550–5.

3. Flynn, J. L. 2004. Immunology of tuberculosis and implications in vaccine development. *Tuberculosis* 84: 93–101.

4. Flynn, J. L., and J. Chan. 2001. Immunology of tuberculosis. *Annu. Rev. Immunol.* 19: 93–129.

5. Gideon, H. P., and J. L. Flynn. 2011. Latent tuberculosis: what the host "sees"? *Immunol. Res.* 50: 202–12.

6. Ford, C. B., P. L. Lin, M. R. Chase, R. R. Shah, O. Iartchouk, J. Galagan, N. Mohaideen, T. R. Ioerger, J. C. Sacchettini, M. Lipsitch, J. L. Flynn, and S. M. Fortune. 2011. Use of whole genome sequencing to estimate the mutation rate of Mycobacterium tuberculosis during latent infection. *Nat. Genet.* 43: 482–6.

7. Davis, J. M., and L. Ramakrishnan. 2008. "The very pulse of the machine": the tuberculous granuloma in motion. *Immunity* 28: 146–8.

8. Tsai, M. C., S. Chakravarty, G. Zhu, J. Xu, K. Tanaka, C. Koch, J. Tufariello, J. Flynn, and J. Chan. 2006. Characterization of the tuberculous granuloma in murine and human lungs: cellular composition and relative tissue oxygen tension. *Cell. Microbiol.* 8: 218–32.

9. Lin, P. L., S. Pawar, A. Myers, A. Pegu, C. Fuhrman, T. a Reinhart, S. V Capuano, E. Klein, and J. L. Flynn. 2006. Early events in Mycobacterium tuberculosis infection in cynomolgus macaques. *Infect. Immun.* 74: 3790–803.

10. Flynn, J. L. 2006. Lessons from experimental Mycobacterium tuberculosis infections. *Microbes Infect.* 8: 1179–88.

11. Ramakrishnan, L. 2012. Revisiting the role of the granuloma in tuberculosis. *Nat. Rev. Immunol.* 12: 352–66.

12. Russell, D. G., C. E. Barry, and J. L. Flynn. 2010. Tuberculosis: what we don't know can, and does, hurt us. *Science* 328: 852–6.

13. Fallahi-Sichani, M., M. El-Kebir, S. Marino, D. E. Kirschner, and J. J. Linderman. 2011. Multiscale computational modeling reveals a critical role for TNF-α receptor 1 dynamics in tuberculosis granuloma formation. *J. Immunol.* 186: 3472–83.

14. Ray, J. C. J., J. L. Flynn, and D. E. Kirschner. 2009. Synergy between individual TNF-dependent functions determines granuloma performance for controlling Mycobacterium tuberculosis infection. *J. Immunol.* 182: 3706–17.

15. Algood, H. M. S., P. L. Lin, D. Yankura, A. Jones, J. Chan, and J. L. Flynn. 2004. TNF influences chemokine expression of macrophages in vitro and that of CD11b+ cells in vivo during Mycobacterium tuberculosis infection. *J. Immunol.* 172: 6846–57.

16. Lin, P. L., and J. L. Flynn. 2010. Understanding latent tuberculosis: a moving target. *J. Immunol.* 185: 15–22.

17. Flynn, J. L., M. M. Goldstein, J. Chan, K. J. Triebold, K. Pfeffer, C. J. Lowenstein, R. Schreiber, T. W. Mak, and B. R. Bloom. 1995. Tumor necrosis factor-alpha is required in the protective immune response against Mycobacterium tuberculosis in mice. *Immunity* 2: 561–72.

18. Egen, J. G., A. G. Rothfuchs, C. G. Feng, N. Winter, A. Sher, and R. N. Germain. 2008. Macrophage and T cell dynamics during the development and disintegration of mycobacterial granulomas. *Immunity* 28: 271–84.

19. Davis, J. M., and L. Ramakrishnan. 2009. The role of the granuloma in expansion and dissemination of early tuberculous infection. *Cell* 136: 37–49.

20. Redford, P., P. Murray, and A. O'Garra. 2011. The role of IL-10 in immune regulation during M. tuberculosis infection. *Mucosal Immunol.* 4: 1–10.

21. Saraiva, M., and A. O'Garra. 2010. The regulation of IL-10 production by immune cells. *Nat. Rev. Immunol.* 10: 170–181.

22. O'Garra, A., P. Vieira, P. Vieira, and A. E. Goldfeld. 2004. IL-10–producing and naturally occurring CD4+ Tregs: limiting collateral damage. *J. Clin. Invest.* 114: 1–7.

23. Cyktor, J. C., and J. Turner. 2011. Interleukin-10 and immunity against prokaryotic and eukaryotic intracellular pathogens. *Infect. Immun.* 79: 2964–73.

24. O'Garra, A., F. Barrat, and A. Castro. 2008. Strategies for use of IL-10 or its antagonists in human disease. *Immunol. Rev.* 223: 114–131.

25. Duell, B. L., C. K. Tan, A. J. Carey, F. Wu, A. W. Cripps, and G. C. Ulett. 2012. Recent insights into microbial triggers of interleukin-10 production in the host and the impact on infectious disease pathogenesis. *FEMS Immunol. Med. Microbiol.* .

26. Moore, K. W., R. de Waal Malefyt, R. L. Coffman, and A. O'Garra. 2001. Interleukin-10 and the interleukin-10 receptor. *Annu. Rev. Immunol.* 1: 683–765.

27. Redpath, S., P. Ghazal, and N. R. Gascoigne. 2001. Hijacking and exploitation of IL-10 by intracellular pathogens. *Trends Microbiol.* 9: 86–92.

28. Roncarolo, M. G., M. Battaglia, R. Bacchetta, K. Fleischhauer, and M. K. Levings. 2006. Interleukin-10-secreting type 1 regulatory T cells in rodents and humans. *Immunol. Rev.* 212: 28–50.

29. Mosser, D., and X. Zhang. 2008. Interleukin-10: new perspectives on an old cytokine. *Immunol. Rev.* 205–218.

30. Fickenscher, H., S. Hör, H. Küpers, A. Knappe, S. Wittmann, and H. Sticht. 2002. The interleukin-10 family of cytokines. *Trends Immunol.* 23: 89–96.

31. Mege, J., S. Meghari, A. Honstettre, C. Capo, and D. Raoult. 2006. The two faces of interleukin 10 in human infectious diseases. *Lancet Infect. Dis.* 6: 557–569.

32. Ouyang, W., S. Rutz, N. K. Crellin, P. a Valdez, and S. G. Hymowitz. 2011. Regulation and functions of the IL-10 family of cytokines in inflammation and disease. *Annu. Rev. Immunol.* 29: 71–109.

33. Bouabe, H., Y. Liu, M. Moser, M. R. Bösl, and J. Heesemann. 2011. Novel Highly Sensitive IL-10-{beta}-Lactamase Reporter Mouse Reveals Cells of the Innate Immune System as a Substantial Source of IL-10 In Vivo. *J. Immunol.* 187: 3165–76.

34. Yssel, H., R. De Waal Malefyt, M. G. Roncarolo, J. S. Abrams, R. Lahesmaa, H. Spits, and J. E. de Vries. 1992. IL-10 is produced by subsets of human CD4+ T cell clones and peripheral blood T cells. *J. Immunol.* 149: 2378–84.

35. Smallie, T., G. Ricchetti, N. J. Horwood, M. Feldmann, A. R. Clark, and L. M. Williams. 2010. IL-10 inhibits transcription elongation of the human TNF gene in primary macrophages. *J. Exp. Med.* 207: 2081–8.

36. Balcewicz-Sablinska, M., H. Gan, and H. G. Remold. 1999. Interleukin 10 produced by macrophages inoculated with Mycobacterium avium attenuates mycobacteria-induced apoptosis by reduction of TNF-α activity. *J. Infect. Dis.* 180: 1230–1237.

37. Brennan, F. M., P. Green, P. Amjadi, H. J. Robertshaw, M. Alvarez-Iglesias, and M. Takata. 2008. Interleukin-10 regulates TNF-α-converting enzyme (TACE/ADAM17) involving a TIMP3 dependent and independent mechanism. *Eur. J. Immunol.* 38: 1106–17.

38. Dagvadorj, J., Y. Naiki, G. Tumurkhuu, F. Hassan, S. Islam, N. Koide, I. Mori, T. Yoshida, and T. Yokochi. 2008. Interleukin-10 inhibits tumor necrosis factor-alpha production in lipopolysaccharide-stimulated RAW 264.7 cells through reduced MyD88 expression. *Innate Immun.* 14: 109–15.

39. Murray, P. J. 2005. The primary mechanism of the IL-10-regulated antiinflammatory response is to selectively inhibit transcription. *Proc. Natl. Acad. Sci.* 102: 8686–91.

40. Lang, R., D. Patel, J. J. Morris, R. L. Rutschman, and P. J. Murray. 2002. Shaping gene expression in activated and resting primary macrophages by IL-10. *J. Immunol.* 169: 2253–63.

41. Denys, A., I. A. Udalova, C. Smith, L. M. Williams, C. J. Ciesielski, J. Campbell, C. Andrews, D. Kwaitkowski, and B. M. J. Foxwell. 2002. Evidence for a dual mechanism for IL-10 suppression of TNF-alpha production that does not involve inhibition of p38 mitogen-activated protein kinase or NF-kappa B in primary human macrophages. *J. Immunol.* 168: 4837–4845.

42. Bogdan, C., Y. Vodovotz, and C. Nathan. 1991. Macrophage Deactivation by Interleukin 10. *J. Exp. Med.* 174.

43. Fiorentino, D. F., A. Zlotnik, T. R. Mosmann, M. Howard, and A. O'Garra. 1991. IL-10 inhibits cytokine production by activated macrophages. *J. Immunolgy* 147: 3815–3822.

44. Agbanoma, G., C. Li, D. Ennis, A. C. Palfreeman, L. M. Williams, and F. M. Brennan. 2012. Production of TNF-α in macrophages activated by T cells, compared with lipopolysaccharide, uses distinct IL-10-dependent regulatory mechanism. *J. Immunol.* 188: 1307–17.

45. Hosokawa, Y., I. Hosokawa, K. Ozaki, H. Nakae, and T. Matsuo. 2009. Cytokines differentially regulate CXCL10 production by interferon-gamma-stimulated or tumor

necrosis factor-alpha-stimulated human gingival fibroblasts. *J. Periodontal Res.* 44: 225–31.

46. Ikeda, T., K. Sato, N. Kuwada, T. Matsumura, T. Yamashita, F. Kimura, K. Hatake, K. Ikeda, and K. Motoyoshi. 2002. Interleukin-10 differently regulates monocyte chemoattractant protein-1 gene expression depending on the environment in a human monoblastic cell line, UG3. *J. Leukoc. Biol.* 72: 1198–205.

47. Cheeran, M. C.-J., S. Hu, W. S. Sheng, P. K. Peterson, and J. R. Lokensgard. 2003. CXCL10 production from cytomegalovirus-stimulated microglia is regulated by both human and viral interleukin-10. *J. Virol.* 77: 4502–15.

48. Marfaing-Koka, a, M. Maravic, M. Humbert, P. Galanaud, and D. Emilie. 1996. Contrasting effects of IL-4, IL-10 and corticosteroids on RANTES production by human monocytes. *Int. Immunol.* 8: 1587–94.

49. Tang, Q., and J. a Bluestone. 2008. The Foxp3+ regulatory T cell: a jack of all trades, master of regulation. *Nat. Immunol.* 9: 239–44.

50. Rubtsov, Y. P., J. P. Rasmussen, E. Y. Chi, J. Fontenot, L. Castelli, X. Ye, P. Treuting, L. Siewe, A. Roers, W. R. Henderson, W. Muller, and A. Y. Rudensky. 2008. Regulatory T cell-derived interleukin-10 limits inflammation at environmental interfaces. *Immunity* 28: 546–58.

51. Shevach, E. M. 2009. Mechanisms of foxp3+ T regulatory cell-mediated suppression. *Immunity* 30: 636–45.

52. Higgins, D. M., J. Sanchez-Campillo, A. G. Rosas-Taraco, E. J. Lee, I. M. Orme, and M. Gonzalez-Juarrero. 2009. Lack of IL-10 alters inflammatory and immune responses during pulmonary Mycobacterium tuberculosis infection. *Tuberculosis (Edinb).* 89: 149–57.

53. Shaler, C. R., K. Kugathasan, S. McCormick, D. Damjanovic, C. Horvath, C.-L. Small, M. Jeyanathan, X. Chen, P.-C. Yang, and Z. Xing. 2011. Pulmonary mycobacterial granuloma increased IL-10 production contributes to establishing a symbiotic host-microbe microenvironment. *Am. J. Pathol.* 178: 1622–34.

54. Pitt, J. M., E. Stavropoulos, P. S. Redford, A. M. Beebe, G. J. Bancroft, D. B. Young, and A. O'Garra. 2012. Blockade of IL-10 signaling during bacillus Calmette-Guérin vaccination enhances and sustains Th1, Th17, and innate lymphoid IFN-γ and IL-17 responses and increases protection to Mycobacterium tuberculosis infection. *J. Immunol.* 189: 4079–87.

55. Turner, J., M. Gonzalez-Juarrero, D. L. Ellis, R. J. Basaraba, A. Kipnis, I. M. Orme, and A. M. Cooper. 2002. In vivo IL-10 production reactivates chronic pulmonary tuberculosis in C57BL/6 mice. *J. Immunol.* 169: 6343–51.

56. Beamer, G. L., D. K. Flaherty, B. D. Assogba, P. Stromberg, M. Gonzalez-Juarrero, R. de Waal Malefyt, B. Vesosky, and J. Turner. 2008. Interleukin-10 promotes Mycobacterium tuberculosis disease progression in CBA/J mice. *J. Immunol.* 181: 5545–50.

57. Redford, P. S., A. Boonstra, S. Read, J. Pitt, C. Graham, E. Stavropoulos, G. J. Bancroft, and A. O'Garra. 2010. Enhanced protection to Mycobacterium tuberculosis infection in IL-10-deficient mice is accompanied by early and enhanced Th1 responses in the lung. *Eur. J. Immunol.* 40: 2200–10.

58. Junqueira-Kipnis, A. P., A. Kipnis, M. Henao Tamayo, M. Harton, M. Gonzalez Juarrero, R. J. Basaraba, and I. M. Orme. 2005. Interleukin-10 production by lung macrophages in CBA xid mutant mice infected with Mycobacterium tuberculosis. *Immunology* 115: 246–52.

59. Roach, D. R., E. Martin, a G. Bean, D. M. Rennick, H. Briscoe, and W. J. Britton. 2001. Endogenous inhibition of antimycobacterial immunity by IL-10 varies between mycobacterial species. *Scand. J. Immunol.* 54: 163–70.

60. North, R. J. 1998. Mice incapable of making IL-4 or IL-10 display normal resistance to infection with Mycobacterium tuberculosis. *Clin. Exp. Immunol.* 113: 55–58.

61. Brooks, D. G., M. J. Trifilo, K. H. Edelmann, L. Teyton, D. B. McGavern, and M. B. A. Oldstone. 2006. Interleukin-10 determines viral clearance or persistence in vivo. *Nat. Med.* 12: 1301–9.

62. Jung, Y.-J., L. Ryan, R. LaCourse, and R. J. North. 2003. Increased interleukin-10 expression is not responsible for failure of T helper 1 immunity to resolve airborne Mycobacterium tuberculosis infection in mice. *Immunology* 109: 295–9.

63. Wigginton, J. E., and D. Kirschner. 2001. A model to predict cell-mediated immune regulatory mechanisms during human infection with Mycobacterium tuberculosis. *J. Immunol.* 166: 1951–67.

64. Marino, S., A. Myers, J. L. Flynn, and D. E. Kirschner. 2010. TNF and IL-10 are major factors in modulation of the phagocytic cell environment in lung and lymph node in tuberculosis: a next-generation two-compartmental model. *J. Theor. Biol.* 265: 586–98.

65. Saunders, B. M., H. Briscoe, and W. J. Britton. 2004. T cell-derived tumour necrosis factor is essential, but not sufficient, for protection against Mycobacterium tuberculosis infection. *Clin. Exp. Immunol.* 137: 279–87.

66. Harris, J., J. C. Hope, and J. Keane. 2008. Tumor necrosis factor blockers influence macrophage responses to Mycobacterium tuberculosis. *J. Infect. Dis.* 198: 1842–50.

67. Gutierrez, M. G., B. B. Mishra, L. Jordao, E. Elliott, E. Anes, and G. Griffiths. 2008. NF-kappa B activation controls phagolysosome fusion-mediated killing of mycobacteria by macrophages. *J. Immunol.* 181: 2651–63.

68. Mosser, D. M., and J. P. Edwards. 2008. Exploring the full spectrum of macrophage activation. *Nat. Rev. Immunol.* 8: 958–69.

69. Tay, S., J. J. Hughey, T. K. Lee, T. Lipniacki, S. R. Quake, and M. W. Covert. 2010. Single-cell NF-kappaB dynamics reveal digital activation and analogue information processing. *Nature* 466: 267–71.

70. Wajant, H., K. Pfizenmaier, and P. Scheurich. 2003. Tumor necrosis factor signaling. *Cell Death Differ.* 10: 45–65.

71. Zhou, Z., M. C. Connell, and D. J. MacEwan. 2007. TNFR1-induced NF-kappaB, but not ERK, p38MAPK or JNK activation, mediates TNF-induced ICAM-1 and VCAM-1 expression on endothelial cells. *Cell. Signal.* 19: 1238–48.

72. Keane, J., B. Shurtleff, and H. Kornfeld. 2002. TNF-dependent BALB/c murine macrophage apoptosis following Mycobacterium tuberculosis infection inhibits bacillary growth in an IFN-gamma independent manner. *Tuberculosis (Edinb).* 82: 55–61.

73. Wanidworanun, C., and W. Strober. 1993. Predominant role of tumor necrosis factor-alpha in human monocyte IL-10 synthesis. *J. Immunol.* 151: 6853–61.

74. Flynn, J. L., J. Chan, and P. L. Lin. 2011. Macrophages and control of granulomatous inflammation in tuberculosis. *Mucosal Immunol.* 4: 271–8.

75. Platzer, C., C. Meisel, K. Vogt, M. Platzer, and H. D. Volk. 1995. Up-regulation of monocytic IL-10 by tumor necrosis factor-alpha and cAMP elevating drugs. *Int. Immunol.* 7: 517–23.

76. Chakravarty, S. D., G. Zhu, M. C. Tsai, V. P. Mohan, S. Marino, D. E. Kirschner, L. Huang, J. Flynn, and J. Chan. 2008. Tumor necrosis factor blockade in chronic murine tuberculosis enhances granulomatous inflammation and disorganizes granulomas in the lungs. *Infect. Immun.* 76: 916–26.

77. Lin, P. L., A. Myers, L. Smith, C. Bigbee, M. Bigbee, C. Fuhrman, H. Grieser, I. Chiosea, N. N. Voitenek, S. V Capuano, E. Klein, and J. L. Flynn. 2010. Tumor necrosis factor neutralization results in disseminated disease in acute and latent Mycobacterium tuberculosis infection with normal granuloma structure in a cynomolgus macaque model. *Arthritis Rheum.* 62: 340–50.

78. Fallahi-Sichani, M., D. E. Kirschner, and J. J. Linderman. 2012. NF-κB Signaling Dynamics Play a Key Role in Infection Control in Tuberculosis. *Front. Physiol.* 3: 170.

79. Fallahi-Sichani, M., J. L. Flynn, J. J. Linderman, and D. E. Kirschner. 2012. Differential risk of tuberculosis reactivation among anti-TNF therapies is due to drug binding kinetics and permeability. *J. Immunol.* 188: 3169–78.

80. Fallahi-Sichani, M., M. a Schaller, D. E. Kirschner, S. L. Kunkel, and J. J. Linderman. 2010. Identification of key processes that control tumor necrosis factor availability in a tuberculosis granuloma. *PLoS Comput. Biol.* 6: e1000778.

81. Wallis, R. S. 2009. Infectious complications of tumor necrosis factor blockade. *Curr. Opin. Infect. Dis.* 22: 403–9.

82. Wallis, R. S. 2008. Tumour necrosis factor antagonists: structure, function, and tuberculosis risks. *Lancet Infect. Dis.* 8: 601–11.

83. Lucas, T. A. 2008. Operator Splitting for an Immunology Model Using Reaction-Diffusion Equations with Stochastic Source Terms. *SIAM J. Numer. Anal.* 46: 3113–3135.

84. Guo, Z., P. M. a Sloot, and J. C. Tay. 2008. A hybrid agent-based approach for modeling microbiological systems. *J. Theor. Biol.* 255: 163–75.

85. Ma, J., T. Chen, J. Mandelin, A. Ceponis, N. E. Miller, M. Hukkanen, G. F. Ma, and Y. T. Konttinen. 2003. Regulation of macrophage activation. *Cell. Mol. Life Sci.* 60: 2334–46.

86. Theus, S. a, M. D. Cave, and K. D. Eisenach. 2005. Intracellular macrophage growth rates and cytokine profiles of Mycobacterium tuberculosis strains with different transmission dynamics. *J. Infect. Dis.* 191: 453–60.

87. Grosset, J. 2003. Mycobacterium tuberculosis in the extracellular compartment: an underestimated adversary. *Antimicrob. Agents Chemother.* 47: 833–6.

88. Vesosky, B., E. K. Rottinghaus, P. Stromberg, J. Turner, and G. Beamer. 2010. CCL5 participates in early protection against Mycobacterium tuberculosis. *J. Leukoc. Biol.* 87: 1153–65.

89. Algood, H. M. S., and J. L. Flynn. 2004. CCR5-deficient mice control Mycobacterium tuberculosis infection despite increased pulmonary lymphocytic infiltration. *J. Immunol.* 173: 3287–96.

90. Chabot, V., P. Reverdiau, S. Iochmann, A. Rico, D. Sénécal, C. Goupille, P. Sizaret, and L. Sensebé. 2006. CCL5-enhanced human immature dendritic cell migration through the basement membrane in vitro depends on matrix metalloproteinase-9. *J. Leukoc. Biol.* 79: 767–78.

91. Wu, K., J. Koo, X. Jiang, R. Chen, S. N. Cohen, and C. Nathan. 2012. Improved control of tuberculosis and activation of macrophages in mice lacking protein kinase R. *PLoS One* 7: e30512.

92. Giacomini, E., E. Iona, L. Ferroni, M. Miettinen, L. Fattorini, G. Orefici, I. Julkunen, and E. M. Coccia. 2001. Infection of human macrophages and dendritic cells with Mycobacterium tuberculosis induces a differential cytokine gene expression that modulates T cell response. *J. Immunol.* 166: 7033–41.

93. Meyaard, L., E. Hovenkamp, S. A. Otto, and F. Miedema. 1996. IL-12-induced IL-10 production by human T cells as a negative feedback for IL-12-induced immune responses. *J. Immunol.* 156: 2776–82.

94. Orme, I. M., A. D. Roberts, J. P. Griffin, and J. S. Abrams. 1993. Cytokine secretion by CD4 T lymphocytes acquired in response to Mycobacterium tuberculosis infection. *J. Immunol.* 151: 518–25.

95. Shaw, T. C., L. H. Thomas, and J. S. Friedland. 2000. Regulation of IL-10 secretion after phagocytosis of Mycobacterium tuberculosis by human monocytic cells. *Cytokine* 12: 483–6.

96. Tan, J. C., S. R. Indelicato, S. K. Narula, P. J. Zavodny, and C. C. Chou. 1993. Characterization of interleukin-10 receptors on human and mouse cells. *J. Biol. Chem.* 268: 21053–9.

97. Weber-Nordt, R. M., M. a Meraz, and R. D. Schreiber. 1994. Lipopolysaccharide-dependent induction of IL-10 receptor expression on murine fibroblasts. *J. Immunol.* 153: 3734–44.

98. Figueiredo, A. S., T. Höfer, C. Klotz, C. Sers, S. Hartmann, R. Lucius, and P. Hammerstein. 2009. Modelling and simulating interleukin-10 production and regulation by macrophages after stimulation with an immunomodulator of parasitic nematodes. *FEBS J.* 276: 3454–69.

99. Moya, C., Z. Huang, P. Cheng, A. Jayaraman, and J. Hahn. 2011. Investigation of IL-6 and IL-10 signalling via mathematical modelling. *IET Syst. Biol.* 5: 15.

100. Lauffenburger, D. A., and J. J. Linderman. 1993. Receptors: Models For Binding, Trafficking, and Signaling. In Oxford University Press, New York.

101. Wei, S. H.-Y., A. Ming-Lum, Y. Liu, D. Wallach, C. J. Ong, S. W. Chung, K. W. Moore, and A. L.-F. Mui. 2006. Proteasome-mediated proteolysis of the interleukin-10 receptor is important for signal downregulation. *J. Interferon Cytokine Res.* 26: 281–90.

102. Schreiber, T., S. Ehlers, L. Heitmann, A. Rausch, J. Mages, P. J. Murray, R. Lang, and C. Hölscher. 2009. Autocrine IL-10 induces hallmarks of alternative activation in

macrophages and suppresses antituberculosis effector mechanisms without compromising T cell immunity. *J. Immunol.* 183: 1301–12.

103. Verreck, F. a W., T. de Boer, D. M. L. Langenberg, M. a Hoeve, M. Kramer, E. Vaisberg, R. Kastelein, A. Kolk, R. de Waal-Malefyt, and T. H. M. Ottenhoff. 2004. Human IL-23-producing type 1 macrophages promote but IL-10-producing type 2 macrophages subvert immunity to (myco)bacteria. *Proc. Natl. Acad. Sci. U. S. A.* 101: 4560–5.

104. Joyce, D. A., D. P. Gibbons, P. Green, J. H. Steer, M. Feldmann, and F. M. Brennan. 1994. Two inhibitors of pro-inflammatory cytokine release, interleukin-10 and interleukin-4, have contrasting effects on release of soluble p75 tumor necrosis factor receptor by cultured monocytes. *Eur. J. Immunol.* 24: 2699–705.

105. Hart, P. H., E. K. Hunt, C. S. Bonder, C. J. Watson, and J. J. Finlay-Jones. 1996. Regulation of surface and soluble TNF receptor expression on human monocytes and synovial fluid macrophages by IL-4 and IL-10. *J. Immunol.* 157: 3672–80.

106. Barakat, H. Z., and J. A. Clark. 1966. On the Solution of the Diffusion Equations by Numerical Methods. *J. Heat Transfer* 88: 421.

107. Marino, S., I. B. Hogue, C. J. Ray, and D. E. Kirschner. 2008. A methodology for performing global uncertainty and sensitivity analysis in systems biology. *J. Theor. Biol.* 254: 178–96.

108. Marino, S., M. El-Kebir, and D. Kirschner. 2011. A hybrid multi-compartment model of granuloma formation and T cell priming in tuberculosis. *J. Theor. Biol.* 280: 50–62.

109. Bird, R. B., W. E. Stewart, and E. N. Lightfoot. 1994. *Transport Phenomena*,. John Wiley & Sons, New York.

110. Riley, J. K., K. Takeda, S. Akira, and R. D. Schreiber. 1999. Interleukin-10 Receptor Signaling through the JAK-STAT Pathway. 274: 16513–16521.

111. Dannenberg, A. M. 1989. Immune mechanisms in the pathogenesis of pulmonary tuberculosis. *Rev. Infect. Dis.* 11 Suppl 2: S369–78.

112. Newton, S. M., R. J. Smith, K. A. Wilkinson, M. P. Nicol, N. J. Garton, K. J. Staples, G. R. Stewart, J. R. Wain, A. R. Martineau, S. Fandrich, T. Smallie, B. Foxwell, A. Al-Obaidi, J. Shafi, K. Rajakumar, B. Kampmann, P. W. Andrew, L. Ziegler-Heitbrock, M. R. Barer, and R. J. Wilkinson. 2006. A deletion defining a common Asian lineage of Mycobacterium tuberculosis associates with immune subversion. *Proc. Natl. Acad. Sci. U. S. A.* 103: 15594–8.

Chapter 4

Macrophage Polarization Drives Granuloma Outcome During *Mycobacterium tuberculosis* Infection

The work in Chapter 4 has been submitted as part of: Marino, S., Cilfone, N.A., Mattila, J.T., Linderman, J.J., Flynn, J.L., Kirschner, D.E. Macrophage polarization drives granuloma outcome during *Mycobacterium tuberculosis* infection. (2014).

4.1 Introduction

Macrophages are the initial site of *Mycobacterium tuberculosis* infection following inhalation of the bacterium and continue to harbor the pathogen in the intracellular space during the chronic state of *Mtb* infection (1). In response to inflammatory molecules (both cytokines and chemokines), a significant number of monocytes migrate from the bloodstream to the site of infection (1). Therefore, the majority of immune cells found in granulomas, the organized cluster of cells that forms in response to *Mtb* infection, are macrophages. In granulomas, macrophages function to control inflammation, contribute to antimicrobial processes, and harbor the pathogen (1–3).

Recent work has demonstrated that macrophage differentiation and activation in response to different stimuli represents a spectrum of activation, similar to T cells, rather than a single state of activation (4–8). At the extremes of the spectrum, macrophages are

classified into two different populations, known as polarization states (Figure 4.1). M1 (or classically activated) macrophages display a pro-inflammatory phenotype, expressing high levels of pro-inflammatory cytokines (e.g. TNF), high production of reactive nitrogen and oxygen species, and strong antimicrobial capabilities (Figure 4.1) (6, 9, 10). M2 (or alternatively activated) macrophages display an anti-inflammatory phenotype, expressing high levels of anti-inflammatory cytokines (e.g. IL-10), promoting wound healing and tissue remodeling, and demonstrating reduced bactericidal action (Figure 4.1) (8, 11, 12). In granulomas, macrophages are exposed to multiple different polarizing stimuli leading to a spectrum of polarization between the M1 and M2 extremes. More M1-like macrophages are thought to be associated with early antimicrobial responses, while more M2-like macrophages are thought to control late stage inflammation to prevent excess tissue damage and promote granuloma healing (1).

Stimulation of macrophages with TNF and IFN-γ leads to induction of NFκB and STAT1 signaling pathways, causing macrophages to polarize towards an M1 phenotype (Figure 4.1) (6, 7). Conversely, stimulation of macrophages with IL-10, along with other cytokines, induces STAT3 signaling, which polarizes macrophages towards an M2 phenotype (Figure 4.1) (6, 8). Using the model constructed in Chapter 3 as a framework, we extend the descriptions of TNF-α, IL-10, and IFN-γ action in this Chapter to include simple models of downstream signaling pathways (NFκB, STAT3, and STAT1 respectively) that influence macrophage polarization (Figure 4.1B). We define a macrophage polarization ratio to translate how combinations of cytokine signals influence the plasticity of macrophages in a granuloma, which in turn modulates macrophage functions including anti-microbial activity and cytokine production (Figure

4.1A). Next, we define a granuloma polarization ratio by averaging individual macrophage polarization ratios in a granuloma, thus defining a metric of polarization at a tissue scale. Using these metrics we predict how cytokines influence the spectrum of macrophage polarization in granulomas over the course of infection, spatially organize, and eventually determine infection outcome.

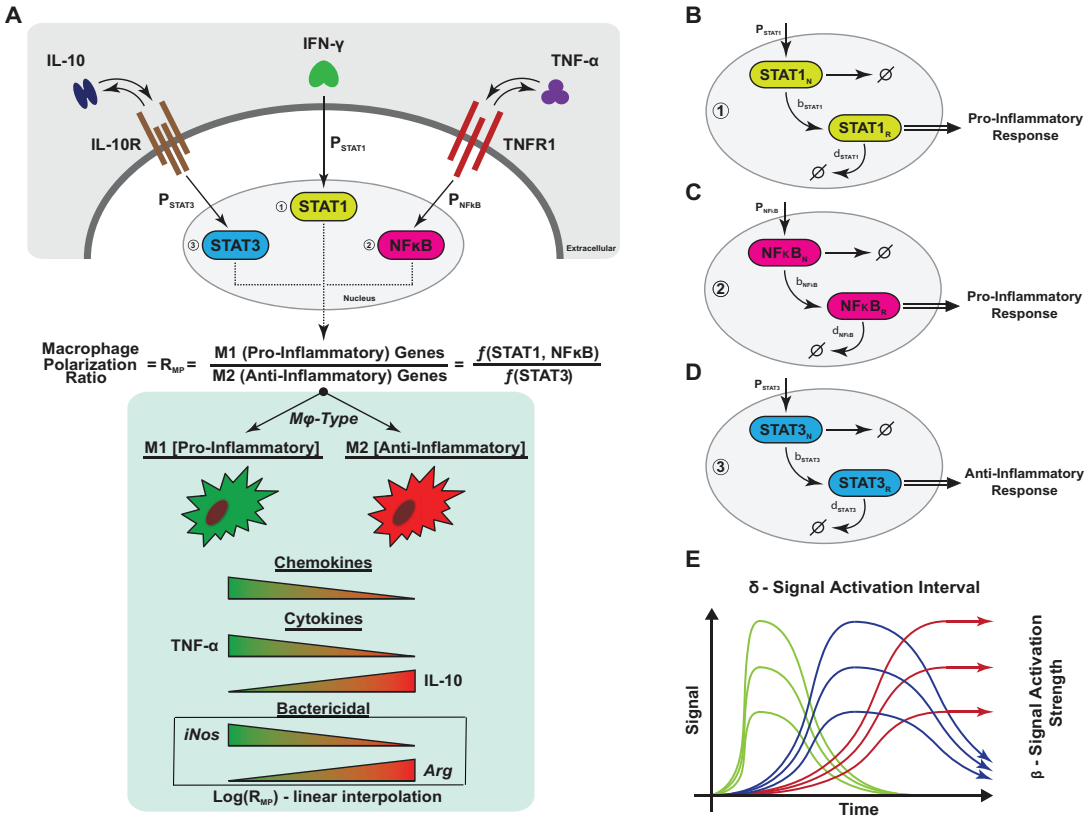

Figure 4.1 Schematic representation of macrophage polarization and gene expression dynamics captured in the ABM
(A) Macrophage signaling pathways used to capture M1 (pro-inflammatory) and M2 (anti-inflammatory) cues. Each signal is quantified and used to calculate a ratio that is then used to modulate several immune functions of the macrophage (chemokine and cytokine [TNF, IL10] synthesis, bacterial killing). The modulation of macrophage function is implemented as a linear interpolation of the log of the macrophage polarization ratio (the value of the ratio is normalized and multiplied by the parameter value regulating the correspondent immune function). (B-D) Models of signaling pathways used for STAT1, STAT3, and NFκB. For each pathway there is a nuclear species (subscript N) and a response species (subscript R). The details are given in the Materials and Methods section. (E) Different gene transcription dynamic regimes (fast-green, intermediate-blue and slow-red) can be recapitulated in the signaling pathway models by varying signal degradation time (or length, δ) and response/signal strength (β) of the response.

4.2 Materials and Methods

4.2.1 Multi-Scale Agent-Based Model

In Chapter 3 we described a model of granuloma formation and function during *Mtb* infection where immunological processes were captured over three different biological scales: molecular, cellular, and tissue scales (13). Briefly, an agent-based model represents the cellular scale by modeling macrophages and T cells as distinct agents within the simulation environment (14, 15). Sub-models inside each individual agent capture molecular scale events by describing receptor-ligand dynamics of IL-10 and TNF using ordinary differential equations models (ODEs) (13, 16). Diffusion and degradation of IL-10 and TNF in lung tissue and the granuloma are calculated using partial differential equation models (PDEs) (details can be found in Chapters 2 and 3) (13, 16–19). In this Chapter, TNF, IFN-γ and IL-10 drive macrophage polarization and modulate macrophage immune functions, such as cytokine synthesis and bactericidal activity.

The two-dimensional model environment represents a 4 mm^2 section of lung tissue, discretized into 100x100 micro-compartments of size 20 μm^2. The lattice is initialized with macrophages and vascular sources for recruitment of cells to the site of infection. Recruitment of cells into the simulation environment is based on the recruitment algorithms described in Chapter 3 (13–16). We initiate infection by placing a macrophage in the middle of the simulation lattice and infecting it with a single intracellular *Mtb* (20, 21). We simulate 200 days post-infection, with agent rules and interactions solved on a 10 min time step, while STAT1, STAT3, and NFκB dynamics are updated every 6 seconds. Full model details including agent rules, soluble molecule

diffusion and degradation, and TNF and IL-10 receptor-ligand dynamics can be found in Chapter 3 (13–16).

Bacterial growth rates of *Mtb* are heterogeneous, and thus simulated bacterial growth rates are assigned from a distribution of extra- and intra-cellular doubling times measured in experimental systems (21). Extracellular *Mtb* growth rates are sampled from a uniform distribution (defined by minimum and maximum values inferred from data, see Table 4.1) at the beginning of the simulation and assigned to each of the 100x100 micro-compartments. Intracellular growth rates are chosen from a uniform distribution upon infection of a resting macrophage with *Mtb*. Ranges for intracellular and extracellular bacterial growth rates are shown in Table 4.1, together with other parameters used in the model.

Table 4.1 Macrophage Polarization Related Model Parameters

Parameter	Parameter Description	Value(s)	Reference(s)
$\tau_{NF\kappa B}$ (#/cell)	Cell surface sTNF/TNFR1 threshold for TNF-induced NFκB activation	40-60	(13, 16)
$k_{NF\kappa B}$ ((#/cell)$^{-1}$s^{-1})	Rate constant for TNF-induced NFκB activation in macrophages	5×10^{-6}-1×10^{-5}	(13, 16)
$\tau_{STAT3\text{-}IL10}$ (#/cell)	Cell surface sIL10/IL10R threshold for IL10-induced STAT3	10-20	Estimated
$k_{NF\kappa BSTAT3IL10}$ ((#/cell)$^{-1}$s^{-1})	Rate constant for IL10-induced STAT3 activation in macrophages	7.5×10^{-4}-1.6×10^{-3}	Estimated
$Synth_{IL10\text{-}MI}$ (#/cell.s)	Full synthesis rate of soluble IL10 by M_i	0.06-0.22	(22, 23)
$Synth_{IL10\text{-}MA}$ (#/cell.s)	Full synthesis rate of soluble IL10 by M_a	0.04-0.65	(22, 23)
a_{IntMtb} (days)	Doubling time for intracellular Mtb	1-2	(21)
a_{ExtMtb} (days)	Doubling time for extracellular Mtb	2-5	(21)
$prob_{KillExtMtbM0}$	Probability of M_0 killing extracellular bacteria	0.05-0.25	Estimated
$prob_{KillExtMtb}$	Probability of non-M_0 killing extracellular bacteria	0.75-1	Estimated
$prob_{KillIntMtb}$	Probability of non-M_0 killing intracellular bacteria	1×10^{-3}-1.0	Estimated
b_{STAT1} (min^{-1})	Rate of signal activation strength of STAT1	1-25	(24, 25)
b_{STAT3} (min^{-1})	Rate of signal activation strength of STAT3	1-25	(26–29)
$b_{NF\text{-}B}$ (min^{-1})	Rate of signal activation strength of NFκB	1-25	(18, 30)
d_{STAT1} (min^{-1})	Rate of signal activation "inhibition" of STAT1	1×10^{-4}-1×10^{-1}	(24, 25)
d_{STAT3} (min^{-1})	Rate of signal activation "inhibition" of STAT3	1×10^{-4}-1×10^{-1}	(26–29)
$d_{NF\text{-}B}$ (min^{-1})	Rate of signal activation "inhibition" of NFκB	1×10^{-4}-1×10^{-1}	(18, 30)
$t_{AgeTransition}$	Normalized macrophage polarization ratio threshold for transitioning to a shorter lifespan	0.7-0.9	Estimated
$time_{RecEnabled}$ (days)	Days when effector T cells recruitment is enabled	20-30	Estimated
$prob_{Stat1Tg}$	Probability of macrophage STAT1 activation induced by IFNg-producing T cells	1×10^{-3}-1×10^{-1}	Estimated

4.2.2 Models of STAT1, STAT3, and NFκB Dynamics

To study the influence of cytokines on macrophage activation and polarization, we modified our existing multi-scale model to account for the intracellular signaling pathways mediated by STAT1, STAT3, and NFκB. We describe STAT1, STAT3 and

NFκB signal pathways when macrophages are stimulated with IFNγ, IL-10, and TNF, respectively. We utilize simplified versions of recently published models for STAT1, STAT3, and NFκB pathways (18, 24–26, 30).

We use two representative intracellular species for each signaling pathway: a phosphorylated nuclear species (denoted with N) and a response species (denoted with R) (Figure 4.1B-D). The phosphorylated nuclear species ($STAT1_N$, $STAT3_N$, and $NF\kappa B_N$) represent the phosphorylated forms of STAT1, STAT3 and NFκB that exist in the nucleus following ligand stimulation. These nuclear phosphorylated species lead to downstream signaling (including transcription factors and mRNA) where they are referred to as the response species ($STAT1_R$, $STAT3_R$, and $NF\kappa B_R$) (18, 24–26, 30). In this context, inhibition of signal activation for the response species represents the combined deactivation of these signal transducers in the nucleus, events mediated by de-phosphorylation (STAT1 and STAT3) and coupling with inhibitory subunits (NFκB), and degradation of signaling molecules by proteolytic processes (18, 24–26, 30). The phosphorylated nuclear species have a maximum level (defined by $STAT1_{MaxLevel}$, $STAT3_{MaxLevel}$, $NF\kappa B_{MaxLevel}$) to capture saturation of ligand-induced stimulation. The included cytokines and signaling pathways are not the only mediators of macrophage polarization. We note that molecules such as IFNα/β (STAT1), IL-6 (STAT3), and TLR4, T cell-, B cell-, or IL-1 receptor can also contribute to the spectrum of macrophage activation. However, more work is needed to identify their influences on macrophage polarization in the granuloma (8, 11).

Although the intracellular pathways are simplified representations of signaling, the models are able to recapitulate three expression regimes observed in many signaling

pathways – fast expression, intermediate expression, and stable expression (31, 32). This is possible by altering two model parameters for each pathway (see Figure 4.1E), the signal activation interval (δ) and the signal strength (β). The signal activation interval for each pathway represents the length of time the signal is turned on. This interval is controlled by a degradation rate of the response species in the simplified signaling model (see Figures 4.1B-D).

These simplified signaling pathways are linked to the existing multi-scale model, described in Chapter 3, trough the molecular species IL-10, TNF and INF-γ. The molecular scale models of IL-10 and TNF, described in Chapter 3, are linked to the models of STAT3 and NFκB respectively via binding of the soluble molecule to its corresponding cell-associated receptor (see Figure 4.1) (13, 16). STAT1 is linked to IFN-γ simulation of macrophages. T cells secrete IFN-γ and its impact is restricted locally at the immunological synapse, thus it is not necessary to explicitly model IFN-γ dynamics at the receptor scale (as we do for IL-10 and TNF) (33). Thus, in the model T cells produce IFN-γ as a proxy for activating $STAT1_N$ in neighboring macrophages with a given probability (P_{STAT1}).

We use Poisson processes to describe the probability (P_{STAT3} and $P_{NF\kappa B}$) of ligand-induced activation of $STAT3_N$ and $NF\kappa B_N$ based on rate parameters (k_{STAT3} or $k_{NF\kappa B}$), threshold values (τ_{STAT3} or $\tau_{NF\kappa B}$), and respective concentrations of IL-10 bound to IL-10R and TNF bound to TNFR1 (13, 16, 18):

$$P_{STAT3} = \begin{cases} 1 - e^{-k_{STAT3}\left(\left[IL10 \cdot IL10R\right] - \tau_{STAT3}\Delta t\right)} \\ 0 \end{cases} \begin{cases} \left[IL10 \cdot IL10R\right] \geq \tau_{STAT3} \\ \left[IL10 \cdot IL10R\right] < \tau_{STAT3} \end{cases} \qquad (Eqn.\ 4.1)$$

$$P_{NF\kappa B} = \begin{cases} 1 - e^{-k_{NF\kappa B}\left(\left[TNF \cdot TNFR1\right] - \tau_{NF\kappa B}\Delta t\right)} & \left[TNF \cdot TNFR1\right] \geq \tau_{NF\kappa B} \\ 0 & \left[TNF \cdot TNFR1\right] < \tau_{NF\kappa B} \end{cases} \quad (Eqn.\ 4.2)$$

4.2.3 Macrophage Polarization States

In Chapter 3 we modeled macrophage states as resting, activated, infected and chronically infected (13, 14, 16). In order to explore macrophage polarization, we introduce new macrophage states: M_0, M_1, M_2, and M_1M_2. M_0 macrophages represent the initial resident alveolar macrophages and any un-polarized/non-activated macrophages. M_0 macrophages have no capabilities to secrete cytokines or chemokines, and perform limited bactericidal functions (similar to the resting macrophage state in Chapter 3). The states M_1, M_2, and M_1M_2 can all be considered subtypes of the activated macrophage state in Chapter 3. Macrophages characterized as M_1 have been polarized via stimulation of STAT1, NFκB, or both. Macrophages characterized as M_2 have been polarized via stimulation of STAT3. M_1M_2 macrophages capture the spectrum of macrophage polarization between the M_1 and M_2 extremes, wherein these macrophages have been stimulated with a combination of STAT1, NFκB, and STAT3 (6, 8).

4.2.4 Macrophage (R_{MP}) and Granuloma (R_{GP}) Polarization Ratios

To determine the polarization of a macrophage towards a pro-inflammatory (i.e. (M1) or anti- inflammatory (i.e., M2) phenotype, we define a macrophage polarization ratio (R_{MP}) (see Figure 4.1A-B). R_{MP} is a dynamic ratio comparing the amount of pro-inflammatory signals ($STAT1_R$ and $NF\kappa B_R$) received to the amount of anti-inflammatory signals received ($STAT3_R$) on an individual macrophage basis:

$$R_{MP} = \frac{STAT1_R + NF\kappa B_R}{2 * STAT3_R} \quad (Eqn.4.3)$$

We normalize the log of R_{MP} between the minimum and maximum values of $STAT1_R$, $STAT3_R$, and $NF\kappa B_R$ dictated by the intracellular signaling model parameters. Thus, macrophages that have a high value of R_{MP} are polarized towards the M1 phenotype, while macrophages with a low value of R_{MP} are polarized towards the M2 phenotype. We use a threshold of 1 for R_{MP} as a theoretical value to label a macrophage as either M1 ($R_{MP}>1$) or M2 ($R_{MP}<1$).

In order to use R_{MP} (a cell scale measure) at a tissue scale (i.e., granuloma level), we collect macrophage polarization ratios for all macrophages within a single granuloma and average them. We call this composite average the granuloma polarization ratio (R_{GP}), and use it as a metric at the granuloma scale. To make the average consistent across different granuloma simulations, we only account for macrophages within a typical lesion size (~1.5 mm diameter) and exclude from the average all the M_0 (un-polarized/un-activated) macrophages.

4.2.5 Linking Immune Function with Macrophage Polarization using R_{MP}

We use the macrophage polarization ratio, R_{MP}, to link multiple immune functions (secretion of chemokines, secretion of two cytokines, and bactericidal ability) directly to macrophage polarization values (Figure 4.1A). At the extremes of polarization, M1 macrophages secrete high levels of TNF and chemokines (CCL2, CCL5, and CXCL9/10/11), and very low levels of IL-10, while M2 macrophages secrete high levels of IL-10 and low levels of both TNF and chemokines (1, 6). Considering that a broad spectrum of macrophage polarization exists *in vivo*, we capture this by modeling

secretion of TNF, IL-10, and chemokines as linear functions of the log of R_{MP} (see Figure 4.1A, bottom). M1 macrophages express high levels of iNOS and low levels of arginase (Arg), while M2 macrophages express high levels of Arg and low levels of iNOS (1, 34). Both of these species compete for arginine as a substrate, which in the case of iNOS is used to produce antimicrobial RNI species and in the case of arginase, to convert arginase to urea and L-ornithine, an upstream precursor of collagen (35, 36). Macrophages can simultaneously express iNOS and Arg enzymes, suggesting that macrophage bactericidal characteristics are a consequence of enzyme abundance in that cell, not simply enzyme presence or absence (34, 35). Thus, we model macrophage bactericidal capabilities, condensing the iNOS and Arg pathways into a single response, as linear function of the log of R_{MP} (see Figure 4.1A).

4.2.6 Model Validation and Uncertainty and Sensitivity Analysis

Model parameter values are derived from Chapter 3, while parameters related to macrophage polarization and intracellular signaling pathways are given in Table 4.1 (13, 14, 16). We used semi-quantitative studies from the literature on STAT1 (24, 25), STAT3 (26–29) and NFκB (18, 30) to specify ranges for parameters related to the macrophage polarization ratio introduced in this Chapter (see Table 4.1 for details). Additionally, we rely on uncertainty and sensitivity analyses techniques as discussed in Chapter 3. These techniques can be used to efficiently explore the parameter space to inform baseline behaviors of the system (uncertainty analysis - UA), as well as to quantify how parameter uncertainty impacts model outcomes. This allows for efficient identification of critical

model parameters that drive model behavior (101). Details of the parameters varied in our sensitivity analysis are shown in Table 4.1.

Uncertainty analysis is also used to generate a spectrum of granulomas related to bacterial numbers (colony forming units, CFU) per granuloma over time (9, 102). The *in silico* granulomas are obtained without any bias in signal activation interval (δ) and signal strengths (β) towards any of the three pathways (STAT1, STAT3, and NFκB) (Figure 4.1E). The same parameter ranges were used to describe all three of the intracellular signaling pathways: signal activation interval parameters δ (e.g., [0.0001,0.1] min^{-1}, see Table 4.1), signal strength parameters β (e.g., [1, 25] min^{-1}, see Table 4.1). These ranges allow us to recapitulate the three typical expression regimes shown in Figure 4.1E (i.e., fast, intermediate, and sustained expression), as observed in many signaling pathway systems (84, 90). We used a standard t-test to compare the impact of the three different pathways (i.e., STAT1, STAT3 and NFκB) on granuloma development and maintenance.

4.2.7 Simulated Granuloma Classification

Recent NHP data demonstrated that the median bacterial levels at 4 weeks post-infection in individual granulomas was ~10^4 CFU, with a large variability (between 10^2 to 10^6 CFU per lesion) (21, 37). Beyond 4 weeks post-infection the bacterial loads decline to levels below ~10^4 CFU in both active and latent classifications of NHPs (21, 37). As our *in silico* model tracks infection a single granuloma level, we use total bacterial load (CFU) to classify infection outcome at the single granuloma level. Simulated granulomas classified as containment have bacterial loads below ~10^4 CFU at

200 days post-infection, while simulated granulomas that have bacterial loads above ~10^4 CFU at 200 days post-infection are classified as disseminating.

4.3 Results

The model described in this chapter has been submitted as part of the manuscript: Marino, S., Cilfone, N.A., Mattila, J.T., Linderman, J.J., Flynn, J.L., Kirschner, D.E. Macrophage polarization drives granuloma outcome during *Mycobacterium tuberculosis* infection. (2014). Outlined below are two of the important predictions and conclusions derived from the model described and constructed in this Chapter.

4.3.1 Granuloma Polarization Ratio Dynamics are Predictive of Granuloma Outcome

To understand how the spectrum of macrophage polarization influences granuloma outcome, we explored granuloma polarization ratios (R_{GP}) in granulomas classified as containment or dissemination (described in Materials and Methods). Figure 4.2 shows the mean R_{GP} of granulomas classified as containment or dissemination. There are no significant differences in R_{GP} in classified granulomas until day 60 post-infection. In granulomas classified as containment, R_{GP} increases towards more M1-polarized macrophages at days 70-80 post-infection. After 170 days post-infection, the granulomas classified as containment have a reduced R_{GP} demonstrate polarization back towards a more M2-like phenotype. Therefore, early macrophage polarization (~2 months post-infection) towards a more M1-like phenotype is necessary to control bacterial loads in granulomas. In addition, the granulomas that are able to contain bacterial loads have

more M2-like polarized macrophages at late stages of infection (~8 months post-infection) indicating reduced inflammation and possibly a resolving/healing granuloma.

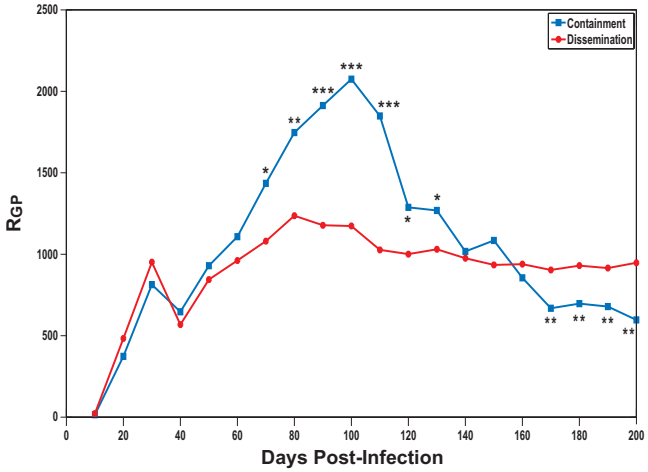

Figure 4.2 Granuloma Polarization Ratio dynamics over time for both contained and disseminated granulomas
The x-axis represents days post infection. The y-axis represents average Granuloma Polarization Ratio (R_{GP}) time courses for granulomas classified as containment or dissemination. Error bars are not shown for ease of illustration. The time points between day 70 and 130, as well as after day 170 show strong statistically significant differences between the two trajectories (* p<1e-2, ** p<1e-3, *** p<1e-4). Contained granulomas, N=377. Disseminated granulomas, N=1119.

4.3.2 NFκB Signal Activation Dynamics Characterize Granuloma Outcome

To understand why early polarization towards an M1-like phenotype is critical for control of bacterial loads in granulomas, we explored differences in intracellular signaling dynamics of STAT1, STAT3, and NFκB. We compared signal activation intervals (δ_{STAT1}, δ_{STAT3}, $\delta_{NF\kappa B}$) and signal activation strengths (β_{STAT1}, β_{STAT3}, $\beta_{NF\kappa B}$) between granuloma classifications (containment vs. dissemination). Shorter activation intervals indicate reduced periods of signal activation (e.g. reduced time the signal is turned on), which are regulated by proteolytic degradation or inhibition of the response species in the simplified signaling models (see Figure 4.1B-D). Higher signal activation strengths indicate increased number of activated molecules per stimulation event.

The model predicts that simulated granulomas with reduced NFκB activation intervals control granulomas more efficiently than granulomas with longer activation intervals (Figure 4.3A, p-value ~1e-8). In addition, simulated granulomas classified as containment have significantly shorter NFκB signal activation intervals than both STAT1 ($\delta_{NF\kappa B} >> \delta_{STAT1}$, p~7e-6) and STAT3 signal activation intervals ($\delta_{NF\kappa B} >> \delta_{STAT3}$, p~0.0115). Conversely, simulated granulomas classified as disseminating have significantly shorter STAT1 ($\delta_{NF\kappa B} << \delta_{STAT1}$, p~0.0018) and STAT3 ($\delta_{STAT3} > \delta_{NF\kappa B}$, p~0.05) activation intervals. Taken together, these model predictions indicate the importance of NFκB signaling in controlling macrophage polarization and eventually infection outcome at the individual granuloma level. Disrupting tightly regulated signal activation intervals can interfere with intracellular dynamics and inhibit protective responses (31, 32, 38, 39).

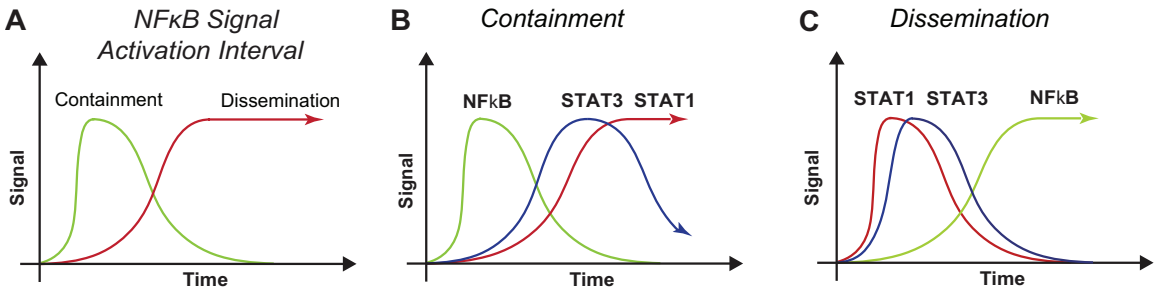

Figure 4.3 Gene transcription dynamics comparisons between and within granuloma outcomes
(A) Comparison of NFκB signal activation intervals between containment and dissemination classified granulomas. NFκB signal activation interval is shorter (less stable) in containment compared to dissemination (p<1e-8). (B) Comparison between signal activation intervals for the three different pathways in the containment scenario. NFκB signal activation interval is shorter (less stable) than STAT1 (p<8e-6) and STAT3 (p<0.012). (C) Comparison between signal activation intervals for the three different pathways in dissemination scenario. NFκB signal activation interval is longer (more stable) than STAT1 (p<2e-3) and STAT3 (p<0.05). The signal activation interval (δ) parameters are shown since they are significant parameters from sensitivity analysis.

4.4 Discussion

In this Chapter we extended our model of *Mtb* infection from Chapter 3 to further characterize the role of macrophage polarization in controlling infection outcome at the individual granuloma scale. We use simplified models of STAT1, STAT3, and NFκB intracellular signaling pathways, induced by IFNγ, IL-10, and TNF stimulation respectively, to drive macrophage functionality towards M1-like or M2-like phenotypes. Our model predicts the importance of early polarization towards M1-like phenotypes and shorter NFκB activation intervals are critical to control of infection at the individual granuloma scale.

Previous modeling studies have established the concept of *switching time* as the time needed to change from an M1-dominated macrophage phenotype to an M2-dominated phenotype in the granuloma environment (17, 40). Increased switching times (beyond ~50 days post-infection), wherein the polarization towards an M1-biased macrophage population was delayed, prevented early antimicrobial responses and allowed bacteria to gain an initial advantage. Additionally, if the switching time was delayed beyond a critical timeframe, dissemination of bacteria in the lung was more likely (17, 40). In this Chapter we investigated how the dynamic balance between pro- and anti-inflammatory cytokines translates into macrophage polarization and how polarization evolves over time in order to effectively control bacteria at the individual granuloma scale. Our model predicts that early (2-3 months post infection) polarization of macrophages towards an M1-like phenotype results in increased antimicrobial activity and leads to granulomas that are able to effectively control bacteria. Additionally, at late stages of infection (~5-6 months post-infection), granulomas that effectively contain

bacteria polarize more towards an M2-like phenotype consistent with infection resolution and healing. Granulomas unable to effectively control bacteria display mainly un-polarized macrophages, indicating that early M1 polarization is a significant mechanism that contributes to effective control of bacteria at the individual granuloma scale.

Differences in NFκB gene transcription dynamics between containment and dissemination granuloma outcomes suggest possible key regulatory mechanisms in driving protective immune responses (Figure 4.3). Granulomas that efficiently contain bacteria have shorter NFκB signal activation intervals compared to granulomas that are unable to control bacterial replication. Recent experimental work demonstrated that inhibition of NFκB activation (i.e., shorter signal activation intervals) decreases survival of *Mtb* in human macrophages (39). However, granulomas are significantly more complex structures in comparison with *in vitro* conditions with a much broader spectrum of macrophage polarization. Taken together with our model predictions, pharmacological targeting of the NFκB pathway may be an effective therapeutic strategy to transiently promote M1 polarization in granulomas and improve infection outcome at the individual granuloma scale (18).

In this Chapter we extended our model of TNF and IL-10 from the previous Chapter in order to better understand macrophage polarization at a single granuloma scale. This model demonstrates the extensibility of our *in silico* models of *Mtb* infection and how these models can lead to a better fundamental understanding of the immune responses leading to effective control of bacteria.

4.5 References

1. Flynn, J. L., J. Chan, and P. L. Lin. 2011. Macrophages and control of granulomatous inflammation in tuberculosis. *Mucosal Immunol.* 4: 271–8.

2. Ramakrishnan, L. 2012. Revisiting the role of the granuloma in tuberculosis. *Nat. Rev. Immunol.* 12: 352–66.

3. Shaler, C. R., C. N. Horvath, M. Jeyanathan, and Z. Xing. 2013. Within the Enemy's Camp: contribution of the granuloma to the dissemination, persistence and transmission of Mycobacterium tuberculosis. *Front. Immunol.* 4: 30.

4. Sierra-Filardi, E., C. Nieto, A. Domínguez-Soto, R. Barroso, P. Sánchez-Mateos, A. Puig-Kroger, M. López-Bravo, J. Joven, C. Ardavín, J. L. Rodríguez-Fernández, C. Sánchez-Torres, M. Mellado, and A. L. Corbí. 2014. CCL2 Shapes Macrophage Polarization by GM-CSF and M-CSF: Identification of CCL2/CCR2-Dependent Gene Expression Profile. *J. Immunol.* .

5. Spence, S., A. Fitzsimons, C. R. Boyd, J. Kessler, D. Fitzgerald, J. Elliott, J. N. Gabhann, S. Smith, A. Sica, E. Hams, S. P. Saunders, C. A. Jefferies, P. G. Fallon, D. F. McAuley, A. Kissenpfennig, and J. A. Johnston. 2012. Suppressors of Cytokine Signaling 2 and 3 Diametrically Control Macrophage Polarization. *Immunity* 24: 1–13.

6. Mantovani, A., A. Sica, S. Sozzani, P. Allavena, A. Vecchi, and M. Locati. 2004. The chemokine system in diverse forms of macrophage activation and polarization. *Trends Immunol.* 25: 677–86.

7. Qin, H., A. T. Holdbrooks, Y. Liu, S. L. Reynolds, L. L. Yanagisawa, and E. N. Benveniste. 2012. SOCS3 Deficiency Promotes M1 Macrophage Polarization and Inflammation. *J. Immunol.* 189: 3439–48.

8. Gordon, S., and P. R. Taylor. 2005. Monocyte and macrophage heterogeneity. *Nat. Rev. Immunol.* 5: 953–64.

9. Biswas, S. K., and A. Mantovani. 2010. Macrophage plasticity and interaction with lymphocyte subsets: cancer as a paradigm. *Nat. Immunol.* 11: 889–96.

10. Mosser, D. M., and J. P. Edwards. 2008. Exploring the full spectrum of macrophage activation. *Nat. Rev. Immunol.* 8: 958–69.

11. Gordon, S. 2003. Alternative activation of macrophages. *Nat. Rev. Immunol.* 3: 23–35.

12. Martinez, F. O., L. Helming, and S. Gordon. 2009. Alternative activation of macrophages: an immunologic functional perspective. *Annu. Rev. Immunol.* 27: 451–83.

13. Cilfone, N. A., C. R. Perry, D. E. Kirschner, and J. J. Linderman. 2013. Multi-Scale Modeling Predicts a Balance of Tumor Necrosis Factor-α and Interleukin-10 Controls the Granuloma Environment during Mycobacterium tuberculosis Infection. *PLoS One* 8: e68680.

14. Ray, J. C. J., J. L. Flynn, and D. E. Kirschner. 2009. Synergy between individual TNF-dependent functions determines granuloma performance for controlling Mycobacterium tuberculosis infection. *J. Immunol.* 182: 3706–17.

15. Segovia-Juarez, J. L., S. Ganguli, and D. Kirschner. 2004. Identifying control mechanisms of granuloma formation during M. tuberculosis infection using an agent-based model. *J. Theor. Biol.* 231: 357–76.

16. Fallahi-Sichani, M., M. El-Kebir, S. Marino, D. E. Kirschner, and J. J. Linderman. 2011. Multiscale computational modeling reveals a critical role for TNF-α receptor 1 dynamics in tuberculosis granuloma formation. *J. Immunol.* 186: 3472–83.

17. Marino, S., A. Myers, J. L. Flynn, and D. E. Kirschner. 2010. TNF and IL-10 are major factors in modulation of the phagocytic cell environment in lung and lymph node in tuberculosis: a next-generation two-compartmental model. *J. Theor. Biol.* 265: 586–98.

18. Fallahi-Sichani, M., D. E. Kirschner, and J. J. Linderman. 2012. NF-κB Signaling Dynamics Play a Key Role in Infection Control in Tuberculosis. *Front. Physiol.* 3: 170.

19. Marino, S., M. El-Kebir, and D. Kirschner. 2011. A hybrid multi-compartment model of granuloma formation and T cell priming in tuberculosis. *J. Theor. Biol.* 280: 50–62.

20. Ford, C. B., P. L. Lin, M. R. Chase, R. R. Shah, O. Iartchouk, J. Galagan, N. Mohaideen, T. R. Ioerger, J. C. Sacchettini, M. Lipsitch, J. L. Flynn, and S. M. Fortune. 2011. Use of whole genome sequencing to estimate the mutation rate of Mycobacterium tuberculosis during latent infection. *Nat. Genet.* 43: 482–6.

21. Lin, P. L., C. B. Ford, M. T. Coleman, A. J. Myers, R. Gawande, T. Ioerger, J. Sacchettini, S. M. Fortune, and J. L. Flynn. 2014. Sterilization of granulomas is common in active and latent tuberculosis despite within-host variability in bacterial killing. *Nat. Med.* 20: 75–9.

22. Giacomini, E., E. Iona, L. Ferroni, M. Miettinen, L. Fattorini, G. Orefici, I. Julkunen, and E. M. Coccia. 2001. Infection of human macrophages and dendritic cells with Mycobacterium tuberculosis induces a differential cytokine gene expression that modulates T cell response. *J. Immunol.* 166: 7033–41.

23. Shaw, T. C., L. H. Thomas, and J. S. Friedland. 2000. Regulation of IL-10 secretion after phagocytosis of Mycobacterium tuberculosis by human monocytic cells. *Cytokine* 12: 483–6.

24. Rateitschak, K., A. Karger, B. Fitzner, F. Lange, O. Wolkenhauer, and R. Jaster. 2010. Mathematical modelling of interferon-gamma signalling in pancreatic stellate cells reflects and predicts the dynamics of STAT1 pathway activity. *Cell. Signal.* 22: 97–105.

25. Lange, F., K. Rateitschak, B. Fitzner, R. Pöhland, O. Wolkenhauer, and R. Jaster. 2011. Studies on mechanisms of interferon-gamma action in pancreatic cancer using a data-driven and model-based approach. *Mol. Cancer* 10: 13.

26. Braun, D. a, M. Fribourg, and S. C. Sealfon. 2013. Cytokine Response Is Determined by Duration of Receptor and Signal Transducers and Activators of Transcription 3 (STAT3) Activation. *J. Biol. Chem.* 288: 2986–93.

27. Sharma, S., B. Yang, X. Xi, J. C. Grotta, J. Aronowski, and S. I. Savitz. 2011. IL-10 directly protects cortical neurons by activating PI-3 kinase and STAT-3 pathways. *Brain Res.* 1373: 189–94.

28. Naiyer, M. M., S. Saha, V. Hemke, S. Roy, S. Singh, K. V Musti, and B. Saha. 2013. Identification and characterization of a human IL-10 receptor antagonist. *Hum. Immunol.* 74: 28–31.

29. Qualls, J. E., G. Neale, A. M. Smith, M.-S. Koo, A. a DeFreitas, H. Zhang, G. Kaplan, S. S. Watowich, and P. J. Murray. 2010. Arginine usage in mycobacteria-infected macrophages depends on autocrine-paracrine cytokine signaling. *Sci. Signal.* 3: ra62.

30. Tay, S., J. J. Hughey, T. K. Lee, T. Lipniacki, S. R. Quake, and M. W. Covert. 2010. Single-cell NF-kappaB dynamics reveal digital activation and analogue information processing. *Nature* 466: 267–71.

31. Hao, S., and D. Baltimore. 2009. The stability of mRNA influences the temporal order of the induction of genes encoding inflammatory molecules. *Nat. Immunol.* 10: 281–8.

32. Basak, S., M. Behar, and A. Hoffmann. 2012. Lessons from mathematically modeling the NF-κB pathway. *Immunol. Rev.* 246: 221–38.

33. Sanderson, N. S. R., M. Puntel, K. M. Kroeger, N. S. Bondale, M. Swerdlow, N. Iranmanesh, H. Yagita, A. Ibrahim, M. G. Castro, and P. R. Lowenstein. 2012. Cytotoxic immunological synapses do not restrict the action of interferon-γ to antigenic target cells. *Proc. Natl. Acad. Sci. U. S. A.* 109: 7835–40.

34. Mattila, J. T., O. O. Ojo, D. Kepka-Lenhart, S. Marino, J. H. Kim, S. Y. Eum, L. E. Via, C. E. Barry, E. Klein, D. E. Kirschner, S. M. Morris, P. L. Lin, and J. L. Flynn. 2013. Microenvironments in tuberculous granulomas are delineated by distinct populations of macrophage subsets and expression of nitric oxide synthase and arginase isoforms. *J. Immunol.* 191: 773–84.

35. Bratt, J. M., A. a Zeki, J. a Last, and N. J. Kenyon. 2011. Competitive metabolism of L-arginine: arginase as a therapeutic target in asthma. *J. Biomed. Res.* 25: 299–308.

36. Morris, S. M. 2007. Arginine metabolism: boundaries of our knowledge. *J. Nutr.* 137: 1602S–1609S.

37. Lin, P. L., T. Coleman, J. P. J. Carney, B. J. Lopresti, J. Tomko, D. Fillmore, V. Dartois, C. Scanga, L. J. Frye, C. Janssen, E. Klein, C. E. Barry, and J. L. Flynn. 2013. Radiologic responses in cynomolgous macaques for assessing tuberculosis chemotherapy regimens. *Antimicrob. Agents Chemother.* .

38. Behar, M., D. Barken, S. L. Werner, and A. Hoffmann. 2013. The dynamics of signaling as a pharmacological target. *Cell* 155: 448–61.

39. Bai, X., N. E. Feldman, K. Chmura, A. R. Ovrutsky, W.-L. Su, L. Griffin, D. Pyeon, M. T. McGibney, M. J. Strand, M. Numata, S. Murakami, L. Gaido, J. R. Honda, W. H. Kinney, R. E. Oberley-Deegan, D. R. Voelker, D. J. Ordway, and E. D. Chan. 2013. Inhibition of nuclear factor-kappa B activation decreases survival of Mycobacterium tuberculosis in human macrophages. *PLoS One* 8: e61925.

40. Day, J., A. Friedman, and L. S. Schlesinger. 2009. Modeling the immune rheostat of macrophages in the lung in response to infection. *Proc. Natl. Acad. Sci. U. S. A.* 106: 11246–51.

Chapter 5

Interleukin-10 Controls Lesion Sterilization By Balancing Early Host-Immunity-Mediated Antimicrobial Responses With Tissue Damage During *Mycobacterium tuberculosis* Infection

The work in Chapter 5 has been submitted as: Cilfone, N. A., Ford, C.B., Marino, S., Mattila, J.T., Gideon, H.P., Flynn, J.L., Kirschner, D.E., Linderman, J.J. Interleukin-10 Balances Early Host-Immunity-Mediated Antimicrobial Responses and Tissue Damage to Control Lesion Sterilization During *Mycobacterium tuberculosis* Infection. (2014).

5.1 Introduction

Tuberculosis (TB), a deadly infectious disease caused by the bacterium *Mycobacterium tuberculosis* (*Mtb*), results in 1-2 million deaths per year (1). Control of the TB epidemic is limited by a complicated drug regimen, development of antibiotic resistance, and the lack of an effective vaccine against infection and disease. Understanding the complex host response to *Mtb* is essential for developing new and improved strategies to fight infection. Granulomas, organized collections of immune cells and bacteria that form in lungs and other organs, are an essential feature of the immune response to *Mtb* and serve as the central site of host-pathogen interaction. Cytokines are critical to coordinating an effective yet controlled immune response to *Mtb* within a granuloma. Human and animal models have demonstrated that the pro-inflammatory

cytokines tumor necrosis factor-α (TNF) and interferon-γ (IFN-γ) are essential to the host-response against *Mtb*; however, other cytokines also participate in the response (1–3). Our focus in this Chapter is on the regulatory cytokine interleukin-10 (IL-10), whose role remains unclear in *Mtb* infection.

IL-10, a regulatory cytokine, functions by inhibiting cytokine/chemokine production, preventing cellular apoptosis/necrosis, and altering macrophage activation phenotype (2, 4–6). IL-10 is produced by a spectrum of immune cells during infection, including macrophages, T-cell subsets, and neutrophils (7). Macrophages are a large source of IL-10 during *Mtb* infection, and activated-macrophage derived IL-10 may function to limit host-induced tissue damage (2, 8–10). *Mtb*-infected macrophages produce IL-10 when toll-like receptors and other pattern recognition receptors interact with *Mtb*-derived lipids and other molecules (1, 11–16). HN-878 and CH strains of *Mtb* induce greater production of IL-10 from macrophages than the lab strain H37Rv, which may be linked to increased pathogen virulence (1). However the question remains: Do *Mtb* strains that induce higher levels of IL-10 production disrupt the host antimicrobial response to prevent bacterial clearance. T cells, including CD4+, CD8+, and regulatory T cells can also produce ample quantities of IL-10 and may contribute to control of host damage (17–22). CD4+ T cell clones from human BAL fluid with active TB primarily produced interferon-γ and IL-10 upon re-stimulation (23, 24). Recently, neutrophils have been identified as a possible source of IL-10, although the level of production is uncharacterized; they do not produce IL-10 when stimulated with *Mtb* antigens, but function in those conditions to stimulate IL-10 production from macrophages (25–27).

Due to the spectrum of cellular sources it has been difficult to determine the primary source of IL-10 in a granuloma and its main functional role in experimental systems.

IL-10 may dampen the strength of the immune response to *Mtb*, minimizing lung damage and pathology (1, 7, 8, 28). A central feature of many TB granulomas is an acellular caseous necrotic core (3, 29). Caseous necrosis provides the opportunity for airway erosion and can lead to calcification and fibrosis of lesions, both highly damaging to host lung tissue (29). Both host-immunity and pathogenic mechanisms, including *Mtb*-induced macrophage bursting, TNFR1-induced apoptosis/necrosis, Fas ligand-induced cell death, perforin/granulysin from cytotoxic T cells, and reactive nitrogen/oxygen species (RNS and ROS) produced within macrophages, contribute to caseous necrosis (29–35). IL-10 has been proven to limit macrophage apoptosis/necrosis in the context of *Mtb* infection, but how that translates to prevention of tissue damage is still unclear (6, 29, 30, 33, 35–43). In addition, what effect does limiting tissue damage have on the success of the antimicrobial response? This question has been difficult to answer in an experimental setting due to limitations of detection methods and differences among animal models.

Most *in vivo* investigations into the role of IL-10 during *Mtb* infection have been performed in murine models. However, studies using *Il10*$^{-/-}$ mice have shown contradicting results. Initial reports demonstrated no difference in bacterial load, while more recent studies have shown increased inflammatory responses and reduced bacterial burdens in both lungs and spleen (1, 44, 45). Additionally, some reports indicated reduction in bacterial load was associated with increased pathology and inflammatory cytokines (28). Transgenic mice that overexpress IL-10 have significantly higher

bacterial loads that normal mice (46, 47). Abrogation of IL-10 signaling in the CBA/J murine model using anti-IL-10R antibodies reduced bacterial burdens in the lungs and enhanced host inflammatory-responses (1, 44). Although these results lend insight into the role of IL-10 during the immune response to *Mtb,* murine models of TB lack many characteristics of human lesions, including the ability to recapitulate a true latent state of infection, the characteristic granuloma organization, and the spectrum of cell types producing IL-10 (48–50). The murine model of *Mtb* infection is progressive with bacterial burdens inconsistent with human and non-human primate infections (51). Therefore, conclusions drawn about the influence of IL-10 on bacterial load in the murine model may not be reflective of TB in humans. In addition, studies of the effects of IL-10 on bacterial loads at a single granuloma scale have not been performed in the murine model of TB. Thus, the question of how IL-10 influences bacterial loads at a single granuloma level in a model of TB with accurate *Mtb* dynamics remains unanswered.

Recent studies in a non-human primate (NHP) model of *Mtb* have indicated large variability among lesions within a single host (51). Genomes (chromosomal equivalents, or CEQ, i.e. total chromosomal DNA in lesions) from non-viable *Mtb* degrade very slowly in lesions (estimated at maximum of ~4% per day), and thus measuring CEQ using PCR on a housekeeping gene provides an estimate of total bacterial burden (both viable and dead bacteria) in a lesion. The ratio of colony-forming units (CFU, i.e. viable bacteria) to CEQ reflects antimicrobial activity at the individual lesion scale (51). In lesions from macaques with either active or latent infection, the killing capacity of the immune response is similar at the individual granuloma scale, with a significant number of sterile lesions (a lesion with no detectable bacteria) existing in both outcomes. This

heterogeneity at the lesional scale makes it difficult to identify predictors of disease outcome, but is critical to recapitulating the immune response in humans. What remains unanswered is how cytokines could control the sterility of lesions. Specifically, does IL-10 control antimicrobial activity thus determining the frequency of sterile lesions? Although the NHP model of TB is the most representative experimental model of human TB, studies investigating the role of IL-10 during *Mtb* infection have not yet been reported in this model.

We use an *in silico* approach to investigate the role of IL-10 in controlling antimicrobial activity, lesional sterility, and tissue damage during *Mtb* infection. We utilize our hybrid agent-based model (*GranSim*) from Chapter 3, which includes IL-10 receptor-ligand dynamics, to understand how IL-10 dynamics control infection outcome at the individual granuloma scale (8). We first extend and validate *GranSim* based on new data on CFU trajectories from the NHP model of TB (51). We then use *GranSim* to probe the role of IL-10 at the lesional scale by performing complete IL-10 knockouts, cell-specific IL-10 knockouts, and perturbations of lesional IL-10 levels. Simulations predict that IL-10 restricts antimicrobial activity during the early adaptive immunity phase, preventing sterilization of lesions and inhibiting host-induced tissue damage. We predict that activated macrophage-derived IL-10 is the most important source of IL-10 in our model, balancing lesion sterility and host-induced tissue damage. Lastly, we describe how increased secretion of IL-10 from infected macrophages can be an effective immune-evasion strategy by shifting control of bacterial dynamics, through antimicrobial responses, within a granuloma from host to pathogen. These findings provide new

avenues for testing in animal systems and suggest important mechanisms that could be targets for adjunctive therapy in humans with TB.

5.2 Methods

5.2.1 Overview

We developed a new version of *GranSim* in Chapter 3*,* a hybrid agent-based model (ABM) of *Mtb* infection, that incorporates IL-10 and TNF dynamics across multiple temporal and spatial scales (8, 52, 53). We are now able to calibrate this model with new data derived from an NHP model of TB infection on CFU per lesion (51, 54–56). We subsequently validate the model by comparing model predictions of bacterial doubling time against measured values in the NHP model and perform virtual deletions (TNF and IFN-γ) of previously identified essential mediators (51, 57, 58). As this model now incorporates detailed descriptions of both IL-10/IL-10R and TNF/TNFR-associated molecular interactions and a representation of *Mtb* dynamics similar to humans, it is poised to predict the effects of IL-10 at a single granuloma scale. We perform *virtual experiments* that are currently difficult or infeasible in animal models of TB, including cessation of IL-10 production from specific cell types and tracking the temporal dynamics of sterile lesions. Furthermore, we explore the effects of increased production of IL-10 derived from infected macrophages. Details for these virtual experiments are given below.

5.2.2 Hybrid Multi-Scale Agent Based Model of Mtb Infection

Our multi-scale ABM of *Mtb* infection from Chapter 3, *GranSim*, describes immune processes over three different scales: tissue, cellular, and molecular (8, 52, 53). Briefly, at the tissue and cellular scale, *GranSim* includes macrophages and T-cells (agents), each with multiple states: resting macrophages, infected macrophages, chronically infected macrophages, activated macrophages, pro-inflammatory T-cells, cytotoxic T-cells, and regulatory T-cells. Included in the model are three bacterial sub-populations: intracellular *Mtb*, extracellular *Mtb*, and non-replicating *Mtb*. The agents and bacterial population interactions are described by a well-defined set of rules and interactions between immune cells and *Mtb* in the lung and can be found in (8, 52, 53). At the molecular scale we capture receptor-ligand binding and trafficking, as well as the secretion, diffusion, and degradation of the cytokines IL-10 and TNF (see Chapter 3 for details). We assume IL-10 and TNF binding and internalization directly modulate cellular processes such as down regulation of TNF production (8). Cellular sources of IL-10 include infected macrophages, activated macrophages, and regulatory T-cells. As neutrophils appear to increase IL-10 production rates from infected macrophages, we do not explicitly model neutrophil IL-10 production (25–27). We link molecular scale events to cellular and tissue scale events by allowing dynamics within each scale to influence behavior on other scales (e.g. TNF-induced apoptosis/necrosis) (8). The ABM is two dimensional (2D) and represents a 4 mm^2 cross-section of lung tissue. Infecting a single macrophage with *Mtb* leads to the development of ~1 mm diameter lesions, which falls into the range of individual granuloma sizes observed in the NHP model (1-5mm) of TB (54, 56). The ABM can reproduce larger lesion sizes by simulating a larger cross-section

of lung tissue (e.g. 16 mm^2) (unpublished data). A key feature of our ABM is the flexibility to include data as they become available; therefore we update some *GranSim* rules from Chapter 3 to better reflect current biological knowledge of the immune response to *Mtb* (Table B.1 in Appendix B).

5.2.3 Non-Human Primate Infection, Classification, CFU, and CEQ

In previously published work (51, 54–56), 32 healthy cynomolgus macaques (*Macaca fascicularis*) were infected with ~25 CFU of the Erdman strain of *Mycobacterium tuberculosis* via bronchoscopic instillation. Lesions were excised at various time points (between 26 and 296 days post-infection) where bacterial burden and chromosomal equivalents were measured (Table B.2 in Appendix B). Bacterial burden was measured by enumeration of colonies (CFU) after 3 weeks of culture on 7H10 agar. Sterile lesions were defined as lesions with no detectable colonies after 6 weeks of culture (see (51) for justification). Chromosomal equivalents (CEQ) were measured by real-time quantitative PCR of isolated *Mtb* genomic DNA from lesions. Full descriptions of NHP infection and data collection methods, as well as the data used in this Chapter, can be found in (51, 54–56).

5.2.4 Calculation of CFU and CEQ

The sum of intracellular *Mtb*, extracellular *Mtb*, and non-replicating *Mtb* is the total bacterial burden, and is comparable to CFU in the NHP model of *Mtb* infection. Thus, we refer to all total bacterial burden measurements generated by *GranSim* as CFU. Since CFU data collected in the NHP model of TB are from whole lesions, we scale our

2D model-generated CFU results to 3D to allow for direct comparison. For the scaling, we calculate the minimum radius of a granuloma sphere that encompasses the entire CFU population and determine an appropriate 2D to 3D scaling factor. Scaled CFU data is only shown when comparing to NHP data. We measure CEQ in *GranSim* by tracking each bacterium division. For simplicity, we assume no degradation of CEQ in the lesion (51). The ratio CFU/CEQ reflects the degree of killing, with smaller values reflecting a more efficient bactericidal response.

5.2.5 Calculated Measures of Inflammation and Tissue Damage

We report *TNF concentration* (pg/mL) as a general biomarker of inflammation in a granuloma. We calculate average TNF concentrations by summing soluble TNF in all compartments contained within the lesion and converting to a concentration using the volume of a 2D grid compartment (assuming a uniform depth of the 2D simulation environment of one compartment; similar to a planar sheet). *GranSim* measures caseous necrosis as a proxy for tissue damage by monitoring levels of infected macrophage bursting, Fas/FasL killing by T cells, perforin/granulysin killing by cytotoxic T cells, activated macrophage death (high levels of ROS/RNS), and TNF-induced apoptosis/necrosis within each grid compartment. *GranSim* considers TNF-induced apoptosis/necrosis to be a general process of induced cell-death and does not differentiate between apoptosis, necrosis, necroptosis, or apoptotic necrosis, thus TNF-induced cell death contributes to caseous necrosis (29, 30). Although this is not a perfect measure of tissue damage, caseous necrosis results as a consequence of infection and inflammation can be detrimental to host tissues. A grid compartment is classified as caseous necrotic

when the number of aforementioned events passes a threshold defined by a model parameter (Table B.3 in Appendix B), the idea being that after a certain number of these events occur, the tissue in that compartment is likely to become caseous necrotic. We also use two previously established measures to examine tissue damage: the ratio of infected macrophage apoptosis/necrosis to healthy macrophage apoptosis/necrosis, $R_{apoptosis}$, and a modified version of the *Host-Pathogen Index* (H.P.I) from Chapter 3, which is a combined metric of CFU and healthy macrophage apoptosis/necrosis scaled between zero and one (8, 53). These latter measures are examined fully in the Appendix B.

5.2.6 Calculation of Instantaneous Mtb Doubling Time

We calculate an instantaneous doubling time of *Mtb* by assuming that during the first 20 days of infection the bacteria is able to replicate freely following an exponential growth curve (51). Thus, the instantaneous doubling time (t_d) is calculated by:

$$t_d = \frac{ln(2)}{ln\big(CEQ(t)\big)}t \qquad (Eqn. 5.1)$$

Here, t is the time point of interest post-infection and CEQ(t) is the CEQ at the time point of interest post-infection. Comparisons of doubling times beyond the onset of the adaptive immunity (~25-35 days post-infection) cannot be drawn since the CFU and CEQ curves do not follow classical exponential growth due to host bactericidal processes (51).

5.2.7 Classification of Lesions

We classify simulated lesions at 200 days post-infection into 2 outcomes at the granuloma scale: *sterile lesions*, and *non-sterile lesions* (59). *Non-sterile lesions* are defined as lesions that have a non-zero CFU at 200 days post-infection. *Non-sterile*

lesions can be split into two types: *controlled growth* or *uncontrolled growth. Controlled growth* is defined as robust control of *Mtb* within a lesion with CFU levels comparable to lesions in the NHP model of TB (51, 54, 60, 61). *Uncontrolled growth* is defined by an immune response incapable of limiting the growth of *Mtb* in a lesion. In the NHP model of TB, this corresponds to lesions that either split into multiple lesions or disseminate. The pathogen is able to replicate freely and the CFU is well above levels in the *controlled growth* outcome. *Sterile lesions* are defined as the complete removal of live *Mtb* in the lesion (zero CFU) at any time post inoculum. The classification of a lesion at day 200 is used for any previous time points where data is separated by outcome (e.g., a lesion that becomes sterile at day 150 is always counted in the sterile category).

5.2.8 Virtual Deletion of IL-10 (Complete Il10$^{-/-}$)

Included in the model are multiple cellular sources of IL-10: infected macrophages, chronically infected macrophages, activated macrophages, and regulatory T-cells. We perform virtual IL-10 deletion simulations that mimic an experimental *Il10*$^{-/-}$ phenotype by setting IL-10 synthesis by all cell-types to zero at the beginning of a simulation and simulating 200 days of infection. We report: CFU/lesion at 200 days post-infection, CFU/CEQ at 25, 50, 100, and 200 days post-infection, TNF concentrations at 25, 35, 45, 55, 100, and 200 days post-infection, and caseous necrosis per lesion at 25, 35, 45, 55, 100, and 200 days post-infection. An advantage of our *in* silico approach is that we can analyze sterile granulomas from WT simulations compared to sterile granulomas from IL-10 deletion simulations. We report the fraction of infected macrophages that undergo apoptosis, fraction of resting macrophages that become NFκB

activated, the number of macrophages that have been exposed to *Mtb*, and CFU/lesion at day 45 post-infection. We then create an IL-10 deletion parameter set that has reduced rates of NFκB activation and TNF-induced apoptosis (termed IL-10 K/O Low Apop/Act) in order to understand the underlying processes leading to lesion sterilization.

5.2.9 Virtual Transgenic IL-10

We perform virtual IL-10 transgenic experiments by increasing or decreasing the IL-10 production rate of each cellular source of IL-10. Rates from 1/5 to 5 times the normal production rate are tested, with production from all cell types changed by the same factor. We then simulate 200 days of infection post inoculum. We report CFU/lesion and CFU/CEQ at 200 days post-infection, while TNF concentrations at reported at 35 days post-infection and caseous necrosis per lesion are reported at 50 days post-infection. In addition, we report the fraction of bacterial populations (intracellular, extracellular, non-replicating) in non-sterile granulomas at 200 days post-infection. We use these time points of interest due to insights from the virtual deletion of IL-10.

5.2.10 Virtual Deletion of Cell-Specific IL-10 Sources

We perform virtual IL-10 deletions of specific cellular sources by setting IL-10 production from those cells to zero at the beginning of a simulation. Three cell-specific IL-10 deletions are examined: infected macrophage $Il10^{-/-}$ (combined deletion of infected macrophages and chronically infected macrophages), activated macrophage $Il10^{-/-}$, and regulatory T-cell $Il10^{-/-}$. We then simulate 200 days of infection post inoculum. We report: CFU/lesion at 200 days post-infection, CFU/CEQ at 25, 50, 100, and 200 days

post-infection, TNF concentrations at 50 and 100 days post-infection, and caseous necrosis per lesion at 50 and 100 days post-infection.

5.2.11 Virtual Variability in Mtb Strain Induced IL-10

Multiple clonal lineages of *Mtb* have evolved over the long course of its existence (13). Each of these lineages has significant inter-strain variability in levels of induction of IL-10 in macrophages (11–15). In our model, when a macrophage becomes infected with *Mtb* it begins synthesizing IL-10 at a specific rate. We modulate the synthesis rate of IL-10 from infected macrophages (10-fold reduction to 1000-fold increase from its baseline level), while keeping the rates of IL-10 synthesis from activated macrophages and regulatory T cells identical (at baseline rates). In addition, this also explores the indirect effects of neutrophils as they have been shown to increase infected macrophage production of IL-10 (25–27). We then simulate 200 days of infection post inoculum. Changes in infected macrophage IL-10 synthesis rate are reflected in the fractional synthesis rate (f_{Mi}), which is defined as:

$$f_{Mi} = \frac{r_{Mi}}{r_{Mi} + r_{Ma} + r_{Tr}} \qquad (Eqn.\ 5.2)$$

Here, r_{Mi} is the infected macrophage IL-10 synthesis rate, r_{Ma} is the activated macrophage IL-10 synthesis rate, and r_{Tr} is the regulatory T cell IL-10 synthesis rate. We report: percentage of IL-10 derived from infected macrophages, CFU/lesion, CFU/CEQ, number of activated macrophages, and number of infected macrophages at 200 days post-infection.

5.2.12 Uncertainty and Sensitivity Analysis

Uncertainty and sensitivity analysis is used to identify IL-10 model parameters that have significant effects on model outputs. We use Latin hypercube sampling (LHS) to simultaneously vary multiple model parameters and sample the parameter space (62). Partial rank correlation coefficients (PRCCs) quantify the effects of varying each parameter on non-linear outputs, where a PRCC of -1 represents a perfect negative correlation and a PRCC of +1 represents a perfect positive correlation. PRCCs are differentiated based on a students t-test to indicate significance. In this Chapter we generate 250 unique parameter sets, each of which are replicated four times, yielding 1000 simulations. Average values of model outputs (e.g. CFU, CFU/CEQ) are used to calculate PRCC and p-values.

5.2.13 Computational Platform

Our ABM is constructed using the C++ programming language, Boost libraries (distributed under the Boost Software License – www.boost.org), and the Qt framework for visualization (distributed under GPL – www.qt.digia.com). The ABM is cross-platform (Macintosh, Windows, Unix) and can be run with or without our visualization software. Simulations were performed on the Flux computing cluster, provided by Advanced Research Computing at the University of Michigan, and OS X based multi-core personal computers (Intel Quad Core i7 Apple Macbook Pro). Data manipulation was carried out in MATLAB R2012a (Natick, MA). Plots and statistical tests were created using GraphPad Prism 6 (La Jolla, CA).

5.3 Results

5.3.1 Model Calibration and Validation with Non-Human Primate (NHP) Data

We first calibrate our model with new CFU per lesion data from the NHP model of TB. We utilize a previously published data set derived from 32 NHPs in which CFU per lesion data has been collected between 28 and 296 days post-infection (51, 54–56, 61). Each NHP has 3-37 lesions with non-sterile lesions containing ~10 to ~10^6 CFU per lesion. We re-calibrated our previously published version of *GranSim*, by varying multiple model parameters (Table B.3 in Appendix B) in order to best fit the temporal median CFU per lesion data (8). Sterile lesions were excluded from both the NHP derived data set and the model-generated data set during model calibration of median CFU to minimize effects on median CFU of non-sterile lesions. We identify a baseline parameter set (hereafter noted as the wild type, WT, parameter set) that replicates the peak median NHP CFU per lesion data at day 28 and leads to robust control of median CFU per lesion beyond 100 days post-infection (Figure 5.1A). The percentage of model-generated sterile lesions at 200 days post-infection (~15-30%, N=100) is consistent with the number of sterile lesions observed in NHPs (~33%, N=476). Simulated lesions are able to recapitulate histological observations from NHP lesions, wherein infected macrophages and caseation that are located primarily in the core of the lesion are surrounded by an outer cuff of healthy macrophages and a peripheral cuff predominantly comprised of lymphocytes (54, 63, 64). In our model the cellular spatial configuration of the lesion arises from emergent behavior as a consequence of the model rules.

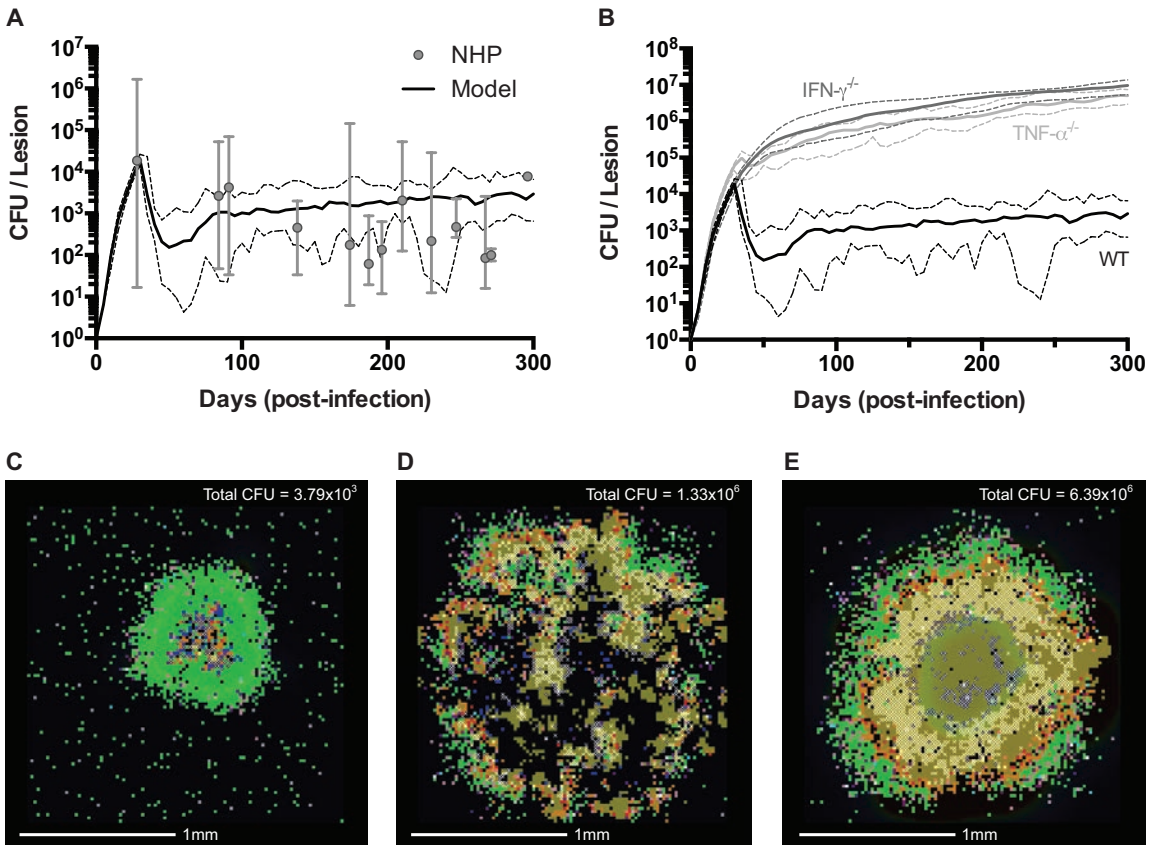

Figure 5.1 Model calibration and validation of simulated lesions
A. Comparison of scaled CFU per lesion between best-fit WT simulated lesions (N = 25) (median – solid black line, min/max – dashed black lines) and NHP data collected between 28 and 296 days post-infection (51) (N = 32) (median – grey filled circles, min/max – grey error bars). B. Comparison of scaled CFU per lesion for simulated lesions of TNF-α (median – light grey line, min/max – dashed light grey lines) and IFN-γ (median – dark grey line, min/max – dashed dark grey lines) deletions compared to WT simulated lesions (median – solid black line, min/max – dashed black lines) (N = 20). C. Snapshot of a WT lesion at 200 days post-infection. D. Snapshot of a TNF-α deletion lesion at 200 days post-infection. E. Snapshot of an IFN-γ lesion at 200 days post-infection. Total scaled CFU for each lesion is indicated in the upper corner. Snapshot legend colors as follows: resting macrophages (green), infected macrophages (orange), chronically infected macrophage (red), activated macrophage (dark blue), pro-inflammatory T cell (pink), cytotoxic T cell (purple), regulatory T cell (aqua), extracellular bacteria (brown), and caseation (cross-hatch). These same colors are used for all subsequent images.

We validate our WT parameter set against two data sets: (1) instantaneous bacterial doubling times calculated from CEQ in the NHP model of TB and (2) deletion of TNF and IFN-γ. Comparison of instantaneous *Mtb* doubling times between simulated (Eqn. 5.1) and NHP lesions show good agreement, with the median simulated doubling times falling within the min-max range of NHP doubling times for both 10 and 20 days

post-infection (Table 1). We then simulate virtual deletions of TNF and IFN-γ at the initialization of infection. Observations in the NHP and murine models of TB have indicated that removal of TNF causes lesions to function poorly, leading to elevated bacterial loads and dissemination (57, 65). Similarly, removal of IFN-γ causes extensive tissue damage with an immune response that is unable to restrict bacterial growth (58). TNF and IFN-γ virtual deletions show an approximately 1000-fold increased in median CFU per lesion (Figure 5.1B) with large, disseminating lesions in the TNF deletion (Figure 5.1D) and extensive tissue damage in the IFN-γ deletion (Figure 5.1E). These simulations mark the first time a computational model of *Mtb* infection has been calibrated and validated with temporal CFU data and apparent *Mtb* doubling times from the non-human primate model. Given this ability of our computational model to recapitulate bacterial dynamics from an experimental model that has comparable bacterial dynamics and clinical classifications as human *Mtb* infection (51, 54, 63), we are now in a unique position to predict the role of IL-10 in modulating antimicrobial activity and granuloma sterility.

Table 5.1 Median instantaneous *Mtb* doubling times in individual lesions

Time (days post infection)	NHP Doubling Time[1] (1/days)	Model Doubling Time[2] (1/days)
10	1.83 (1.59 – 2.18)	1.73 (1.62 – 2.09)
20	1.87 (1.76 – 2.20)	2.09 (1.99 – 2.29)

Parentheses represent the minimum and maximum calculated doubling time for both NHP (N = 32) and ABM data (N = 100) sets
[1] Instantaneous doubling times estimated using median CEQ per lesion as defined in (51)
[2] Instantaneous doubling times estimated using CEQ per lesion and an exponential growth model defined from t(0) to t(t)

5.3.2 Reduced Bacterial Loads in IL-10 Knockouts is Due to Increased Sterilization of Lesions

In order to understand the role of IL-10 during *Mtb* infection at the lesional scale, we simulated a virtual IL-10 deletion (referred to as IL-10 K/O) at the initialization of infection by setting all IL-10 synthesis rates to zero. Measured simulation outputs

included CFU per lesion, CFU/CEQ, fraction of lesions that become sterile, average TNF concentration per lesion, and caseous necrosis per lesion. We analyze model outputs for differing virtual lesion outcomes (sterile vs. non-sterile) in both WT and IL-10 K/O lesions to better understand factors driving infection outcome. Mean CFU per lesion at day 200 was unchanged in IL-10 K/O non-sterile lesions compared to WT non-sterile lesions (Figure 5.2A). Strikingly, we observed a significant change in the number of lesions achieving sterility, with an ~2-fold increase in the number of sterile lesions in the IL-10K/O case (Figure 5.2A). When sterile lesions are included in the analysis of mean CFU per lesion at day 200 we observe a reduction in bacterial burden of ~1.75-fold (Figure 5.2A). Therefore, our model predicts that reduced bacterial loads in IL-10 K/O scenarios are mainly due to an increased number of lesions that are able to sterilize and not an overall reduction in bacterial load across all lesions.

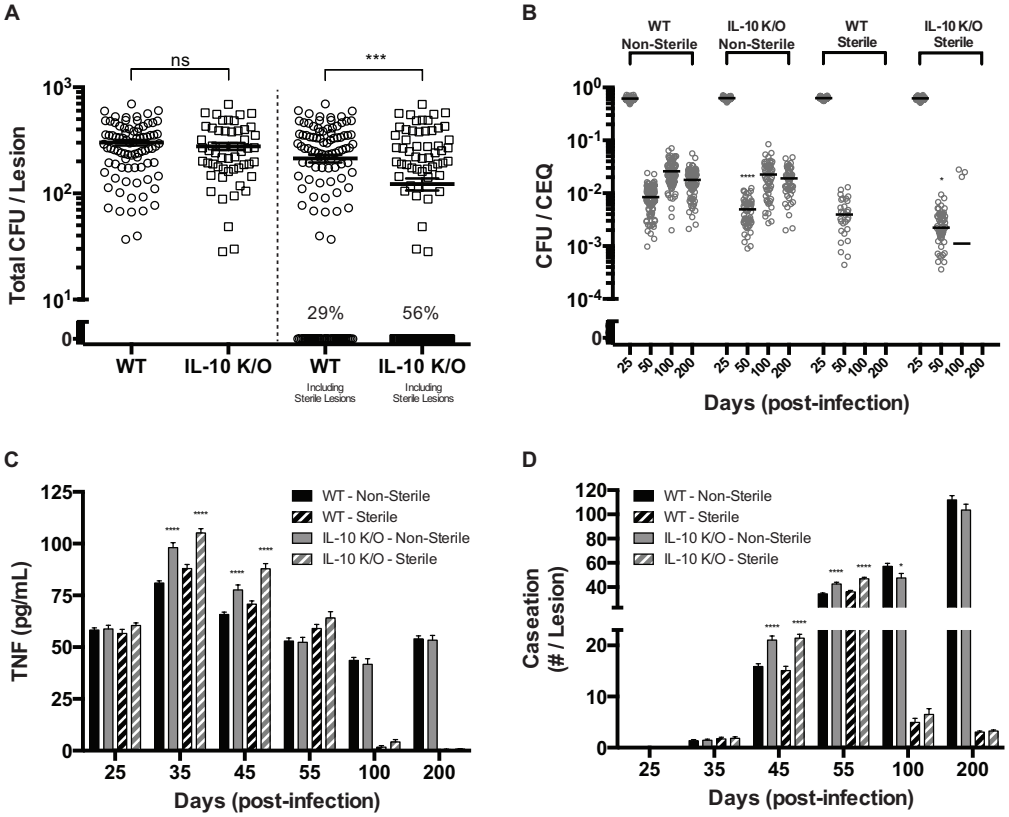

Figure 5.2 Virtual IL-10 deletions demonstrate increased sterilization of lesions and control of the early immune response
A. CFU for WT and IL-10 deletion (IL-10 K/O) lesions at 200 days post-infection. Individual circles and squares represent individual lesions. Lines indicate mean values. Percent of lesions becoming sterile by 200 days (out of 100 simulations) is indicated. B. CFU/CEQ for outcome-specific WT and IL-10 K/O lesions. Outcomes are grouped as non-sterile or sterile. Individual circles represent individual lesions. Lines indicate mean values. C-D. Average lesion TNF-α concentration and caseation for WT (black bars) and IL-10 K/O (grey bars) lesions. Non-sterile lesions are displayed as solid bars and sterile lesions are displayed as striped bars. Bars are representative of mean values with error bars showing SEM. For all panels, comparisons are made between the same granuloma classifications (e.g. non-sterile vs. non-sterile): * $p \leq 0.05$, ** $p \leq 0.01$, *** $p \leq 0.001$, **** $p \leq 0.0001$, N = 100.

5.3.3 IL-10 Controls the Early Immune Response to Mtb at a Lesional Scale

Peak CFU (~10^3-10^4) and CEQ (~10^4) were comparable between WT and IL-10 K/O lesions, occurring 4 weeks post-infection (Figure B.1A-D in Appendix B). Mean CFU/CEQ is ~2-fold lower for IL-10 K/O lesions at days 50, 100, and 200 post infection, indicating increased antimicrobial activity (Figure B.1E in Appendix B). However, when sterile and non-sterile IL-10 K/O lesions are analyzed separately, it becomes apparent that the increased antimicrobial activity is transient. Sterile lesions and non-sterile lesions have lower CFU/CEQ at day 50, compared to WT lesions (~4-fold vs. ~1.75-fold) with no changes to CFU/CEQ levels after day 50 (Figure 5.2B). Increases in antimicrobial activity are coupled to an increased early inflammatory response and increased tissue damage, with elevated levels of TNF at days 35 and 45 (Figure 5.2C) and an ~1.2-1.5-fold increase in caseous necrosis at day 45 and 55 (Figure 5.2D). These results indicate that increases in antimicrobial activity due to IL-10 deletion occur mainly during the early immune response, helping promote sterilization at the cost of early tissue damage. As infection progresses, the levels of caseous necrosis stabilize as healing and tissue remodeling can occur. This occurs since the total CFU in the lesion has declined to significantly lower values than in the early stages of infection and less antimicrobial activity is necessary (Figure 5.1B). Taken together, our model predicts that IL-10

transiently limits early antimicrobial activity, in order to simultaneously limit host-inflammation-induced tissue damage at the individual lesion scale (Figure B.3A in Appendix B). Transient limitation of antimicrobial activity by IL-10 prevents lesions from sterilizing with increased tissue damage.

5.3.4 Increased Sterilization of Lesions in IL-10 Deletions is a Result of Small Differences in Antimicrobial Activity of the Early Immune Response

An advantage of our computational model as compared to experimental systems is that we can track the entire time course of individual lesions. Unlike experimental systems, where determining what antimicrobial processes lead to sterilization of a lesion is very difficult, our model retains the entire history of the immune response in sterilized lesions. Therefore, we sought to understand what immune mechanisms contribute to the increased percentage of sterile lesions in the virtual IL-10 deletions. We compared antimicrobial mechanisms between WT and IL-10 K/O sterile lesions at 45 days post-infection, when the antimicrobial response is the strongest. We noticed small, yet significant, differences in the fraction of infected macrophages that undergo apoptosis (6% increase in IL-10 K/O sterile lesions) and the fraction of $NF\kappa B^{+}$ macrophages (15% increase in IL-10 K/O sterile lesions) (Figure 5.3A). These small increases in antimicrobial activity limit healthy macrophage exposure to *Mtb* (Figure 5.3A), which prevents the bacteria from residing in the intracellular niche where it is more difficult to kill. The mean bacterial load is significantly lower in IL-10 K/O lesions, 27 CFU vs. 48 CFU, and therefore small changes in antimicrobial activity lead to increased sterilization in IL-10 knockouts (Figure 5.3A). In order to verify that changes in antimicrobial activity

were causing the increased frequency of sterile lesions, we created an IL-10 deletion parameter set that has reduced rates of NFκB activation (decreased by 6%) and TNF-induced apoptosis (decreased by 15%), termed IL-10 K/O Low Apop/Act. Using this parameter set, the percentage of sterile lesions returns to WT levels (Figure 5.3B). Therefore, our model predicts that increased frequency of lesion sterilization is due to small changes in antimicrobial activity that prevents the bacteria from persisting in macrophages and infecting new macrophages.

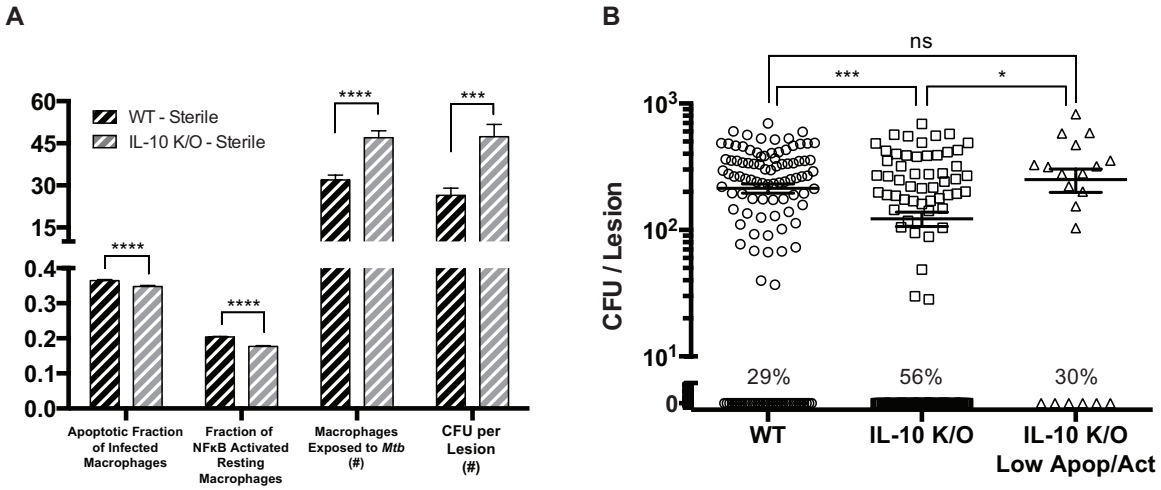

Figure 5.3 Comparison of simulated sterile lesions between WT and IL-10 deletions
A. Apoptotic fraction of infected macrophages, fraction of NFκB activated resting macrophages, number of macrophages exposed to *Mtb*, and CFU per lesion at 45 days post-infection for WT (black bars) and IL-10 K/O (grey bars) granulomas. B. CFU for WT, IL-10 K/O, and IL-10 K/O Low Apop/Act (decreased rates of apoptosis and NFκB activation) lesions at 200 days post-infection. Individual dots represent individual lesions. Lines indicate the mean values. Percentage of lesions becoming sterile by 200 days is indicated. Bars are representative of mean values with error bars showing SEM. For all panels: * $p \leq 0.05$, ** $p \leq 0.01$, *** $p \leq 0.001$, **** $p \leq 0.0001$, N = 100 for WT and IL-10 K/O simulations. N = 20 for IL-10 K/O Low Apop/Act simulations.

5.3.5 Modulating Total IL-10 Concentrations Demonstrates Control of Antimicrobial Activity and Host-Immunity Derived Tissue Damage

Our predictions above suggest that modulating concentrations of IL-10 might be a successful way to increase sterilization of lesions. To test this, we modulated the total concentration of IL-10 within a lesion. An advantage of our modeling approach is the

ability to finely control levels of IL-10 in lesions, which proves difficult in experimental systems. We preform virtual transgenic experiments by increasing or decreasing the synthesis rate of IL-10 simultaneously in all cell populations (5-fold reduction to 5-fold increase in small increments). A 5-fold increase in total IL-10 production rate increases the mean CFU per lesion at day 200 from ~300 to ~10,000 (shifting lesion classification from *controlled growth* to *uncontrolled growth*), while a 5-fold decrease in IL-10 production rate decreases the mean CFU per lesion to ~50 (Figure 5.4A). As IL-10 production increases, no sterile lesions are observed; decreasing total IL-10 production leads to an eventual ~9-fold increase in the number of sterile lesions (chi-squared trend test, $p<0.0001$) (Figure 5.4A). In addition, CFU/CEQ at day 200 is directly correlated with IL-10 levels (Figure 5.4B), while levels of TNF at day 35 (Figure 5.4C) and caseous necrosis at day 50 (Figure 5.4D) are inversely correlated with IL-10 levels. However, our model predicts that changing levels of IL-10 production cause the bacterial populations to change in lesions that do not sterilize (Figure 5.4E). At 200 days post-infection, non-sterile lesions with reduced IL-10 production have larger bacterial fractions of non-replicating *Mtb* (Figure 5.4E). Although reduced IL-10 promotes lesion sterilization, those that do not sterilize have increased caseous necrosis causing an increase in non-replicating bacterial populations (Figure 5.4). The shift to non-replicating states makes the lesions more difficult to sterilize. Taken together, our model predicts that small reductions in IL-10 production rates lead to increased frequency of sterile lesions with only minor increases in inflammation and tissue damage. Overall, these results suggest that modulating IL-10 concentrations in granulomas in a precise manner could be an effective therapeutic strategy to promote lesions to sterilize.

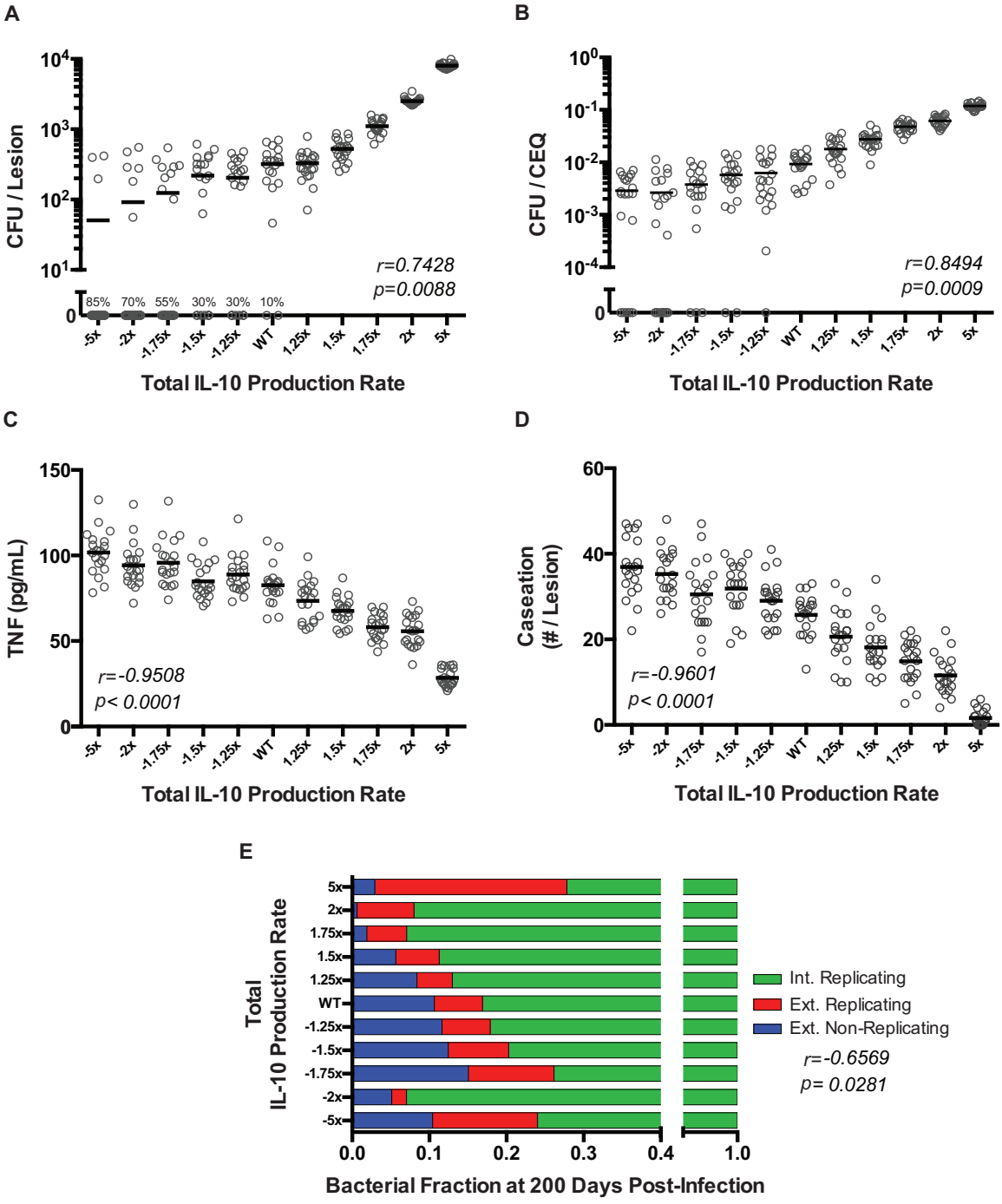

Figure 5.4 Simulations changing total levels of IL-10 production demonstrate control of bacterial set-point, outcome, and tissue damage

A. CFU comparisons for differing levels of total IL-10 production (5-fold reduction to 5-fold increase) at 200 days post-infection. The percentage indicates the number of sterile lesions at 200 days post-infection (chi-squared trend test, $p<0.0001$). B. CFU/CEQ comparisons for differing levels of total IL-10 production (5-fold reduction to 5-fold increase) at 200 days post-infection. C. Average lesion TNF-α concentration for differing levels of total IL-10 production (5-fold reduction to 5-fold increase) at 35 days post-infection. D. Average amounts of caseation for differing levels of total IL-10 production (5-fold reduction to 5-fold increase) at 50 days post-infection. E. Fractions of bacterial populations in non-sterile lesions for differing

levels of total IL-10 production (5-fold reduction to 5-fold increase) at 200 days post-infection. Individual dots represent individual lesions. Lines indicate the mean values. For all panels: Pearson correlation coefficients (*r*) and p-values (*p*) were calculated to determine the significance of observed trends.

5.3.6 Activated Macrophage Derived IL-10 is Necessary for Mediating Antimicrobial Activity and Tissue Damage

To determine which cellular source of IL-10 included in the model is most responsible for controlling antimicrobial activity and tissue damage, we performed individual virtual deletions for each cellular source of IL-10 (activated macrophages, infected macrophages, and regulatory T cells). Deletion of activated macrophage derived IL-10 causes the most significant change to bacterial loads, decreasing the mean CFU per lesion to ~50 CFU and increasing the number of sterile lesions ~8-fold (Figure 5.5A). This is accompanied by a ~9-fold reduction in mean CFU/CEQ at day 50 indicating control over early antimicrobial activity (Figure 5.5B). TNF is significantly elevated only at day 50 in both non-sterile and sterile lesions (Figure 5.5C). In non-sterile lesions, caseous necrosis is increased ~1.4-fold at day 50, while sterile lesions show a ~1.6-fold increase in caseous necrosis at day 50 (Figure 5.5D). Deletion of infected macrophage derived IL-10 leads to only a small decrease in CFU per lesion and a small increase in number of sterile lesions (Figure 5.5A). Similarly, the mean CFU/CEQ is only reduced by ~1.2-fold at day 100 (Figure 5.5B). TNF and caseous necrosis levels are not significantly different in both non-sterile and sterile lesions (Figure 5.5D). Finally, deletion of regulatory T-cell derived IL-10 does not significantly change the mean CFU per lesion, average TNF levels, and caseous necrosis levels, but marginally increases the mean CFU/CEQ at day 50 (Figure 5.5). These results suggest that activated macrophage production of IL-10 is primarily responsible for effectively controlling the antimicrobial

activity of the immune response to infection while limiting the amount of host-induced tissue damage (Figure B.3C, Figure B.4C-D in Appendix B).

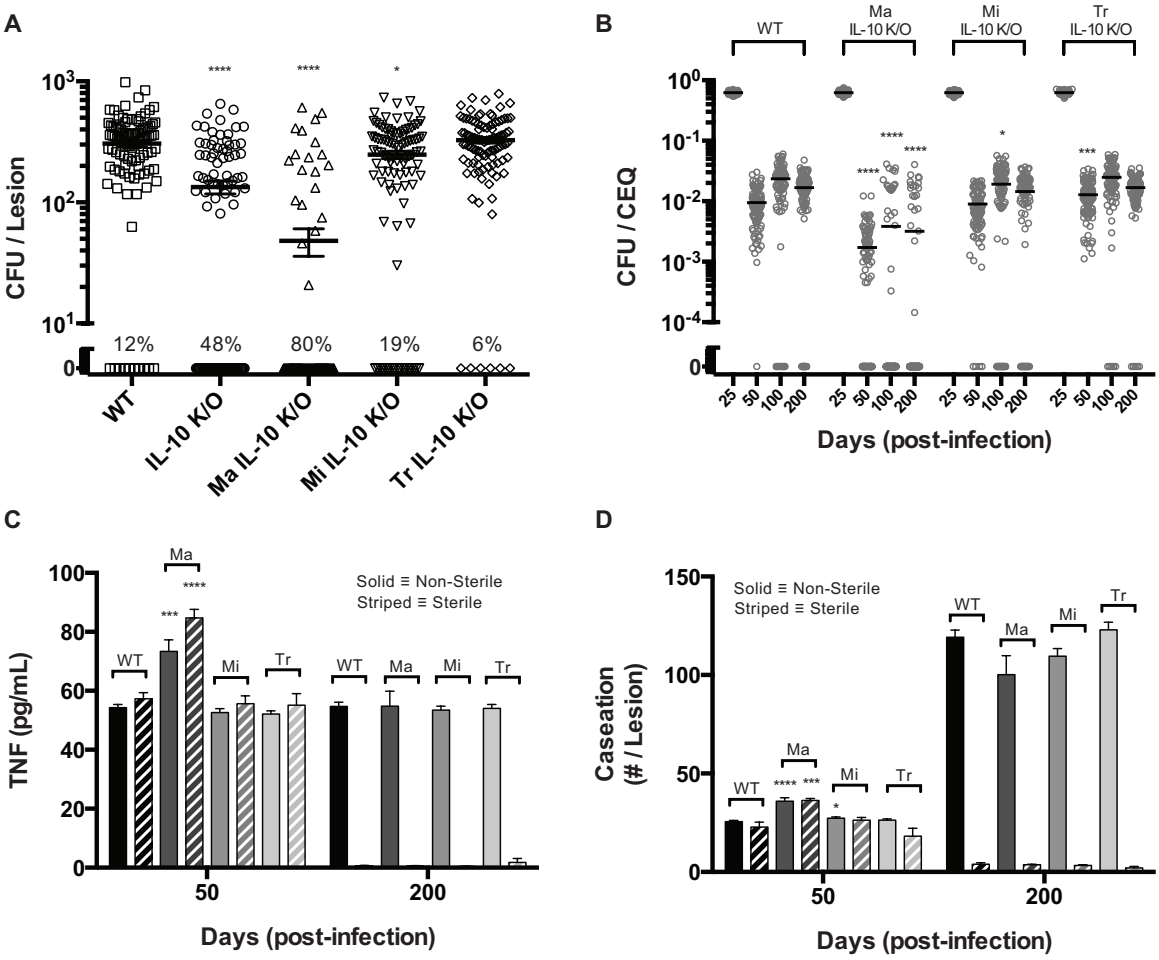

Figure 5.5 Virtual deletion of specific cellular sources of IL-10
A. CFU for WT, IL-10 K/O, activated macrophage IL-10 deletion (Ma IL-10 K/O), infected macrophage IL-10 deletion (Mi IL-10 K/O), regulatory T cell IL-10 deletion (Tr IL-10 K/O) lesions at 200 days post-infection. Both sterile and non-sterile lesions are included. The percentage indicates the number of sterile lesions at 200 days post-infection. B. CFU/CEQ for WT, IL-10 K/O, Ma IL-10 K/O, Mi IL-10 K/O, Tr IL-10 K/O lesions at 200 days post-infection. Both sterile and non-sterile lesions are included. C. Average TNF-α concentration for WT, Ma IL-10 K/O (Ma), Mi IL-10 K/O (Mi), Tr IL-10 K/O (Tr) lesions. Non-sterile lesions are displayed as solid bars and sterile lesions are displayed as striped bars. D. Caseous necrosis for WT, Ma IL-10 K/O (Ma), Mi IL-10 K/O (Mi), Tr IL-10 K/O (Tr) lesions. Non-sterile lesions are displayed as solid bars and sterile lesions are displayed as striped bars. Individual dots represent individual lesions. Lines indicate the mean values. Bars are representative of mean values with error bars showing SEM. For all panels: * $p \leq 0.05$, ** $p \leq 0.01$, *** $p \leq 0.001$, **** $p \leq 0.0001$, N = 100.

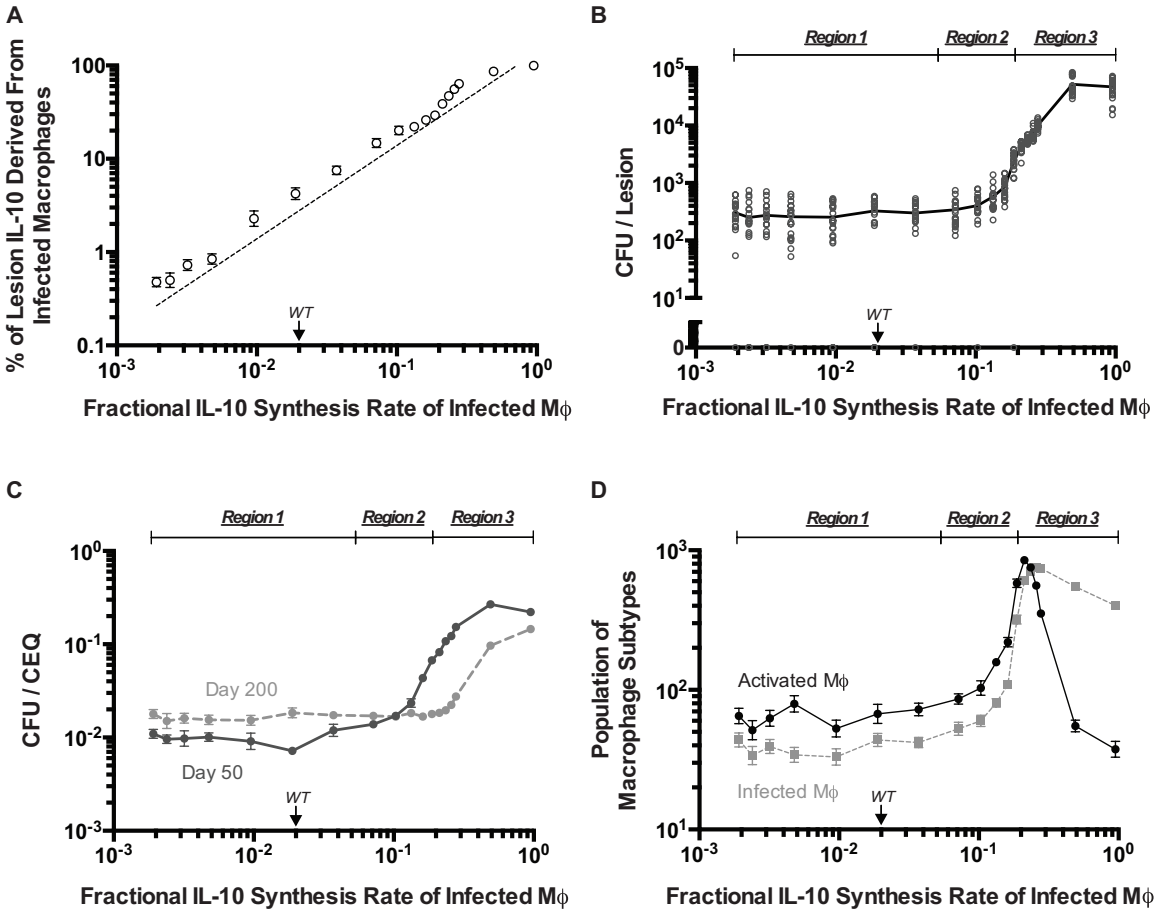

Figure 5.6 Infected macrophage derived IL-10 can undermine host-control of antimicrobial activity
A. Simulated percentage of IL-10 in the lesion at 200 days post-infection that is derived from infected macrophage IL-10 production is highly linearly correlated with infected macrophage IL-10 fractional synthesis (f_{Mi}) (Pearson's r = 0.9265, p < 0.0001). B. Simulated response in CFU at 200 days post-infection for varying levels of infected macrophage IL-10 fractional synthesis (f_{Mi}). C. Simulated response in CFU/CEQ at 200 days post-infection for varying levels of infected macrophage IL-10 fractional synthesis (f_{Mi}). D. Simulated response in macrophage populations at 200 days post-infection (activated macrophages – black circles, infected macrophages – grey squares) for varying levels of infected macrophage IL-10 fractional synthesis (f_{Mi}). For all panels: Region 1 (defined from fractional synthesis rates (f_{Mi}) of ~0.002 to ~0.05) represents the region where IL-10 is under the control of the host-response. Region 2 (defined from factional synthesis rates (f_{Mi}) of ~0.05 to ~0.2) represents the region of transitioning control of the IL-10 response. Region 3 (defined from factional synthesis rates (f_{Mi}) of ~0.2 to ~1.0) represents the region where IL-10 is under the control of the pathogen. Individual open dots represent individual lesions. Solid dots indicate the mean values with error bars showing SEM. N = 20.

5.3.7 Increased Infected Macrophage Derived IL-10 Can Shift Control of the Early Immune Response from Host to Pathogen

Although infected macrophages appear to have minor control of antimicrobial activity, sensitivity analysis demonstrates that production rates of IL-10 for both activated

and infected macrophages are positively correlated with CFU per lesion and CFU/CEQ at day 50 and 200 (Table B.4, Table B.5 in Appendix B). In addition, reports indicate that some strains of *Mtb* can induce greater production of IL-10 from macrophages, which may have evolved as an efficient strategy to limit bacterial sterilization (1). Furthermore, neutrophils may play a key role in dictating increased levels of IL-10 production from infected macrophages (25–27). Therefore, we tested how increased production of IL-10 from infected macrophages might undermine host control of antimicrobial activity and promote pathogen persistence.

As the fractional synthesis rate of infected macrophages (Eqn. 5.2) is increased, there is a linear increase in the percentage of IL-10 in the lesion that is derived from infected macrophages (Pearson's $r = 0.9265$, $p < 0.0001$) (Figure 5.6A). In contrast, CFU per lesion, CFU/CEQ, and macrophage populations respond to increased IL-10 synthesis by infected macrophages in a highly non-linear fashion. At low fractional synthesis rates (Region 1), predictions of CFU, CFU/CEQ, and macrophage populations show no significant deviation from WT values (Figure 5.6B-D). As the fractional synthesis rate increases (Region 2), antimicrobial activity begins to decrease (Figure 5.6C), leading to a small increase in CFU per lesion (Figure 5.6B). Yet, activated macrophages remain the dominant macrophage population (Figure 5.6D). When the fractional synthesis rate increases still further (Region 3), antimicrobial activity is reduced ~10-fold at day 50 and 0 to 10-fold at day 200 (Figure 5.6C). Reduction of antimicrobial activity causes the mean CFU per lesion at day 200 to increase ~100-fold (from lesions classified as *controlled growth* to *uncontrolled growth)* and the dominant macrophage population to switch from activated macrophages to infected macrophages (Figure 5.6B,D). The large

increase in CFU per lesion at high IL-10 levels may reflect a transition towards an outcome similar to TB pneumonia, where there is limited antimicrobial activity leading to uncontrolled bacterial replication causing excessive inflammation and accompanying gross pathology (51). Taken together, we predict multiple regimes of IL-10 control over antimicrobial activity in Figure 5.6 labeled as Regions 1-3. *Region 1*: the host-controlled response wherein activated macrophages are the dominant population producing IL-10, leading to control of CFU per lesion, an efficient antimicrobial response, and limited tissue damage. *Region 2*: the transitional response where activated macrophages are the dominant population yet production of IL-10 from infected macrophages begins to decrease antimicrobial activity causing a rise in CFU per lesion. *Region 3:* the pathogen-controlled response wherein infected macrophages are the dominant IL-10 producing population and antimicrobial activity is drastically reduced. This arises as infected macrophage derived IL-10 causes self-propagation of the infected macrophage population further shifting control of antimicrobial activity from host to pathogen. Together, these findings suggest that increased infected macrophage production rates of IL-10 can be an effective bacterial immune-evasion strategy that shifts control of antimicrobial activity from the host-immune response to the pathogen-derived response, therefore promoting pathogen persistence and survival.

5.4 Discussion

The development of new therapeutics for TB will be aided by a clearer understanding of the complex host-pathogen interactions and immune responses at the granuloma scale. In this Chapter, we use a computational model (*GranSim*) to probe the

role of IL-10 during the immune response to *Mtb* at an individual granuloma scale. Particular strengths of our computational approach include: calibration and validation against bacterial dynamics in the non-human primate model of TB, the ability to temporally track individual lesions regardless of sterilization, modulating levels of IL-10 in granulomas with fine control, and deleting IL-10 production from specific populations. In comparison, many of these strengths are difficult or impossible to measure and track in experimental systems.

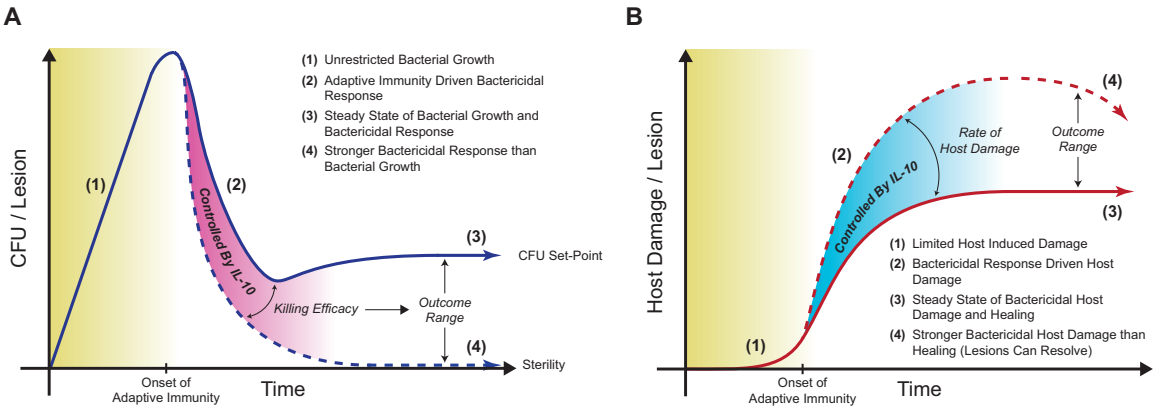

Figure 5.7 IL-10 controls sterility, bacterial set-point, and immunopathology on a per lesion basis
A. IL-10 control of bacterial dynamics in a lesion over time. B. IL-10 control of host damage in a lesion over time. The killing efficacy of the host-immune response is controlled by IL-10. In non-sterile lesions, control of killing efficacy by IL-10 leads to a bacterial set-point that balances bacterial replication with bactericidal processes, with minor host damage. Reducing IL-10 leads to increased killing efficacy, which promotes the lesion to sterilize at the cost of increased host damage. Lesions that sterilize may begin to resolve at later stages of infection (thus the downward slope of host damage), yet this could lead to fibrosis or scarring.

The computational model of *Mtb* infection was calibrated and validated with bacterial dynamics from the non-human primate model providing a model that has comparable bacterial dynamics to human *Mtb* infection. Peak bacterial loads occur at approximately day 28 post-infection followed by a sudden drop due to the onset of host adaptive immunity (Figure 5.7A). Using our model, we predict that IL-10 controls the antimicrobial activity of the early immune response. The strength of the antimicrobial

response, controlled by IL-10, mediates a trade-off between lesion sterilization and early host-induced tissue damage (Figure 5.7). We show, for the first time, that upon abrogation of IL-10, small transient increases in antimicrobial activity increase the likelihood of lesion sterilization. We predict that these small changes change lesion outcome since bacterial loads are reduced to very low levels during the early immune response. These predicted effects would most likely not be present in the murine model of *Mtb* infection as the bacterial dynamics are significantly different (progressive infection) than those in this model, non-human primates, and humans (64).

In humans, IL-10 levels are elevated in the lungs, bronchoalveolar lavage fluid, sputum, and serum of active TB patients (1, 66, 67). Additionally, polymorphisms in IL-10 associated genes have been linked to increased susceptibility to TB (1). In mice, overexpression of IL-10 in macrophages or in entire animals is associated with higher bacterial loads in granulomas (46, 47). Recently, investigations in NHP models of TB suggest similar antimicrobial activity in lesions of both the active and latent disease state. The only significant difference between lesions in differing disease states was a substantially increased fraction of sterile lesions per animal in the latent state (51). Taken in conjunction with our predictions, this suggests that IL-10 might be a key regulator between the clinical outcomes of latent versus active disease by controlling lesional sterility through antimicrobial activity at the cost of increased tissue damage. Thus, novel IL-10 focused treatment strategies (e.g. anti-IL10R antibodies) may be effective if properly timed during the adaptive immune response to promote lesional sterility. Furthermore, modulating IL-10 levels in the context of other important immune molecules (e.g. TNF or IFN-γ) could prove to be beneficial in controlling lesion outcome,

but have yet to be explored (68–70). Unfortunately, these strategies may lack clinical relevance because the short window where IL-10 treatments could be effective is at odds with the long-time-to-diagnosis in clinics. Further work with both experimental and computational models of *Mtb* infection models will be necessary to fully understand correlates of clinical outcomes with IL-10.

Although IL-10 helps control bacterial load after the onset of the host-immune response, an inherent carrying capacity may exist in forming granulomas (51). Indeed the maximal observed CFU in a NHP model of infection is ~10^5 per lesion, comparing well with our calculations that suggest lesions without host-immunity have a maximal CFU of ~10^4-10^6 per lesion (when scaled to 3D). If the antimicrobial activity is not sufficient to sterilize a lesion, the level of IL-10 controls a bacterial set-point of the lesion, which is the balance between bacterial replication and antimicrobial response, with the benefit of reduced tissue damage (Figure 5.7). The idea of a set-point stems from studies on HIV-1 infection; post peak viremia, after host immunity is initiated, the virus is suppressed to a specific level (i.e. the set-point) that determines long-term progression to disease (71, 72). Thus, we predict that IL-10 transiently influences antimicrobial activity, controls granuloma outcome (sterile vs. non-sterile lesions), determines bacterial set-point, and limits the extent of host-induced tissue damage at the lesional scale.

It has long been thought that IL-10 may play a central role in preventing an over-exuberant immune response during *Mtb* infection that leads to tissue damage (1, 7, 10, 28, 73, 74). Data from murine models are surprisingly limited, with only a single report of IL-10 K/O mice demonstrating increased pulmonary inflammation causing animals to succumb to infection earlier than WT mice (28). Using our *in silico* model we predict that

IL-10 controls host-immunity induced damage, especially during the initial burst of antimicrobial processes after the onset of adaptive immunity (30-60 days post-infection). Furthermore, we predict that increases in lesional sterility, due to increased antimicrobial effects, are at the expense of increased host damage (Figure 5.7). This is in agreement with Chapter 3, which predicted that the ratio of TNF and IL-10 is a critical mediator of infection control with limited host-induced damage (8). Although we approximated tissue damage by measuring levels of caseous necrosis, it is important to note that tissue damage *in vivo* is a much more complicated process attributed to a myriad of host processes. We are currently evaluating better measurements of tissue damage (e.g. differentiating between apoptosis and necrosis, as well as fibrosis) and immunopathology (e.g. neutrophils) that could be added to our model. Because *Mtb* infection can lead to chronic cell death and high levels of caseous necrosis, we anticipate that better measurements of tissue damage could point to an even clearer role for IL-10 and help define the mechanisms preventing host-immunity induced tissue damage. Our predictions agree well with the balance of damage and host response seen in many forms of disease pathogenesis (39).

It is important to note that IL-10 is not the only regulatory and anti-inflammatory cytokine present during infection. It has been suggested in murine models that a lack of data indicating a role for IL-10 in preventing tissue damage may be due the role of other regulatory mechanisms (such as PD-1 bearing T cells or TGF-β) (7, 28, 75, 76). Our model indicates that in the absence of IL-10, increased tissue damage at later stages post-infection (150-300 days) can be partially controlled by other regulatory mechanisms included in the model, such as cell-cell contact mediated down-regulation by T cells and

tissue remodeling (data not shown). Additionally, many human and macaque lesions develop fibrosis, which is a scarring-like response to caseous necrosis and tissue damage most likely driven by TGF-β (3). We are currently working on integrating fibrotic pathways into our model to understand the basis of fibrosis during TB. This should lead to a deeper understanding of how IL-10-based control of early tissue damage may be important in preventing later development of fibrosis and scarring in lesions.

IL-10 production may not only be a host-derived protective mechanism, but a pathogen-evolved bactericidal evasion mechanism. In many chronic infection scenarios (both viral and bacterial) pathogenic IL-10 induction can be used to dull the efficacy of the immune response (1, 7, 77). Specifically, in TB infection the *Mtb* clinical strains HN878 and CH have been shown to induce increased levels of IL-10 production from infected macrophages that could help establish a state of chronic infection (1, 11–16). Additionally, increased IL-10 levels in human patients are correlated with poor outcomes of TB infection (66, 67, 78, 79). Using our computational model we predicted that high levels of IL-10 derived from infected macrophages promotes pathogen persistence by limiting antimicrobial activity of the early immune response to *Mtb*. Reduction of antimicrobial activity increases the chances that a healthy macrophage will engulf *Mtb* (promoting pathogen persistence), while allowing the pathogen to survive in its intracellular niche by preventing cellular apoptosis/necrosis (77). These mechanisms prevent lesions from sterilizing and increase the bacterial set-point at the late stages of infection (Figure 5.7A). Furthermore, we show that a switch in lesional control occurs at high levels of IL-10 derived from infected macrophages (Figure 5.6) where the ability of activated macrophages to use IL-10 as a regulatory mechanism for host protection

(prevention of host-induced tissue damage) is lost and the pathogen is able to repurpose IL-10 as a mechanism of persistence ('immune-evasion').

The major contributor of IL-10 found in our studies is activated macrophages, although regulatory T cells produced IL-10 at twice the rate of activated macrophages. We predict that the limited number of regulatory T cells that are recruited to the lesion and their localization in the periphery restricts effectiveness of their IL-10 production. Further studies into the role of IL-10 producing T cells during *Mtb* infection are needed. In addition, neutrophils and their production of IL-10 were not included in this model. However, it has recently been shown that neutrophils only produce IL-10 in response to infection with *Mtb* and not in response to stimulation with *Mtb* antigens (25). Therefore, neutrophils would be a similar population to infected macrophages in our model, providing phagocytosis capabilities, an intracellular niche for *Mtb* growth, and production of IL-10 upon infection (26, 27, 80–82). As we predicted the contribution of increased IL-10 production from infected macrophages in disrupting antimicrobial activity during the early immune response, parallels could be theorized for neutrophil IL-10 production. We are currently working on gathering experimental data regarding neutrophils in the non-human primate model of infection and integrating neutrophils into our computational model (see Chapter 8). These efforts should lead to a clearer understanding of the role of neutrophil derived IL-10.

Our computational platform has allowed us to understand the role of IL-10 in controlling the trade-off between antimicrobial activity of the early immune response to *Mtb*, lesional sterility, and host-immunity derived tissue damage. Our unique multi-scale computational platform used in parallel with experimental models provides an integrated

systems biology approach to better understand the complex immune response to *Mtb*, which will allow us to rapidly hypothesize and test novel therapeutic interventions.

5.5 References

1. O'Garra, A., P. S. Redford, F. W. McNab, C. I. Bloom, R. J. Wilkinson, and M. P. R. Berry. 2013. The immune response in tuberculosis. *Annu. Rev. Immunol.* 31: 475–527.

2. Ouyang, W., S. Rutz, N. K. Crellin, P. a Valdez, and S. G. Hymowitz. 2011. Regulation and functions of the IL-10 family of cytokines in inflammation and disease. *Annu. Rev. Immunol.* 29: 71–109.

3. Flynn, J. L., and J. Chan. 2001. Immunology of tuberculosis. *Annu. Rev. Immunol.* 19: 93–129.

4. Moore, K. W., R. de Waal Malefyt, R. L. Coffman, and A. O'Garra. 2001. Interleukin-10 and the interleukin-10 receptor. *Annu. Rev. Immunol.* 1: 683–765.

5. Bogdan, C., Y. Vodovotz, and C. Nathan. 1991. Macrophage Deactivation by Interleukin 10. *J. Exp. Med.* 174.

6. Balcewicz-Sablinska, M., H. Gan, and H. G. Remold. 1999. Interleukin 10 produced by macrophages inoculated with Mycobacterium avium attenuates mycobacteria-induced apoptosis by reduction of TNF-α activity. *J. Infect. Dis.* 180: 1230–1237.

7. Redford, P., P. Murray, and A. O'Garra. 2011. The role of IL-10 in immune regulation during M. tuberculosis infection. *Mucosal Immunol.* 4: 1–10.

8. Cilfone, N. A., C. R. Perry, D. E. Kirschner, and J. J. Linderman. 2013. Multi-Scale Modeling Predicts a Balance of Tumor Necrosis Factor-α and Interleukin-10 Controls the Granuloma Environment during Mycobacterium tuberculosis Infection. *PLoS One* 8: e68680.

9. Gordon, S. 2003. Alternative activation of macrophages. *Nat. Rev. Immunol.* 3: 23–35.

10. Wigginton, J. E., and D. Kirschner. 2001. A model to predict cell-mediated immune regulatory mechanisms during human infection with Mycobacterium tuberculosis. *J. Immunol.* 166: 1951–67.

11. Manca, C., L. Tsenova, C. E. Barry, A. Bergtold, S. Freeman, P. a Haslett, J. M. Musser, V. H. Freedman, and G. Kaplan. 1999. Mycobacterium tuberculosis CDC1551

induces a more vigorous host response in vivo and in vitro, but is not more virulent than other clinical isolates. *J. Immunol.* 162: 6740–6.

12. Ordway, D., M. Henao-Tamayo, M. Harton, G. Palanisamy, J. Troudt, C. Shanley, R. J. Basaraba, and I. M. Orme. 2007. The hypervirulent Mycobacterium tuberculosis strain HN878 induces a potent TH1 response followed by rapid down-regulation. *J. Immunol.* 179: 522–31.

13. Portevin, D., S. Gagneux, I. Comas, and D. C.-3048359 Young. 2011. Human macrophage responses to clinical isolates from the Mycobacterium tuberculosis complex discriminate between ancient and modern lineages. *PLoS Pathog* 7: e1001307 ST – Human macrophage responses to clini.

14. Newton, S. M., R. J. Smith, K. A. Wilkinson, M. P. Nicol, N. J. Garton, K. J. Staples, G. R. Stewart, J. R. Wain, A. R. Martineau, S. Fandrich, T. Smallie, B. Foxwell, A. Al-Obaidi, J. Shafi, K. Rajakumar, B. Kampmann, P. W. Andrew, L. Ziegler-Heitbrock, M. R. Barer, and R. J. Wilkinson. 2006. A deletion defining a common Asian lineage of Mycobacterium tuberculosis associates with immune subversion. *Proc. Natl. Acad. Sci. U. S. A.* 103: 15594–8.

15. Nair, S., P. a Ramaswamy, S. Ghosh, D. C. Joshi, N. Pathak, I. Siddiqui, P. Sharma, S. E. Hasnain, S. C. Mande, and S. Mukhopadhyay. 2009. The PPE18 of Mycobacterium tuberculosis interacts with TLR2 and activates IL-10 induction in macrophage. *J. Immunol.* 183: 6269–81.

16. Cyktor, J. C., and J. Turner. 2011. Interleukin-10 and immunity against prokaryotic and eukaryotic intracellular pathogens. *Infect. Immun.* 79: 2964–73.

17. O'Garra, A., P. Vieira, P. Vieira, and A. E. Goldfeld. 2004. IL-10–producing and naturally occurring CD4+ Tregs: limiting collateral damage. *J. Clin. Invest.* 114: 1–7.

18. Yssel, H., R. De Waal Malefyt, M. G. Roncarolo, J. S. Abrams, R. Lahesmaa, H. Spits, and J. E. de Vries. 1992. IL-10 is produced by subsets of human CD4+ T cell clones and peripheral blood T cells. *J. Immunol.* 149: 2378–84.

19. Madura Larsen, J., C. S. Benn, Y. Fillie, D. van der Kleij, P. Aaby, and M. Yazdanbakhsh. 2007. BCG stimulated dendritic cells induce an interleukin-10 producing T-cell population with no T helper 1 or T helper 2 bias in vitro. *Immunology* 121: 276–82.

20. Scott-Browne, J. P., S. Shafiani, G. Tucker-Heard, K. Ishida-Tsubota, J. D. Fontenot, A. Y. Rudensky, M. J. Bevan, and K. B. Urdahl. 2007. Expansion and function of Foxp3-expressing T regulatory cells during tuberculosis. *J. Exp. Med.* 204: 2159–69.

21. Roncarolo, M. G., M. Battaglia, R. Bacchetta, K. Fleischhauer, and M. K. Levings. 2006. Interleukin-10-secreting type 1 regulatory T cells in rodents and humans. *Immunol. Rev.* 212: 28–50.

22. Ribeiro-Rodrigues, R., T. Resende Co, R. Rojas, Z. Toossi, R. Dietze, W. H. Boom, E. Maciel, and C. S. Hirsch. 2006. A role for CD4+CD25+ T cells in regulation of the immune response during human tuberculosis. *Clin. Exp. Immunol.* 144: 25–34.

23. Gerosa, F., C. Nisii, S. Righetti, R. Micciolo, M. Marchesini, A. Cazzadori, and G. Trinchieri. 1999. CD4(+) T cell clones producing both interferon-gamma and interleukin-10 predominate in bronchoalveolar lavages of active pulmonary tuberculosis patients. *Clin. Immunol.* 92: 224–34.

24. Trinchieri, G. 2001. Regulatory Role of T Cells Producing both Interferon gamma and Interleukin 10 in Persistent Infection. *J. Exp. Med.* 194: 53F–57.

25. Braian, C., V. Hogea, and O. Stendahl. 2013. Mycobacterium tuberculosis- induced neutrophil extracellular traps activate human macrophages. *J. Innate Immun.* 5: 591–602.

26. Doz, E., R. Lombard, F. Carreras, D. Buzoni-Gatel, and N. Winter. 2013. Mycobacteria-infected dendritic cells attract neutrophils that produce IL-10 and specifically shut down Th17 CD4 T cells through their IL-10 receptor. *J. Immunol.* 191: 3818–26.

27. Marzo, E., C. Vilaplana, G. Tapia, J. Diaz, V. Garcia, and P.-J. Cardona. 2014. Damaging role of neutrophilic infiltration in a mouse model of progressive tuberculosis. *Tuberculosis (Edinb).* 94: 55–64.

28. Higgins, D. M., J. Sanchez-Campillo, A. G. Rosas-Taraco, E. J. Lee, I. M. Orme, and M. Gonzalez-Juarrero. 2009. Lack of IL-10 alters inflammatory and immune responses during pulmonary Mycobacterium tuberculosis infection. *Tuberculosis (Edinb).* 89: 149–57.

29. Saunders, B. M., and W. J. Britton. 2007. Life and death in the granuloma: immunopathology of tuberculosis. *Immunol. Cell Biol.* 85: 103–11.

30. Kaufmann, S. H. E., and A. Dorhoi. 2013. Inflammation in tuberculosis: interactions, imbalances and interventions. *Curr. Opin. Immunol.* 25: 441–9.

31. Wang, L., F. Du, and X. Wang. 2008. TNF-alpha induces two distinct caspase-8 activation pathways. *Cell* 133: 693–703.

32. Fink, S. L., and B. T. Cookson. 2005. Apoptosis, pyroptosis, and necrosis: mechanistic description of dead and dying eukaryotic cells. *Infect. Immun.* 73: 1907–16.

33. Fayyazi, a, B. Eichmeyer, a Soruri, S. Schweyer, J. Herms, P. Schwarz, and H. J. Radzun. 2000. Apoptosis of macrophages and T cells in tuberculosis associated caseous necrosis. *J. Pathol.* 191: 417–25.

34. Arcila, M. L., M. D. Sánchez, B. Ortiz, L. F. Barrera, L. F. García, and M. Rojas. 2007. Activation of apoptosis, but not necrosis, during Mycobacterium tuberculosis infection correlated with decreased bacterial growth: role of TNF-alpha, IL-10, caspases and phospholipase A2. *Cell. Immunol.* 249: 80–93.

35. Rojas, M., M. Olivier, P. Gros, L. F. Barrera, and L. F. García. 1999. TNF-alpha and IL-10 modulate the induction of apoptosis by virulent Mycobacterium tuberculosis in murine macrophages. *J. Immunol.* 162: 6122–31.

36. Keane, J., H. G. Remold, and H. Kornfeld. 2000. Virulent Mycobacterium tuberculosis strains evade apoptosis of infected alveolar macrophages. *J. Immunol.* 164: 2016–20.

37. Majno, G., and I. Joris. 1995. Apoptosis, oncosis, and necrosis. An overview of cell death. *Am. J. Pathol.* 146: 3–15.

38. Laskin, D. L., and K. J. Pendino. 1995. Macrophages and inflammatory mediators in tissue injury. *Annu. Rev. Pharmacol. Toxicol.* 35: 655–77.

39. Casadevall, A., and L. Pirofski. 2003. The damage-response framework of microbial pathogenesis. *Nat. Rev. Microbiol.* 1: 17–24.

40. Balcewicz-Sablinska, M. K., J. Keane, H. Kornfeld, and H. G. Remold. 1998. Pathogenic Mycobacterium tuberculosis evades apoptosis of host macrophages by release of TNF-R2, resulting in inactivation of TNF-alpha. *J. Immunol.* 161: 2636–41.

41. Zhang, D.-W., J. Shao, J. Lin, N. Zhang, B.-J. Lu, S.-C. Lin, M.-Q. Dong, and J. Han. 2009. RIP3, an energy metabolism regulator that switches TNF-induced cell death from apoptosis to necrosis. *Science* 325: 332–6.

42. He, S., L. Wang, L. Miao, T. Wang, F. Du, L. Zhao, and X. Wang. 2009. Receptor interacting protein kinase-3 determines cellular necrotic response to TNF-alpha. *Cell* 137: 1100–11.

43. Roca, F. J., and L. Ramakrishnan. 2013. TNF Dually Mediates Resistance and Susceptibility to Mycobacteria via Mitochondrial Reactive Oxygen Species. *Cell* 1–14.

44. Cyktor, J. C., B. Carruthers, R. a Kominsky, G. L. Beamer, P. Stromberg, and J. Turner. 2013. IL-10 inhibits mature fibrotic granuloma formation during Mycobacterium tuberculosis infection. *J. Immunol.* 190: 2778–90.

45. Pitt, J. M., E. Stavropoulos, P. S. Redford, A. M. Beebe, G. J. Bancroft, D. B. Young, and A. O'Garra. 2012. Blockade of IL-10 signaling during bacillus Calmette-Guérin vaccination enhances and sustains Th1, Th17, and innate lymphoid IFN-γ and IL-17 responses and increases protection to Mycobacterium tuberculosis infection. *J. Immunol.* 189: 4079–87.

46. Lang, R., R. L. Rutschman, D. R. Greaves, and P. J. Murray. 2002. Autocrine deactivation of macrophages in transgenic mice constitutively overexpressing IL-10 under control of the human CD68 promoter. *J. Immunol.* 168: 3402–11.

47. Turner, J., M. Gonzalez-Juarrero, D. L. Ellis, R. J. Basaraba, A. Kipnis, I. M. Orme, and A. M. Cooper. 2002. In vivo IL-10 production reactivates chronic pulmonary tuberculosis in C57BL/6 mice. *J. Immunol.* 169: 6343–51.

48. Shaler, C. R., C. N. Horvath, M. Jeyanathan, and Z. Xing. 2013. Within the Enemy's Camp: contribution of the granuloma to the dissemination, persistence and transmission of Mycobacterium tuberculosis. *Front. Immunol.* 4: 30.

49. Modlin, R. L., and B. R. Bloom. 2013. TB or not TB: that is no longer the question. *Sci. Transl. Med.* 5: 213sr6.

50. Seok, J., H. S. Warren, A. G. Cuenca, M. N. Mindrinos, H. V Baker, W. Xu, D. R. Richards, G. P. McDonald-Smith, H. Gao, L. Hennessy, C. C. Finnerty, C. M. López, S. Honari, E. E. Moore, J. P. Minei, J. Cuschieri, P. E. Bankey, J. L. Johnson, J. Sperry, A. B. Nathens, T. R. Billiar, M. a West, M. G. Jeschke, M. B. Klein, R. L. Gamelli, N. S. Gibran, B. H. Brownstein, C. Miller-Graziano, S. E. Calvano, P. H. Mason, J. P. Cobb, L. G. Rahme, S. F. Lowry, R. V Maier, L. L. Moldawer, D. N. Herndon, R. W. Davis, W. Xiao, and R. G. Tompkins. 2013. Genomic responses in mouse models poorly mimic human inflammatory diseases. *Proc. Natl. Acad. Sci. U. S. A.* 110: 3507–12.

51. Lin, P. L., C. B. Ford, M. T. Coleman, A. J. Myers, R. Gawande, T. Ioerger, J. Sacchettini, S. M. Fortune, and J. L. Flynn. 2014. Sterilization of granulomas is common in active and latent tuberculosis despite within-host variability in bacterial killing. *Nat. Med.* 20: 75–9.

52. Ray, J. C. J., J. L. Flynn, and D. E. Kirschner. 2009. Synergy between individual TNF-dependent functions determines granuloma performance for controlling Mycobacterium tuberculosis infection. *J. Immunol.* 182: 3706–17.

53. Fallahi-Sichani, M., M. El-Kebir, S. Marino, D. E. Kirschner, and J. J. Linderman. 2011. Multiscale computational modeling reveals a critical role for TNF-α receptor 1 dynamics in tuberculosis granuloma formation. *J. Immunol.* 186: 3472–83.

54. Lin, P. L., M. Rodgers, L. Smith, M. Bigbee, A. Myers, C. Bigbee, I. Chiosea, S. V Capuano, C. Fuhrman, E. Klein, and J. L. Flynn. 2009. Quantitative comparison of active and latent tuberculosis in the cynomolgus macaque model. *Infect. Immun.* 77: 4631–42.

55. Lin, P. L., V. Dartois, P. J. Johnston, C. Janssen, L. Via, M. B. Goodwin, E. Klein, C. E. Barry, and J. L. Flynn. 2012. Metronidazole prevents reactivation of latent Mycobacterium tuberculosis infection in macaques. *Proc. Natl. Acad. Sci. U. S. A.* 109: 14188–93.

56. Lin, P. L., T. Coleman, J. P. J. Carney, B. J. Lopresti, J. Tomko, D. Fillmore, V. Dartois, C. Scanga, L. J. Frye, C. Janssen, E. Klein, C. E. Barry, and J. L. Flynn. 2013. Radiologic responses in cynomolgous macaques for assessing tuberculosis chemotherapy regimens. *Antimicrob. Agents Chemother.* .

57. Lin, P. L., A. Myers, L. Smith, C. Bigbee, M. Bigbee, C. Fuhrman, H. Grieser, I. Chiosea, N. N. Voitenek, S. V Capuano, E. Klein, and J. L. Flynn. 2010. Tumor necrosis factor neutralization results in disseminated disease in acute and latent Mycobacterium tuberculosis infection with normal granuloma structure in a cynomolgus macaque model. *Arthritis Rheum.* 62: 340–50.

58. Flynn, J. L., J. Chan, K. J. Triebold, D. K. Dalton, T. a Stewart, and B. R. Bloom. 1993. An essential role for interferon gamma in resistance to Mycobacterium tuberculosis infection. *J. Exp. Med.* 178: 2249–54.

59. Gideon, H. P., and J. L. Flynn. 2011. Latent tuberculosis: what the host "sees"? *Immunol. Res.* 50: 202–12.

60. Lin, P. L., and J. L. Flynn. 2010. Understanding latent tuberculosis: a moving target. *J. Immunol.* 185: 15–22.

61. Via, L. E., D. M. Weiner, D. Schimel, P. L. Lin, E. Dayao, S. L. Tankersley, Y. Cai, M. T. Coleman, J. Tomko, P. Paripati, M. Orandle, R. J. Kastenmayer, M. Tartakovsky, A. Rosenthal, D. Portevin, S. Y. Eum, S. Lahouar, S. Gagneux, D. B. Young, J. L. Flynn, and C. E. Barry. 2013. Differential Virulence and Disease Progression following Mycobacterium tuberculosis Complex Infection of the Common Marmoset (Callithrix jacchus). *Infect. Immun.* 81: 2909–19.

62. Marino, S., I. B. Hogue, C. J. Ray, and D. E. Kirschner. 2008. A methodology for performing global uncertainty and sensitivity analysis in systems biology. *J. Theor. Biol.* 254: 178–96.

63. Lin, P. L., S. Pawar, A. Myers, A. Pegu, C. Fuhrman, T. a Reinhart, S. V Capuano, E. Klein, and J. L. Flynn. 2006. Early events in Mycobacterium tuberculosis infection in cynomolgus macaques. *Infect. Immun.* 74: 3790–803.

64. Flynn, J. L. 2006. Lessons from experimental Mycobacterium tuberculosis infections. *Microbes Infect.* 8: 1179–88.

65. Bean, A. G., D. R. Roach, H. Briscoe, M. P. France, H. Korner, J. D. Sedgwick, and W. J. Britton. 1999. Structural deficiencies in granuloma formation in TNF gene-targeted

mice underlie the heightened susceptibility to aerosol Mycobacterium tuberculosis infection, which is not compensated for by lymphotoxin. *J. Immunol.* 162: 3504–11.

66. Verbon, a, N. Juffermans, S. J. Van Deventer, P. Speelman, H. Van Deutekom, and T. Van Der Poll. 1999. Serum concentrations of cytokines in patients with active tuberculosis (TB) and after treatment. *Clin. Exp. Immunol.* 115: 110–3.

67. Bonecini-Almeida, M. G., J. L. Ho, N. Boechat, R. C. Huard, S. Chitale, H. Doo, J. Geng, L. Rego, L. C. O. Lazzarini, A. L. Kritski, W. D. Johnson, T. A. McCaffrey, and J. R. L. e Silva. 2004. Down-Modulation of Lung Immune Responses by Interleukin-10 and Transforming Growth Factor (TGF-) and Analysis of TGF- Receptors I and II in Active Tuberculosis. *Infect. Immun.* 72: 2628–2634.

68. Debs, R. J., H. J. Fuchs, R. Philip, A. B. Montgomery, E. N. Brunette, D. Liggitt, J. S. Patton, and J. E. Shellito. 1988. Lung-specific delivery of cytokines induces sustained pulmonary and systemic immunomodulation in rats. *J. Immunol.* 140: 3482–8.

69. Huhn, R. D., E. Radwanski, S. M. O'Connell, M. G. Sturgill, L. Clarke, R. P. Cody, M. B. Affrime, and D. L. Cutler. 1996. Pharmacokinetics and immunomodulatory properties of intravenously administered recombinant human interleukin-10 in healthy volunteers. *Blood* 87: 699–705.

70. Kramp, J. C., D. N. McMurray, C. Formichella, and A. Jeevan. 2011. The in vivo immunomodulatory effect of recombinant tumour necrosis factor-alpha in guinea pigs vaccinated with Mycobacterium bovis bacille Calmette-Guérin. *Clin. Exp. Immunol.* 165: 110–20.

71. Ho, D. D., A. U. Neumann, A. S. Perelson, W. Chen, J. M. Leonard, and M. Markowitz. 1995. Rapid turnover of plasma virions and CD4 lymphocytes in HIV-1 infection. *Nature* 373: 123–6.

72. Masel, J., R. A. Arnaout, T. R. O'Brien, J. J. Goedert, and A. L. Lloyd. 2000. Fluctuations in HIV-1 viral load are correlated to CD4+ T-lymphocyte count during the natural course of infection. *J. Acquir. Immune Defic. Syndr.* 23: 375–9.

73. Lin, C.-L., M. H. Tawhai, and E. a. Hoffman. 2013. Multiscale image-based modeling and simulation of gas flow and particle transport in the human lungs. *Wiley Interdiscip. Rev. Syst. Biol. Med.* n/a–n/a.

74. Flynn, J. L., J. Chan, and P. L. Lin. 2011. Macrophages and control of granulomatous inflammation in tuberculosis. *Mucosal Immunol.* 4: 271–8.

75. Barber, D. L., K. D. Mayer-Barber, C. G. Feng, A. H. Sharpe, and A. Sher. 2011. CD4 T cells promote rather than control tuberculosis in the absence of PD-1-mediated inhibition. *J. Immunol.* 186: 1598–607.

76. Lázár-Molnár, E., B. Chen, K. a Sweeney, E. J. Wang, W. Liu, J. Lin, S. a Porcelli, S. C. Almo, S. G. Nathenson, and W. R. Jacobs. 2010. Programmed death-1 (PD-1)-deficient mice are extraordinarily sensitive to tuberculosis. *Proc. Natl. Acad. Sci. U. S. A.* 107: 13402–7.

77. Redpath, S., P. Ghazal, and N. R. Gascoigne. 2001. Hijacking and exploitation of IL-10 by intracellular pathogens. *Trends Microbiol.* 9: 86–92.

78. Olobo, J. O., M. Geletu, a Demissie, T. Eguale, K. Hiwot, G. Aderaye, and S. Britton. 2001. Circulating TNF-alpha, TGF-beta, and IL-10 in tuberculosis patients and healthy contacts. *Scand. J. Immunol.* 53: 85–91.

79. Jamil, B., F. Shahid, Z. Hasan, N. Nasir, T. Razzaki, G. Dawood, and R. Hussain. 2007. Interferon gamma/IL10 ratio defines the disease severity in pulmonary and extra pulmonary tuberculosis. *Tuberculosis (Edinb).* 87: 279–87.

80. Blomgran, R., L. Desvignes, V. Briken, and J. D. Ernst. 2012. Mycobacterium tuberculosis inhibits neutrophil apoptosis, leading to delayed activation of naive CD4 T cells. *Cell Host Microbe* 11: 81–90.

81. Eum, S.-Y., J.-H. Kong, M.-S. Hong, Y.-J. Lee, J.-H. Kim, S.-H. Hwang, S.-N. Cho, L. E. Via, and C. E. Barry. 2010. Neutrophils are the predominant infected phagocytic cells in the airways of patients with active pulmonary TB. *Chest* 137: 122–8.

82. Bru, A., and P.-J. Cardona. 2010. Mathematical modeling of tuberculosis bacillary counts and cellular populations in the organs of infected mice. *PLoS One* 5: e12985.

Chapter 6

A Systems Pharmacology Approach Towards Design and Understanding of Inhaled Formulations of Rifampicin and Isoniazid For the Treatment of TB

The work in Chapter 6 was submitted as: Cilfone, N.A., Pienaar, E., Thurber, G.M., Kirschner, D.E., Linderman, J.J. A systems pharmacology approach towards design and understanding of inhaled formulations of rifampicin and isoniazid for the treatment of TB. (2014).

6.1 Introduction

Tuberculosis (TB), caused by inhalation of the bacterium *Mycobacterium tuberculosis* (*Mtb*), remains a widespread concern even with the availability of curative antibiotics (1–3). Current antibiotic regimens require a minimum of 6 months of treatment; daily oral doses with a combination of rifampicin (RIF), isoniazid (INH), pyrazinamide (PZA), and ethambutol (EMB) for 2 months, followed by 4-months of RIF and INH (4). The length and combinatorial nature of 'first-line' drug regimens may result in patient compliance issues as well as chronic toxicity (1, 2, 5). There is a desperate need for new treatment strategies that can shorten the lengthy treatment period and also reduce dose frequency (1, 5, 6).

A central feature of the immune response to *Mtb* is the formation of a granuloma, an organized structure of macrophages and lymphocytes that forms around infected

macrophages and extracellular *Mtb* in lungs (1, 3, 7). Multiple granulomas form in a host's lungs and evolve independently (8, 9). As granulomas are the pathologic structures that harbor *Mtb*, distribution of antibiotics in granulomas is critical for sterilizing bacteria. The heterogeneity of *Mtb* populations in granulomas, with bacteria residing in both intra- and extracellular compartments, and varying growth states all impacts the effectiveness of antibiotics (e.g. those that rely on disruption of replication). (1, 10). In addition, current oral antibiotic regimens can lead to poor antibiotic penetration into granulomas causing sub-optimal exposure and permitting bacterial re-growth between doses, necessitating long treatment durations (see Appendix C) (1, 10) (Pienaar et al. submitted).

Delivery of antibiotics by an inhaled route could overcome limitations of oral dosing for treatment of TB (2, 11–13). The underlying hypothesis for inhaled formulations is that a fabricated carrier loaded with antibiotics is dosed into the lungs via an aerosol delivery system (e.g. nebulizer) (12, 13). Based on physical characteristics, carriers settle in different regions of the lungs and are taken up by alveolar macrophages and lung endothelial cells (2, 11). Once deposited in lung tissue, carriers release the pre-loaded antibiotic based on tunable physio-chemical properties of the carrier such as size and diffusivity of antibiotics through the carrier. The most extensively used carriers are poly-lactic acid (PLA) and poly-lactic-co-glycolic acid (PLGA) formulations that are tuned for slow and sustained release of antibiotics (2, 11). As granulomas are found in the host's lungs, an inhaled dose should elevate antibiotic concentrations in the lung and avoid first-pass effects thus increasing sterilizing capabilities. Additionally, targeting carriers to macrophages might further augment the sterilizing capabilities of antibiotics

by directly elevating concentrations within the bacterial niche (11, 12, 14–17). With increased sterilizing capabilities the dose frequency could be reduced, alleviating compliance and toxicity concerns associated with daily oral treatment. However, due to many issues such as granuloma dynamics, the design space of carrier release properties, pharmacodynamics, and the system pharmacokinetics, we still lack a basic understanding of what controls the efficacy of inhaled formulations.

Encapsulated formulations are rapidly phagocytosed by infected macrophages *in vitro,* elevating intracellular concentrations and improving sterilization capabilities (14–16, 18–20). However, these studies do not reflect the dense macrophage-laden characteristics of granulomas. Improved efficacy of inhaled doses compared to oral doses has been demonstrated in murine, rat, and guinea pig models of *Mtb* infection (11–13, 21). For example, RIF and INH were co-loaded into a PLGA carrier and were given to *Mtb*-infected guinea pigs. Three doses of this inhaled formulation had similar sterilizing capability as 45 oral doses of antibiotics, with antibiotics detectable in the plasma up to 10 days after a single inhaled dose (2, 22). Although these studies have shed light on the efficacy of inhaled formulations, murine, rat, and guinea pig models have differing antibiotic pharmacokinetics than humans and lack many characteristics of human TB, such as latent infection and the typical granuloma organization (12, 23). The most relevant *in vivo* studies are single doses of inhaled formulations into the lungs of healthy non-human primates (INH and rifabutin – a rifampicin derivative) and humans (capreomycin – a second line antibiotic) (24, 25). An inhaled formulation of INH had a 2-fold higher AUC/MIC index measured from plasma, compared to oral doses (24). The highest dose of an inhaled formulation of capreomycin leads to plasma concentrations

above MIC, but for less than 4 hours (25). Although promising, most clinically relevant *in vivo* studies are only able to measure temporal plasma concentrations after inhaled dosing. For inhaled formulations, it is assumed that extended periods of elevated antibiotic concentrations in plasma directly translates to increased exposure in granulomas (1, 18, 24–27). However, oral dosing studies demonstrate that antibiotic exposure in the granuloma is significantly different than antibiotic exposure in the plasma (1, 10) (Appendix C, Pienaar et al. submitted).

To better understand the potential for inhaled antibiotic formulations to improve sterilization of bacteria in granulomas, we need an approach that simultaneously accounts for granuloma dynamics, inhaled carrier behavior and release kinetics, pharmacokinetics, and pharmacodynamics of antibiotics. We use a systems pharmacology approach and extend our computational model of granuloma function and antibiotic treatment, from Appendix C, to include inhaled dosing and antibiotic release from a generalized carrier system. We follow concentrations of RIF and INH in granulomas over 200 days of treatment for both inhaled and oral dosing. We use our computational model to understand the effects of carrier physio-chemical properties and release kinetics (e.g. size, diffusivity, etc.), dosing frequency, and pharmacokinetics on treatment efficacy. We use understanding gained from these studies to rationally design inhaled formulations of RIF and INH that require reduced dose frequencies and have equivalent or better sterilizing capabilities compared to daily oral dosing. These findings illuminate fundamental mechanisms driving efficacy of inhaled formulations and inform design of superior carriers for animal and clinical testing.

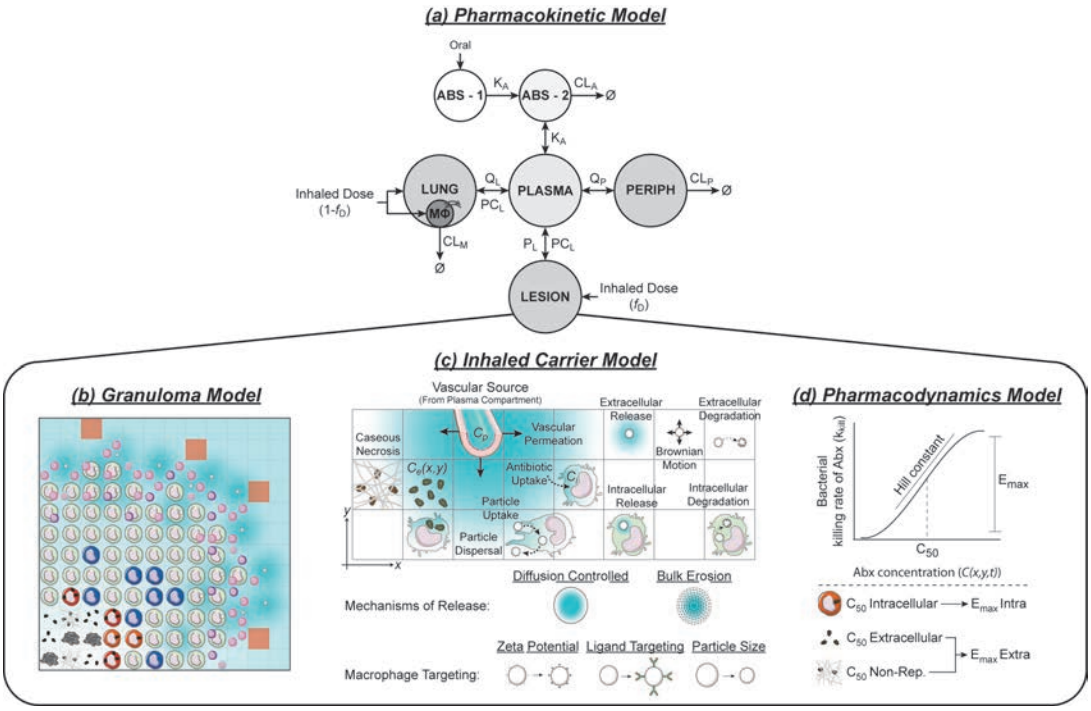

Figure 6.1 Overall model structure that captures relevant dynamics across multiple compartments (a) The pharmacokinetic (PK) model includes two transit compartments (*ABS-1* and *ABS-2*), a plasma compartment (*PLASMA*), a peripheral compartment (*PERIPH.*), a non-infected lung compartment (*LUNG*), and an intracellular macrophage compartment (*MΦ*) that is at pseudo-steady state. Oral doses enter into the first transit compartment. Inhaled doses are partitioned between the non-infected lung (1-f_D) and lesion (f_D) models based on representative sizes. The dose (1-f_D) into the non-infected lung compartment is further partitioned between extracellular non-infected lung and intracellular macrophage compartments. We assume no trafficking of macrophages in or out of the non-infected lungs. (b) Our granuloma model, a hybrid multi-scale agent-based model, includes spatial and temporal dynamics of antibiotics and captures diffusion, extracellular degradation, cellular uptake and intracellular degradation. Antibiotics exit the plasma compartment and enter the granuloma model at vascular sources designated in the simulation grid based on vascular permeability coefficients and concentration gradients between the plasma compartment and the granuloma mode. The inhaled formulation is modeled by agent representations of each carrier. (c) Model of the behavior and release of antibiotics by inhaled carriers. Carriers move by random walk, are phagocytosed by macrophages based on size, zeta potential, and density of targeting ligand (Figure D.1b-d in Appendix D), degrade in both the extra- and intracellular space, and release antibiotics in both the intra- and extracellular space. (d) The pharmacodynamics model uses E_{max} functions (using C_{50} values and Hill-constants, H) to describe the antibacterial activity of antibiotics against multiple bacterial subpopulations (intracellular, extracellular, and non-replicating) based on the local antibiotic concentration ($C(x,y,t)$). Art adapted from Servier Medical Art (http://servier.com/Powerpoint-image-bank) provided under the Creative Commons Unported License 3.0.

6.2 Methods

6.2.1 Pharmacokinetic (PK) Model

The four-components of our computational model are shown in Figure 6.1. We modify the PK model from Appendix C to allow for dosing via both inhaled and oral

routes. The PK model (Eqn. 6.3-6.8) includes two transit compartments (C_{A1} and C_{A2}), a plasma compartment (C_{PL}), a peripheral compartment (C_{PE}), a non-infected lung compartment (C_L), an intracellular macrophage sub-compartment (C_M) at pseudo-steady state, and a granuloma compartment (described below) (Figure 6.1a).

$$\frac{dC_{A1}}{dt} = -K_A \cdot C_{A1} \qquad (Eqn.\ 6.1)$$

$$\frac{dC_{A2}}{dt} = K_A \cdot C_{A1} - K_A \cdot C_{A2} - CL_A \cdot C_{A2} \qquad (Eqn.\ 6.2)$$

$$\frac{dC_{PL}}{dt} = K_A \cdot C_{A2} - Q_P \left(\frac{C_{PL}}{V_{PL}} - \frac{C_{PE}}{V_{PE}}\right) - Q_L \left(PC_L \cdot \frac{C_{PL}}{V_{PL}} - \frac{C_L}{V_L}\right) \qquad (Eqn.\ 6.3)$$

$$\frac{dC_{PE}}{dt} = Q_P \left(\frac{C_{PL}}{V_{PL}} - \frac{C_{PE}}{V_{PE}}\right) - CL_{PE} \cdot \frac{C_{PE}}{V_{PE}} \qquad (Eqn.\ 6.4)$$

$$\frac{dC_L}{dt} = Q_L \left(PC_L \cdot \frac{C_{PL}}{V_{PL}} - \frac{C_L}{V_L}\right) + \sum_{N_{Ext}(t)} \left(M_{DL}(t)\left(\frac{V_L}{L_L}\right)\right) \qquad (Eqn.\ 6.5)$$

$$\frac{dC_M}{dt} = \sum_{N_{Int}(t)} \left(M_{DM}(t)(N_M \cdot L_M)\right) - CL_M \cdot C_M \qquad (Eqn.\ 6.6)$$

K_A is absorption rate (h^{-1}); CL_A, CL_{PE}, CL_M are clearance rate constants (L/kg*h) from second transit, peripheral, and macrophage compartments; Q_P and Q_L are between compartment transfer rate constants (h^{-1}) for plasma to peripheral or non-infected lung compartments; V_{PL}, V_{PE}, and V_L are apparent distribution volumes (L/kg) of plasma, peripheral, and non-infected lung compartments; PC_L is permeability coefficient for non-infected lung compartment; $M_{DL}(t)$ and $M_{DM}(t)$ are time-varying antibiotic mass release rates (mg/h) from inhaled carriers (described in Inhaled Carrier Model below); N_{Ext} and N_{Int} are time-varying number of inhaled carriers in non-infected lung and macrophage compartments; L_L is total lung volume (L), and N_M is number of macrophages in non-

infected lung. The pseudo-steady state between non-infected lung and intracellular macrophage compartments is given by:

$$C_L = \frac{A_T}{L_L + E_M \cdot N_M \cdot L_M} \quad (Eqn.\ 6.7)$$

$$C_M = E_M \cdot C_L \quad (Eqn.\ 6.8)$$

A_T is total mass (mg) of antibiotics (sum of intra- and extracellular); E_M is equilibrium partition coefficient, and L_M is volume (mL) of a macrophage. Antibiotics exit the PK plasma compartment and enter the granuloma compartment at vascular sources designated in the simulation grid (Figure 6.1b) based on the concentration gradients between the plasma compartment and the granuloma compartment (C_{Ext}) (28) (Pienaar et al. submitted).

$$\frac{dC_{Ext}(x,y,t)}{dt} = (p \cdot A_S)\left(PC_L \cdot C_{PL} - C_{Ext}(x,y,t)\right) \quad (Eqn.\ 6.9)$$

A_S is the surface area of a vascular source (cm^2), p is the vascular permeability (cm/s), and PC_L is the partition coefficient. PK model parameters are given in Table D.1 in Appendix D.

6.2.2 Granuloma Model of Mtb Infection

Our 2-dimensional hybrid multi-scale agent-based model of granuloma formation and function during *Mtb* infection describes processes across three scales (see Appendix C): tissue, cellular, and molecular (Figure 6.1b) (29–31) (Pienaar et al. submitted). Briefly, the granuloma model represents a 16 mm^2 section of lung tissue and describes macrophages, T-cells, and three *Mtb* sub-populations: intracellular, extracellular, and non-replicating. The formation of a granuloma is an emergent behavior in response to

infection. The model tracks agent states and interactions, as well as chemokine and cytokine diffusion, degradation. Receptor-ligand trafficking and signaling events are estimated using a tuneable resolution approach, demonstrated in Chapter 2 and Appendix C (29, 31, 32) (Pienaar et al. submitted). The model captures the spatial and temporal dynamics of RIF and INH through extracellular diffusion and degradation, cellular uptake and intracellular degradation as described in Appendix C (Pienaar et al. submitted). Cellular accumulation of soluble antibiotics is assumed at pseudo-steady state given by:

$$C_{Ext}(x,y,t) = \frac{A_T(x,y,t)}{L_{Grid} + E_M \cdot L_M} \qquad (Eqn.\,6.10)$$

$$C_{Int}(x,y,t) = E_M \cdot C_{Ext}(x,y,t) \qquad (Eqn.\,6.11)$$

C_{Ext} and C_{Int} are extra- and intracellular concentrations (mg/mL), and L_{Grid} is volume (mL) of a grid compartment. Parameter values for apparent RIF and INH diffusivity (cm^2/s), intra- and extracellular degradation rate (s^{-1}), and equilibrium partition coefficient were fit to experimental measurements of antibiotic distribution in Appendix C. Granuloma model parameters are given in Table D.2 in Appendix D.

6.2.3 Inhaled Carrier Model: Granuloma Compartment

An inhaled dose arrives in the granuloma model, as fraction f_D of the total dose (Figure 6.1a). The granuloma model represents a small section of lung tissue where infection occurs, and individual carriers (~10^3 deposited carriers) are modeled as agents (Figure 6.1c). We assume the representative section of lung tissue is well distributed with alveolar space, and thus an inhaled dose is randomly deposited into the simulation environment. Deposition does not occur in micro-compartments characterized as part of the granuloma, as alveolar space is not observed inside granulomas (Figure D.1a in

Appendix D) (9, 33). We do not model a specific carrier, but instead describe a general carrier formulation similar to polymer-encapsulated antibiotics (14–16, 18–20). Carrier behavior is illustrated in Figure 6.1c and includes carrier movement, macrophage phagocytosis of carriers (Figure D.1b-d in Appendix D), dispersal from macrophages, and extra- and intracellular degradation (17, 34–38).

Release of antibiotics from carriers occurs in both the intra- and extracellular environment (Figure 6.1c) (14–16, 18–20). We model release kinetics by describing diffusion of antibiotics through a spherical carrier and degradation of the carrier system itself, with time varying boundary conditions (39–41).

$$\frac{\partial C_D}{\partial t} = \frac{D(t)}{r^2}\frac{\partial}{\partial r}r^2\frac{\partial C_D}{\partial r} \qquad C_D(R) = C_B(x,y,t) \qquad (Eqn.\ 6.12)$$

C_D is the antibiotic concentration in the carrier (mg/μm^3), D is the time-varying diffusivity of antibiotics in the carrier (μm^2/s), r is the radial coordinate (μm), R is the carrier radius (μm), and C_B is the boundary concentration (mg/μm^3) – an intra- or extracellular concentration.

We assume first-order degradation kinetics, which directly affects the diffusivity of antibiotics in the carrier (40):

$$D(t) = P_{drugDiff}e^{(-P_{deg}t)} \qquad (Eqn.\ 6.13)$$

$P_{drugDiff}$ is the initial diffusivity of antibiotics in the carrier (μm^2/s) and P_{deg} is the carrier degradation rate (s^{-1}) – specific to whether the carrier is intra- or extracellular. Based on relative rates of diffusion and degradation specified the carrier release kinetics can be either diffusion-controlled or degradation-controlled (Figure 6.1c) (39–41). All carrier parameters are given in Table D.1 in Appendix D.

6.2.4 Inhaled Carrier Model: Non-Infected Lung Compartment

An inhaled dose arrives in the non-infected lung and intracellular macrophage compartments, as fraction $(1\text{-}f_D)$ of the total dose (Figure 6.1a). The number of carriers deposited is large ($\sim 10^9$) and a homogenous representation of carriers is used (Figure 6.1a). We partition the $(1\text{-}f_D)$ dose into both compartments, based on the probability of macrophage uptake. We solve the carrier release equations (Eqns. 6.12, 6.13) for a representative carrier in each compartment with appropriate boundary conditions, C_L and C_M, and scale the mass of antibiotic release by the total dose in each compartment. The carrier degradation rates are set as the extracellular degradation rate for the non-infected lung compartment and the intracellular degradation rate for the intracellular macrophage compartment.

6.2.5 Pharmacodynamics (PD) Model

We utilize the PD model (Figure 6.1d) designed and calibrated in Appendix C (Pienaar et al. submitted). Briefly, E_{max} functions (using C_{50} values and Hill-constants, H) describe the antibacterial activity of RIF and INH against multiple bacterial subpopulations (intracellular, extracellular, and non-replicating) based on the local antibiotic concentration (intra- or extracellular), which varies in both space and time in the granuloma model. Estimates of C_{50} and H were based on *in vitro* dose-response curves, while estimates of E_{max} were determined from comparisons to non-human primate data of CFU and sterilized granulomas after 2 months of daily doing with RIF or INH (42) (Pienaar et al. submitted). PD model parameters are given in Table D.1 in Appendix D.

6.2.6 Model Analysis

Our work investigates antibiotic efficacy at the single granuloma scale. We simulate 100 days post-infection and subsequently treat with antibiotics for an additional 200 days via the inhaled or oral route at two dosing frequencies: daily or every two-weeks. We define successful treatment as the complete sterilization of all bacteria in a granuloma by 200 days post-treatment initiation. We track average concentrations of antibiotics over time in granulomas and in PK compartments. We calculate cumulative granuloma and peripheral antibiotic exposure (AUC) for 14-day timeframes. Peripheral AUC is a metric of toxicity as the peripheral compartment represents organs such as the liver and kidneys (10). We evaluate hazard ratios (HR) to determine the cumulative risk between inhaled and oral treatments. Uncertainty and sensitivity analysis is used to identify inhaled antibiotic model parameters that have significant effects on model outputs related to treatment efficacy (43). Additional model details can be found in the Supplemental Text in Appendix D.

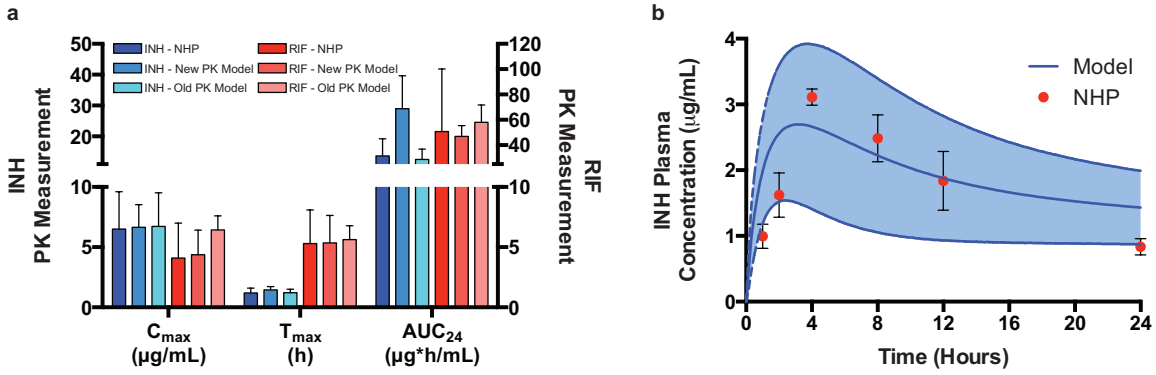

Figure 6.2 Model calibration and validation for oral and inhaled doses
(a) Comparison of the modified PK model and previous PK model (from Appendix C) to maximum plasma concentration (C_{max}), time to maximum plasma concentration (T_{max}), and 24-hour AUC (AUC_{24}) for oral doses of RIF and INH in the NHP model of TB available from the Flynn Lab (Pienaar et al. submitted) (6). Ranges are used for multiple model PK parameters to give inter-individual variability. Bars are representative of mean values with error bars showing SD. Model: N = 50, NHP: N = 7. **(b)** Validation of the model against observed plasma concentrations of INH after single inhalation to healthy NHPs estimated from (17, 24). Dots represent mean values with error bars showing SD. Line represents mean values with

dotted lines showing SD. Ranges are used for multiple model PK parameters to give inter-individual variability. Model: N = 10, NHP: N = 4.

6.3 Results

6.3.1 Model Calibration with Non-Human Primate Experimental Data

Our granuloma model of *Mtb* infection, without antibiotic treatment, was previously calibrated and validated against temporal measurements of colony forming units (CFU) per granuloma from a non-human primate (NHP) model of TB infection (see Chapter 5 and Appendix C) (8) (Pienaar et al. submitted). We calibrate our new antibiotic model with two dose formulations from NHP models of TB (Figure 6.2): (1) four oral doses of RIF (20 mg/kg) or INH (15 mg/kg) were given and temporal plasma concentrations were measured after the fourth dose (6), (2) a single inhaled dose of INH loaded PLA micro-particles was given and temporal plasma concentrations of INH were measured (17, 24). Based on measured micro-particle size, aerodynamic diameter, and fractional lung deposition (~10-30%) we estimate the total deposited inhaled dose (input to our model) to be $1.2x10^{9}$ particles (24, 44). We fix the deposited dose at this physiologically relevant value here and in all further simulations as determining and optimizing the deposition of inhaled particles in lungs is not the focus of this work (and poses its own challenges). Carrier-related parameters for the single inhaled dose were estimated based on data and Eqns. 6.12-6.13: $D = 1.85x10^{-6}$ ($\mu m^2/s$), $\delta_c = 1.65x10^{-5}$ (s^{-1}), and INH loading estimated as $1.45x10^{-8}$ (mg/particle) (17). Using the oral doses and calculated carrier-related parameters, we vary multiple PK parameters in order to best fit plasma compartment kinetics of single oral doses of RIF and INH (matching well with our previous model from Appendix C) and a single inhaled dose of INH loaded carriers

(Figure 6.2) (6, 17, 24). We establish a baseline range of PK related parameters that accounts for host-to-host variability (Table D.1 in Appendix D).

Table 6.1 Sensitivity analysis of inhaled RIF model parameters at different dose frequencies on treatment related model outputs

		Carrier Release Parameters					*Mϕ Targeting Parameters*						*PK Parameters*			
	RIFAMPICIN	P_{load}	P_{size}	$P_{drugDiff}$	P_{intDeg}	P_{extDeg}	P_{zeta}	P_{diff}	M_{uptake}	P_{TL}	M_{TR}	$K_{D\text{-}TLR}$	k_{TLR}	k_{abs}	CL_{abs}	V_p	CL_p
Daily	*CFU*	---	+	---	-												+
	Lesion AUC	+++	--	+++	+++	+++	+ +	-	---		-						---
	Peripheral AUC	+++	---	+++	+++	+++										+++	---
	Time to Sterilization	---		--											-		+
Two Weeks	*CFU*	---			+	+++											+
	Lesion AUC	+++		+++	++	+	+		-		+						---
	Peripheral AUC	+++		+		+				-						+++	---
	Time to Sterilization	---															

Carrier Dose Used: 1.2×10^9 carriers. P_{load} – load mass of drug (mg/carrier), P_{size} – size of carrier (μm), $P_{drugDiff}$ – diffusivity of drug in carrier ($\mu m^2/s$), P_{intDeg} – carrier intracellular degradation rate (1/s), P_{extDeg} – carrier extracellular degradation rate (1/s), P_{zeta} – carrier zeta-potential (mV), P_{diff} – diffusivity of carrier in lung tissue (cm^2/s), M_{uptake} – macrophage maximum carrier uptake probability (), P_{TL} – carrier density of targeting ligand (#/carrier), M_{TR} – macrophage density of targeting receptor (#/cell), $K_{D\text{-}TLR}$ – ligand-receptor dissociation constant (M), k_{TLR} – ligand-receptor carrier uptake rate (#/cell*s), k_{abs} – absorption rate constant (1/hr), CL_{abs} – clearance rate from 2nd absorption compartment (L/hr*kg), V_p – peripheral volume distribution (L/kg), CL_p – clearance rate from peripheral compartment (L/hr*kg). -/+ $p < 0.05$, --/++ $p < 0.001$, ---/+++ $p < 0.0001$ from sensitivity analysis.

6.3.2 A Combination of Pharmacokinetic and Carrier-Release Properties Control the Efficacy of Inhaled Formulations

We use sensitivity analysis to understand which dynamics most affect treatment efficacy (CFU, granuloma AUC, peripheral AUC, and time to sterilization) for inhaled formulations of RIF and INH (Supplemental Text in Appendix D). We analyzed daily and two-weeks dosing frequencies to compare changes in treatment dynamics at reduced frequencies. Tables 6.1 and 6.2 demonstrate that: (1) increased antibiotic loading promotes bacterial sterilization, (2) carrier release kinetics control treatment efficacy and differ with dosing frequency, and (3) system pharmacokinetics influence the availability of antibiotics at the site of infection.

For both RIF and INH, more frequent inhaled dosing (e.g. daily) allows carriers to be designed with faster carrier-release profiles (higher diffusivity in the carrier and degradation rates) as another dose is given after a short interval (Tables 6.1 and 6.2).

Faster carrier release profiles are negatively correlated with CFU and time to sterilization, while positively correlated with granuloma and peripheral AUC. With less frequent dosing (every two-weeks) INH requires a carrier designed with slower carrier-release and degradation profiles in order to maintain high levels of granuloma exposure with decreased CFU (Table 6.2), while RIF requires a carrier designed with faster carrier-release profiles to increase granuloma exposure but with limited effects on CFU (Table 6.2). The system pharmacokinetics have large influences on the antibiotic exposure at the site of infection for both dosing frequencies, with clearance of RIF and INH from the peripheral compartment correlated with many facets of treatment dynamics (Tables 6.1 and 6.2).

Table 6.2 Sensitivity analysis of inhaled INH model parameters at different dose frequencies on treatment related model outputs

		Carrier Release Parameters					***Mϕ Targeting Parameters***							***PK Parameters***			
	ISONIAZID	P_{load}	P_{size}	$P_{drugDiff}$	P_{intDeg}	P_{extDeg}	P_{zeta}	P_{diff}	M_{uptake}	P_{TL}	M_{TR}	$K_{D\text{-}TLR}$	k_{TLR}	k_{abs}	CL_{abs}	V_p	CL_p
Daily	*CFU*	---		---	--		-										+++
	Lesion AUC	+++	--	+++	+++	++											---
	Peripheral AUC	+++	-	+++	+++	++										+++	---
	Time to Sterilization	---	+	---	-												+++
Two Weeks	*CFU*	---	-	+	+									-			+++
	Lesion AUC	+++		+	+									+	-		---
	Peripheral AUC	+++		+										+		+++	---
	Time to Sterilization	---															+++

Carrier Dose Used: 1.2×10^9 carriers. P_{load} – load mass of drug (mg/carrier), P_{size} – size of carrier (μm), $P_{drugDiff}$ – diffusivity of drug in carrier ($\mu m^2/s$), P_{intDeg} – carrier intracellular degradation rate (1/s), P_{extDeg} – carrier extracellular degradation rate (1/s), P_{zeta} – carrier zeta-potential (mV), P_{diff} – diffusivity of carrier in lung tissue (cm^2/s), M_{uptake} – macrophage maximum carrier uptake probability (), P_{TL} – carrier density of targeting ligand (#/carrier), M_{TR} – macrophage density of targeting receptor (#/cell), $K_{D\text{-}TLR}$ – ligand-receptor dissociation constant (M), k_{TLR} – ligand-receptor carrier uptake rate (#/cell*s), k_{abs} – absorption rate constant (1/hr), CL_{abs} – clearance rate from 2nd absorption compartment (L/hr*kg), V_p – peripheral volume distribution (L/kg), CL_p – clearance rate from peripheral compartment (L/hr*kg). -/+ $p < 0.05$, --/++ $p < 0.001$, ---/+++ $p < 0.0001$ from sensitivity analysis.

6.3.3 Targeting Inhaled Formulations to Macrophages Has Limited Effects on Treatment Efficacy Due to the Dynamics of Granulomas

Targeting inhaled carriers to macrophages (the bacterial niche) could enhance the efficacy of inhaled treatments, as phagocytosis of carriers *in vitro* leads to increased intracellular concentrations of antibiotics (14–16, 18–20). Yet, there is no direct evidence that targeting an inhaled carrier to macrophages in granulomas provides any treatment

advantage. Using sensitivity analysis we explored the effects of macrophage targeting on treatment efficacy (CFU, granuloma AUC, peripheral AUC, and time to sterilization) for inhaled formulations of RIF and INH. We varied parameters that control the rate of macrophage uptake including carrier charge, movement rate, and a generalized form of ligand targeting (Tables 6.1 and 6.2).

Our analysis predicts that parameters influencing targeting of inhaled carriers to macrophages have limited effects on treatment efficacy for both RIF and INH. At both dosing frequencies of inhaled formulations of RIF, increased macrophage targeting leads to decreased antibiotic exposure in the granuloma and actually hinders antibiotic treatment (Table 6.1). For daily dosing of an inhaled formulation of INH, increased carrier charge (from negative to neutral – causing decreased uptake) is negatively correlated with CFU (Table 6.2). Macrophage targeting is limited by the granuloma structure as it prevents inhaled carriers from trafficking to and being phacoytosed by infected macrophages in the core of granulomas, which restricts any proposed advantage of elevated intracellular antibiotic concentrations. This limits macrophage uptake to outer regions of the granuloma where populations are largely healthy macrophages (see Movies at http://malthus.micro.med.umich.edu/lab/movies/InhaledAbx/). Therefore, our model predicts that there are no significant treatment benefits in designing inhaled carriers that specifically target macrophages due to the spatial organization of granulomas.

6.3.4 An Inhaled Formulation of RIF Can Reduce the Necessary Dose Frequency but Requires High Antibiotic Loading Which Can Lead to Increased Toxicity

We identified 14 different inhaled formulations of RIF dosed every two-weeks from sensitivity analysis that had equivalent CFU and reduced peripheral AUC at 7 days post-treatment initiation compared to daily dosed oral formulations (see Appendix D). Using these candidates along with an understanding of which dynamics most affect treatment efficacy we designed an ideal *in silico* inhaled formulation of RIF to be dosed every two-weeks. We design the carrier with a RIF loading of 1.18×10^{-6} mg/particle, an extracellular degradation rate 3-fold lower than the intracellular rate, and a high RIF carrier diffusivity, which promotes rapid-release of antibiotics from the carrier (Figure 6.3a). This equates to the entire total two-week dose given in the oral formulation. We observed no significant difference between the inhaled formulation, given every two weeks, and the oral formulation, given daily, when comparing the hazard ratio (Figure 6.3b). The inhaled formulation may prevent treatment failures by increasing early sterilizing capabilities of RIF compared to daily oral dosing (Figure D.2a in Appendix D).

Comparing average granuloma concentrations of RIF between the two formulations, we observe a significant difference in temporal dynamics: the inhaled formulation only eclipses the C_{50} of extracellular *Mtb* immediately after dosing and never surpasses the C_{50} for intracellular or non-replicating *Mtb* (Figure 6.3c) (see Movies at http://malthus.micro.med.umich.edu/lab/movies/InhaledAbx/). The average granuloma concentration of RIF steadily decreases, indicating that high antibiotic loading and fast carrier-release kinetics cannot maintain effective concentrations of RIF over the two-

week dosing window (Figure 6.3c). In part, this is due to the pharmacokinetics of RIF as it distributes rapidly from the site of dosing (lung) to other tissues, as demonstrated by the limited changes in the normalized ratio of granuloma AUC to peripheral AUC (16%) and granuloma AUC to plasma AUC (17%) (Figure 6.3d). The early granuloma and peripheral AUC are elevated after dosing compared to oral dosing, indicating that early granuloma exposure is associated with elevated toxicity (Figure D.2b-d in Appendix D). Daily oral dosing has similar problems surpassing the C_{50} values for intracellular and non-replicating *Mtb*, but the higher dosing frequency leads to average granuloma concentrations that exceed the C_{50} of extracellular *Mtb* after each dose (Figure 6.3c). Taken together, these results suggest that the dosing frequency of RIF could be reduced by appropriately designing an inhaled formulation, but that there is increased risk of early toxicity, a danger in reducing RIF to a bacteriostatic agent due to low granuloma concentrations, and limited feasibility based on the high carrier loading that would be required.

a

	Dosing Method	
	Oral	*Inhaled*
Dose Frequency	Daily	2 Weeks
Single Dose (mg/kg)	20	280
Total 2 Week Dose (mg/kg)	280	280
Inhaled Carrier Properties		
Intracellular $t_{1/2}$ (h)	59.2	
Extracellular $t_{1/2}$ (h)	192.5	
Diffusivity in Carrier ($\mu m^2/s$)	$2x10^{-7}$	

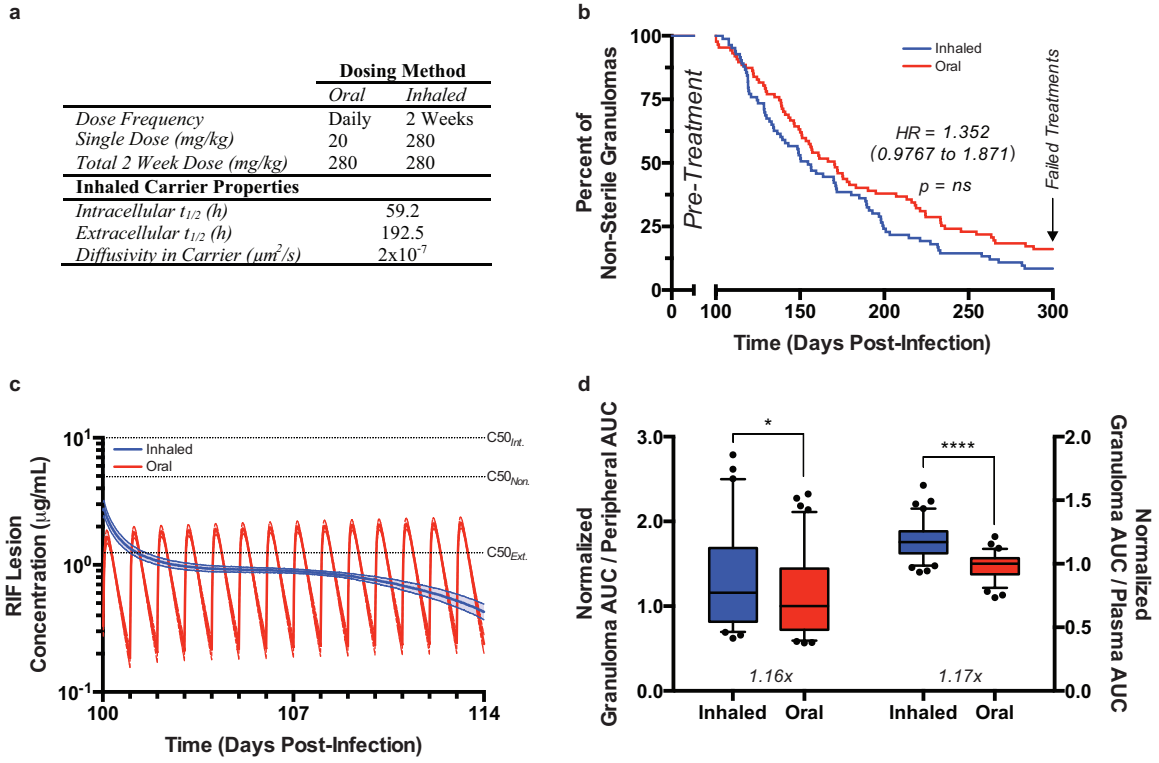

Figure 6.3 Comparison of an inhaled RIF formulation given every two-weeks with an oral RIF formulation given daily
(a) Comparison of the total two-week dose between formulations and the properties of the inhaled formulation. **(b)** Percent of granulomas not sterilized at indicated times after the initiation of treatment. Granulomas still present at 300 days post-infection are considered failed treatments. **(c)** Average RIF concentration in the granuloma for the first 14-day dosing window. Solid lines indicate average values while dotted lines represent SD. Dotted black lines indicate $C50_{Int}$, $C50_{Non}$, $C50_{Ext}$ for RIF. **(d)** Granuloma AUC/Peripheral AUC and Granuloma AUC/Plasma AUC for the first 14-day dosing window. Values are normalized to the median value of the oral dosing. Box and whiskers represents the 5 to 95 percentage range with data points outside the interval shown as black dots. * $p \leq 0.05$, ** $p \leq 0.01$, *** $p \leq 0.001$, **** $p \leq 0.0001$. Inhaled (N = 83), Oral (N = 87). (http://malthus.micro.med.umich.edu/lab/movies/InhaledAbx/)

6.3.5 An Inhaled Formulation of INH Can Reduce the Necessary Dose Frequency, Increase Therapeutic Efficacy, and Lessen Toxicity

We also identified 8 different inhaled formulations of INH dosed every two-weeks from sensitivity analysis that had equivalent or reduced CFU and reduced peripheral AUC at 7 days post-treatment initiation compared to daily dosed oral formulations (see Appendix D). Using these candidates along with an understanding of which dynamics most affect treatment efficacy we designed an ideal *in silico* inhaled

formulation of INH to be dosed every two-weeks. Based on the parameter values of the candidate formulations, we design the carrier with an INH loading of 7.2×10^{-8} mg/particle, a similar intra- and extracellular degradation rate, and a low INH carrier diffusivity, which promotes slow-release of antibiotics from the carrier (Figure 6.4a). This equates to a 12-fold lower total two-week dose compared to the oral formulation. We observe a significant difference in sterilizing capabilities between the inhaled formulation, given every two-weeks, and the oral formulation, given daily (Figure 6.4b). The hazard ratio is 1.6 (95% CI: 1.2 to 2.3) demonstrating decreased time to sterilization (all sterilized by 100 days post-treatment) and less failed treatments with an inhaled formulation (Figure 6.4b).

a

	Dosing Method	
	Oral	*Inhaled*
Dose Frequency	Daily	2 Weeks
Single Dose (mg/kg)	15	17.1
Total 2 Week Dose (mg/kg)	210	17.1
Inhaled Carrier Properties		
Intracellular $t_{1/2}$ (h)	50.6	
Extracellular $t_{1/2}$ (h)	50.6	
Diffusivity in Carrier ($\mu m^2/s$)	5.8×10^{-8}	

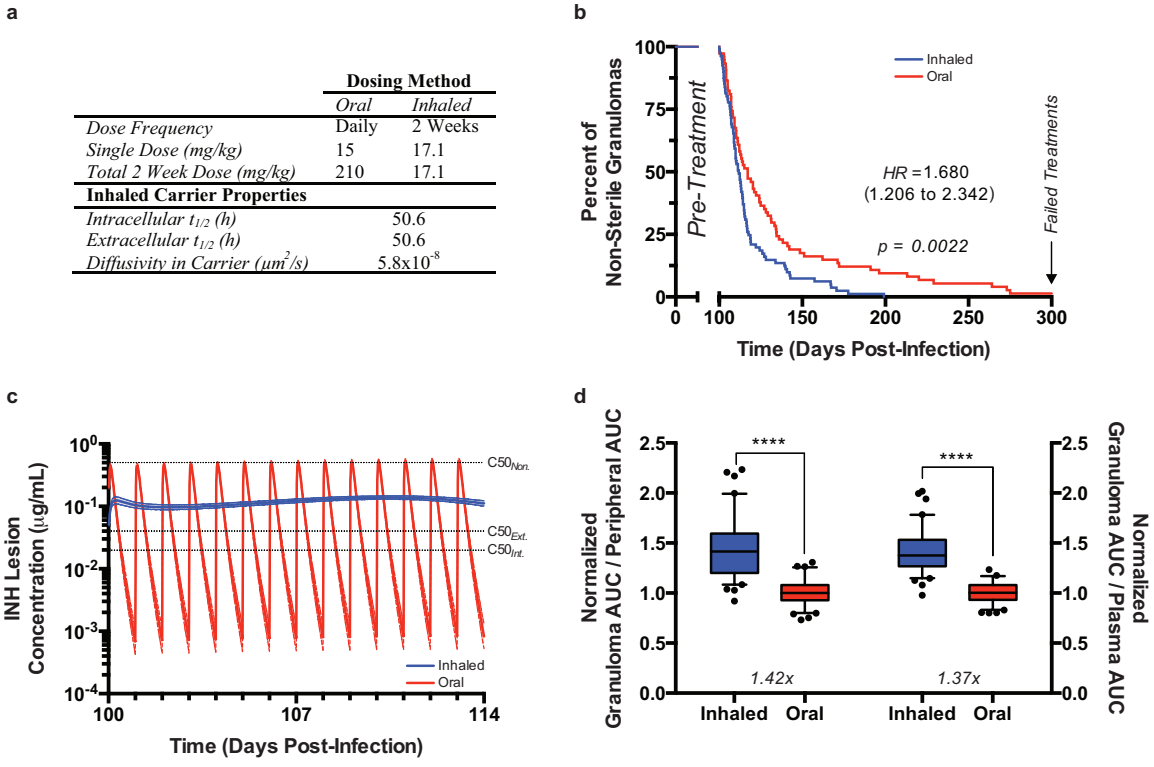

Figure 6.4 Comparison of an inhaled INH formulation given every two-weeks with an oral INH formulation given daily
(a) Comparison of the total two-week dose between formulations and the properties of the inhaled formulation. **(b)** Percent of granulomas not sterilized at indicated times after the initiation of treatment. Granulomas still present at 300 days post-infection are considered failed treatments. **(c)** Average INH concentration in the granuloma for the first 14-day dosing window. Solid lines indicate average values while dotted lines represent SD. Dotted black lines indicate $C50_{Int}$, $C50_{Non}$, $C50_{Ext}$ for INH. **(d)** Granuloma AUC/Peripheral AUC and Granuloma AUC/Plasma AUC for the first 14-day dosing window. Values are normalized to the median value of the oral dosing. Box and whiskers represents the 5 to 95 percentage range with data points outside the interval shown as black dots. * $p \leq 0.05$, ** $p \leq 0.01$, *** $p \leq 0.001$, **** $p \leq 0.0001$. Inhaled (N = 81), Oral (N = 87). (http://malthus.micro.med.umich.edu/lab/movies/InhaledAbx/)

The average INH granuloma concentrations during treatment with the inhaled formulation are sustained above C_{50} values for intra- and extracellular *Mtb* populations for the entire dosing window, compared to the daily dosed oral formulation (Figure 6.4c) (see Movies at http://malthus.micro.med.umich.edu/lab/movies/InhaledAbx/). Sustained granuloma concentrations of INH during treatment prevent bacterial re-growth between doses associated with daily oral INH dosing (Figure D.3a in Appendix D). The ability of an inhaled formulation to maintain effective granuloma concentrations of INH is due to the combination of slow carrier-release kinetics, dosing to the site of infection, and gradual distribution of INH from the lung to other tissues. The normalized ratio of granuloma AUC to peripheral AUC is increased 42% and granuloma AUC to plasma AUC is increased 37% (Figure 6.3d), indicating that the inhaled formulation is able to provide additional granuloma exposure with only a fraction of the associated toxicity (Figure D.3b-d in Appendix D). This increase in relative exposure in the granuloma of an inhaled formulation occurs at a significantly reduced total two-week dose (Figure 6.4a). Together, these results demonstrate that a suitably designed inhaled formulation of INH can reduce dose frequency, increase the sterilizing capability, and reduce toxicity of INH by maintaining suitable concentrations in the granuloma for the entire dosing window.

6.4 Discussion

Rational development of inhaled antibiotic formulations for treatment of TB necessitates a systems pharmacology approach that simultaneously captures pharmacokinetics, granuloma dynamics, carrier-release dynamics and behavior, and pharmacodynamics to understand what controls treatment efficacy. We developed a computational model that tracks these dynamics and used it to understand and rationally design inhaled formulations with reduced dosing frequencies. We predict that an inhaled formulation of INH, dosed every two-weeks, is feasible and would have better sterilizing capabilities with reduced toxicity compared to daily oral dose formulations. Inhaled formulations of RIF, dosed every two-weeks, have equivalent sterilizing capabilities as daily oral dose formulations, but early toxicity and impractical carrier loadings likely render it a non-viable alternative.

Compliance is a long-standing concern for TB treatment. Current oral regimens are lengthy and complex which contributes to a significant number of failed treatments (1). Direct-observed treatment short-course (DOTS) now accompanies most regimens in an attempt to prevent failures, and yet in many non-developed countries DOTS is not feasible (45). Even in countries with effective DOTS programs the successful treatment rate of antibiotic-susceptible TB is only 34-76% (46). Thus, new treatment strategies that can reduce dose frequency and alleviate the ‘pill-burden’ would revolutionize treatment compliance. Our model predicts that properly designed inhaled formulations of INH could be promising avenues to accomplish these goals. Yet, the applicability of inhaled formulations must be taken in context with other antibiotics, as orally dosed mono-

therapies are not used for treatment of active TB due to the development of antibiotic resistance.

Previous work on the design of inhaled antibiotics for TB treatment has largely focused on single aspects of treatment dynamics. For instance, considerable work has been dedicated to targeting inhaled carriers to macrophages under the assumption that increasing intracellular antibiotic concentrations would increase sterilization in the bacterial niche (11, 12, 14–17). Using our systems pharmacology-based model, we predict that targeting carriers to macrophages has limited and or negative effects on overall treatment efficacy. This is principally due to discrepancies between *in vitro* settings, where the majority of macrophages are infected and an abundance of carriers are available for phagocytosis, and *in vivo* infection scenarios, where infected macrophages reside in the center of a densely packed granuloma. Specifically for RIF, macrophage targeting increases carrier uptake by uninfected macrophages in the outer regions of the granuloma, reducing RIF exposure in the interior of the granuloma since it is more rapidly consumed than INH (1, 10).

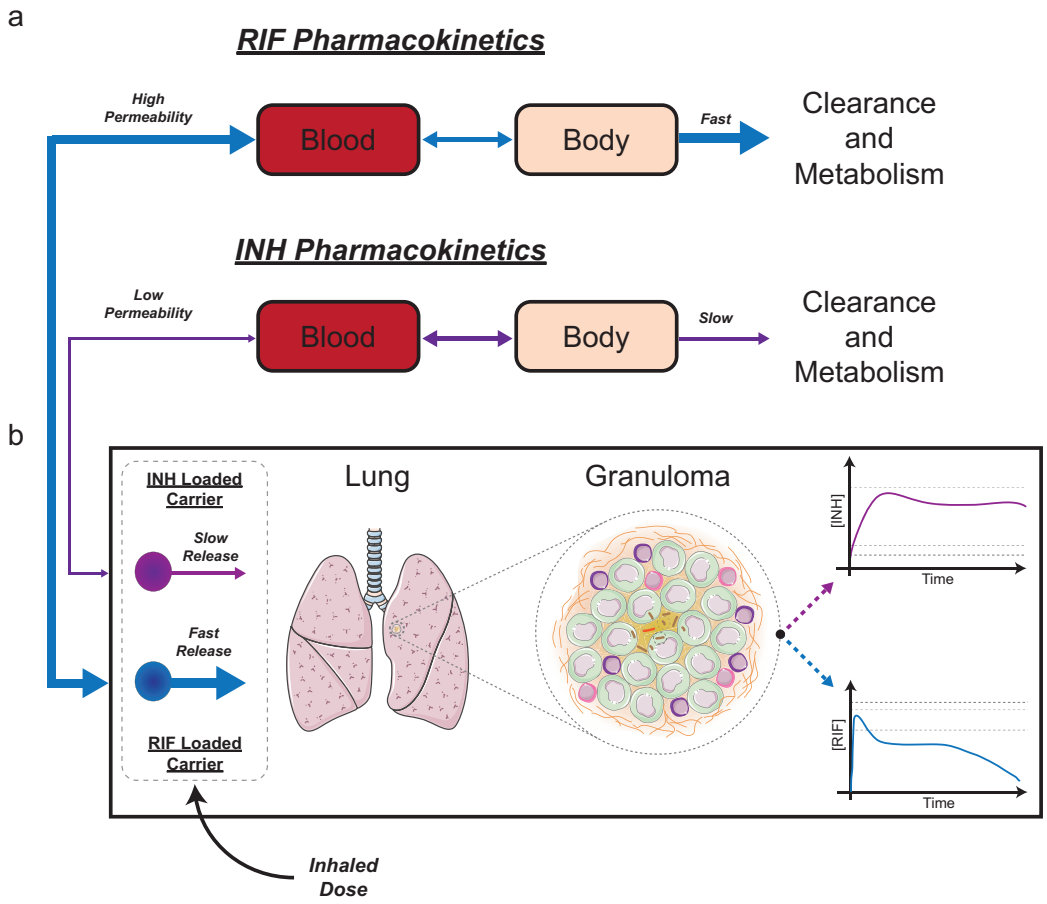

Figure 6.5 Schematic showing the relative aspects of inhaled formulations for RIF and INH
(a) Pharmacokinetics of RIF and INH demonstrating relative rates of lung permeability, inter-compartment transport, and clearance. RIF: high lung permeability and fast clearance and metabolism. INH: low lung permeability and slow clearance and metabolism. (b) Inhaled carrier release kinetics need to be designed by considering granuloma dynamics, antibiotic pharmacodynamics, and non-lung pharmacokinetics. The increased permeability and distribution of RIF to other organs must be compensated for by faster inhaled carrier release kinetics. Although faster carrier release kinetics can elevate concentrations of RIF in granulomas, the high concentrations necessary (based on the pharmacodynamics of RIF) prevent increased efficacy. The decreased permeability and slower distribution of INH to other organs allows inhaled carrier release kinetics to be more gradual. Based on pharmacodynamics of INH, carrier release kinetics must maintain relatively low concentrations of INH within granulomas to increase efficacy.

It is important to understand the effects of carrier-release kinetics at the site of infection and how they can be influenced by pharmacokinetic distribution. Our model suggests that pharmacokinetics outside of lungs play a significant role in determining efficacy of inhaled carriers as transport rates of antibiotics out of lungs must be compensated for by carrier-release kinetics (Fig. 5). We predict that an inhaled

formulation dosed every two-weeks must be designed differently for RIF and INH. Since RIF distributes to all parts of the body, the carrier loading must be more than 10-fold higher than INH and needs to be released significantly faster in order to maintain effective concentrations in granulomas (47). Indeed, the necessary antibiotic loading for RIF may exceed 90% by weight, a current limitation of many carrier systems (12, 13). Combined with early increased toxicity, a RIF-loaded inhaled formulation may not be a useful therapeutic. In contrast, the antibiotic loading of INH is highly feasible (~30-50% weight percent) and the slow release kinetics would be straightforward to control by modulating physio-chemical properties of the carrier such as polymer molecular weight or monomer ratio (20). Further studies into better design of inhaled formulations, combinatorial treatment, and the cost and distribution issues associated with a new TB treatment regimens are needed (12, 13, 48).

The incidence of both multi-drug resistant and extensively-drug resistant TB cases is rising (49). Although inhaled formulations could reduce dosing frequency, exposing *Mtb* to extended periods of low antibiotic concentrations might cause rapid onset of drug-resistance (1, 50). Our model predicts that antibiotic exposure in granulomas is lower than plasma exposure for inhaled formulations, similar to orally dosed antibiotics (1, 10). Thus, previous *in vivo* studies of inhaled formulations that assumed elevated plasma concentrations of antibiotics translated to increased antibiotic concentrations in granuloma could have been exposing bacteria to sub-optimal concentrations promoting the onset of drug-resistance (1, 11–13, 50). It is possible that inhaled formulations of RIF may contribute to resistance due to diminishing concentrations in the lesion during the reduced dosing window (Figure 6.3c). Conversely, an inhaled formulation of INH might

reduce resistance due to reduced cycling between effective and non-effective antibiotic concentrations associated with daily oral dosing, but this remains to be tested. Additionally, faster times to sterilization could reduce the probability of *Mtb* gaining resistance mutations (Figure 6.4c). Further work is needed to pair an accurate model of antibiotic-resistance with our systems pharmacology approach.

Current treatment strategies for TB rely on antibiotics developed half a century ago, well before the advent of PK/PD models (1). We develop a computational approach to help rationally design inhaled formulations to increase efficacy and reduce non-compliance and toxicity issues of existing antibiotics. Our platform captures antibiotic dynamics (PK, PD, granuloma, carrier) across multiple transport compartments, and demonstrates that these dynamics must be considered together when developing inhaled formulations. Although we demonstrate this platform using RIF and INH, it can be readily adapted to prototype possible inhaled formulations of 'second-line' antibiotics used to treat drug-resistant TB. These antibiotics, such as fluroquinolones and aminoglycosides, are given for 18-24 months and for some, toxicity concerns necessitate intravenous dosing (1). The ability to quickly assess which antibiotics would be the most promising candidates for an inhaled formulation would considerably reduce development time of new treatments. Our unique computational platform, used in parallel with experimental models, provides an integrated approach to improve treatment of TB.

6.5 References

1. Dartois, V. 2014. The path of anti-tuberculosis drugs: from blood to lesions to mycobacterial cells. *Nat. Rev. Microbiol.* 12: 159–167.

2. Griffiths, G., B. Nyström, S. B. Sable, and G. K. Khuller. 2010. Nanobead-based interventions for the treatment and prevention of tuberculosis. *Nat. Rev. Microbiol.* 8: 827–34.

3. O'Garra, A., P. S. Redford, F. W. McNab, C. I. Bloom, R. J. Wilkinson, and M. P. R. Berry. 2013. The immune response in tuberculosis. *Annu. Rev. Immunol.* 31: 475–527.

4. *Global Tuberculosis Report 2013*,. World Health Organization, Geneva ; :1–145.

5. Zumla, A., P. Nahid, and S. T. Cole. 2013. Advances in the development of new tuberculosis drugs and treatment regimens. *Nat. Rev. Drug Discov.* 12: 388–404.

6. Lin, P. L., V. Dartois, P. J. Johnston, C. Janssen, L. Via, M. B. Goodwin, E. Klein, C. E. Barry, and J. L. Flynn. 2012. Metronidazole prevents reactivation of latent Mycobacterium tuberculosis infection in macaques. *Proc. Natl. Acad. Sci. U. S. A.* 109: 14188–93.

7. Flynn, J. L., and J. Chan. 2001. Immunology of tuberculosis. *Annu. Rev. Immunol.* 19: 93–129.

8. Lin, P. L., C. B. Ford, M. T. Coleman, A. J. Myers, R. Gawande, T. Ioerger, J. Sacchettini, S. M. Fortune, and J. L. Flynn. 2014. Sterilization of granulomas is common in active and latent tuberculosis despite within-host variability in bacterial killing. *Nat. Med.* 20: 75–9.

9. Lin, P. L., S. Pawar, A. Myers, A. Pegu, C. Fuhrman, T. a Reinhart, S. V Capuano, E. Klein, and J. L. Flynn. 2006. Early events in Mycobacterium tuberculosis infection in cynomolgus macaques. *Infect. Immun.* 74: 3790–803.

10. Kjellsson, M. C., L. E. Via, A. Goh, D. Weiner, K. M. Low, S. Kern, G. Pillai, C. E. Barry, and V. Dartois. 2012. Pharmacokinetic evaluation of the penetration of antituberculosis agents in rabbit pulmonary lesions. *Antimicrob. Agents Chemother.* 56: 446–57.

11. Misra, A., A. J. Hickey, C. Rossi, G. Borchard, H. Terada, K. Makino, P. B. Fourie, and P. Colombo. 2011. Inhaled drug therapy for treatment of tuberculosis. *Tuberculosis (Edinb).* 91: 71–81.

12. Muttil, P., C. Wang, and A. J. Hickey. 2009. Inhaled drug delivery for tuberculosis therapy. *Pharm. Res.* 26: 2401–16.

13. Sosnik, A., A. M. Carcaboso, R. J. Glisoni, M. a Moretton, and D. a Chiappetta. 2010. New old challenges in tuberculosis: potentially effective nanotechnologies in drug delivery. *Adv. Drug Deliv. Rev.* 62: 547–59.

14. Zhou, H., Y. Zhang, D. L. Biggs, M. C. Manning, T. W. Randolph, U. Christians, B. M. Hybertson, and K. Ng. 2005. Microparticle-based lung delivery of INH decreases INH metabolism and targets alveolar macrophages. *J. Control. Release* 107: 288–99.

15. Hirota, K., T. Hasegawa, H. Hinata, F. Ito, H. Inagawa, C. Kochi, G.-I. Soma, K. Makino, and H. Terada. 2007. Optimum conditions for efficient phagocytosis of rifampicin-loaded PLGA microspheres by alveolar macrophages. *J. Control. Release* 119: 69–76.

16. Parikh, R., S. Dalwadi, P. Aboti, and L. Patel. 2014. Inhaled microparticles of antitubercular antibiotic for in vitro and in vivo alveolar macrophage targeting and activation of phagocytosis. *J. Antibiot. (Tokyo).* 1–8.

17. Muttil, P., J. Kaur, K. Kumar, A. B. Yadav, R. Sharma, and A. Misra. 2007. Inhalable microparticles containing large payload of anti-tuberculosis drugs. *Eur. J. Pharm. Sci.* 32: 140–50.

18. Verma, R. K., J. Kaur, K. Kumar, A. B. Yadav, and A. Misra. 2008. Intracellular time course, pharmacokinetics, and biodistribution of isoniazid and rifabutin following pulmonary delivery of inhalable microparticles to mice. *Antimicrob. Agents Chemother.* 52: 3195–201.

19. Yoshida, A., M. Matumoto, H. Hshizume, Y. Oba, T. Tomishige, H. Inagawa, C. Kohchi, M. Hino, F. Ito, K. Tomoda, T. Nakajima, K. Makino, H. Terada, H. Hori, and G.-I. Soma. 2006. Selective delivery of rifampicin incorporated into poly(DL-lactic-co-glycolic) acid microspheres after phagocytotic uptake by alveolar macrophages, and the killing effect against intracellular Mycobacterium bovis Calmette-Guérin. *Microbes Infect.* 8: 2484–91.

20. Makino, K., T. Nakajima, M. Shikamura, F. Ito, S. Ando, C. Kochi, H. Inagawa, G.-I. Soma, and H. Terada. 2004. Efficient intracellular delivery of rifampicin to alveolar macrophages using rifampicin-loaded PLGA microspheres: effects of molecular weight and composition of PLGA on release of rifampicin. *Colloids Surf. B. Biointerfaces* 36: 35–42.

21. Ain, Q., S. Sharma, S. K. Garg, and G. K. Khuller. 2002. Role of poly [DL-lactide-co-glycolide] in development of a sustained oral delivery system for antitubercular drug(s). *Int. J. Pharm.* 239: 37–46.

22. Sharma, A., S. Sharma, and G. K. Khuller. 2004. Lectin-functionalized poly (lactide-co-glycolide) nanoparticles as oral/aerosolized antitubercular drug carriers for treatment of tuberculosis. *J. Antimicrob. Chemother.* 54: 761–6.

23. Flynn, J. L. 2006. Lessons from experimental Mycobacterium tuberculosis infections. *Microbes Infect.* 8: 1179–88.

24. Kumar Verma, R., J. K. Mukker, R. S. P. Singh, K. Kumar, P. R. P. Verma, and A. Misra. 2012. Partial biodistribution and pharmacokinetics of isoniazid and rifabutin following pulmonary delivery of inhalable microparticles to rhesus macaques. *Mol. Pharm.* 9: 1011–6.

25. Dharmadhikari, A. S., M. Kabadi, B. Gerety, A. J. Hickey, P. B. Fourie, and E. Nardell. 2013. Phase I, single-dose, dose-escalating study of inhaled dry powder capreomycin: a new approach to therapy of drug-resistant tuberculosis. *Antimicrob. Agents Chemother.* 57: 2613–9.

26. Pandey, R., A. Sharma, a Zahoor, S. Sharma, G. K. Khuller, and B. Prasad. 2003. Poly (DL-lactide-co-glycolide) nanoparticle-based inhalable sustained drug delivery system for experimental tuberculosis. *J. Antimicrob. Chemother.* 52: 981–6.

27. Coowanitwong, I., V. Arya, P. Kulvanich, and G. Hochhaus. 2008. Slow release formulations of inhaled rifampin. *AAPS J.* 10: 342–8.

28. Fallahi-Sichani, M., J. L. Flynn, J. J. Linderman, and D. E. Kirschner. 2012. Differential risk of tuberculosis reactivation among anti-TNF therapies is due to drug binding kinetics and permeability. *J. Immunol.* 188: 3169–78.

29. Fallahi-Sichani, M., M. El-Kebir, S. Marino, D. E. Kirschner, and J. J. Linderman. 2011. Multiscale computational modeling reveals a critical role for TNF-α receptor 1 dynamics in tuberculosis granuloma formation. *J. Immunol.* 186: 3472–83.

30. Ray, J. C. J., J. L. Flynn, and D. E. Kirschner. 2009. Synergy between individual TNF-dependent functions determines granuloma performance for controlling Mycobacterium tuberculosis infection. *J. Immunol.* 182: 3706–17.

31. Cilfone, N. A., C. R. Perry, D. E. Kirschner, and J. J. Linderman. 2013. Multi-Scale Modeling Predicts a Balance of Tumor Necrosis Factor-α and Interleukin-10 Controls the Granuloma Environment during Mycobacterium tuberculosis Infection. *PLoS One* 8: e68680.

32. Linderman, J. J., C. A. Hunt, S. Marino, M. Fallahi-Sichani, and D. Kirschner. 2014. Tuneable resolution as an approach to study multi-scale, multi-organ models in systems biology. *WIRES Syst. Biol. Med.* In Press.

33. Lin, P. L., M. Rodgers, L. Smith, M. Bigbee, A. Myers, C. Bigbee, I. Chiosea, S. V Capuano, C. Fuhrman, E. Klein, and J. L. Flynn. 2009. Quantitative comparison of active and latent tuberculosis in the cynomolgus macaque model. *Infect. Immun.* 77: 4631–42.

34. Tabata, Y., and Y. Ikada. 1988. Effect of the size and surface charge of polymer microspheres on their phagocytosis by macrophage. *Biomaterials* 9: 356–62.

35. Champion, J. a, A. Walker, and S. Mitragotri. 2008. Role of particle size in phagocytosis of polymeric microspheres. *Pharm. Res.* 25: 1815–21.

36. Hasegawa, T., K. Hirota, K. Tomoda, F. Ito, H. Inagawa, C. Kochi, G.-I. Soma, K. Makino, and H. Terada. 2007. Phagocytic activity of alveolar macrophages toward polystyrene latex microspheres and PLGA microspheres loaded with anti-tuberculosis agent. *Colloids Surf. B. Biointerfaces* 60: 221–8.

37. Kalluru, R., F. Fenaroli, D. Westmoreland, L. Ulanova, A. Maleki, N. Roos, M. Paulsen Madsen, G. Koster, W. Egge-Jacobsen, S. Wilson, H. Roberg-Larsen, G. K. Khuller, A. Singh, B. Nyström, and G. Griffiths. 2013. Poly(lactide-co-glycolide)-rifampicin nanoparticles efficiently clear Mycobacterium bovis BCG infection in macrophages and remain membrane-bound in phago-lysosomes. *J. Cell Sci.* 126: 3043–54.

38. Cu, Y., and W. M. Saltzman. 2010. Controlled surface modification with poly(ethylene)glycol enhances diffusion of PLGA nanoparticles in human cervical mucus. *Mol. Pharm.* 6: 173–81.

39. Siepmann, J., and F. Siepmann. 2008. Mathematical modeling of drug delivery. *Int. J. Pharm.* 364: 328–43.

40. Kanjickal, D. G., and S. T. Lopina. 2004. Modeling of drug release from polymeric delivery systems--a review. *Crit. Rev. Ther. Drug Carrier Syst.* 21: 345–86.

41. Arifin, D. Y., L. Y. Lee, and C.-H. Wang. 2006. Mathematical modeling and simulation of drug release from microspheres: Implications to drug delivery systems. *Adv. Drug Deliv. Rev.* 58: 1274–325.

42. Lin, P. L., T. Coleman, J. P. J. Carney, B. J. Lopresti, J. Tomko, D. Fillmore, V. Dartois, C. Scanga, L. J. Frye, C. Janssen, E. Klein, C. E. Barry, and J. L. Flynn. 2013. Radiologic responses in cynomolgous macaques for assessing tuberculosis chemotherapy regimens. *Antimicrob. Agents Chemother.* .

43. Marino, S., I. B. Hogue, C. J. Ray, and D. E. Kirschner. 2008. A methodology for performing global uncertainty and sensitivity analysis in systems biology. *J. Theor. Biol.* 254: 178–96.

44. Yeh, H.-C., and G. M. Schum. 1980. Models of human lung airways and their application to inhaled particle deposition. *Bull. Math. Biol.* 42: 461–480.

45. Phillips, L. 2013. Infectious disease: TB's revenge. *Nature* 493: 14–6.

46. Pasipanodya, J., and T. Gumbo. 2011. An oracle: antituberculosis pharmacokinetics-pharmacodynamics, clinical correlation, and clinical trial simulations to predict the future. *Antimicrob. Agents Chemother.* 55: 24–34.

47. Nitti, V., R. Virgilio, M. R. Patricolo, and A. Iuliano. 1977. Pharmacokinetic study of intravenous rifampicin. *Chemotherapy* 23: 1–6.

48. Forbes, B., B. Asgharian, L. A. Dailey, D. Ferguson, P. Gerde, M. Gumbleton, L. Gustavsson, C. Hardy, D. Hassall, R. Jones, R. Lock, J. Maas, T. McGovern, G. R. Pitcairn, G. Somers, and R. K. Wolff. 2011. Challenges in inhaled product development and opportunities for open innovation. *Adv. Drug Deliv. Rev.* 63: 69–87.

49. Dheda, K., T. Gumbo, N. R. Gandhi, M. Murray, G. Theron, Z. Uwadia, G. B. Migliori, and R. Warren. 2014. Global control of tuberculosis: from extensively drug-resistant to untreatable tuberculosis. *Lancet Respir. Med.* 2600: 1–18.

50. Duncan, K., and C. E. Barry. 2004. Prospects for new antitubercular drugs. *Curr. Opin. Microbiol.* 7: 460–5.

Chapter 7

Measuring Soluble TNF Concentration Gradients in Granuloma

7.1 Introduction

Gradients of soluble molecules are predicted to control many aspects of biological processes, including embryonic development, tumor growth, and immune responses (1–9). Gradients can form due to distinct spatial patterns of soluble molecule secreting cells, diffusion of soluble molecules through the extracellular space in tissues, and differential cellular trafficking of soluble molecules. Because a cellular response may depend upon the concentration of a soluble molecule, the positional information contained in gradients may control the diversity of cellular responses to the same soluble molecule (2, 3).

Upon inhalation of *Mycobacterium tuberculosis* (*Mtb*), bacteria are phagocytosed by alveolar macrophages. Subsequent recruitment of additional macrophages, dendritic cells, T cells, and B cells to the site of infection leads to a self-organizing structure called a granuloma, which creates a physical and immunological barrier around infection (10–12). Granulomas have a distinct cellular organization with macrophages and dendritic cells in the core surrounded by an outer region of lymphocytes, forming a roughly spherical immune microenvironment for bacterial control (10–12).

An artificial model of granuloma formation can be induced in pre-sensitized mice following pulmonary embolism of injected beads conjugated to *Mycobacterium* purified protein derivative (PPD) (13–16). Although this model does not use live bacteria, the

spatial organization of dendritic cells, macrophages, and T cells recruited to the bead is similar to those observed in live infection models (13, 14). In addition, the cytokine and chemokine responses in this model are primarily Th-1 based, similar to those associated with granuloma formation and function in other models of infection (15, 17). Unlike live-infection models, which take weeks to develop granulomas in response to bacterial challenge, granulomas develop within 2 days in the PPD bead model of infection (14). Due to the significantly shorter time frame to granuloma formation, lung granulomas from the PPD bead model can be rapidly isolated and studied.

Recent computational models of *Mtb* infection predict that gradients of the pro-inflammatory cytokine tumor necrosis factor-α (TNF) form in granulomas (6, 7, 18). In addition, we predicted spatial gradients of both TNF and IL-10 in Chapters 3, 4, and 5. These spatial gradients of TNF lead to differential activation of related signaling pathways that are critical to control of infection (6, 7, 18). Higher TNF concentrations near the core of granulomas would preferentially induce apoptosis of infected macrophages while lower TNF concentrations in outer regions of granulomas are still high enough to activate NFκB signaling, promoting macrophage activation and survival of activated T cells (6, 7, 18). Although the presence of TNF gradients in granulomas appears critical to immunological control of *Mtb* infection, we know of no attempts to measure these gradients in the context of granulomas.

Previous efforts to measure concentrations of TNF in *ex vivo* tissues have relied on more common probes such as anti-TNF antibodies or in-situ hybridization of TNF DNA/RNA (19–21). However, due to long perfusion and fixation times and the ability of soluble molecules to diffuse in the extracellular tissue space and perfusion media,

gradients and spatial information of soluble molecules are easily lost or interrupted. Furthermore, the specificity of anti-TNF antibodies is typically against both bound and unbound forms of TNF. Thus, it was necessary to develop a new method in order to measure soluble TNF gradients in granulomas.

In this Chapter, we develop a method for detecting soluble TNF gradients in *ex vivo* granuloma tissue. The novelty of our method is the combination of a simple receptor-ligand model, known cellular organization, and easily gathered flow cytometry data from homogenized populations in order to reconstruct soluble gradients. We construct a molecular probe based on biotinylation of recombinant TNF that specifically targets unbound TNF receptors (22–26). Using immunofluorescence techniques we identify the spatial organization of cells in granulomas. Using the combination of flow cytometry data, granuloma organization, and fluorescent microscopy of unbound TNF receptors we are able to reconstruct relative soluble TNF gradients.

7.2 Materials and Methods

7.2.1 Methodology for Reconstructing Soluble TNF Gradients

In an *in vivo* granuloma at the single cell-level, we assume soluble TNF binds to the TNF receptor based on the following kinetics:

$$[TNF] + [TNFR_{Free}] \overset{K_D}{\leftrightarrow} [TNF \cdot TNFR] \qquad (Eqn.\,7.1)$$

where K_D is the equilibrium dissociation constant. The receptor TNFR here includes both TNFR1 and TNFR2. The TNFR mass balance is given by:

$$[TNFR_{Free}] + [TNF \cdot TNFR] = [TNFR_{Total}] \qquad (Eqn.\,7.2)$$

We assume the association and dissociation reactions were in equilibrium in the granuloma before lung excision, and thus upon substitution and rearrangement:

$$\frac{[TNF]}{K_D} + 1 = \frac{[TNFR_{Total}]}{[TNFR_{Free}]} \qquad (Eqn. 7.3)$$

The left hand side of the equation is dimensionless as both the concentration of soluble TNF and equilibrium dissociation constant have the units M. As a result, the dimensionless soluble concentration of TNF (ψ) is directly proportional to the state of the TNFR system:

$$\psi = \frac{[TNFR_{Total}]}{[TNFR_{Free}]} \qquad (Eqn. 7.4)$$

Therefore, a dual probe system that measures total TNFR and free TNFR concentrations provides enough data to estimate dimensionless soluble TNF concentrations. Furthermore, measurements must contain relative spatial information in order to reconstruct a gradient, as total TNFR numbers vary between cell-types. Total TNFR concentrations from the PPD bead model granulomas were previously measured via flow-cytometry for dendritic cells, macrophages, and T cells (7). Therefore, we must measure two additional quantities from the PPD granuloma model using fluorescent microscopy techniques: (1) the spatial organization of cell-types in the PPD granuloma and (2) free TNFR concentrations as a function of radial distance. The first measurement will allow us to add spatial information to the existing flow cytometry data by identifying the locations of specific cell-types in granulomas. This is accomplished using traditional immunofluorescence protocols for identifying cell-types in the PPD granuloma model (13). The second measurement provides a direct measurement of free TNFR as a function of position, to be used in Eqn. 7.4. We accomplish this by cross-linking any existing TNF

bound to TNFR present in the granuloma through brief chemical fixation (Figure 7.1). Therefore, the only available TNFR binding sites for a molecular probe should be free TNFR in the granuloma tissue (Figure 7.1). We construct a molecular probe that measures these free TNF receptors by biotinylating recombinant TNF and visualizing it with fluorescence (Figure 7.1).

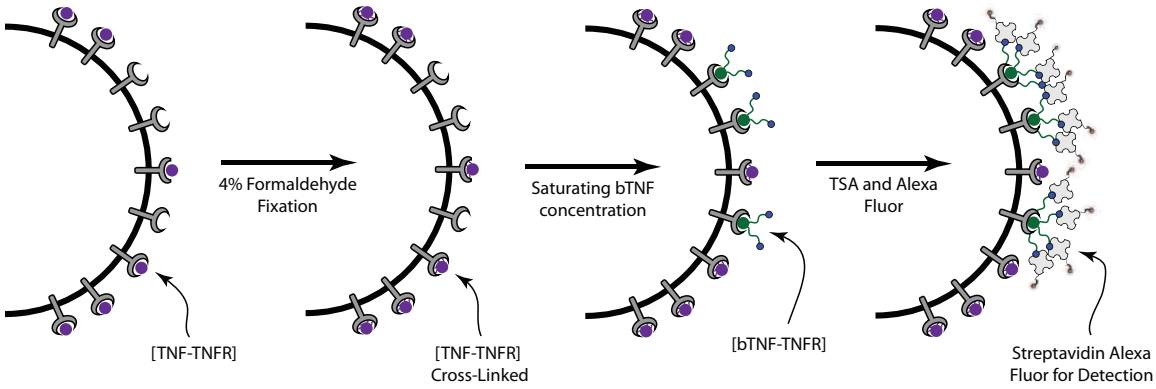

Figure 7.1. Schematic representation of the protocol to identify free TNFR
Any existing TNF bound to TNFR is cross-linked in a fixation step, which prevents dissociation. Therefore, the only available sites for biotinylated TNF to bind are free TNFR sites. Biotiylated TNF is added in excess in order to saturate all free TNFR sites and is subsequently detected using fluorescent labels described in Section 7.2.5.

7.2.2 Preparation of Tissue Sections From a Mouse Granuloma Model

C57BL/6 mice (N = 6, Jackson Laboratory) were pre-sensitized with 20 μg of *Mycobacterium bovis* purified protein derivative (PPD) incorporated with 0.25 mL of complete Freund's adjuvant (CFA) by subcutaneous injection. Fourteen days later Sepharose 4B beads covalently coupled to *Mycobacterium* purified protein derivative (PPD), as previously described (15, 17), were intravenous injected into the tail vein. The mice were sacrificed four days after bead embolism, coinciding with maximum granuloma size. Lungs were perfused with cold RPMI-1640 (BioWhittiker) and then excised from the mice. Lung tissue was embedded in Tissue-Tek OCT compound in a

cryomold and flash frozen in liquid nitrogen. 4-8 μm thick cryosections were cut on a cryotome and two subsequent cryosections were adjacently mounted on a single silanized slide and dried with a cold drier. Slides were stored at -70°C for future use.

7.2.3 Biotinylation of TNF

5 μg of recombinant mouse TNF (BioLegend) was biotinylated using Ez-Link Sulfo-NHS-Biotin (Pierce) at a 1:66 ratio. 1.913 μL of 10 mM Sulfo-NHS-Biotin solution was mixed with 500 μL of 10 μg/mL recombinant mouse TNF diluted in 0.1 M sodium citrate at pH 5.8 for 3 hours at 4°C with mixing every 60 minutes (23). The solution was dialyzed against PBS using Pierce Slide-A-Lyzer dialysis cassetes at 4°C overnight to exchange buffers. Excess unconjugated biotin was removed using Pierce Zebra-Desalt Columns with a 10K MW cutoff. Verification of successful biotinylation was carried out using a FRET based reporter assay (AnaSpec) and a Bradford assay to assess protein concentration.

7.2.4 Biotinylated TNF Staining Protocol

Cryosections were removed from storage at -70°C and quickly fixed in 4% formaldehyde (Sigma-Aldrich) at -20°C for 5 min. Sections were surrounded with an ImmEdge pen (DAKO) to prevent reagent leakage. Slides are washed in 1X PBS (Sigma-Aldrich) for 10 min then rinsed with 1X PBS + 0.05% Tween20 (PBST) (Sigma-Aldrich). All further steps were carried out in a humidified chamber. Peroxidase was blocked with 3% peroxide diluted in PBS for 15 minutes. Slides were then washed 3 times in PBS for 2 minutes and rinsed with PBST for 1 minute. Exogenous and

endogenous streptavidin and biotin was blocked with a Streptavidin/Biotin Blocking Kit (Invitrogen) for 15 minutes each with rinsing steps in between. Sections were then blocked with 1X PBS + 7% BSA + 1% FCS + 2% NGS + 0.02% Azide (incubation buffer) for 30 min to reduce background staining.

Biotinylated TNF, as prepared above, was diluted to 5 μg/mL in incubation buffer and incubated with tissues for 60 minutes at room temperature. Negative controls were further incubated with 10 μg/mL of recombinant TNF in PBS for an additional 60 minutes at room temperature as a competitive inhibitor. Slides were washed 3 times in PBS for 2 minutes and rinsed with PBST for 1 minute. Tyramide signal amplification was carried out using a TSA kit (Perkin-Elmer), which involved 30 minutes of streptavidin-HRP (1:100 dilution) incubation followed by 10 minutes of incubation with biotinyl-tyramide (1:50 dilution) at room temperature. Slides were washed 3 times in PBS for 2 minutes and rinsed with PBST for 1 minute. Tissues were incubated with streptavidin-Alexa 568 (1:500 dilution, Invitrogen) for 30 minutes at room temperature. Slides were washed 3 times in PBS for 2 minutes and rinsed with PBST for 1 minute. Cover glass (Fisher Scientific) was mounted using ProLong® Gold anti-fade reagent with DAPI (Invitrogen). Slides were shielded from light and allowed to cure overnight. Tissues were imaged with a Leica Inverted SP5 Confocal microscope at a magnification of 40X (Microscopy and Imaging Laboratory, University of Michigan).

7.2.5 Immunofluorescence Staining Protocol

Cryosections were removed from storage at -70°C and fixed in acetone (Sigma-Aldrich) at -20°C for 5 min and subsequently air-dried for 30 min. Sections were

surrounded with an ImmEdge pen (DAKO) to prevent reagent leakage. Slides are washed in 1X PBS (Sigma-Aldrich) for 10 min then rinsed with 1X PBS + 0.05% Tween20 (PBST) (Sigma-Aldrich). All further steps were carried out in a humidified chamber. Exogenous and endogenous streptavidin and biotin was blocked with a Streptavidin/Biotin Blocking Kit (Invitrogen) for 15 minutes each with rinsing steps in between. Sections were then blocked with 1X PBS + 7% BSA + 1% FCS + 2% NGS + 0.02% Azide (incubation buffer) for 30 min to reduce background staining.

Primary antibodies were CD11c (1:20 dilution, hamster anti-mouse, BD Pharmingen), F4/80 (1:80 dilution, rat anti-mouse, Serotec), CD3 (1:20 dilution, rabbit anti-mouse, Novus Biologicals). Sections were stained with a cocktail of primary antibodies for 60 minutes at room temperature. Slides were washed 3 times in PBS for 2 minutes and rinsed with PBST for 1 minute. Secondary antibodies were biotin goat anti-hamster IgG (1:20 dilution, SantaCruz Biotech), anti-rat Alexa 488 (1:200 dilution, Invitrogen), biotin goat anti-rabbit IgG (1:20 dilution, SantaCruz Biotech). Secondary antibodies were diluted in incubation buffer and incubated with the tissue for 60 minutes at room temperature. Slides were washed 3 times in PBS for 2 minutes and rinsed with PBST for 1 min. Tertiary antibodies were streptavidin-Alexa 647 (1:200 dilution, Invitrogen) and streptavidin-Alexa 568 (1:66 dilution, Invitrogen). Tertiary fluorophores were diluted in incubation buffer and incubated with the tissue for 60 minutes at room temperature. Multiple rounds of staining were done as the biotin-streptavidin bond was utilized multiple times to detect the probe of interest. Slides were washed 3 times in PBS for 2 minutes and rinsed with PBST for 1 minute. Cover glass (Fisher Scientific) was mounted using ProLong® Gold anti-fade reagent with DAPI (Invitrogen). Slides are

shielded from light and allowed to cure overnight. Tissues were imaged with a Leica Inverted SP5 Confocal microscope at a magnification of 40X.

7.2.6 Image Analysis

Images of biotinylated TNF stained tissues were analyzed using a CellProfiler (Version 2.1 – www.cellprofiler.org) pipeline. Cell nuclei and positions were determined using thresholds of DAPI staining. Cell regions were identified using nuclei positions and growing regions outward until reaching a neighboring cell or meeting a cutoff threshold. Absolute fluorescence intensities of biotinylated TNF were measured in each determined cell region. Radial distances from the PPD coated bead were calculated based on nuclei positions and binned into 25 pixel distances. All data was exported and further analyzed in MATLAB (The Mathworks Inc. – Natick, MA) and GraphPad Prism (GraphPad Software Inc. – La Jolla, CA).

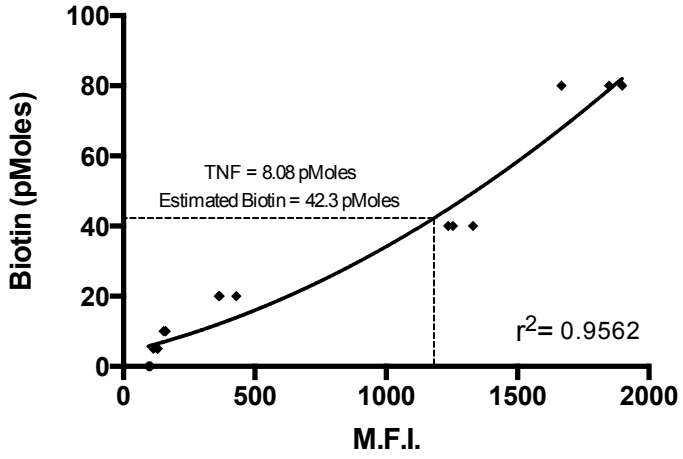

Figure 7.2. Characterization of biotinylated TNF
FRET based assay of diluted biotin standards at 80, 40, 20, 10, 5, and 0 pMoles. Standard curve was fit to a quadratic function as per the manufacturers instructions (r^2 = 0.9562). M.F.I. of biotinyalted TNF was measured in triplicate.

7.3 Results

7.3.1 Characterization of Biotinylated TNF

5 μg of unlabeled recombinant mouse TNF yielded 2.75 μg of biotinylated TNF, a 55% yield. Using the FRET based assay the degree of biotinylation was estimated to be 5 biotin molecules per recombinant TNF protein (Figure 7.2). Optimal concentration of biotinylated TNF for staining was determined using serial dilutions (0.5-10 μg/mL) of cryosections as described in Materials and Methods.

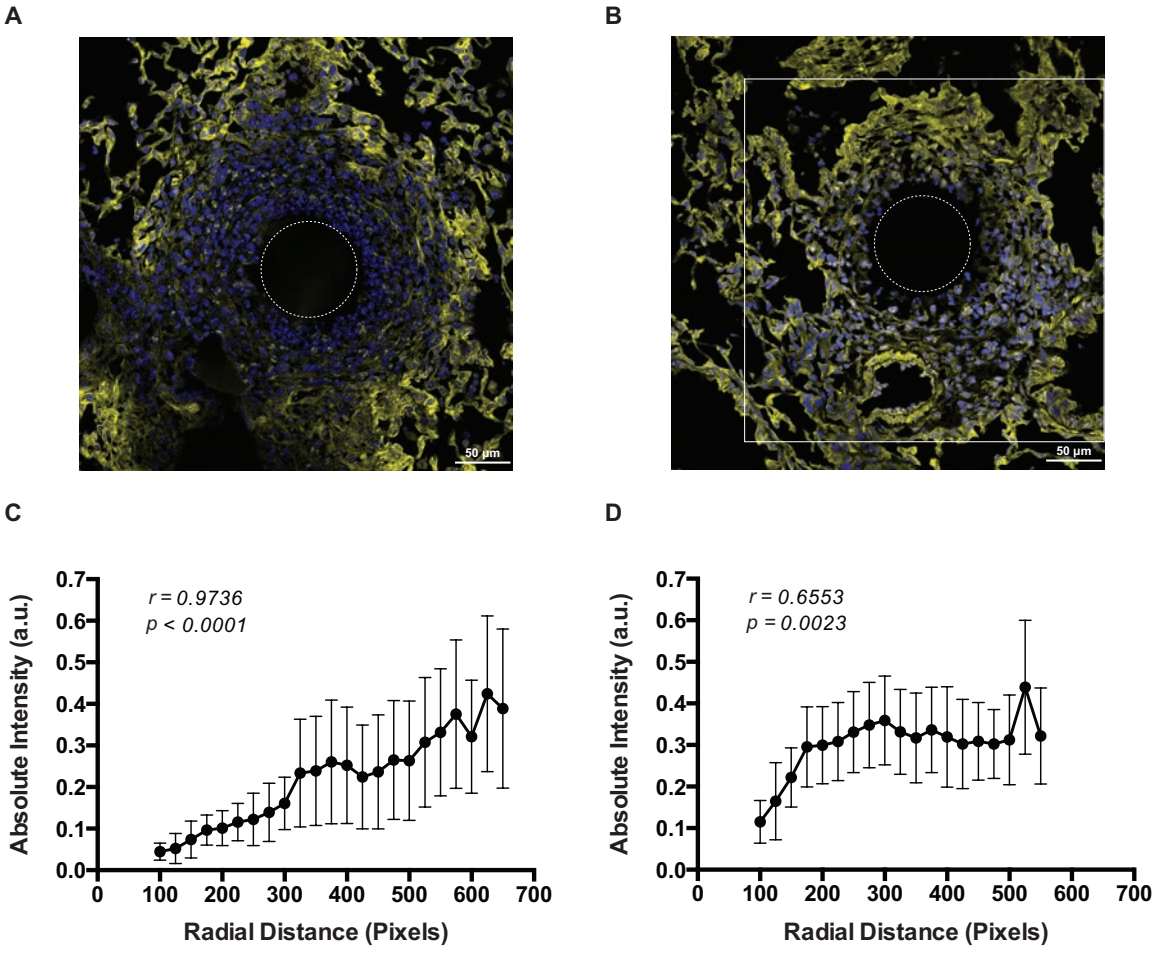

Figure 7.3. Distribution of Free TNFR in PPD Bead Granulomas
(A)–(B) Representative PPD bead granulomas stained for free TNFR (yellow) using biotinylated TNF and nuclei (blue) using DAPI. Dashed white circle indicates approximate PPD bead location. White box shows area of quantification. Entire image was used in A. (C)-(D) Intensity of biotinylated TNF as a function of radial distance from the center of the PPD bead, binned into 25 pixel lengths. C corresponds to the image in A and D corresponds to the image in B. Bars indicate SD. Significance of trends was calculated using Pearson correlation coefficients (r) with a two-tailed t-test (p) with a 95% confidence interval.

7.3.2 Measuring Free TNFR in PPD Granulomas Using Biotinylated TNF

Lung cryosections containing PPD bead granulomas were briefly fixed in formaldehyde to cross-link existing TNF bound to TNFR (Figure 7.1), and then stained with biotinylated TNF. This methodology provides a direct measurement of free TNFR as a function of position. PPD bead granulomas identified in cryosections were characterized by high signal intensity in peripheral regions with lower intensity in the inner regions (Figure 7.3A, 7.3B). Quantitating the signal intensity in the granuloma as a function of radial position demonstrates a 2.5 to 9-fold increase in mean signal intensity in the outer regions of the granuloma compared to the inner regions (Figure 7.3C, 7.3D). These results indicate that there is high availability of free TNFR in peripheral regions and low availability of free TNFR in the inner regions and near the PPD bead.

7.3.3 Determining Cellular Organization of PPD Granulomas

PPD bead granulomas were stained for CD11c, F4/80, and CD3 to identify dendritic cells, macrophages, and T cells respectively (Figure 7.4A). We observed dendritic cells mainly in the inner area of the granuloma surrounding the PPD bead. Macrophages were principally located in a cuff surrounding dendritic cells, with a few near the PPD bead. T cells were predominantly found in the peripheral of the granuloma, although some were interspersed with macrophages nearer to the center of the granuloma. The relative proportion of cells and their spatial organization are in agreement with previous studies of PPD bead granulomas (7, 13). We created an approximate cellular organization mask by identifying regions that primarily contain a specific cell-type based on four samples regions drawn in ordinal directions from the center of the bead (Figure

7.4B). We used the sample regions to estimate a radial length from the center of the bead containing individual cell-types – dendritic cells (R_{DC}), macrophages (R_M), and T cells (R_T) – as shown in Figure 7.4B.

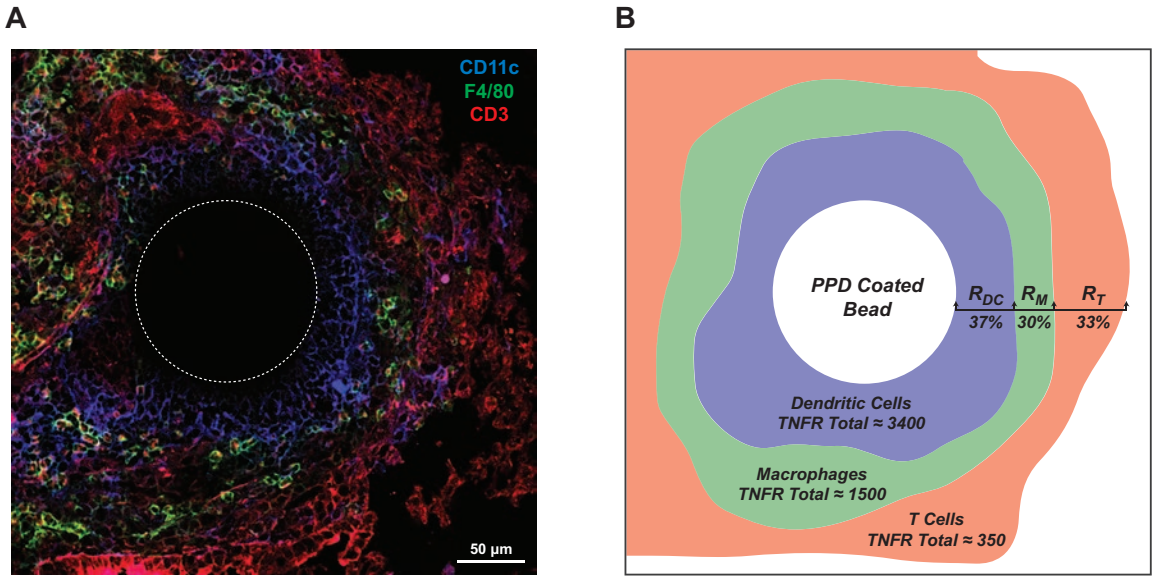

Figure 7.4. Immunofluorescence staining to identify cell types and their spatial organization in PPD bead granulomas
(A) Representative image demonstrating CD11c+ (blue) dendritic cells closest to the PPD bead, an inner cuff of F4/80+ (green) macrophages, and an outer cuff of CD3+ (red) T cells. Dotted white circle indicates approximate PPD bead location. (B) Pseudo-colored representation of the approximate cellular organization identifying regions that primarily contain a specific cell-type. Flow cytometry data of total TNFR per cell, from (7), is also indicated in the specified regions for the specific cell-type.

7.3.4 Estimating Soluble TNF Gradients in PPD Granulomas

With the data collected above, we now have enough information to use Eqn. 7.4 to reconstruct the dimensionless soluble TNF gradient in a granuloma. We use the estimated radial length calculated above to approximate regions of cellular organization in the granulomas shown in Figure 7.3A and 7.3B. We use flow cytometry measurements of total TNFR for the specific cell-type associated with the region (7). At each radial position, from the 25 pixel bins, we use Eqn. 7.4 to calculate the dimensionless soluble TNF concentration, ψ. We use total TNFR data based on the specific cell-type

determined at the specific radial position (indicated on the x-axis of Figure 7.4.) and the mean intensity data of free TNFR as a function of radius. Dimensionless soluble TNF concentration, ψ, estimated for the granulomas pictured in Figure 7.3A and 7.3B is given in Figure 7.5.

With perfectly separated cellular organization of dendritic cells, macrophages, and T cells, where distinct cell-types only reside in the estimated region of organization, there is a significant dimensionless soluble TNF gradient. Dendritic cells and macrophages are exposed to 1 to 2 orders of magnitude higher dimensionless soluble TNF concentrations as compared to T cells (Figure 7.5 – red curve). Because the cell-types in a PPD granuloma are not perfectly separated, we also calculate the soluble TNF gradient using three other cellular organizations: (1) '25% mixed' – 75% of the cells are of the indicated cell-type and 25% are split between the other two cell-types, (2) '50% mixed' – 50% of the cells are of the indicated cell-type and 50% are split between the other two cell-types, and (3) '100% mixed' – cell-types are evenly dispersed in all regions. As the cell-types in the granuloma become less spatially organized, the calculated dimensionless soluble TNF gradients are less steep, with anywhere from a 4 to 10-fold difference in the inner region compared to the peripheral regions (Figure 7.5). These results demonstrate that significant gradients of soluble TNF still exist in PPD granulomas even with a high level of cellular disorganization.

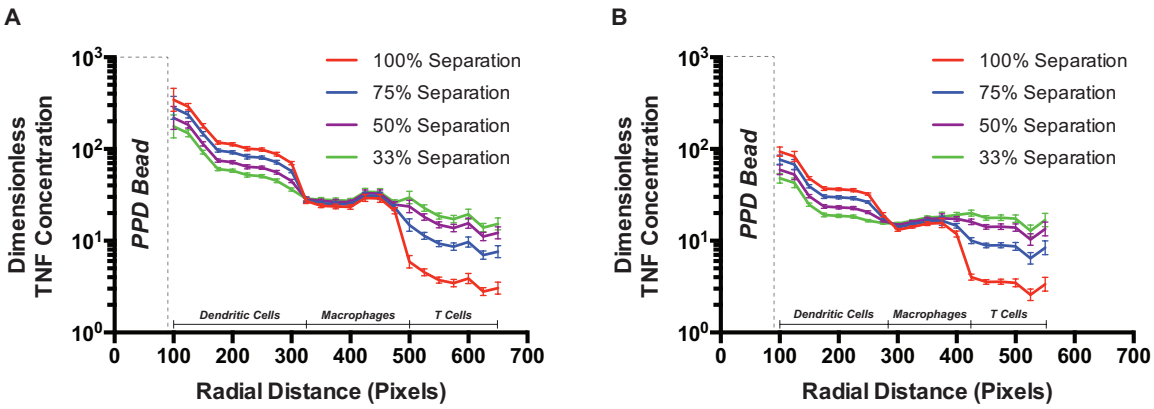

Figure 7.5 Reconstructing soluble TNF gradients in two PPD granulomas
Estimation of the dimensionless soluble TNF gradient calculated using Eqn. 7.4. Approximate regions of cellular organization are shown on the x-axis (dendritic cells, macrophages, and T cells). Border of the PPD bead is shown with the gray dotted line. 100% Separation – Perfectly separated organization, 25% Mixed – 25% of other cell-types, 50% - 50% of other cell-types, 100% Mixed – Evenly dispersed cell-types. (A) Estimation using radial intensity data from Figure 7.2C. 100% Separation – $p < 0.0001$ and $r = -0.8243$. 25% Mixed – $p < 0.0001$ and $r = -0.8151$. 50% Mixed – $p < 0.0001$ and $r = -0.7974$. 100% Mixed – $p < 0.0001$ and $r = -0.7739$. (B) Estimation using radial intensity data from Figure 7.2D. 100% Separation – $p < 0.0001$ and $r = -0.8722$. 25% Mixed – $p < 0.0001$ and $r = -0.8409$. 50% Mixed – $p = 0.0002$ and $r = -0.7616$. 100% Mixed – $p = 0.0052$ and $r = -0.6139$. Bars indicate SEM. Significance of trends was calculated using Pearson correlation coefficients (r) with a two-tailed t-test (p) with a 95% confidence interval.

7.4 Discussion

We developed a method for reconstructing soluble TNF gradients in granulomas in the PPD bead model of *Mtb* infection. We constructed a molecular probe that targets free TNFR and developed a novel protocol for reconstructing gradients from data on cellular organization, total TNF receptor expression by cell type, and radial intensity measurements of biotinylated TNF. We show for the first time that gradients of TNF exist in *Mtb*-induced granulomas and are of significant magnitude. Furthermore, we demonstrate that cellular organization plays a role in determining the magnitude and steepness of TNF gradients, yet gradients of soluble TNF are found at all levels of cellular organization. Taken in conjunction with the predictions from computational models (such as those in Chapter 3, 4, and 5), the experimentally reconstructed gradients

support the concept of differential induction of TNF-mediated signaling pathways according to spatial position in the granuloma during *Mtb* infection (7).

A computational model of the dynamics of TNF in the PPD bead model of *Mtb* infection predicted soluble TNF gradients of approximately 1 order of magnitude across granulomas with idealized cellular organization (7). Our experimental results agree well with these predictions, with reconstructed TNF gradients anywhere from 1 to 2 orders of magnitude in the case of perfect cellular separation. Although we estimated dimensionless soluble TNF gradients from our measurements on PPD granulomas, the relative magnitude of the gradient should be similar if we were able to quantitate fluorescent signals (in the linear-response regions) and estimate actual soluble concentrations. Methods for quantitation of fluorescent signals exist, however they are difficult to carry out and may lack the sensitivity required to differentiate between weak signals (27, 28). In addition, our results may underestimate the magnitude of the soluble TNF gradient as we neglect many of the receptor-ligand trafficking dynamics known to be occurring in cells such as receptor internalization and recycling (6, 7). Using the computational model of TNF dynamics in the PPD bead model from (7), we have shown that assuming equilibrium between TNF and TNFR and neglecting other trafficking dynamics could underestimate the gradient by 2-35%. Trafficking processes such as receptor internalization and degradation would increase the steepness of gradients, as these mechanisms remove soluble TNF from the environment.

The PPD bead model of *Mtb* infection does not use live bacteria (13, 15, 17). The cytokine responses to PPD bead challenge are primarily Th1, indicating a strong pro-inflammatory response with high levels of TNF and interferon-γ production (15).

Whether the gradients of soluble TNF in a live model of *Mtb* infection will be as significant must be elucidated, but the method developed here can easily be adapted to a more realistic infection setting. Furthermore, it is important to note that not every PPD bead granuloma isolated from mouse lungs displayed significant and easily measureable soluble gradients of TNF. The granuloma sizes and the planes of the cryosections play a large part in determining the radial dependence of signal intensity (data not shown). Therefore, the sample size and effort necessary to identify ideal sections and granuloma sizes is large and could be a significant barrier to overcome in a more realistic infection setting.

Gradients of soluble molecules are a basic principle driving many basic biological phenomenon including development, organogenesis, tumor growth, antibiotic resistance, and chemotaxis (1, 5, 7, 8, 29). However, gradients of cytokines, specifically TNF, during the immune response to *Mtb* have only been predicted as important processes that lead to efficient control of infection. Herein, we demonstrate the existence of soluble TNF gradients during *Mtb* infection and validate a methodology for characterizing soluble molecule gradients in tissues. This new method, used in conjunction with a live *Mtb* infection scenario, will allow us to measure gradients of many soluble molecules (e.g. interleukin-10 or chemotactic factors) critical to the immune response. For instance, we also predict significant gradients of IL-10 in granulomas (see Chapter 3, 4, and 5) and using the methodology presented here should be able to easily reconstruct gradients of IL-10 during infection. This will lead to a better understanding of how gradients of soluble molecules influence differential cell behavior vital to control of *Mtb* infection.

7.5 References

1. McDowell, N., J. B. Gurdon, and D. J. Grainger. 2001. Formation of a functional morphogen gradient by a passive process in tissue from the early Xenopus embryo. *Int. J. Dev. Biol.* 45: 199–207.

2. Gregor, T., W. Bialek, R. R. de Ruyter van Steveninck, D. W. Tank, and E. F. Wieschaus. 2005. Diffusion and scaling during early embryonic pattern formation. *Proc. Natl. Acad. Sci. U. S. A.* 102: 18403–7.

3. Gregor, T., D. W. Tank, E. F. Wieschaus, and W. Bialek. 2007. Probing the limits to positional information. *Cell* 130: 153–64.

4. Houchmandzadeh, B., E. Wieschaus, and S. Leibler. 2002. Establishment of developmental precision and proportions in the early Drosophila embryo. *Nature* 415: 798–802.

5. Toyoda, R., S. Assimacopoulos, J. Wilcoxon, A. Taylor, P. Feldman, A. Suzuki-Hirano, T. Shimogori, and E. a Grove. 2010. FGF8 acts as a classic diffusible morphogen to pattern the neocortex. *Development* 137: 3439–48.

6. Fallahi-Sichani, M., M. El-Kebir, S. Marino, D. E. Kirschner, and J. J. Linderman. 2011. Multiscale computational modeling reveals a critical role for TNF-α receptor 1 dynamics in tuberculosis granuloma formation. *J. Immunol.* 186: 3472–83.

7. Fallahi-Sichani, M., M. a Schaller, D. E. Kirschner, S. L. Kunkel, and J. J. Linderman. 2010. Identification of key processes that control tumor necrosis factor availability in a tuberculosis granuloma. *PLoS Comput. Biol.* 6: e1000778.

8. Hashambhoy, Y. L., J. C. Chappell, S. M. Peirce, V. L. Bautch, and F. Mac Gabhann. 2011. Computational modeling of interacting VEGF and soluble VEGF receptor concentration gradients. *Front. Physiol.* 2: 62.

9. Carmona-Fontaine, C., V. Bucci, L. Akkari, M. Deforet, J. A. Joyce, and J. B. Xavier. 2013. Emergence of spatial structure in the tumor microenvironment due to the Warburg effect. *Proc. Natl. Acad. Sci. U. S. A.* 110: 19402–7.

10. Flynn, J. L., and J. Chan. 2001. Immunology of tuberculosis. *Annu. Rev. Immunol.* 19: 93–129.

11. O'Garra, A., P. S. Redford, F. W. McNab, C. I. Bloom, R. J. Wilkinson, and M. P. R. Berry. 2013. The immune response in tuberculosis. *Annu. Rev. Immunol.* 31: 475–527.

12. Ramakrishnan, L. 2012. Revisiting the role of the granuloma in tuberculosis. *Nat. Rev. Immunol.* 12: 352–66.

13. Ito, T., M. Schaller, C. M. Hogaboam, T. J. Standiford, M. Sandor, N. W. Lukacs, S. W. Chensue, and S. L. Kunkel. 2009. TLR9 regulates the mycobacteria-elicited pulmonary granulomatous immune response in mice through DC-derived Notch ligand delta-like 4. *J. Clin. Invest.* 119: 33–46.

14. Chensue, S. W., K. Warmington, J. H. Ruth, N. Lukacs, and S. L. Kunkel. 1997. Mycobacterial and schistosomal antigen-elicited granuloma formation in IFN-gamma and IL-4 knockout mice: analysis of local and regional cytokine and chemokine networks. *J. Immunol.* 159: 3565–73.

15. Chensue, S. W., K. Warmington, J. Ruth, P. Lincoln, M. C. Kuo, and S. L. Kunkel. 1994. Cytokine responses during mycobacterial and schistosomal antigen-induced pulmonary granuloma formation. Production of Th1 and Th2 cytokines and relative contribution of tumor necrosis factor. *Am. J. Pathol.* 145: 1105–13.

16. Chensue, S. W., J. H. Ruth, K. Warmington, P. Lincoln, and S. L. Kunkel. 1995. In vivo regulation of macrophage IL-12 production during type 1 and type 2 cytokine-mediated granuloma formation. *J. Immunol.* 155: 3546–51.

17. Qiu, B., K. A. Frait, F. Reich, E. Komuniecki, and S. W. Chensue. 2001. Chemokine expression dynamics in mycobacterial (type-1) and schistosomal (type-2) antigen-elicited pulmonary granuloma formation. *Am. J. Pathol.* 158: 1503–15.

18. Fallahi-Sichani, M., D. E. Kirschner, and J. J. Linderman. 2012. NF-κB Signaling Dynamics Play a Key Role in Infection Control in Tuberculosis. *Front. Physiol.* 3: 170.

19. Ermert, M., C. Pantazis, H.-R. Duncker, F. Grimminger, W. Seeger, and L. Ermert. 2003. In situ localization of TNFα/β, TACE AND TNF receptors TNF-R1 and TNF-R2 in control and LPS-treated lung tissue. *Cytokine* 22: 89–100.

20. Al-Lamki, R. S., J. Wang, P. Vandenabeele, J. A. Bradley, S. Thiru, D. Luo, W. Min, J. S. Pober, and J. R. Bradley. 2005. TNFR1- and TNFR2-mediated signaling pathways in human kidney are cell type-specific and differentially contribute to renal injury. *FASEB J.* 19: 1637–45.

21. Riehl, T. E., R. D. Newberry, R. G. Lorenz, and W. F. Stenson. 2004. TNFR1 mediates the radioprotective effects of lipopolysaccharide in the mouse intestine. *Am. J. Physiol. Gastrointest. Liver Physiol.* 286: G166–73.

22. Reeves, J. R., T. G. Cooke, D. Fenton-Lee, a M. McNicol, B. W. Ozanne, R. C. Richards, and A. Walsh. 1994. Localization of EGF receptors in frozen tissue sections by antibody and biotinylated EGF-based techniques. *J. Histochem. Cytochem.* 42: 307–14.

23. Corti, a, a Gasparri, a Sacchi, F. Curnis, R. Sangregorio, B. Colombo, a G. Siccardi, and F. Magni. 1998. Tumor targeting with biotinylated tumor necrosis factor alpha:

structure-activity relationships and mechanism of action on avidin pretargeted tumor cells. *Cancer Res.* 58: 3866–72.

24. Zimmermann, V. S., A. Bondanza, A. Monno, P. Rovere-Querini, A. Corti, and A. a Manfredi. 2004. TNF-alpha coupled to membrane of apoptotic cells favors the cross-priming to melanoma antigens. *J. Immunol.* 172: 2643–50.

25. Desnoyers, L., R. a. Simonette, R. L. Vandlen, and B. M. Fendly. 2001. Novel Non-isotopic Method for the Localization of Receptors in Tissue Sections. *J. Histochem. Cytochem.* 49: 1509–1517.

26. Wiley, H. S., and D. D. Cunningham. 1982. The endocytotic rate constant. A cellular parameter for quantitating receptor-mediated endocytosis. *J. Biol. Chem.* 257: 4222–9.

27. Dmochowski, I. J., J. E. Dmochowski, P. Oliveri, E. H. Davidson, and S. E. Fraser. 2002. Quantitative imaging of cis-regulatory reporters in living embryos. *Proc. Natl. Acad. Sci. U. S. A.* 99: 12895–900.

28. Wu, Y., S. K. Campos, G. P. Lopez, M. A. Ozbun, L. A. Sklar, and T. Buranda. 2007. The development of quantum dot calibration beads and quantitative multicolor bioassays in flow cytometry and microscopy. *Anal. Biochem.* 364: 180–92.

29. Hermsen, R., J. B. Deris, and T. Hwa. 2012. On the rapidity of antibiotic resistance evolution facilitated by a concentration gradient. *Proc. Natl. Acad. Sci. U. S. A.* 109: 10775–80.

Chapter 8

Conclusions and Future Directions

8.1 Summary

Tuberculosis (TB), caused by the pathogen *Mycobacterium tuberculosis* (*Mtb*), has endured for centuries as a burden on global health. TB is the second leading cause of death due to infectious disease, behind the human immunodeficiency virus (HIV) (1). Without treatment it is estimated that nearly 70% of individuals die within 10 years of infection (1). Treatment with antibiotics is 87% effective; however, drug-resistant cases of *Mtb* infection are on the rise (1). In 1993 the World Health Organization (WHO) declared TB a public health emergency. Although great strides have been made since that declaration, with an estimated 22 million lives saved due to new prevention, control, and treatment strategies, many basic questions surrounding TB still remain (1).

Central to both the host immune response to *Mtb* infection and subsequently antibiotic treatment is a structure known as a granuloma. Granulomas are densely packed aggregates of cells that form in response to persistent stimuli from *Mtb* infection of macrophages (2–4). The basic idea has always been that such a concentrated immune response should be sufficient to control and eradicate the pathogen in these structures. However, granulomas form in both active and latently classified individuals indicating that not all granulomas can sufficiently control *Mtb* infection (5, 6). Why do some granulomas effectively control bacteria, while some are unable to prevent bacterial

growth? The keys to understanding this dichotomy lie in the processes that lead to granuloma formation and function and understanding how each contributes to bacterial control, bacterial persistence, or both.

As granulomas are the structures that harbor *Mtb* during infection, it is important to understand how they contribute to the efficacy of antibiotic treatment. Current antibiotic regimens to treat *Mtb* infection must overcome significant transport barriers to reach their intended target mechanism (7). Antibiotics must be absorbed into systemic circulation, transported to the lungs, diffuse through dense granulomas, and permeate *Mtb* cell walls (7). Understanding the mechanisms and dynamics that drive antibiotic distribution in granulomas is critical to designing better antibiotics or increasing efficacy of current antibiotics.

In this dissertation we used both experimental and computational techniques to better understand the roles of the cytokines tumor necrosis factor-α (TNF) and interleukin-10 (IL-10) in controlling *Mycobacterium tuberculosis* (*Mtb*) infection at a single granuloma level. In addition, we developed computational models of first-line antibiotics used to treat *Mtb* in order to understand why current therapies fail and to predict novel formulations that can improve efficacy and increase patient compliance. The major conclusions of this dissertation are given below, organized by specific aim.

8.1.1 Aim 1: Development of a Computationally Efficient Hybrid Multi-Scale Agent-Based Model of TB Infection

In Chapter 2, we explored ways to improve the computational tractability of the hybrid multi-scale ABM in order to include new biological processes of interest. We

implemented forward-time-central-space, alternating-direction explicit, and spectral based numerical methods to solve soluble molecule diffusion. In addition we used forward Euler and 4th order Runge-Kutta to solve agent-associated reactions. We demonstrated how different combinations of numerical algorithms and correct choice of time steps lead to 5 to 25-fold increases in computational speed. Furthermore, we demonstrated the concept of tuneable resolution and showed that it leads to further enhancements in computational speeds near 1.5 to 63.5-fold. These improvements in computational tractability were key to all model development in subsequent chapters. Additionally, efficient solution of hybrid multi-scale ABMs is key to model portability, modularity, and their use in understanding biological phenomena at a systems level.

8.1.2 Aim 2: Identifying the Roles of TNF and IL-10 During Granuloma Formation Using Multi-Scale Computational Modeling

In Chapter 3, we addressed the multi-scale effects of TNF and IL-10 during *Mtb* infection using a systems biology approach. Building on our previous work, we developed a hybrid multi-scale ABM of *Mtb* infection that integrated both TNF and IL-10 experimental data, including single-cell level receptor-ligand dynamics. We demonstrated that three groups of TNF and IL-10 related processes relevant to cytokine synthesis, signaling, and spatial distribution, control concentrations of TNF and IL-10 in a granuloma environment. These three groups of processes were critical in determining infection outcome, at the granuloma scale, over the long-term. We then devised an overall measure of granuloma function based on three metrics – total bacterial load, macrophage activation levels, and apoptosis of resting macrophages – and used this

metric to demonstrate that a balance of TNF and IL-10 concentrations is essential to *Mtb* infection control with minimal host-induced tissue damage. These results suggest that a balance of TNF and IL-10 defines a granuloma environment. Furthermore, the balance of cytokines in a granuloma is beneficial for both host and pathogen, but perturbing the balance could be used as a novel therapeutic strategy to modulate infection outcomes.

In Chapter 4, we better characterized the mechanisms that drive macrophage polarization and functionality in granulomas. We extended our description of TNF and IL-10 receptor ligand dynamics by including simplified models of NFκB and STAT3 downstream signaling, respectively. In addition, we included a simplified downstream signaling pathway for STAT1 induced by interferon-γ stimulation. We defined a macrophage polarization ratio based on relative levels of STAT1, STAT3, and NFκB in macrophages, which modulated macrophage functions including anti-microbial activity and cytokine production. Additionally, we extended this macrophage ratio to the scale of a single granuloma and defined a granuloma polarization ratio. Using this model, our results suggest that temporal dynamics of granuloma polarization ratios are predictive of granuloma outcome. We found that the kinetics of NFκB gene transcription is a key determinant of granuloma outcome. Granulomas with low bacterial loads and limited inflammation are characterized by short intervals of NFκB activation, while those with elevated bacterial loads have extended intervals of NFκB activation. Our results suggest that the dynamics of NFκB signaling might be a target therapeutic candidate to help control of infection.

In Chapter 5, we focused on determining the role of IL-10 in controlling bacterial control versus sterilization at the single granuloma level. We predicted a transient role for

IL-10 in controlling a trade-off between the antimicrobial activity of the immune response to *Mtb* and host-immunity driven tissue damage, which at high levels can be as detrimental as bacterial burden to host lungs. We predicted that small changes in early antimicrobial activity promote lesion sterility due to low bacterial loads. We predicted that decreased levels of IL-10 promote granuloma sterilization at the cost of increased early host-induced damage. In addition, we showed that IL-10 derived from activated macrophages is the main macrophage cell-type balancing bactericidal responses versus host-induced damage. Finally, we predicted that increasing levels of infected macrophage derived IL-10 promotes bacterial persistence by shifting control of antimicrobial responses from activated macrophages to infected macrophages. This allows *Mtb* to replicate and spread to healthy macrophages at a greater rate. Our findings suggest that IL-10 at the individual granuloma scale is a critical regulator of lesion outcome.

8.1.3 Aim 3: Understanding and Improving the Efficacy of Antibiotics in Granulomas during TB Infection

In Appendix C, we constructed a pharmacokinetic (PK) and pharmacodynamics (PD) model of two first-line antibiotics, rifampin (RIF) and isoniazid (INH), used to treat *Mtb* infection and incorporated it into our hybrid multi-scale ABM. The distribution and action of RIF and INH in individual granulomas was calibrated to PK and PD measurements in rabbit and non-human primate models of infection. We used this model to simulate different oral treatment regimens and make predictions about the efficacy of treatment at the individual granuloma scale.

In Chapter 6, we extended our PK and hybrid multi-scale ABM platform to include a description of inhaled antibiotic formulations dosed to the lungs. This model captured the simultaneous effects of pharmacokinetics, granuloma dynamics, carrier-release dynamics and behavior, and pharmacodynamics on treatment efficacy. We used sensitivity analysis to determine which dynamics most affect treatment efficacy at reduced dosing frequencies. We predicted that carrier antibiotic loading, carrier release kinetics, and system pharmacokinetics all influence the efficacy of treatment. In addition, we predicted that targeting inhaled carriers directly to macrophages provides no increase in treatment efficacy due to the densely packed nature of granulomas. We designed ideal *in silico* inhaled formulations of RIF and INH to be dosed every two-weeks. We predicted that inhaled formulations of INH dosed every two-weeks are feasible and have increased sterilization capabilities with reduced toxicity. Furthermore, we predicted that inhaled formulations of RIF dosed every two-weeks have equivalent sterilization capabilities but with early associated toxicity and infeasible carrier loadings. Our model suggests that the pharmacokinetics outside of the lung play a significant role in the efficacy of inhaled carriers as transport rates of antibiotics out of the lungs must be compensated for by carrier-release kinetics. This platform will allow for rapid assessment of ideal candidates for inhaled formulations, thus reducing the development time of new therapeutics.

8.1.4 Aim 4: Measuring TNF Concentration Gradients in TB Granulomas

Simulations of TNF and IL-10 receptor-ligand and trafficking dynamics predicted significant concentration gradients of soluble TNF in granulomas. In Chapter 7 we used a

simple murine model, where granulomas form in response to injected beads conjugated to *Mycobacterium* purified protein derivative (PPD), to develop a fluorescent microscopy technique to reconstruct soluble TNF gradient from ex vivo lung tissue samples. We used biotinylated TNF to specifically target unbound TNF receptors and measured the spatial distribution in granulomas using fluorescent microscopy. We used traditional immunofluorescence techniques to identify the spatial organization of cells in granulomas. Using these data together with an equilibrium model of TNF receptor-ligand dynamics, in combination with flow cytometry data on receptor number, we estimated dimensionless soluble gradients of TNF in granulomas. We showed for the first time that gradients of TNF exist in granulomas and are of significant magnitude. Furthermore, we demonstrated that cellular organization plays a role in determining the magnitude and steepness of TNF gradients. These results suggest that gradients of cytokines are critical to differential induction of signaling pathways according to spatial position, which can have significant effects on bacterial control in granulomas.

8.2 Future Directions

8.2.1 Implementation of Advanced Numerical Algorithms and Techniques for More Efficient Hybrid Multi-Scale Agent-Based Models

In Chapter 2, we focused considerable attention on implementing better numerical algorithms for more computationally tractable hybrid multi-scale agent-based model (ABM) of *Mtb* infection. Even with advances in modern computing, the biological details and complexity included in computational models is still inherently limited by computational requirements. More effort needs to be devoted to improving the tractability

of the ABM as constant development and implementation of new biological processes and mechanisms requires more computational power. Furthermore, expansion of the ABM to larger grid sizes or increased dimensionality (3D) incurs substantial computational cost. I suggest incorporating multiple new numerical algorithms and techniques to further reduce computational burdens: (1) in situ adaptive tabulation, (2) multigrid methods, and (3) an event scheduler update scheme.

In Chapters 3, 4, and 5, we used ordinary differential equations (ODEs) to describe single-cell receptor ligand dynamics of TNF and IL-10 (8). The set of ODEs was solved for every agent in the ABM at every time step, which required significant computational effort. In computational models of combustion in turbulent flames a similar situation arises where a large number of ODEs are evaluated millions of times over the course of simulation (9, 10). In situ adaptive tabulation (ISAT) is a technique that reduces the computational demands by searching a set of stored solutions, tabulated during simulation, and approximating a solution to the specified conditions without ever requiring a call to a numerical method (9–11). As search and retrieval of existing solutions is fast (such as O($log\ n$)) compared to repeated calls of the numerical method (O(n)), the increases in efficiency are usually large. However, there is an initial cost to ISAT as the database of solutions must be built during the early phases of simulation (12). In one implementation from literature, using ISAT in the context of 16 modeled species and 41 reactions the computational speed increased nearly 1,000-fold (10). Implementing ISAT in the context of the ABM will require efficient storage of previously calculated solutions and implementations of fast search methods such as binary trees.

Implementation of newer and more efficient numerical methods for solving PDEs than those described in Chapter 2 could further reduce the computational burden of the hybrid multi-scale model. Multigrid (MG) methods are a set of algorithms based on cycles of successive relaxation, prolongation, and injection of a system of equations on hierarchical discretizations of coarse and fine grids (13, 14). An ABM of the generalized immune system (MSIM) recently implemented a MG based algorithm for solving soluble molecule diffusion, which lead to an order of magnitude speed-up (15). In addition, an adaptive MG method was used to simulate solid tumor growth leading to a 14-fold increase in computational speed in comparison to traditional MG algorithms (13). Implementing MG methods in the context of the ABM will require the use of PETSc or Trilinos libraries or constructing in-house versions using C++.

The ABM used in this dissertation still relies on sequential updates of agent behavior, states, and interactions. This is computationally inefficient, as updates to a large population of agents are trivial with no changes to behavior, states, or interactions. In addition, this poorly reflects biology, which does not act in such a sequential manner. Event-scheduling approaches allow for asynchronous updates to agents with arbitrary time steps and avoid computational inefficiencies associated with trivial updates (16, 17). In an ABM of the B cell life-cycle an event-scheduling approach was 40-fold faster than a sequential approach (17). Taken together, implementing new numerical algorithms and techniques such as these will allow new biological mechanisms and dynamics to be added to the ABM along with model expansion to higher dimensions. This will allow the ABM to be used in a greater variety of contexts to better understand the immune response to *Mtb* infection.

8.2.2 Understanding the Influence of Cytokine Networks on the Control of Mtb During Infection

The immune response to *Mtb* infection is highly complex and remains poorly understood. We still lack a basic understanding of how the plethora of cytokines found at the site of infection dictate effective versus poor control of infection (18–20). In Chapters 3, 4, and 5 we elucidated the effects of a balance of TNF and IL-10 in controlling infection outcome and macrophage polarization (8). However, many more cytokines are present at the site of infection, such as IL-17 and type-I interferons, with overlapping functions and abilities to influence infection control (18, 21, 22). For instance, mice treated with exogenous interferon-α and interferon-β show increased bacterial loads in the lungs (22). Computational models must maintain tractability and therefore it is difficult to implement descriptions of every single new cytokine that is present in granulomas. Thus, it is necessary to determine the most important cytokines at the site of infection and include these in the ABM of infection. I propose both experimental and computational work to measure and understand the relative strengths of cytokines in the network present at the site of infection.

Recently, multiplex assays were used to measure 50 different cytokines present in peritoneal aspirates from patients who were either healthy or diagnosed with endometriosis (23). Using statistical techniques, a network of important cytokines and cells was established in patients with endometriosis (23). Applying this technique to bronchoalveolar lavage (BAL) fluid from healthy, actively TB, and latently TB individuals could lead to a better understanding of the complex cytokine network at the site of infection and identify critical cytokines to add to the ABM of *Mtb* infection. The

network of cytokines measured experimentally is only a snapshot in time, preventing an understanding of what lead to that specific state or where that state leads to with respect to infection. The ABM can then be used to understand the temporal dynamics of the influence of the identified cytokines and sources on controlling infection outcome. Additionally, the cytokine network would incorporate dynamic influences of cytokines on cells and overlapping cytokine functions leading to a better understanding of the interactions of cytokines during infection. In the past, cytokine networks and interactions have been successfully integrated into a petri-net model of *Leishmania donovani* infection and a general model of the immune system (24, 25). This type of study will lead to a better fundamental understanding of the host immune response to *Mtb* infection and help drive efficient addition of cytokine networks to the ABM of infection.

8.2.3 Determining the Fate of Apoptotic Cells During Mtb Infection

The method of macrophage cell death is critical during infection with *Mtb* (18, 26). Since *Mtb* is an intracellular pathogen, programmed cell-death, known as apoptosis, is often used as an antimicrobial tool against infection. However, apoptosis occurs in a variety of different forms including true apoptosis, necrosis, and necroptosis (27, 28). The cellular contents and intracellular bacteria of infected cells that die through an apoptotic pathway are packaged into apoptotic bodies that are efficiently taken up by phagocytes (28). Furthermore, intracellular bacteria contained in apoptotic bodies are efficiently killed after ingestion by phagocytes (29–31). Conversely, infected cells that die via necrosis are not packaged into vesicles and their intracellular contents and bacteria are exposed to the environment causing significant inflammation and tissue damage (27, 28).

In addition, phagocytes cannot efficiently ingest necrotic cells nor sterilize the intracellular bacteria contained in a necrotic cell.

Infected macrophage apoptosis through TNF-induced caspase signaling pathways has been identified as critical to controlling *Mtb* infection (30, 32, 33). Yet there are also significant levels of TNF-induced necrosis observed during infection that could be limiting bacterial sterilization and promoting bacterial infection of healthy macrophages (34, 35). Recently, receptor-interacting protein 3 (RIP3) its associated kinase, receptor-interacting protein 3 kinase (RIP3K), were determined as an underlying mechanism controlling TNF induction of apoptosis or necrosis (36–38). Uncovering the differences between TNF induction of apoptosis or necrosis in the context of *Mtb* infection is critical to understanding bacterial pathogenesis versus bacterial control. I propose including a simple molecular scale model of RIP3/RIP3K into the hybrid ABM of *Mtb* infectionin the existing ABM of *Mtb* infection and linking it to cell-death through apoptotic or necrotic pathways (36, 38, 39). Analysis of the dynamics leading to cell-death via apoptosis versus necrosis will lead to a better understanding of programmed cell-death mechanisms contributing to bacterial pathogenesis. Additionally, it can help motivate discovery of therapeutics targeted to preventing necrotic cell death.

8.2.4 Determining the Role of IL-10 Production by Neutrophils During Mtb Infection

In Chapters 3, 4, and 5 we described the cellular sources and receptor-ligand trafficking dynamics of IL-10. New evidence indicates that neutrophils are a significant source of IL-10, and yet why neutrophils produce IL-10 is still not well understood (40, 41). Neutrophils are professional phagocytes that ingest *Mtb* and undergo cell-death in

order to be phagocytosed by macrophages (41). BAL fluid from patients with active pulmonary TB shows that neutrophils are the most predominant cell during infection and allow bacteria to replicate rapidly in the intracellular niche (42). In addition, histological staining of non-human-primate granulomas shows a large region of neutrophils in the center of granulomas, with murine models of TB demonstrating similar observations (43, 44). Neutrophils produce neutrophil extracellular traps (NETs), which trap bacteria, have antimicrobial properties, and cause significant tissue damage (45).

I propose the inclusion of neutrophils as a new cell-type in the ABM of *Mtb* infection, as neutrophils are a significant cell population that drives inflammation and bacterial uptake. Neutrophils would be implemented in the model similar to macrophages with resting, activated, and infected states and the ability to secrete cytokines such as IL-10. However, neutrophils would have a significantly shorter lifespan than macrophages. Understanding this cell-type is crucial to understand the effects of various levels of IL-10 production on infection outcome. Furthermore, as neutrophil apoptosis and NETs lead to tissue damage and formation of caseum the model can help in understanding whether the production of IL-10 from neutrophils helps alleviate substantial tissue damage. An ABM of the immune response to *Mtb* infection in mice included neutrophils and demonstrated their role in keeping bacterial in the center of granulomas (46). However, this model is based on *Mtb* infection in mice, which significantly differs from infection in humans, and did not include the ability of *Mtb* to be phagocytosed by neutrophils. Additionally, cytokines were not included in the model, therefore the effects of neutrophil IL-10 production on infection outcome was not considered (46).

8.2.5 Understanding Antibiotic Factors that Contribute to the Development of Mtb Antibiotic Resistance

TB requires a rigorous regimen of multiple antibiotics lasting anywhere from 6 to 24 months. In Appendix C we showed why current oral treatment regimens using two first-line antibiotics, rifampin (RIF) and isoniazid (INH), are ineffective. We predicted that these antibiotics have poor antibiotic penetration into granulomas, leading to sub-optimal exposure. In Chapter 6, we predicted that novel inhaled formulations of RIF and isoniazid INH could improve efficacy. Yet, during clinical treatment mono-therapies cannot be prescribed due to the rapid onset of antibiotic resistance (7, 47, 48). In addition, non-adherence to the complicated oral drug regimen leads to a significant number of individual developing multi-drug resistant TB (MDR-TB). There is growing evidence that concentration gradients of antibiotics substantially contributes to the development of resistance (49–51). I suggest incorporating development of antibiotic resistance in the ABM model including both random mutations and antibiotic-driven mutations.

The genetic basis of antibiotic resistance to TB drugs is well known. For instance RIF resistance develops mainly due to mutations in *rpoB*, while INH resistance can involve multiple genes such as *katC*, *inhA*, and *oxyR* (48). The risks of mutation for RIF and INH have been established as 3.32×10^{-9} and 2.56×10^{-8} mutations per bacterium division (48). Mutation rates can be implemented using simple models such as the Luria-Delbrück model during bacterial division or more detailed models such as stochastic models (52). Successful mutations would limit the ability of antibiotics to effectively kill the resistant *Mtb* population. Analysis of how gradients of antibiotics contribute to the onset of resistance at the granuloma level will be critical to improving existing treatments

and developing new antibiotics that avoid the onset of resistance. Furthermore, dosing strategies can be optimized in order to better prevent the onset of resistance using current first line antibiotics. Lastly, it will be important to understand how resistance may spontaneously develop before antibiotic treatment and how to determine the best course of action thereafter (53).

8.2.6 Understanding and Improving the Efficacy of Second- and Third-Line Antibiotics Used to Treat TB

If a patient develops multi-drug resistant TB, most commonly due to RIF and/or INH resistance, treatment is extended another 18-24 months with antibiotics that are considerably more toxic and less effective (7). Typically these regimens involve four to six different antibiotics and require at least one flouroquinolone and one intravenously dosed agent such as capreomycin (7, 47). As these drug are used when others fail it is important to optimize their efficacy and dose in order to prevent further development of resistance (54). In conjunction with addition of antibiotic resistance to the ABM as stated above, I propose addition of pharmacokinetic-pharmacodynamics (PK-PD) models of second- and third-line antibiotics used in the treatment of TB.

The existing PK-PD platform established in the ABM can easily be adapted to incorporate the parameters to describe the dynamics of antibiotics such as moxifloxacin and capreomycin, which have been established in literature (55–57). The ABM with mechanisms describing antibiotic resistance and second line antibiotics can be used to help understand how measurable quantities (such as colony forming units from sputum smears) could indicate the onset of resistance (48). Furthermore, the ABM could be used

to develop better strategies to intervene earlier with more effective second- and third-line dosing regimens. In addition, our platform describing inhaled formulations provides the ability to quickly assess which inhaled formulations of second- and third-line antibiotics would be the most promising candidates, thus considerably reducing development time of new treatments.

8.3 References

1. *Global Tuberculosis Report 2013*,. World Health Organization, Geneva ; :1–145.

2. Ramakrishnan, L. 2012. Revisiting the role of the granuloma in tuberculosis. *Nat. Rev. Immunol.* 12: 352–66.

3. Rubin, E. J. 2009. The granuloma in tuberculosis--friend or foe? *N. Engl. J. Med.* 360: 2471–3.

4. Ehlers, S., and U. E. Schaible. 2012. The granuloma in tuberculosis: dynamics of a host-pathogen collusion. *Front. Immunol.* 3: 411.

5. Lin, P. L., and J. L. Flynn. 2010. Understanding latent tuberculosis: a moving target. *J. Immunol.* 185: 15–22.

6. Russell, D. G., C. E. Barry, and J. L. Flynn. 2010. Tuberculosis: what we don't know can, and does, hurt us. *Science* 328: 852–6.

7. Dartois, V. 2014. The path of anti-tuberculosis drugs: from blood to lesions to mycobacterial cells. *Nat. Rev. Microbiol.* 12: 159–167.

8. Cilfone, N. A., C. R. Perry, D. E. Kirschner, and J. J. Linderman. 2013. Multi-Scale Modeling Predicts a Balance of Tumor Necrosis Factor-α and Interleukin-10 Controls the Granuloma Environment during Mycobacterium tuberculosis Infection. *PLoS One* 8: e68680.

9. Dada, J. O., and P. Mendes. 2011. Multi-scale modelling and simulation in systems biology. *Integr. Biol. (Camb).* 3: 86–96.

10. Pope, S. B. 1997. Computationally efficient implementation of combustion chemistry using in situ adaptive tabulation. *Combust. Theory Model.* 1: 41–63.

11. Singer, M., S. Pope, and H. Najm. 2006. Modeling unsteady reacting flow with operator splitting and ISAT. *Combust. Flame* 147: 150–162.

12. Hedengren, J. D., and T. F. Edgar. 2005. In Situ Adaptive Tabulation for Real-Time Control. *Ind. Eng. Chem. Res.* 44: 2716–2724.

13. Wise, S. M., J. S. Lowengrub, and V. Cristini. 2011. An Adaptive Multigrid Algorithm for Simulating Solid Tumor Growth Using Mixture Models. *Math. Comput. Model.* 53: 1–20.

14. Wise, S., J. Kim, and J. Lowengrub. 2007. Solving the regularized, strongly anisotropic Cahn–Hilliard equation by an adaptive nonlinear multigrid method. *J. Comput. Phys.* 226: 414–446.

15. Mitha, F., T. a Lucas, F. Feng, T. B. Kepler, and C. Chan. 2008. The Multiscale Systems Immunology project: software for cell-based immunological simulation. *Source Code Biol. Med.* 3: 6.

16. Guo, Z., P. M. a Sloot, and J. C. Tay. 2008. A hybrid agent-based approach for modeling microbiological systems. *J. Theor. Biol.* 255: 163–75.

17. Guo, Z., and J. C. Tay. 2008. Multi-timescale event-scheduling in multi-agent immune simulation models. *Biosystems.* 91: 126–45.

18. O'Garra, A., P. S. Redford, F. W. McNab, C. I. Bloom, R. J. Wilkinson, and M. P. R. Berry. 2013. The immune response in tuberculosis. *Annu. Rev. Immunol.* 31: 475–527.

19. Flynn, J. L., and J. Chan. 2001. Immunology of tuberculosis. *Annu. Rev. Immunol.* 19: 93–129.

20. Cooper, a M., K. D. Mayer-Barber, and a Sher. 2011. Role of innate cytokines in mycobacterial infection. *Mucosal Immunol.* 4: 252–60.

21. Olobo, J. O., M. Geletu, a Demissie, T. Eguale, K. Hiwot, G. Aderaye, and S. Britton. 2001. Circulating TNF-alpha, TGF-beta, and IL-10 in tuberculosis patients and healthy contacts. *Scand. J. Immunol.* 53: 85–91.

22. Manca, C., L. Tsenova, S. Freeman, A. K. Barczak, M. Tovey, P. J. Murray, C. Barry, and G. Kaplan. 2005. Hypervirulent M. tuberculosis W/Beijing strains upregulate type I IFNs and increase expression of negative regulators of the Jak-Stat pathway. *J. Interferon Cytokine Res.* 25: 694–701.

23. Beste, M. T., N. Pfäffle-Doyle, E. a Prentice, S. N. Morris, D. a Lauffenburger, K. B. Isaacson, and L. G. Griffith. 2014. Molecular Network Analysis of Endometriosis Reveals a Role for c-Jun-Regulated Macrophage Activation. *Sci. Transl. Med.* 6: 222ra16.

24. Albergante, L., J. Timmis, L. Beattie, and P. M. Kaye. 2013. A Petri net model of granulomatous inflammation: implications for IL-10 mediated control of Leishmania donovani infection. *PLoS Comput. Biol.* 9: e1003334.

25. Palsson, S., T. P. Hickling, E. L. Bradshaw-Pierce, M. Zager, K. Jooss, P. J. O'Brien, M. E. Spilker, B. O. Palsson, P. Vicini, and P. J. O Brien. 2013. The development of a fully-integrated immune response model (FIRM) simulator of the immune response through integration of multiple subset models. *BMC Syst. Biol.* 7: 95.

26. Lee, J., M. Hartman, and H. Kornfeld. 2009. Macrophage apoptosis in tuberculosis. *Yonsei Med. J.* 50: 1–11.

27. Fink, S. L., and B. T. Cookson. 2005. Apoptosis, pyroptosis, and necrosis: mechanistic description of dead and dying eukaryotic cells. *Infect. Immun.* 73: 1907–16.

28. Majno, G., and I. Joris. 1995. Apoptosis, oncosis, and necrosis. An overview of cell death. *Am. J. Pathol.* 146: 3–15.

29. Brouckaert, G., M. Kalai, D. V Krysko, X. Saelens, D. Vercammen, M. N. Ndlovu, M. Ndlovu, G. Haegeman, K. D'Herde, and P. Vandenabeele. 2004. Phagocytosis of necrotic cells by macrophages is phosphatidylserine dependent and does not induce inflammatory cytokine production. *Mol. Biol. Cell* 15: 1089–100.

30. Lee, J., H. G. Remold, M. H. Ieong, and H. Kornfeld. 2006. Macrophage apoptosis in response to high intracellular burden of Mycobacterium tuberculosis is mediated by a novel caspase-independent pathway. *J. Immunol.* 176: 4267–74.

31. Keane, J., M. K. Balcewicz-Sablinska, H. G. Remold, G. L. Chupp, B. B. Meek, M. J. Fenton, and H. Kornfeld. 1997. Infection by Mycobacterium tuberculosis promotes human alveolar macrophage apoptosis. *Infect. Immun.* 65: 298–304.

32. Watson, V. E., L. L. Hill, L. B. Owen-Schaub, D. W. Davis, D. J. McConkey, C. Jagannath, R. L. Hunter, and J. K. Actor. 2000. Apoptosis in mycobacterium tuberculosis infection in mice exhibiting varied immunopathology. *J. Pathol.* 190: 211–20.

33. Fallahi-Sichani, M., M. El-Kebir, S. Marino, D. E. Kirschner, and J. J. Linderman. 2011. Multiscale computational modeling reveals a critical role for TNF-α receptor 1 dynamics in tuberculosis granuloma formation. *J. Immunol.* 186: 3472–83.

34. Gil, D. P., L. G. León, L. I. Correa, J. R. Maya, S. C. París, L. F. García, and M. Rojas. 2004. Differential induction of apoptosis and necrosis in monocytes from patients with tuberculosis and healthy control subjects. *J. Infect. Dis.* 189: 2120–8.

35. Arcila, M. L., M. D. Sánchez, B. Ortiz, L. F. Barrera, L. F. García, and M. Rojas. 2007. Activation of apoptosis, but not necrosis, during Mycobacterium tuberculosis

infection correlated with decreased bacterial growth: role of TNF-alpha, IL-10, caspases and phospholipase A2. *Cell. Immunol.* 249: 80–93.

36. Zhang, D.-W., J. Shao, J. Lin, N. Zhang, B.-J. Lu, S.-C. Lin, M.-Q. Dong, and J. Han. 2009. RIP3, an energy metabolism regulator that switches TNF-induced cell death from apoptosis to necrosis. *Science* 325: 332–6.

37. He, S., L. Wang, L. Miao, T. Wang, F. Du, L. Zhao, and X. Wang. 2009. Receptor interacting protein kinase-3 determines cellular necrotic response to TNF-alpha. *Cell* 137: 1100–11.

38. Roca, F. J., and L. Ramakrishnan. 2013. TNF Dually Mediates Resistance and Susceptibility to Mycobacteria via Mitochondrial Reactive Oxygen Species. *Cell* 1–14.

39. Nikoletopoulou, V., M. Markaki, K. Palikaras, and N. Tavernarakis. 2013. Crosstalk between apoptosis, necrosis and autophagy. *Biochim. Biophys. Acta* 1833: 3448–59.

40. Doz, E., R. Lombard, F. Carreras, D. Buzoni-Gatel, and N. Winter. 2013. Mycobacteria-infected dendritic cells attract neutrophils that produce IL-10 and specifically shut down Th17 CD4 T cells through their IL-10 receptor. *J. Immunol.* 191: 3818–26.

41. Michlewska, S., I. Dransfield, I. L. Megson, and A. G. Rossi. 2009. Macrophage phagocytosis of apoptotic neutrophils is critically regulated by the opposing actions of pro-inflammatory and anti-inflammatory agents: key role for TNF-alpha. *FASEB J.* 23: 844–54.

42. Eum, S.-Y., J.-H. Kong, M.-S. Hong, Y.-J. Lee, J.-H. Kim, S.-H. Hwang, S.-N. Cho, L. E. Via, and C. E. Barry. 2010. Neutrophils are the predominant infected phagocytic cells in the airways of patients with active pulmonary TB. *Chest* 137: 122–8.

43. Tsai, M. C., S. Chakravarty, G. Zhu, J. Xu, K. Tanaka, C. Koch, J. Tufariello, J. Flynn, and J. Chan. 2006. Characterization of the tuberculous granuloma in murine and human lungs: cellular composition and relative tissue oxygen tension. *Cell. Microbiol.* 8: 218–32.

44. Mattila, J. T., O. O. Ojo, D. Kepka-Lenhart, S. Marino, J. H. Kim, S. Y. Eum, L. E. Via, C. E. Barry, E. Klein, D. E. Kirschner, S. M. Morris, P. L. Lin, and J. L. Flynn. 2013. Microenvironments in tuberculous granulomas are delineated by distinct populations of macrophage subsets and expression of nitric oxide synthase and arginase isoforms. *J. Immunol.* 191: 773–84.

45. Braian, C., V. Hogea, and O. Stendahl. 2013. Mycobacterium tuberculosis- induced neutrophil extracellular traps activate human macrophages. *J. Innate Immun.* 5: 591–602.

46. Bru, A., and P.-J. Cardona. 2010. Mathematical modeling of tuberculosis bacillary counts and cellular populations in the organs of infected mice. *PLoS One* 5: e12985.

47. Sarathy, J., V. Dartois, and E. Lee. 2012. The Role of Transport Mechanisms in Mycobacterium Tuberculosis Drug Resistance and Tolerance. *Pharmaceuticals* 5: 1210–1235.

48. Gillespie, S. H. 2002. Evolution of Drug Resistance in Mycobacterium tuberculosis : Clinical and Molecular Perspective MINIREVIEW Evolution of Drug Resistance in Mycobacterium tuberculosis : Clinical and Molecular Perspective. 46.

49. Hermsen, R., J. B. Deris, and T. Hwa. 2012. On the rapidity of antibiotic resistance evolution facilitated by a concentration gradient. *Proc. Natl. Acad. Sci. U. S. A.* 109: 10775–80.

50. Deris, J. B., M. Kim, Z. Zhang, H. Okano, R. Hermsen, A. Groisman, and T. Hwa. 2013. The Innate Growth Bistability and Fitness Landscapes of Antibiotic-Resistant Bacteria. *Science (80-.).* 342: 1237435–1237435.

51. Wu, A., K. Loutherback, G. Lambert, L. Estévez-Salmerón, T. D. Tlsty, R. H. Austin, and J. C. Sturm. 2013. Cell motility and drug gradients in the emergence of resistance to chemotherapy. *Proc. Natl. Acad. Sci. U. S. A.* 110: 16103–8.

52. Foo, J., and F. Michor. 2014. Evolution of acquired resistance to anti-cancer therapy. *J. Theor. Biol.* 355: 10–20.

53. Colijn, C., T. Cohen, A. Ganesh, and M. Murray. 2011. Spontaneous emergence of multiple drug resistance in tuberculosis before and during therapy. *PLoS One* 6: e18327.

54. Dheda, K., T. Gumbo, N. R. Gandhi, M. Murray, G. Theron, Z. Uwadia, G. B. Migliori, and R. Warren. 2014. Global control of tuberculosis: from extensively drug-resistant to untreatable tuberculosis. *Lancet Respir. Med.* 2600: 1–18.

55. Reisfeld, B., C. P. Metzler, M. a Lyons, a N. Mayeno, E. J. Brooks, and M. a Degroote. 2012. A physiologically based pharmacokinetic model for capreomycin. *Antimicrob. Agents Chemother.* 56: 926–34.

56. Ankomah, P., and B. R. Levin. 2012. Two-drug antimicrobial chemotherapy: a mathematical model and experiments with Mycobacterium marinum. *PLoS Pathog.* 8: e1002487.

57. Kjellsson, M. C., L. E. Via, A. Goh, D. Weiner, K. M. Low, S. Kern, G. Pillai, C. E. Barry, and V. Dartois. 2012. Pharmacokinetic evaluation of the penetration of antituberculosis agents in rabbit pulmonary lesions. *Antimicrob. Agents Chemother.* 56: 446–57.

58. Flynn, J. L. 2006. Lessons from experimental Mycobacterium tuberculosis infections. *Microbes Infect.* 8: 1179–88.

59. Lin, P. L., C. B. Ford, M. T. Coleman, A. J. Myers, R. Gawande, T. Ioerger, J. Sacchettini, S. M. Fortune, and J. L. Flynn. 2014. Sterilization of granulomas is common in active and latent tuberculosis despite within-host variability in bacterial killing. *Nat. Med.* 20: 75–9.

Appendix A

Supplementary Information for Chapter 3

A.1 Agent-Based Model Rules and Interactions

The overall structure of the agent-based model (ABM) for the immune response to *Mtb* infection in the lung is presented below (Figure A.1). Figure 3.2 in the Chapter 3 indicates how individual models exist separately and how they are linked. In this Appendix, we describe the cellular and tissue scale model termed GranSim.

A.1.1 Overall Structure of GranSim

GranSim was developed based on four considerations: an environment, agents (immune cells), ABM rules that govern the agents and their interactions, and the time-step (Δt) used to update events. The environment represents a two-dimensional section of lung parenchyma as a 100 × 100 square lattice that simulates an area of 2 mm × 2 mm. Each grid micro-compartment is thus scaled to the approximate size of a single human macrophage, 20 μm in diameter. Discrete agents (macrophages and T cells) are recruited from specific micro-compartments on the lattice that represent vascular sources. Cells move on the lattice and interact with each other and the environment based on the ABM rules that are defined based on known biological activities. Due to the size difference between macrophages and T cells, up to two T cells are permitted to enter the same micro-compartment (with probability T_{moveT}). A T cell may also move into the same

micro-compartment as a macrophage (with probability T_{moveM}). This model of cell spacing is a compromise between a realistic spatial representation and computational tractability and is consistent with observations on macrophage and T cell dynamics during development of mycobacterial granulomas that show granuloma-associated T cells squeeze through cell junctions created by a dense macrophage network (1).

Extracellular *Mtb* and soluble molecules, including chemokines (CCL2, CCL5 and CXCL9/10/11), soluble TNF-α (sTNF), shed TNFR2, and soluble IL-10, are simulated as continuous entities that can reside anywhere on the lattice. Extracellular Mtb grow in each micro-compartment. Soluble molecules diffuse and degrade among micro-compartments. Caseation represents inflammation of and damage to the lung parenchyma from macrophage cell death. In the ABM, caseation is defined to occur when a specific number (N_{caseum}) of infected or activated macrophages die in a micro-compartment. When a micro-compartment becomes caseated, any T cell present in the micro-compartment is killed and no further cells are permitted to enter the micro-compartment.

There are two major types of discrete agents in the model, macrophages and T cells. Macrophages are either resting (M_r, uninfected), infected (M_i; have taken up *Mtb*), chronically infected (M_{ci}; are unable to clear their intracellular *Mtb* due to a high bacterial load), or activated (M_a; can effectively kill bacteria). Three distinct T cell classes based on their functions are modeled. The T_γ class represents CD4 and CD8 pro-inflammatory T cells; T_c class represents cytotoxic T cells (CTLs); and T_r class represents regulatory T cells including FOXP3+ and FOXP3- cells.

Cell-cell interactions are governed by ABM rules that are updated within every ABM time-step of dt_A = 10 min and will be discussed in the next section. Diffusion and

degradation of soluble molecules on the lattice and secretion of chemokines from individual cells occurs is solved within each ABM time-step at a time step of $dt_D = 30$ seconds. TNF-α/TNFR and IL-10/IL-10R dynamics at the single-cell level are updated within the diffusion time-step with a shorter time-step of $dt_M = 6$ seconds. Molecular scale events are described in detail in Appendix A.2. Thus, each single-cell event is updated 5 times within each diffusion time-step while the diffusion, degradation, and secretion events are updated 20 times with each ABM time-step. The overall algorithm of the simulation takes the form outlined in Figure A.1 and will be presented in detail in the following sections.

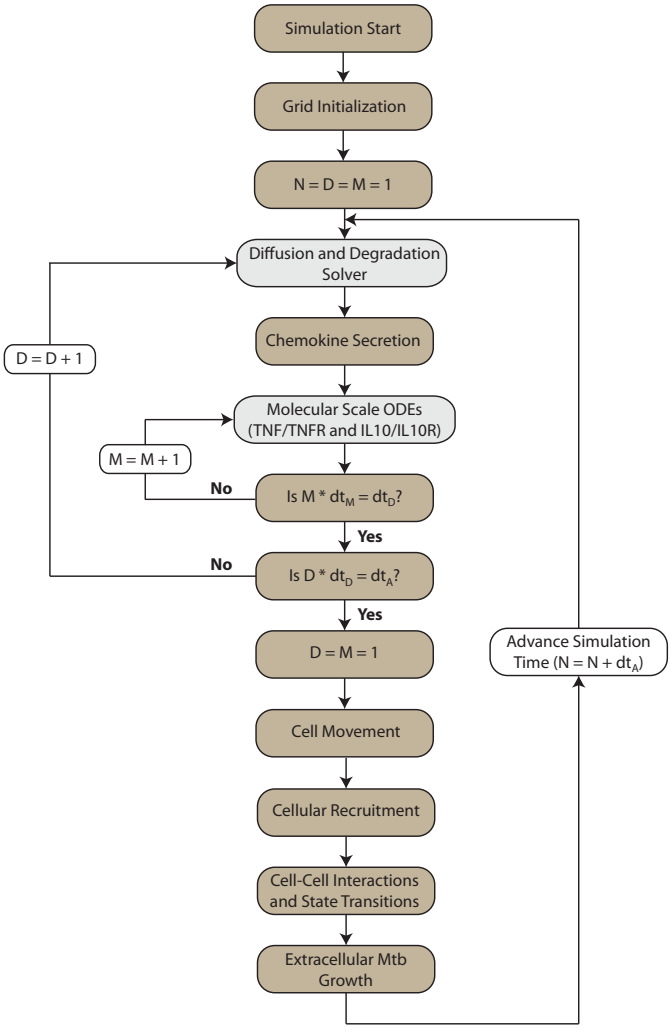

Figure A.1 Overall outline of the hybrid multi-scale ABM granuloma simulations
The boxes in gold are part of the tissue and cellular scale GRSim while the boxes in grey are part of the molecular scale model. dt_A is the ABM time-step. dt_D is the diffusion time step. dt_M is the single cell receptor ligand dynamics time-step.

A.1.2 Grid Initialization

A 100 × 100 two-dimensional grid is created. Periodic boundary conditions for cell movement and Dirichlet boundary conditions (zero outside grid perimeter) for molecular diffusion are used. 50 vascular source locations (N_{source}) are distributed on the grid. 49 of the vascular sources are randomly distributed in 7 × 7 approximately equally sized partitions on the grid. One other micro-compartment is randomly selected from the whole grid as the last vascular source. Initial resting macrophages that represent resident alveolar macrophages are randomly placed on the grid (M_{init}). One infected macrophage with one intracellular *Mtb* is placed at the center of the grid. This is consistent with estimations of the minimum infection dose of *Mtb* that range from a single bacterium upward (2).

A.1.3 Cellular and Tissue Scale ABM Rules - Overview (GranSim)

Cells move, become recruited to the site of infection, and respond to local conditions depending on their type and state according to rules that represent known biological activities *in vivo*. ABM rules that govern cell behaviors and interactions are as follows. Since chemokine single cell-level dynamics are not included in our model we discuss chemokine-related secretion and cellular recruitment in addition to cellular scale immunological details of the ABM in this section.

A.1.3.1 Agent Movement

A.1.3.1.1 Macrophages

Macrophages may stay in place or move in 8 possible directions on the grid based on CCL2 and CCL5 chemokine concentrations in their Moore neighborhood, the nine micro-compartments around the cell location including the micro-compartment occupied by the cell. Speed of movement only depends on the state of macrophages with the highest speed for M_r and the smallest speed (zero) for M_{ci}. The differences among macrophage speeds are shown in the model by time intervals in which each macrophage attempts to move (t_{moveMr}, t_{moveMi}, t_{moveMa}). There are minimum concentration thresholds and maximum saturating concentration thresholds (τ_{chem} and s_{chem}) for the effect of each chemokine on cell movement. Chemokine concentrations below τ_{chem} or above s_{chem} do not have any extra effect on direction of movement. For simplicity we assume similar threshold values for all chemokines and cell types. Movement is random if chemokine concentrations in the Moore neighborhood are below τ_{chem} or above s_{chem}. Otherwise, CCL2 and CCL5 concentrations in the Moore neighborhood determine a linear probability distribution for movement. We assume a bias for macrophage movement to the micro-compartment with the highest chemokine concentration. Hence, the highest chemokine concentration in the Moore neighborhood is multiplied by a factor 1.5 before calculation of movement probabilities. Movement is blocked by a caseous micro-compartment or macrophage presence and if blocked, no extra attempt for moving is made.

A.1.3.1.2 T cells

T cell movements are updated in time intervals of length t_{MoveT} that is determined by the speed of T cell migration *in vivo*. Movement of T_γ cells depends on CCL2, CCL5 and CXCL9/10/11 concentrations in the Moore neighborhood. T_c cells move based on CCL5 and CXCL9/10/11 concentrations and T_r cells move based on CCL5 concentrations. The details of T cell chemotactic movements are similar to macrophages as described above. T cell movement is blocked by caseation. However, T cell movement to a micro-compartment that contains one macrophage or one T cell is possible with reduced probabilities, T_{moveM} and T_{moveT}, respectively.

A.1.3.2 Cellular Recruitment

We updated our previous cellular recruitment algorithm by adding chemokine- and cytokine-dependent recruitment rates of immune cells to the infection site. We recruit macrophages (M_r) and T cells (T_γ, T_c, and T_r) from vascular sources randomly distributed across the lung environment. The recruitment rate at each vascular source is dependent upon the concentrations of CCL2, CCL5, CXCL9, and TNF-α in the specified micro-compartment (3, 4). Recruitment at a vascular source that contains one macrophage or one T cell is subject to the same rules as movement with recruitment probabilities reduced by T_{moveM} and T_{moveT}, respectively. The recruitment algorithm is shown in Figure A.2 and described in detail below.

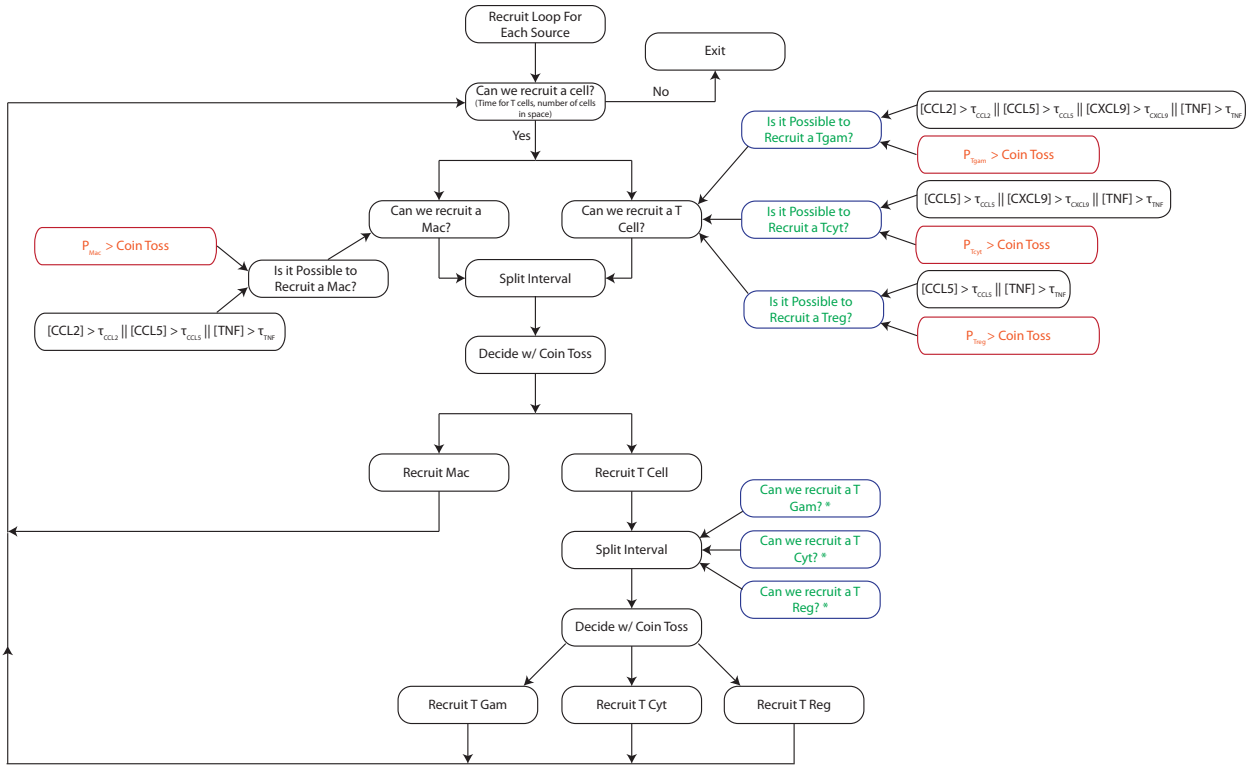

Figure A.2 Overall outline of the cellular recruitment algorithm
The boxes in orange are defined in the appropriate agent section below. The stars represent a saved calculation from previous steps in the algorithm.

A.1.3.2.1 Macrophages

M_r are recruited every time-step from vascular sources based on available TNF-α and CCL2, and CCL5 concentrations at the specific vascular source, provided that the vascular source is not caseated nor blocked by a macrophage or two T cells. The probability of recruitment of M_r is given by:

$$P_{Mr} = M_{recMax}\left[\left(\frac{V_{Max}^{TNF}\left[TNF-\tau_{recMacTNF}\right]}{\left[TNF-\tau_{recMacTNF}\right]+h_{MacTNF}}\right)+\left(\frac{V_{Max}^{CCL2}\left[CCL2-\tau_{recMacCC}\right]}{\left[CCL2-\tau_{recMacCC}\right]+h_{MacCC}}\right)+\left(\frac{V_{Max}^{CCL5}\left[CCL5-\tau_{recMacCC}\right]}{\left[CCL5-\tau_{recMacCC}\right]+h_{MacCC}}\right)\right]$$

Along with the recruitment function the following threshold conditions must be met:

$$\left[CCL2\right]>\tau_{recMacCC}\,\|\left[CCL5\right]>\tau_{recMacCC}\,\|\left[TNF\right]>\tau_{recMacTNF}$$

A.1.3.2.2 T cells

Recruitment of T cells begins after a threshold of number of *Mtb* ($N_{MtbTcell}$) is reached that represents the time required for activation of the adaptive immune response following *Mtb* infection. T_γ are recruited every time-step from vascular sources based on available TNF-α, CCL2, CCL5, and CXCL9/10/11 (written as only CXCL9 from here forth) concentrations at the specific vascular source, provided that the vascular source is not caseated nor blocked by a macrophage or two T cells. The probability of recruitment of T_γ is given by:

$$P_{T\gamma} = T_{recTgamMax}\left[\left(\frac{V_{Max}^{TNF}\left[TNF-\tau_{recTgamTNF}\right]}{\left[TNF-\tau_{recTgamTNF}\right]+h_{TgamTNF}}\right)+\left(\frac{V_{Max}^{CCL2}\left[CCL2-\tau_{recTagmCC}\right]}{\left[CCL2-\tau_{recTgamCC}\right]+h_{TagmCC}}\right)+\left(\frac{V_{Max}^{CCL5}\left[CCL5-\tau_{recTgamCC}\right]}{\left[CCL5-\tau_{recTgamCC}\right]+h_{TgamCC}}\right)+\left(\frac{V_{Max}^{CCL5}\left[CXCL9-\tau_{recTgamCC}\right]}{\left[CXCL9-\tau_{recTgamCC}\right]+h_{TgamCC}}\right)\right]$$

Along with the recruitment function the following threshold conditions must be met:

$$\left[CCL2\right]>\tau_{recMacCC}\ \|\left[CCL5\right]>\tau_{recMacCC}\ \|\left[CXCL9\right]>\tau_{recMacCC}\ \|\left[TNF\right]>\tau_{recMacTNF}$$

T_c are recruited every time-step from vascular sources based on available TNF-α, CCL5, and CXCL9 concentrations at the specific vascular source, provided that the vascular source is not caseated nor blocked by a macrophage or two T cells. The probability of recruitment of T_c is given by:

$$P_{Tc} = T_{recTcytMax}\left[\left(\frac{V_{Max}^{TNF}\left[TNF-\tau_{recTcytTNF}\right]}{\left[TNF-\tau_{recTcytTNF}\right]+h_{TcytTNF}}\right)+\left(\frac{V_{Max}^{CCL5}\left[CCL5-\tau_{recTcytCC}\right]}{\left[CCL5-\tau_{recTcytCC}\right]+h_{TcytCC}}\right)+\left(\frac{V_{Max}^{CCL5}\left[CXCL9-\tau_{recTcytCC}\right]}{\left[CXCL9-\tau_{recTcytCC}\right]+h_{TcytCC}}\right)\right]$$

Along with the recruitment function the following threshold conditions must be met:

$$\left[CCL2\right]>\tau_{recMacCC}\ \|\left[CXCL9\right]>\tau_{recMacCC}\ \|\left[TNF\right]>\tau_{recMacTNF}$$

T_r are recruited every time-step from vascular sources based on available TNF-α and CCL5 concentrations at the specific vascular source, provided that the vascular

source is not caseated nor blocked by a macrophage or two T cells. The probability of recruitment of T_r is given by:

$$P_{Tr} = T_{recTregMax}\left[\left(\frac{V_{Max}^{TNF}\left[TNF - \tau_{recTregTNF}\right]}{\left[TNF - \tau_{recTregTNF}\right] + h_{TregTNF}}\right) + \left(\frac{V_{Max}^{CCL5}\left[CCL5 - \tau_{recTregCC}\right]}{\left[CCL5 - \tau_{recTregCC}\right] + h_{TregCC}}\right)\right]$$

Along with the recruitment function the following threshold conditions must be met:

$$\left[CCL5\right] > \tau_{recMacCC} \,||\, \left[TNF\right] > \tau_{recMacTNF}$$

A.1.3.3 Cell-Cell Interactions and State Transitions

All cell-cell interactions and state transitions described below are updated every ABM time-step for all cells.

A.1.3.3.1 Cell Death Due to Age

All macrophages that are initially distributed or recruited on the grid are assigned a lifespan selected from a uniform distribution between zero and max_{ageMac}. T cells are also assigned a lifespan randomly distributed between zero and $max_{ageTcell}$. M_a has a shortened lifespan of $max_{ageActive}$. At death, M_r and T cells are removed from the grid. At death, M_i and M_{ci} are removed from the grid and any intracellular *Mtb* (B_{int}) is dispersed uniformly in the Moore neighborhood as extracellular bacteria (B_{ext}). M_a death contributes to caseation of the micro-compartment.

A.1.3.3.2 Rules for Resting Macrophages (M_r)

There is a chance of STAT-1 activation in a time-step as a result of interaction between a M_r and IFN-γ producing T_γ cells with a probability (nT_γ * P_{STAT1}); where, nT_γ is the number of T_γ cells surrounding the M_r in the Moore neighborhood including the

micro-compartment occupied by the M_r. M_r can become NF-κB activated through TNF-α induced processes, which is discussed in Appendix A.2. NF-κB activation can also occur if the B_{ext} in the Moore neighborhood exceeds B_{actM}. STAT-1 and NF-κB activation last for the time interval t_{STAT1} and $t_{NF\kappa B}$ after which STAT-1 or NF-κB activation, respectively, is lost. M_r that are either STAT1 or NF-κB can be down-regulated by a T_r in which the M_r loses either STAT1 or NF-κB activation respectively. M_r is able to uptake or to kill B_{ext} that reside in the same micro-compartment. If the number of $B_{ext} \leq N_{rk}$, M_r kills them. Otherwise, it either kills N_{rk} of the B_{ext} with probability P_k or becomes infected (M_i) after uptake of N_{rk} of the B_{ext} as its initial B_{int}. M_r that are either STAT1 or NF-κB activated kill B_{ext} with a probability 2* P_k due to increased anti-microbial capacity. If both STAT1 and NF-κB are activated in a Mr and it is not already down-regulated by a T_r, it becomes activated (M_a). Following Tr down-regulation, M_r does nothing but moves for a fixed period of time t_{regMac}. If the remaining lifespan of such an activated macrophage is greater than $max_{ageActive}$, it will be shortened to $max_{ageActive}$.

A.1.3.3.3 Rules for Infected Macrophages (M_i)

B_{int} replicates in M_i every ABM time-step according to the following equation:

$$B_{\text{int}}(t + \Delta t) = (1 + \alpha_{Bi})B_{\text{int}}(t)$$

M_i is able to uptake but not kill B_{ext} from its micro-compartment with a probability ($P_{uptakeMi}$) that is computed as a function of B_{int} as follows:

$$P_{uptakeMi} = (N_c - B_{\text{int}})/100$$

M_i takes up N_{rk} of extracellular bacteria if $B_{ext} > N_{rk}$. Otherwise, it takes up all extracellular bacteria that are available in the micro-compartment. If the number of B_{int}

exceeds a threshold N_c, the M_i becomes chronically infected (M_{ci}). There is a chance of STAT-1 activation in a time-step as a result of interaction between a M_i and IFN-γ producing T_γ cells with a probability ($nT_\gamma * P_{STAT1}$); where, nT_γ is the number of T_γ cells surrounding the M_r in the Moore neighborhood including the micro-compartment occupied by the M_r. M_i can become NF-κB activated through TNF-α induced processes, which is discussed in Appendix A.2. NF-κB activation can also occur if the B_{ext} in the Moore neighborhood exceeds B_{actM}. STAT-1 and NF-κB activation last for the time interval t_{STAT1} and $t_{NF\kappa B}$ after which STAT-1 or NF-κB activation, respectively, is lost. M_i that are either STAT1 or NF-κB can be down-regulated by a T_r in which the M_i loses either STAT1 or NF-κB activation respectively. Following T_r down-regulation, M_i does nothing but moves for a fixed period of time t_{regMac}, but continues to secrete chemokines. If both STAT1 and NF-κB are activated in a M_i and it is not already down-regulated by a T_r, it becomes activated (M_a). If the remaining lifespan of such an activated macrophage is greater than $max_{ageActive}$, it will be shortened to $max_{ageActive}$.

A.1.3.3.4 Rules for Chronically Infected Macrophages (M_{ci})

B_{int} replicates in M_{ci} every time-step in the same way as M_i. If the B_{int} exceeds a threshold (N_{burst}), the M_{ci} bursts and its B_{int} are evenly distributed to the Moore neighborhood surrounding the M_{ci}. M_{ci} bursting contributes to caseation of the micro-compartment. M_{ci} are always NF-κB activated and cannot become STAT1 activated. M_{ci} cannot be down-regulated by a T_r.

A.1.3.3.5 Rules for Activated Macrophages (M_a)

M_a is capable of effectively killing B_{ext}. Each time-step, Ma kills N_{ak} of the B_{ext} in its micro-compartment. M_a that transitions from M_i kill B_{int} at the same rate that it kills B_{ext} each time-step. M_a can be down-regulated by a T_r in which the M_a loses both STAT1 and NF-κB activation. Following T_r down-regulation, M_a does nothing but moves for a fixed period of time t_{regMac} and subsequently transitions back to M_r after its down-regulated state.

A.1.3.3.6 Rules for Cytotoxic T cells (T_c)

If T_c is not already down-regulated by a T_r and there is a M_i or M_{ci} present in its Moore neighborhood there is a chance of perforin/granulysin-mediated killing of M_i or M_{ci} with probability $P_{cytKill}$. If there are more than one M_i or M_{ci} in the Moore neighborhood one is chosen at random and the chance of perforin/granulysin-mediated killing of M_i or M_{ci} is given by the probability $P_{cytKill}$. M_i killing by a T_c kills all B_{int} and contributes to caseation of the micro-compartment. In the case of M_{ci} killing, the B_{int} are killed with probability $P_{cytKillClean}$. Otherwise, half of the B_{int} will be uniformly distributed in the Moore neighborhood. M_{ci} killing by T_c also contributes to caseation of the micro-compartment. When down-regulated, T_c cells lose their cytotoxic capabilities for a fixed period of time $t_{regTcyt}$.

A.1.3.3.7 Rules for Pro-inflammatory T cells (T_γ)

If T_γ is not already down-regulated by a T_r and there is a M_i or M_{ci} present in its Moore neighborhood there is a chance of Fas/FasL-induced apoptosis of M_i or M_{ci} with probability $P_{apop/Fas}$. If there are more than one M_i or M_{ci} in the Moore neighborhood one

is chosen at random and the chance of Fas/FasL-induced apoptosis of M_i or M_{ci} is given by the probability $P_{apop/Fas}$. As a result of apoptosis, half of the B_{int} in M_i or M_{ci} will be killed and the other half will be equally distributed in the Moore neighborhood as B_{ext}. When down-regulated, T_γ cells lose their apoptotic capabilities for a fixed period of time $t_{regTgam}$.

A.1.3.3.8 Rules for Regulatory T cells (T_r)

T_r suppresses or down-regulates the action of T cells and macrophages through non interleukin-10 mechanisms (CTLA-4, TGF-β, etc.), which are still poorly understood (5–7). Thus, the probability of alternative suppressive functions of T_r occurring is linearly dependent upon the following ratio (Eq. 3), which coarsely simulates the mechanisms of other regulatory mechanisms that are not the focus of this work.

$$BoundRatio = \frac{[TNF \cdot TNFR1]}{[TNF \cdot TNFR1] + [IL10 \cdot IL10R]}$$

T_r here down-regulates all cells (macrophages, T_c and T_γ) in its Moore neighborhood. Down-regulated states last for t_{regMac}, $t_{regTgam}$ and $t_{regTcyt}$ for macrophages, T_c and T_γ cells, respectively. T_r down-regulation for each cell type is explained in sections that describe ABM rules for that specific cell type.

A.1.3.4 Extracellular Mtb Growth

Growth of extracellular *Mtb* (B_{ext}) in all micro-compartments is calculated based on the following equation:

$$B_{ext}(t + \Delta t) = B_{ext}(t) + \alpha_{Be} B_{ext}(t)\left[1 - \frac{B_{ext}(t)}{1.1K_{be}}\right]$$

A.1.3.5 Chemokine Secretion

M_i, M_{ci}, M_a, NF-κB activated M_r, and NF-κB activated M_i are able to secrete chemokines, provided that they are not down-regulated by T_r. The rates of chemokine secretion for different cell types are as follows. M_{ci}, M_a and NF-κB activated M_i are able to secrete chemokines with full secretion rates (r_{CCL2}, r_{CCL5}, and r_{CXCL9}) as listed in Table A.3. NF-κB activated M_r and M_i cells that are not NF-κB activated secrete chemokines with half-full secretion rates ($0.5 \times r_{CCL2}$, $0.5 \times r_{CCL5}$, and $0.5 \times r_{CXCL9}$). Caseated micro-compartments also secrete attractants that attract immune cells. For simplicity, we use quarter-full rates of chemokine secretion to simulate the effect of such attractants ($0.25 \times r_{CCL2}$, $0.25 \times r_{CCL5}$, and $0.25 \times r_{CXCL9}$). Chemokine secretions to the micro-compartments on the grid are updated in time intervals of dt_D. Secretion of TNF and IL-10 is discussed in Appendix A.2.

A.2 Molecular Scale Models

The overall structure of the computational model of the immune response to *Mtb* infection in the lung is presented in Appendix A.1. Figure 3.2 in Chapter 3 indicates how these models exist separately and how they are linked. The overall algorithm of the simulation takes the form outlined in Figure A.1 in Appendix A.1 and the molecular scale will be presented in detail in this section. The solution of molecular scale models of diffusion, degradation, and TNF-α and IL-10 single-cell level receptor-ligand dynamics will be discussed section.

A.2.1 Diffusion of Soluble Molecules

The two-dimensional partial differential equation (PDE) for diffusion of CCL2, CCL5, CXCL9, TNF-α, IL-10, and shed bound TNFR2 is given by the following equation.

$$\frac{\partial C}{\partial t} = D\left(\frac{\partial^2 C}{\partial x^2} + \frac{\partial^2 C}{\partial y^2}\right)$$

C is the concentration of diffusing molecule that changes with time (t) in the x and y directions and D is the diffusion coefficient for the molecule in the tissue environment. This equation can be implemented numerically on the grid by using the alternate-direction explicit finite difference discrete-time discrete-space approximation scheme (8). Let $u_{i,j}$ and $v_{i,j}$ be finite difference solutions of the transient diffusion PDE. Define i as the lattice parameter for the x-direction, j as the lattice parameter for y-direction, n as the current time point, Δx as the x-direction grid size, and Δy as the y-direction grid size. In the case of *u* the iteration proceeds forward in the i, j direction thus any values of *u* at time (n+1) will be known. For the case of *v* the iteration proceeds in the decreasing i, j direction (the iteration starts at the end of the grid and works backwards) therefore all values of *v* at time (n+1) will be known.

$$\frac{u_{i,j}^{n+1} - u_{i,j}^{n}}{\delta t} = \frac{u_{i+1,j}^{n} - u_{i,j}^{n} - u_{i,j}^{n+1} + u_{i-1,j}^{n+1}}{\delta x^2} + \frac{u_{i,j+1}^{n} - u_{i,j}^{n} - u_{i,j}^{n+1} + u_{i,j-1}^{n+1}}{\delta y^2}$$

$$\frac{v_{i,j}^{n+1} - v_{i,j}^{n}}{\delta t} = \frac{v_{i+1,j}^{n+1} - v_{i,j}^{n+1} - v_{i,j}^{n} + v_{i-1,j}^{n}}{\delta x^2} + \frac{v_{i,j+1}^{n+1} - v_{i,j}^{n+1} - v_{i,j}^{n} + v_{i,j-1}^{n}}{\delta y^2}$$

Thus, the concentration at a specific time point is given by the arithmetic average of u and v.

$$C_{i,j}^{n+1} = \frac{u_{i,j}^{n+1} + v_{i,j}^{n+1}}{2}$$

This method is unconditionally stable, allowing us to choose a dt_D = 30 seconds for reasonable numerical accuracy and computational efficiency.

A.2.2 Degradation of Soluble Molecules

Degradation of soluble CCL2, CCL5, CXCL9, TNF-α, IL-10, and shed bound TNFR2 is described by:

$$\frac{\partial C}{\partial t} = -k_{\text{deg}} C$$

where k_{deg} is the degradation rate constant for the specific molecule in the tissue environment. In order to increase the accuracy of the solution degradation and prevent unnecessary computational burden, we calculate degradation using the analytical solution below.

$$\frac{C}{C_0} = e^{-k_{\text{deg}} * dt_D}$$

This is calculated with the same solver time step as the diffusion equation, dt_D.

A.2.3 Single-Cell Level Receptor-Ligand Dynamics

We use ordinary differential equations (ODEs) to describe the TNF/TNFR and IL-10/IL-10R receptor-ligand dynamics occurring at the single-cell level. TNF/TNFR and IL-10/IL-10R ODEs are solved for each individual cell on the grid using the time-step dt_M and the 4^{th} order Runge-Kutta numerical method. Soluble molecules in the model (sTNF, sTNF/$TNFR2_{shed}$, and IL-10) are expressed as volumetric concentration units (e.g. M), whereas cell-associated species are expressed as numbers of molecules per cell. Thus, when a membrane-bound molecule releases to the extracellular space (i.e. the

micro-compartment occupied by the cell), or when a soluble molecule binds to the cell membrane, a scaling factor (ρ/Nav) is required as indicated in Table A.2, where ρ is the cell density in the micro-compartment and can be computed as dx^3 assuming that each micro-compartment is a cube of side dx.

A.2.3.1 Single-Cell Level IL-10/IL-10R Equations

The binding interactions and reactions controlling IL-10/IL-10R dynamics at the single-cell level regardless of the cell type are schematically illustrated in Chapter 3 (Figure 3.2). IL-10 is synthesized by IL-10 producing cells (M_i, M_{ci}, M_a, and T_r), if not down-regulated by T_r cells, and is released directly into the extracellular environment (6, 9–16). IL-10 exists in the extracellular space as a non-covalently bonded dimer where it can bind to cell-surface IL-10R1 and IL-10R2 (17, 18). Signaling occurs through association of bound IL-10R1 with the IL-10R2 subunit (10). IL-10R1 is the high affinity receptor compared to IL-10R2, which mainly exists as a signaling subunit to bound IL-10R1. For simplicity, we include only a general IL-10R that represents both IL-10R1 and IL-10R2 (19, 20). IL-10R is synthesized by the cell and is removed from the membrane by turnover (21). Bound IL-10R can be internalized where it can be degraded or recycled to the surface (22). The processes of degradation and recycling are not explicitly modeled since tracking internalized bound IL10R adds unnecessary complexity to the ODEs. We lump these processes into IL10R turnover and synthesis for simplicity. We modeled these molecular processes based on mass action kinetics as shown in Table A.1; model equations are listed in Table A.2; definitions and values of the rate constants are given in Table A.4.

The rates of IL-10 synthesis and IL-10R synthesis (k_{Synth} and V_r) are cell type/state-specific as indicated in Table A.4, but other rate constant values are common between all cells. In the multi-scale model described in Chapter 3, the rates of IL-10 synthesis for different cell types are as follows. M_i are able to synthesize IL-10 at the full rate $k_{synthMacInf}$, while M_{ci} make IL-10 at 1.5* $k_{synthMacInf}$ shown in Table A.4. M_a synthesize IL-10 at a basal rate of $k_{synthMacAct}$ but the rate is dependent upon the bound TNFR1 concentration as shown in Table A.2. T_r cells express IL-10 at the full rate $k_{synthTcell}$, while T_γ and T_c do not synthesize IL-10 in our model.

A.2.3.2 Single-Cell Level TNF/TNFR Ordinary Equations

The binding interactions and reactions controlling TNF/TNFR dynamics at the single-cell level regardless of the cell type are adapted from (23) and are schematically illustrated in (Figure 3.2). TNF-α mRNA is transcribed by TNF-producing cells (M_i, M_{ci}, M_a, NF-κB activated M_r, T_γ and T_c), if not down-regulated by T_r cells, and subsequently translated into its membrane bound form, mTNF. mTNF is then processed and released as a soluble form (sTNF) into extracellular spaces. This processing occurs via a cell-associated metalloproteinase called TACE. Two types of TNF receptors (TNFR1 and TNFR2) are synthesized and expressed on the cell surface as free receptors. Soluble TNF (sTNF) reversibly binds to TNFRs on the cell membrane. sTNF-bound cell surface TNFR1 internalizes and sTNF-bound cell surface TNFR2 may undergo internalization or shedding into extracellular spaces [8]. Internalized receptors may degrade or recycle to the cell membrane where they can re-bind to sTNF [9]. Ligand-free TNFRs also turn over (internalize) [9,10]. Intact sTNF may dissociate from the shed sTNF/TNFR2 complex in

the extracellular space [11]. We modeled these molecular processes based on mass action kinetics as shown in Table A.1; model equations are listed in Table A.2; definitions and values of the rate constants are given in Table A.4.

The rates of TNF-α mRNA synthesis and release from the cell membrane and TNFR synthesis (k_{mRNA}, k_{Synth}, k_{TACE}, V_{r1} and V_{r2}) are cell type/state-specific as indicated in Table A.4, but other rate constant values are common between all cells. In the multi-scale model described in Chapter 3, the rates of TNF-α mRNA synthesis for different cell types are as follows. M_{ci}, M_a and NF-κB activated M_i are able to synthesize mTNF with a full rate ($k_{mRNA} = k_{mRNA\_Mac}$ and $k_{synth} = k_{synthMac}$) as shown in Table A.4. NF-κB activated M_r and non-NF-κB activated M_i express TNF-α mRNA with a half-full rate ($k_{mRNA} = 0.5*k_{mRNA\_Mac}$ and $k_{synth} = 0.5*k_{synthMac}$). T_γ cells express TNF-α mRNA at a rate of k_{mRNA_Tcell} and $k_{synth} = k_{synthTcell}$, while T_c cells express TNF-α mRNA at a rate of $k_{mRNA} = 0.1*k_{mRNA\_Tcell}$ and $k_{synth} = 0.1*k_{synthTcell}$. T_r cells do not express TNF. TACE activity is also assumed to be cell type-dependent as shown in Table A.4.

A.3.2.3 Linking TNF/TNFR and IL-10/IL-10R Equations

TNF-α and IL-10 receptor-ligand dynamics are linked in two ways as shown in Figure 3.2 in Chapter 3. Bound IL-10R inhibits TNF-α mRNA transcription while bound TNFR1 can induce synthesis of IL-10 in M_a. Inhibition of TNF-α mRNA transcription shows rapid switch-like behavior, thus we modeled these processes with a three-parameter logistic function (24).

$$k_{mRNA-Mod} = k_{mRNA}\left(\beta + \frac{1-\beta}{1+e^{\frac{[IL10\cdot IL10R]-\gamma_I}{\delta_I}}}\right)$$

We captured the ability of bound TNFR1 to induce synthesis of IL-10 in M_a with Michaelis-Menton type kinetics, which roughly approximates the mechanisms influencing the plasticity of M_a to produce IL-10 at lower (classical M_a) or higher (alternative M_a) rates (25–29).

$$k_{synthMacAct-Mod} = k_{synthMacAct}\left(\frac{[sTNF \cdot TNFR1]}{[sTNF \cdot TNFR1] + h_{synthMacAct}}\right)$$

A.3.3 Linking the Molecular Scale to GranSim

The molecular scale sub-models of TNF-α are linked to GRSim through NFκB activation of macrophages, caspase induced cell apoptosis, and cellular recruitment. We describe TNF-α induced NFκB activation of each macrophage and TNF-α induced apoptosis of cells as Poisson processes with a probability of occurrence determined by a rate constant, threshold value, and a saturation value (see Table A.4 for parameter definitions and values) (23). TNF-α induced NFκB activation of macrophages is dependent on the concentration of bound TNFR1 per cell (Eq. 8), while TNF-α induced apoptosis is dependent on the concentration of internalized bound TNFR1 per cell (Eq. 9).

$$P_{NFkB} = \left\{ \begin{array}{cc} 1 - e^{-k_{NFkB}([sTNF-TNFR1]-\tau_{NFkB})\Delta t} & [sTNF - TNFR1] \geq \tau_{NFkB} \\ 0 & [sTNF - TNFR1] < \tau_{NFkB} \end{array} \right\}$$

$$P_{apop} = \left\{ \begin{array}{cc} 1 - e^{-k_{apop}([sTNF-TNFR1_i]-\tau_{apop})\Delta t} & [sTNF - TNFR1_i] \geq \tau_{apop} \\ 0 & [sTNF - TNFR1_i] < \tau_{apop} \end{array} \right\}$$

NF-κB activation is checked once for all M_r and M_i within each ABM time-step (dt_A). TNF-induced apoptosis is checked once for all cells on the grid within each ABM

time-step (dt_A). The molecular scale IL-10 sub-models are linked to GRSim through chemokine down regulation and compensation of alternative suppressive functions. IL-10 inhibits the production of chemokines by macrophages; we use a simple threshold relationship, wherein the synthesis of chemokines is reduced in half once the number of bound IL-10R is above a specified value (30–33). The probability of alternative suppressive functions of T_r occurring is linearly dependent on the ratio of bound TNFR1 to bound IL-10R, which coarsely simulates the mechanisms of other regulatory mechanisms that are not the focus of this work (5–7, 34–36).

Table A.1 Molecular Scale Single-Cell TNF/TNFR and IL10/IL10R Equations – Model Reactions and Rates (v_i)

	TNF-α Model Reactions	
1.	$mTNF_{mRNA}$ synthesis	$v_1 = k_{mRNA-Mod}$
2.	$mTNF_{mRNA} \rightarrow mTNF$	$v_2 = k_{trans}[mTNF_{mRNA}]$
3.	$mTNF \rightarrow sTNF$	$v_3 = k_{TACE}[mTNF]$
4.	$sTNF + TNFR1 \rightleftarrows sTNF \cdot TNFR1$	$v_4 = k_{on1}[sTNF][TNFR1] - k_{off1}[sTNF \cdot TNFR1]$
5.	$sTNF + TNFR2 \rightleftarrows sTNF \cdot TNFR2$	$v_5 = k_{on2}[sTNF][TNFR2] - k_{off2}[sTNF \cdot TNFR2]$
6.	$sTNF \cdot TNFR1 \rightarrow sTNF \cdot TNFR1_i$	$v_6 = k_{int1}[sTNF \cdot TNFR1]$
7.	$sTNF \cdot TNFR2 \rightarrow sTNF \cdot TNFR2_i$	$v_7 = k_{int2}[sTNF \cdot TNFR2]$
8.	$sTNF \cdot TNFR2 \rightarrow sTNF \cdot TNFR2_{shed}$	$v_8 = k_{shed}[sTNF \cdot TNFR2]$
9.	TNFR1 synthesis	$v_9 = V_{r1}$
10.	TNFR2 synthesis	$v_{10} = V_{r2}$
11.	$TNFR1 \rightarrow TNFR1_i$	$v_{11} = k_{t1}[TNFR1]$
12.	$TNFR2 \rightarrow TNFR2_i$	$v_{12} = k_{t2}[TNFR2]$
13.	$sTNF \cdot TNFR1_i \rightarrow$ degradation	$v_{13} = k_{deg1}[sTNF \cdot TNFR1_i]$
14.	$sTNF \cdot TNFR2_i \rightarrow$ degradation	$v_{14} = k_{deg1}[sTNF \cdot TNFR2_i]$
15.	$sTNF \cdot TNFR1_i \rightarrow TNFR1$	$v_{15} = k_{rec1}[sTNF \cdot TNFR1_i]$
16.	$sTNF \cdot TNFR2_i \rightarrow TNFR2$	$v_{16} = k_{rec2}[sTNF \cdot TNFR2_i]$
17.	$sTNF \cdot TNFR2_{shed} \rightarrow sTNF + TNFR2_{shed}$	$v_{17} = k_{off2}[sTNF \cdot TNFR2_{shed}]$
	IL-10 Model Reactions	
18.	IL10 synthesis	$v_{18} = k_{synth}$
19.	$IL10 + IL10R \rightleftarrows IL10 \cdot IL10R$	$v_{19} = k_{on}[IL10][IL10R] - k_{off}[IL10 \cdot IL10R]$
20.	$IL10 \cdot IL10R \rightarrow IL10 \cdot IL10R_i$	$v_{20} = k_{int}[IL10 \cdot IL10R]$
21.	$IL10R \rightarrow$ turnover	$v_{21} = k_t[IL10R]$
22.	IL10R synthesis	$v_{22} = V_r$
	Dependent Rate Constants	
	Inhbition of TNF-α mRNA Synthesis	$k_{mRNA-Mod} = k_{RNA}\left(\beta + \frac{1-\beta}{1+e^{\frac{[IL10 \cdot IL10R]-\gamma}{\delta}}}\right)$
	Induction of IL-10 Synthesis	$k_{synth} = k_{synth}\left(\frac{[sTNF \cdot TNFR1]}{[sTNF \cdot TNFR1] + h_{synthMacAct}}\right)$

Table A.2 Molecular Scale Single-Cell TNF/TNFR and IL10/IL10R Equations

TNF-α Differential Equations

$$\frac{d[mTNF_{mRNA}]}{dt} = v_1 - v_2 \qquad \frac{d[mTNF]}{dt} = v_2 - v_3$$

$$\frac{d[sTNF]}{dt} = \left(\frac{\rho}{N_{av}}\right)(v_3 - v_4 - v_5) + v_{17} \qquad \frac{d[TNFR1]}{dt} = v_9 - v_4 - v_{11} + v_{15}$$

$$\frac{d[TNFR2]}{dt} = v_{10} - v_5 - v_{12} + v_{16} \qquad \frac{d[sTNF \cdot TNFR1]}{dt} = v_4 - v_6$$

$$\frac{d[sTNF \cdot TNFR2]}{dt} = v_5 - v_7 - v_8 \qquad \frac{d[sTNF \cdot TNFR1_i]}{dt} = v_6 - v_{13} - v_{15}$$

$$\frac{d[sTNF \cdot TNFR2_i]}{dt} = v_7 - v_{14} - v_{16} \qquad \frac{d[sTNF \cdot TNFR2_{shed}]}{dt} = \left(\frac{\rho}{N_{av}}\right) v_8 - v_{17}$$

IL-10 Differential Equations

$$\frac{d[IL10]}{dt} = \left(\frac{\rho}{N_{av}}\right)(v_{18} - v_{19}) \qquad \frac{d[IL10 \cdot IL10R]}{dt} = v_{19} - v_{20}$$

$$\frac{d[IL10R]}{dt} = v_{22} - v_{21} - v_{19}$$

Table A.3 Tissue and cellular scale parameters

Parameter	Parameter Description	Value*
	Grid/Simulation Related Parameters	
$t_{diffusion}$	Time step for solving diffusion PDEs	30
$t_{molecular}$	Time step for solving molecular scale ODEs	6
N_{source}	Number of vascular sources	50
N_{caseum}	Number of qualified cell deaths required for caseation	15
K_{be}	Capacity of a micro-compartment for extracellular Mtb	200
	Chemokine Related Parameters	
D_{chem} (cm^2/s)	Diffusion coefficient of chemokines	10^{-8}-10^{-7} (5.2×10^{-8})
$k_{degChem}$(s^{-1})	Chemokine degradation rate constant	$5x10^{-4}$-$5x10^{-3}$ (1.58×10^{-3})
τ_{chem} (molecules)	Minimum chemokine concentration threshold	1-10 (2)
s_{chem} (molecules)	Saturating chemokine concentration threshold	10^3-10^4 (2000)
I_{50IL10} (ng/mL)	IC_{50} for IL10 inhibition of chemokine production	10-30 (20)
	Macrophage Related Parameters	
M_{init}	Initial number of resident macrophages	105
max_{ageMac} (day)	Maximum lifespan of macrophages	100
$max_{ageActive}$ (day)	Maximum lifespan of an active macrophage	10
t_{regMac} (hours)	Macrophage inactivity time after down-regulation by T_{reg}	24
t_{moveMr} (min)	Time interval for M_r movement	20
t_{moveMa} (hour)	Time interval for M_a movement	7.8
t_{moveMi} (hour)	Time interval for Mi movement	24
r_{CCL2} (molecules/s)	Full secretion rate of CCL2 by macrophages	4.14
r_{CCL5} (molecules/s)	Full secretion rate of CCL5 by macrophages	4.14
r_{CXCL9} (molecules/s)	Full secretion rate of CXCL9/10/11 by macrophages	8.28
N_{rk}	Number of extracellular Mtb engulfed by M_r or M_i	1
P_k	Probability of M_r killing bacteria	0.2-0.3 (0.269)
B_{actM}	Number of extracellular Mtb activating NF-κB in a mac	150-300 (239)
N_c	Number of intracellular Mtb for $M_i \rightarrow M_{ci}$ transition	10
N_{burst}	Number of intracellular Mtb that leads to M_{ci} bursting	20-30 (20)

P_{STAT1}	Probability of STAT-1 activation in M_r or M_i	0.001-0.15 (0.0917)
N_{ak}	Number of extracellular Mtb killed by M_a each time-step	2-4 (3)
$\tau_{recMacCC}$	Chemokine threshold for M_r recruitment	0.065-0.65 (0.151)
$\tau_{recMacTNF}$	TNF threshold for M_r recruitment	0.006-0.06 (0.014)
h_{MacCC}	Half-saturation of chemokines for M_r recruitment	1-10 (5)
h_{MacTNF}	Half-saturation of TNF for M_r recruitment	0.09-0.9 (0.5)
M_{recMax}	Maximum recruitment probability for M_r recruitment	0.07-0.11 (0.09)
t_{STAT1} (hours)	Time interval for STAT1 activation of M_r or M_i	25-58 (41)
$t_{NF\kappa B}$ (min)	Time interval for NFκB activation of M_r or M_i	10-500 (100)
	T Cell Related Parameters	
$N_{MtbTcell}$ (# of Mtb)	Number of Mtb required to begin T cell recruitment	50
$max_{ageTcell}$ (days)	Maximum lifespan of T cells	3
T_{moveM}	Probability of T cell moving to a mac-containing location	0.005-0.05 (0.027)
T_{moveT}	Probability of T cell moving to a T cell-containing location	0.01-0.12 (0.08)
$t_{regTgam}$ (hours)	T_γ inactivity time after down-regulation by T_{reg}	6
$P_{Fas/FasL}$	Probability of Fas/FasL apoptosis by T_γ	0.005-0.05 (0.0095)
$\tau_{recTgamCC}$	Chemokine threshold for T_γ recruitment	0.065-0.65 (0.151)
$\tau_{recTgamTNF}$	TNF threshold for T_γ recruitment	0.006-0.06 (0.014)
h_{TgamCC}	Half-saturation of chemokines for T_γ recruitment	0.5-5 (1.5)
$h_{TgamTNF}$	Half-saturation of TNF for T_γ recruitment	0.05-0.5 (0.3)
$T_{recTgamMax}$	Maximum recruitment probability for T_γ recruitment	0.03-0.11 (0.0713)
$t_{regTcyt}$ (hours)	T_c inactivity time after down-regulation by T_{reg}	6
$P_{cytKill}$	Probability of T_c killing M_i or M_{ci}	0.005-0.05 (0.0098)
$P_{cytKillClean}$	Probability of T_c killing all intracellular Mtb by killing M_{ci}	0.75
$\tau_{recTcytCC}$	Chemokine threshold for T_c recruitment	0.08-0.85 (0.3775)
$\tau_{recTcytTNF}$	TNF threshold for T_c recruitment	0.006-0.06 (0.014)
h_{TcytCC}	Half-saturation of chemokines for T_c recruitment	0.5-5 (1.5)
$h_{TcytTNF}$	Half-saturation of TNF for T_c recruitment	0.05-0.5 (0.3)
$T_{recTcytMax}$	Maximum recruitment probability for T_c recruitment	0.01-0.09 (0.0505)
$d_{slopeTreg}$	Slope of deactivation probability function for T_{reg}	0.75-1.0 (0.8905)
$d_{minTreg}$	Minimum of deactivation probability function for T_{reg}	0.0001-0.001 (0.0009)
$\tau_{recTregCC}$	Chemokine threshold for T_{reg} recruitment	0.02-0.12 (0.0755)
$\tau_{recTregTNF}$	TNF threshold for T_{reg} recruitment	0.006-0.06 (0.014)
h_{TregCC}	Half-saturation of chemokines for T_{reg} recruitment	0.5-5 (1.5)
$h_{TregTNF}$	Half-saturation of TNF for T_{reg} recruitment	0.05-0.5 (0.3)
$T_{recTregMax}$	Maximum recruitment probability for T_{reg} recruitment	0.008-0.06 (0.0221)
	Bacteria Related Parameters	
α_{Bi} (per 10 min)	Intracellular Mtb growth rate	5×10^{-4}-5×10^{-3} (1.4×10^{-3})
α_{Be} (per 10 min)	Extracellular Mtb growth rate	10^{-4}-10^{-3} (7×10^{-4})
μ_{BeCas}	Maximum death rate of extracellular Mtb in caseation	0.75-2 (1.5)

* Parameters used for sensitivity analysis are indicated by their ranges of values. Values in parentheses are used to generate the baseline containment parameter set (23, 37).

Table A.4 Molecular scale TNF/TNFR and IL10/IL10R parameters

Parameter	Parameter group	Parameter description	Value*	Reference
		TNF/TNFR Parameters		
$k_{synthMac}$ (#/cell.s)	Synthesis	Minimum synthesis rate of mTNF for macrophages	10^{-1}-1 (0.21)	(38, 39)
$k_{synthTcell}$ (#/cell.s)	Synthesis	Minimum synthesis rate of mTNF for T cells	10^{-2}-10^{-1} (0.021)	(38, 39)
k_{trans} (s^{-1})	Synthesis	TNF mRNA translation rate constant	10^{-5}-10^{-4} (8.0×10^{-5})	
k_{RNA_Mac} (#/cell.s)	Synthesis	Full TNF mRNA synthesis rate constant for macrophages	1-5 (1.5)	(12, 24, 39)
k_{RNA_Tcell} (#/cell.s)	Synthesis	Full TNF mRNA synthesis rate constant for T cells	0.1-0.5 (0.15)	(12, 24, 39)
β_{Mac}	Synthesis	Logistic function lower asymptote for macrophages that describes IL10-IL10R inhibition of TNF mRNA synthesis	$k_{synthMac} / k_{RNA\_Mac}$	
β_{Tcell}	Synthesis	Logistic function lower asymptote for T cells that describes IL10-IL10R inhibition of TNF mRNA synthesis	$k_{synthTcell} / k_{RNA\_Tcell}$	
$TNFR1_{mac}$ (#/cell)	Signaling	TNFR1 density on the surface of macrophages	500-5000 (1100-1900) †	(38, 40–42)
$TNFR1_{Tcell}$ (#/cell)	Signaling	TNFR1 density on the surface of T cells	500-5000 (400-1200) †	(38, 40–42)
$TNFR2_{mac}$ (#/cell)	Signaling	TNFR2 density on the surface of macrophages	500-5000 (400-800) †	(38, 40–42)
$TNFR2_{Tcell}$ (#/cell)	Signaling	TNFR2 density on the surface of T cells	500-5000 (600-800) †	(38, 40–42)
D_{TNF} (cm^2/s) ‡	Spatial	Diffusion coefficient of sTNF	10^{-8}-10^{-7} (5.2×10^{-8})	(43, 44)
$D_{sTNF/TNFR2}$ (cm^2/s) ‡	Spatial	Diffusion coefficient of shed TNF/TNFR2 complex	10^{-8}-10^{-7} (3.2×10^{-8})	(43, 44)
k_{TACE_Mac} (s^{-1})	Synthesis	Rate constant for TNF release by TACE activity on a macrophage	10^{-4}-10^{-3} (4.4×10^{-4})	(38, 45–47)
k_{TACE_Tcell} (s^{-1})	Synthesis	Rate constant for TNF release by TACE activity on a T cell	10^{-8}-10^{-6} (4.4×10^{-5})	(38, 45–47)
k_{deg} (s^{-1})	Spatial	sTNF degradation rate constant	$5x10^{-4}$-$5x10^{-3}$ (1.58×10^{-4})	(48)
K_{d1} (M)	Signaling	Equilibrium dissociation constant of sTNF/TNFR1	10^{-12}-10^{-10} (1.9×10^{-11})	(40, 49)
K_{d2} (M)	Signaling	Equilibrium dissociation constant of sTNF/TNFR2	10^{-10}-10^{-9} (4.2×10^{-10})	(40, 49, 50)
k_{on1} ($M^{-1}s^{-1}$)	Signaling	sTNF/TNFR1 association rate constant	10^7-10^8 (2.8×10^7)	(49)
k_{on2} ($M^{-1}s^{-1}$)	Signaling	sTNF/TNFR2 association rate constant	10^7-10^8 (3.5×10^7)	(49)
k_{off1} (s^{-1})	Signaling	sTNF/TNFR1 dissociation rate constant	$k_{on1}\times K_{d1}$	
k_{off2} (s^{-1})	Signaling	sTNF/TNFR2 dissociation rate constant	$k_{on2}\times K_{d2}$	
k_{int1} (s^{-1})	Signaling	TNFR1 internalization rate constant	1.5×10^{-4}-1.5×10^{-3} (7.7×10^{-4})	(49, 51)
k_{int2} (s^{-1})	Signaling	TNFR2 internalization rate constant	3.9×10^{-4}-5×10^{-4} (4.6×10^{-4})	(50)
k_{shed} (s^{-1})	Spatial	TNFR2 shedding rate constant	3.9×10^{-4}-1.5×10^{-3} (5×10^{-4})	(46, 51)
k_{rec1} (s^{-1})	Signaling	TNFR1 recycling rate constant	8.8×10^{-5}-5.5×10^{-4} (1.8×10^{-5})	(52, 53)
k_{rec2} (s^{-1})	Signaling	TNFR2 recycling rate constant	8.8×10^{-5}-5.5×10^{-4} (1.8×10^{-5})	(52, 53)
k_{t1} (s^{-1})	Signaling	TNFR1 turn-over rate constant	3×10^{-4}-5×10^{-4} (3.8×10^{-4})	(52, 53)
k_{t2} (s^{-1})	Signaling	TNFR2 turn-over rate constant	3×10^{-4}-5×10^{-4} (3.8×10^{-4})	(52, 53)
k_{deg1} (s^{-1})	Signaling	TNFR1 degradation rate constant	10^{-5}-10^{-4} (5×10^{-5})	(40, 52–54)
k_{deg2} (s^{-1})	Signaling	TNFR2 degradation rate constant	10^{-5}-10^{-4} (5×10^{-5})	(40, 52–54)

V_{r1_mac} (#/cell.s)	Signaling	Cell surface TNFR1 synthesis rate constant for macrophages	$k_{t1} \times TNFR1_{mac}$	
V_{r1_Tcell} (#/cell.s)	Signaling	Cell surface TNFR1 synthesis rate constant for T cells	$k_{t1} \times TNFR1_{Tcell}$	
V_{r2_mac} (#/cell.s)	Signaling	Cell surface TNFR2 synthesis rate constant for macrophages	$k_{t2} \times TNF21_{mac}$	
V_{r2_Tcell} (#/cell.s)	Signaling	Cell surface TNFR2 synthesis rate constant for T cells	$k_{t2} \times TNF21_{Tcell}$	
δ_I (# of IL10-IL10R/cell)	Signaling	Inverse growth rate of logistic function that describes IL10-IL10R inhibition of TNF mRNA synthesis	5-10 (7)	(24, 55, 56)
γ_I	Signaling	Time of max growth of logistic function that describes IL10-IL10R inhibition of TNF mRNA synthesis	15-30 (20)	(24, 55, 56)
IL10/IL10R Parameters				
D_{IL10} (cm^2/s) ‡	Spatial	Diffusion coefficient of soluble IL10	10^{-8}-10^{-7} (5.2×10^{-8})	(43, 44)
K_d (M)	Signaling	Equilibrium dissociation constant of IL10/IL10R	10^{-11}-10^{-9} ($4.56\text{x}10^{-10}$)	(17, 18, 57, 58)
k_{on} ($M^{-1}s^{-1}$)	Signaling	IL10/IL10R association rate constant	10^5-10^6 ($5.7\text{x}10^5$)	(17, 18, 57, 58)
k_{off} (s^{-1})	Signaling	IL10/IL10R dissociation rate constant	$k_{on} \times K_d$	
k_t (s^{-1})	Signaling	IL10R turn-over rate constant	$5\text{x}10^{-5}$-$5\text{x}10^{-4}$ ($1.6\text{x}10^{-4}$)	(21, 51, 52)
k_{int} (s^{-1})	Signaling	IL10R internalization rate constant	10^{-4}-10^{-3} (5×10^{-4})	(22)
k_{deg} (s^{-1})	Spatial	Soluble IL10 degradation rate constant	10^{-4}-10^{-3} (4.8×10^{-4})	(19, 20)
V_{r_mac}	Signaling	Cell surface IL10R synthesis rate constant for macrophages	$k_t \times IL10R_{mac}$	
V_{r_Tcell}	Signaling	Cell surface IL10R synthesis rate constant for Tcells	$k_t \times IL10R_{Tcell}$	
$IL10R_{mac}$ (#/cell)	Signaling	IL10R density on the surface of macrophages	500-5000 (1150-1850) †	(17, 18, 58–60)
$IL10R_{Tcell}$ (#/cell)	Signaling	IL10R density on the surface of T cells	100-1000 (250-550) †	(17, 18, 58–60)
$k_{synthMacInf}$ (#/cell.s)	Synthesis	Full synthesis rate of soluble IL10 by infected macrophages	0.01-0.1 (0.061)	(12, 16)
$k_{synthMacAct}$ (#/cell.s)	Synthesis	Full synthesis rate of soluble IL10 by activated macrophages	0.1-1.0 (0.41)	(11, 27)
$k_{synthTcell}$ (#/cell.s)	Synthesis	Full synthesis rate of soluble IL10 by T cells	0.25-1.5 (0.74)	(13–15)
$h_{synthMacAct}$ (# of sTNF-TNFR1/cell)	Synthesis	Half-saturation of IL10 synthesis by activated macrophages induced by bound TNF to TNFR1	50-500 (190)	(11, 27)

* Parameters used for sensitivity analysis are indicated by their ranges of values. Values in parentheses are used to generate the baseline containment parameter set.

† Baseline containment parameter set values for TNFR and IL10R densities on each recruited individual cell were randomly chosen from the ranges shown in parentheses.

‡ Diffusion coefficients of soluble species in granuloma were estimated from values for diffusible factors of similar molecular weight in tumors [17,18].

Table A.5 Molecular scale TNF-α induced cell response parameters

Parameter	Parameter group	Parameter description	Value*	Reference
$k_{NF\kappa B}$ ((#/cell)$^{-1}$s^{-1})	Signaling	Rate constant for TNF-induced NFκB activation in macrophages	$8x10^{-9}$-$3x10^{-8}$ (1.41×10^{-8})	(61)
k_{apopt} ((#/cell)$^{-1}$s^{-1})	Signaling	Rate constant for TNF-induced apoptosis in all cell types	10^{-10}-10^{-9} (3.45×10^{-10})	
$\tau_{NF\kappa B}$ (#/cell)	Signaling	Cell surface sTNF/TNFR1 threshold for TNF-induced NFκB activation	35-100 (65)	(61)
τ_{apopt} (#/cell)	Signaling	Internalized sTNF/TNFR1 threshold for TNF-induced apoptosis	1200-2300 (1728)	
s_{apopt} (#/cell)	Signaling	Saturation concentration of internalized sTNF/TNFR1 for TNF-induced apoptosis	3500-4500 (4022)	
$s_{NF\kappa B}$	Signaling	Saturation fraction of sTNF/TNFR1 for TNF-induced NFκB activation	0.35-0.50 (0.43)	(61)

* Parameters used for sensitivity analysis are indicated by their ranges of values. Values in parentheses are used to generate the baseline containment parameter set.

A.4 Supplemental Data and Figures

In this section, we present data for non-dominant outcomes briefly described in Chapter 3. Our computational model is stochastic and therefore simulations are averaged over multiple replications in order to get a representation of model outputs. Although each simulation run is distinct there are several model outcomes that can occur: uncontrolled bacterial growth, bacterial containment, resolved bacterial clearance, and unresolved bacterial clearance. Resolved granulomas have no bacterial load and have returned to steady state values of Mϕ while unresolved granulomas have no bacterial load but contain Mϕ levels well above steady state values. These unresolved granulomas tend to have large amounts of tissue damage due to the persistence of activated Mϕ beyond clearance of bacterial load. In order to carry out common statistical techniques (such as mean and standard deviation) simulations must be grouped into outcomes to prevent single modal statistics from being calculated on a multi-modal distribution. Therefore, shown below are the non-dominant outcomes for simulation runs presented in the text and figures of Chapter 3.

Table A.6 Signal Parameter Group – Receptor Expression – Non-Dominant Behavior Data

		Number of Simulations	Total Bacterial Load	Number of Activated Macrophages	Number of Apoptotic Resting Macrophages
Low	*Macrophage TNFR Density*	1 out of 30	0 ± N/A	0 ± N/A	0 ± N/A
	*Macrophage IL-10R Density (Resolved Granulomas)**	5 out of 30	0 ± 0	0 ± 0	146 ± 178
	Macrophage IL-10R Density (Unresolved Granulomas)†	5 out of 30	0 ± 0	25 ± 34	1557 ± 1157
Baseline	*Baseline Parameters*	2 out of 30	0 ± 0	0 ± 0	7 ± 1
High	*Macrophage TNFR Density*	6 out of 30	1141 ± 397	100 ± 44	301 ± 66
	Macrophage IL-10R Density	0 out of 30	-	-	-

* Resolved Granulomas – Levels of resting and activated Mϕ have returned to steady state values
† Unresolved Granulomas - Levels of resting and activated Mϕ have not returned to steady state values

Table A.7 Spatial Parameter Group – Non-Dominant Behavior Data

		Number of Simulations	Total Bacterial Load	Number of Activated Macrophages	Number of Apoptotic Resting Macrophages
Low	*TNF-α Spatial Influence*	1 out of 30	0 ± N/A	0 ± N/A	0 ± N/A
	*IL-10 Spatial Influence (Resolved Granulomas) **	6 out of 30	0 ± 0	0 ± 0	746 ± 225
	IL-10 Spatial Influence (Unresolved Granulomas) †	8 out of 30	0 ± 0	479 ± 247	3325 ± 1267
Baseline	*Baseline Parameters*	2 out of 30	0 ± 0	0 ± 0	7 ± 1
High	*TNF-α Spatial Influence*	0 out of 30	-	-	-
	IL-10 Spatial Influence	1 out of 30	0 ± N/A	0 ± N/A	0 ± N/A

* Resolved Granulomas – Levels of resting and activated Mϕ have returned to steady state values
† Unresolved Granulomas - Levels of resting and activated Mϕ have not returned to steady state values

Table A.8 Signal Parameter Group – Internalization Rate – Non-Dominant Behavior Data

		Number of Simulations	Total Bacterial Load	Number of Activated Macrophages	Number of Apoptotic Resting Macrophages
Low	*TNF-α Internalization Rate*	7 out of 30	165 ± 174	2906 ± 145	0 ± 0
	IL-10 Internalization Rate	3 out of 30	0 ± 0	0 ± 0	3 ± 2
Baseline	*Baseline Parameters*	2 out of 30	0 ± 0	0 ± 0	7 ± 1
High	*TNF-α Internalization Rate*	3 out of 30	0 ± 0	0 ± 0	13 ± 7
	IL-10 Internalization Rate	9 out of 30	0 ± 0	0 ± 0	106 ± 116

Table A.9 Synthesis Parameter Group – Non-Dominant Behavior Data

		Number of Simulations	Total Bacterial Load	Number of Activated Macrophages	Number of Apoptotic Resting Macrophages
Low	*TNF-α Synthesis*	0 out of 30	-	-	-
	*IL-10 Synthesis (Resolved) **	4 out of 30	0 ± 0	0 ± 0	121 ± 200
	IL-10 Synthesis (Unresolved) †	7 out of 30	0 ± 0	146± 213	1719 ± 1083
Baseline	*Baseline Parameters*	2 out of 30	0 ± 0	0 ± 0	7 ± 1
High	*TNF-α Synthesis*	13 out of 30	362 ± 302	1040 ± 135	4630 ± 576
	IL-10 Synthesis	1 out of 30	0 ± N/A	0 ± N/A	0 ± N/A

* Resolved Granulomas – Levels of resting and activated Mϕ have returned to steady state values
† Unresolved Granulomas - Levels of resting and activated Mϕ have not returned to steady state values

Table A.10 IL-10 Knockout Parameter Set – Non-Dominant Behavior Data

		Number of Simulations	Total Bacterial Load	Number of Activated Macrophages	Number of Apoptotic Resting Macrophages
Day 200	*Resolved*	7 out of 50	0 ± 0	0 ± 0	382 ± 189
	Unresolved	17 out of 50	3 ± 7	146 ± 177	1931 ± 724

* Resolved Granulomas – Levels of resting and activated Mϕ have returned to steady state values
† Unresolved Granulomas - Levels of resting and activated Mϕ have not returned to steady state values

Table A.11 Uncertainty and Sensitivity Analysis Results For the Effects of TNF and IL-10 Molecular Scale Parameters on Model Outputs at 200 Days Post-Infection

	TNF-Related Parameters														IL10 Related Parameters						
	D_{TNF}	τ_{apop}	$k_{SynthMac}$	k_{RNA_Mac}	K_{d1}	k_{on1}	k_{int1}	k_{rec1}	k_{T2}	k_{deg}	k_{deg1}	$TNFR1_{Mac}$	τ_{NFkB}	k_{NFkB}	K_d	k_{on}	k_{int}	k_{deg}	$IL10R_{Mac}$	D_{IL10}	$k_{SynthMacAct}$
TNF-Induced Outputs																					
Apoptosis – Mac		---		+++	---	+++	+	---		---	--	+++			+	---	+++		---	++	---
Apoptosis – Mr		--		+++	---			---		---						--	+++		---		---
Apoptosis – Mi		--		+++	---	+	+++	---		--	-	++				-	+				
Apoptosis – Mci		---		+++			+++	---	-	-		+									
Apoptosis – Ma		---		+++	---	++		---		---	--	+++			+	---	+++		---	+++	---
Apoptosis – T cells		--		+++	--			---		-	-	---				-	+++		---		--
NFkB – Mr	+++		+	+++	--		---			---			---	+++		---	+++	++	---		---
NFkB – Mi																			++		++
Cellular-Level Outputs																					
IntMtb		+++	-	---	+++	---	+++		-	+		---		---	---	+++	---	-	+++		+++
ExtMtb		++	--	---	+++	---	+++		-	++		---		---	--	+++	---		+++		+++
TotMtb		++	--	---	+++	---	+++		-	++		---		---	--	+++	---		+++		+++
Mr	+						---					-	--				+				-
Mi		+++	-	---	+++	---	+++		--	+		---		---	--	+++	---		+++		+++
Mci		+++	-	---	+++	---	+++		-	+		---		---	---	+++	---	-	+++		+++
Ma	+++						---			--			---	+		---	++		---		--
Tgam	+++						---			-			--								
Tcyt	+++						---			-			--								-
Treg	+++						---			---			-				+		-		-
Tissue-Level Outputs																					
Caseation						-	+++												+++		
Granuloma Size	+++						---					-	-								-
[TNF]	+++		+	+++			---			---		---	--			---	+++	++	---		---
[IL10]	++						---			-			--			---	+	---	---		
[Chemokines]	+++						---			-			---			-			---		

Significant PRCC values are as follows: -/+ 0.001 < p < 0.01 --/++ 0.0001 < p < 0.001 ---/+++ p < 0.0001

Table A.12 Uncertainty and Sensitivity Analysis Results For the Effects of Cellular Scale Parameters on Model Outputs at 200 Days Post-Infection

	Chemokine Parameters		T Cell Parameters				Recruitment Parameters								Bacterial Parameters	
	D_{Chem}	$k_{degChem}$	P_{STAT1}	$P_{Fas/FasL}$	$P_{CytKill}$	T_{MoveM}	M_{recMex}	h_{MacTNF}	h_{MacCC}	$T_{recTgamMax}$	$\tau_{recTgamTNF}$	$T_{recTcytMax}$	$T_{recTregMax}$	$\tau_{recTregTNF}$	α_{Bi}	α_{Be}
TNF-Induced Outputs																
Apoptosis – Mac	+++	---	++	---	-	--	+	---	---				--			
Apoptosis – Mr	+++	---	++	---		--	+	---	---				---			
Apoptosis – Mi	+++	---		---	--	--	++	---	---							
Apoptosis – Mci	+++	---		---	---	---	+	---	---			--			++	
Apoptosis – Ma	+++	---	+++	---		-		-	--	+			---	+	+	
Apoptosis – T cells	+++	---		---	---			---	---				---		+++	
NFkB – Mr	+++	---	++	---		--	+	---	---				---	+		
NFkB – Mi	+++	---		---	--	--	++	---	---				-		+	
Cellular-Level Outputs																
IntMtb	+++	---		---	--	--	+	--	---		+	--		+	+	
ExtMtb	+++	---	--	---	---	---	++	--	---	--	+	---	++		+++	++
TotMtb	+++	---	--	---	---	---	++	--	---	--	+	---	++		+++	+
Mr	+++	---						-	-						---	
Mi	+++	---		---	-	-	+	---	--			--			+++	
Mci	+++	---		---	-	--		--	---		+	--		+		
Ma	+++	---	+++	---		-		-	--				---	+		
Tgam	+++	---		---		-				+++					+++	
Tcyt	+++	---		---	---	-		-				+++			+++	
Treg	+++	---		---	-	-		-		-		--	+++		+++	
Tissue-Level Outputs																
Caseation		---						--							+++	+
Granuloma Size	+++	---		---	---	---	+++	---	---		+	---			+++	
[TNF]	+++	---	+	---	-	--	+	--	---			-		+	+	
[IL10]	+++	---	+	---		-		-	-						+++	
[Chemokines]	+++	---	+	---		--		-	-						+	

Significant PRCC values are as follows: -/+ 0.001 < p < 0.01 --/++ 0.0001 < p < 0.001 ---/+++ p < 0.0001

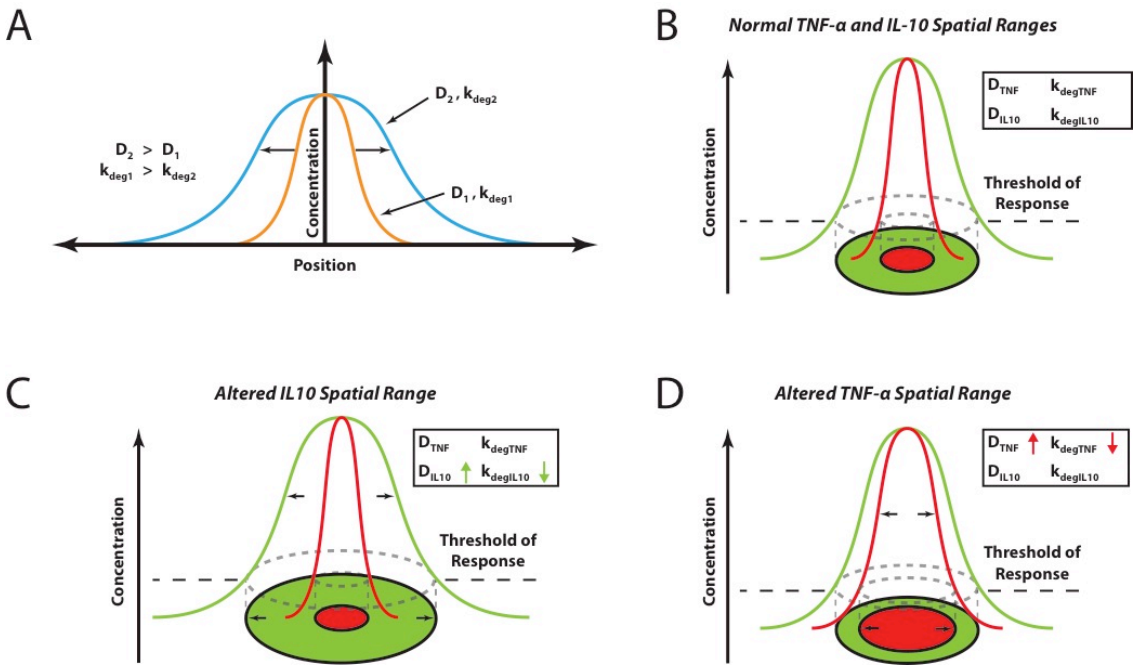

Figure A.3 Schematic diagram showing how the spatial ranges of TNF-α and IL-10 are manipulated A. As the diffusivity is increased and the degradation rate is decreased the spatial range of the molecule is increased (blue curve vs. the orange curve). B. Representation of the spatial range of TNF-α (red curve) and IL-10 (green curve) using the baseline parameters (Table S2 in Appendix S3). C. Increasing the diffusivity and decreasing the degradation rate constants of IL-10 increases the spatial range of IL-10 (green curve). D. Increasing the diffusivity and decreasing the degradation rate constants of TNF-α increases the spatial range of TNF-α (red curve).

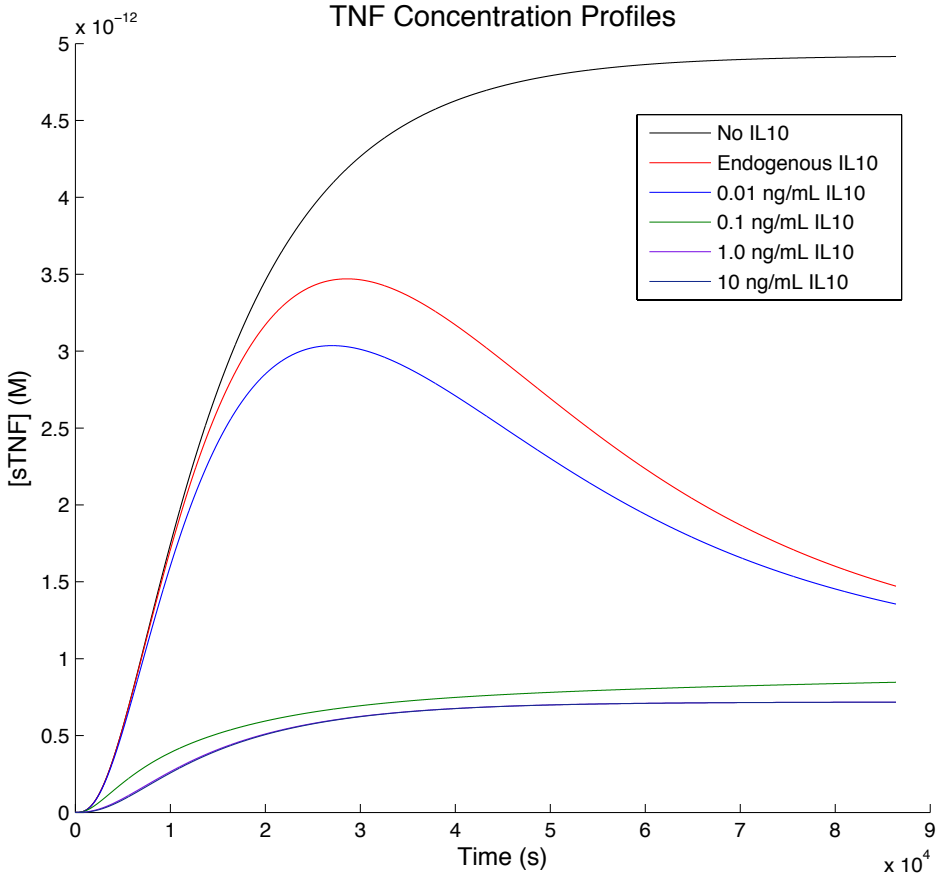

Figure A.4 Solution of the coupled IL-10 and TNF-α ODEs
IL-10 and TNF-α ODE solutions for $1x10^6$ cells/mL at various initial exogenous IL-10 conditions.

A.5 Visualization and Cross-Platform Capabilities

We have revised the user interface for performing our modeling studies so that we can easily visualize and track different aspects of the granuloma, including the structure and molecular concentration gradients, as it forms and is maintained. In order to satisfy the cross-platform requirement, we make use of the Qt framework. Qt is a C++ framework for developing cross-platform applications with a graphical user-interface (open-source, distributed under GPL – available at qt.digia.com).

A.6 References

1. Egen, J. G., A. G. Rothfuchs, C. G. Feng, N. Winter, A. Sher, and R. N. Germain. 2008. Macrophage and T cell dynamics during the development and disintegration of mycobacterial granulomas. *Immunity* 28: 271–84.

2. Ford, C. B., P. L. Lin, M. R. Chase, R. R. Shah, O. Iartchouk, J. Galagan, N. Mohaideen, T. R. Ioerger, J. C. Sacchettini, M. Lipsitch, J. L. Flynn, and S. M. Fortune. 2011. Use of whole genome sequencing to estimate the mutation rate of Mycobacterium tuberculosis during latent infection. *Nat. Genet.* 43: 482–6.

3. Vesosky, B., E. K. Rottinghaus, P. Stromberg, J. Turner, and G. Beamer. 2010. CCL5 participates in early protection against Mycobacterium tuberculosis. *J. Leukoc. Biol.* 87: 1153–65.

4. Chabot, V., P. Reverdiau, S. Iochmann, A. Rico, D. Sénécal, C. Goupille, P. Sizaret, and L. Sensebé. 2006. CCL5-enhanced human immature dendritic cell migration through the basement membrane in vitro depends on matrix metalloproteinase-9. *J. Leukoc. Biol.* 79: 767–78.

5. Tang, Q., and J. a Bluestone. 2008. The Foxp3+ regulatory T cell: a jack of all trades, master of regulation. *Nat. Immunol.* 9: 239–44.

6. Rubtsov, Y. P., J. P. Rasmussen, E. Y. Chi, J. Fontenot, L. Castelli, X. Ye, P. Treuting, L. Siewe, A. Roers, W. R. Henderson, W. Muller, and A. Y. Rudensky. 2008. Regulatory T cell-derived interleukin-10 limits inflammation at environmental interfaces. *Immunity* 28: 546–58.

7. Shevach, E. M. 2009. Mechanisms of foxp3+ T regulatory cell-mediated suppression. *Immunity* 30: 636–45.

8. Barakat, H. Z., and J. A. Clark. 1966. On the Solution of the Diffusion Equations by Numerical Methods. *J. Heat Transfer* 88: 421.

9. Duell, B. L., C. K. Tan, A. J. Carey, F. Wu, A. W. Cripps, and G. C. Ulett. 2012. Recent insights into microbial triggers of interleukin-10 production in the host and the impact on infectious disease pathogenesis. *FEMS Immunol. Med. Microbiol.* .

10. Moore, K. W., R. de Waal Malefyt, R. L. Coffman, and A. O'Garra. 2001. Interleukin-10 and the interleukin-10 receptor. *Annu. Rev. Immunol.* 1: 683–765.

11. Wu, K., J. Koo, X. Jiang, R. Chen, S. N. Cohen, and C. Nathan. 2012. Improved control of tuberculosis and activation of macrophages in mice lacking protein kinase R. *PLoS One* 7: e30512.

12. Giacomini, E., E. Iona, L. Ferroni, M. Miettinen, L. Fattorini, G. Orefici, I. Julkunen, and E. M. Coccia. 2001. Infection of human macrophages and dendritic cells with

Mycobacterium tuberculosis induces a differential cytokine gene expression that modulates T cell response. *J. Immunol.* 166: 7033–41.

13. Yssel, H., R. De Waal Malefyt, M. G. Roncarolo, J. S. Abrams, R. Lahesmaa, H. Spits, and J. E. de Vries. 1992. IL-10 is produced by subsets of human CD4+ T cell clones and peripheral blood T cells. *J. Immunol.* 149: 2378–84.

14. Meyaard, L., E. Hovenkamp, S. A. Otto, and F. Miedema. 1996. IL-12-induced IL-10 production by human T cells as a negative feedback for IL-12-induced immune responses. *J. Immunol.* 156: 2776–82.

15. Orme, I. M., A. D. Roberts, J. P. Griffin, and J. S. Abrams. 1993. Cytokine secretion by CD4 T lymphocytes acquired in response to Mycobacterium tuberculosis infection. *J. Immunol.* 151: 518–25.

16. Shaw, T. C., L. H. Thomas, and J. S. Friedland. 2000. Regulation of IL-10 secretion after phagocytosis of Mycobacterium tuberculosis by human monocytic cells. *Cytokine* 12: 483–6.

17. Tan, J. C., S. R. Indelicato, S. K. Narula, P. J. Zavodny, and C. C. Chou. 1993. Characterization of interleukin-10 receptors on human and mouse cells. *J. Biol. Chem.* 268: 21053–9.

18. Weber-Nordt, R. M., M. a Meraz, and R. D. Schreiber. 1994. Lipopolysaccharide-dependent induction of IL-10 receptor expression on murine fibroblasts. *J. Immunol.* 153: 3734–44.

19. Figueiredo, A. S., T. Höfer, C. Klotz, C. Sers, S. Hartmann, R. Lucius, and P. Hammerstein. 2009. Modelling and simulating interleukin-10 production and regulation by macrophages after stimulation with an immunomodulator of parasitic nematodes. *FEBS J.* 276: 3454–69.

20. Moya, C., Z. Huang, P. Cheng, A. Jayaraman, and J. Hahn. 2011. Investigation of IL-6 and IL-10 signalling via mathematical modelling. *IET Syst. Biol.* 5: 15.

21. Lauffenburger, D. A., and J. J. Linderman. 1993. Receptors: Models For Binding, Trafficking, and Signaling. In Oxford University Press, New York.

22. Wei, S. H.-Y., A. Ming-Lum, Y. Liu, D. Wallach, C. J. Ong, S. W. Chung, K. W. Moore, and A. L.-F. Mui. 2006. Proteasome-mediated proteolysis of the interleukin-10 receptor is important for signal downregulation. *J. Interferon Cytokine Res.* 26: 281–90.

23. Fallahi-Sichani, M., M. El-Kebir, S. Marino, D. E. Kirschner, and J. J. Linderman. 2011. Multiscale computational modeling reveals a critical role for TNF-α receptor 1 dynamics in tuberculosis granuloma formation. *J. Immunol.* 186: 3472–83.

24. Smallie, T., G. Ricchetti, N. J. Horwood, M. Feldmann, A. R. Clark, and L. M. Williams. 2010. IL-10 inhibits transcription elongation of the human TNF gene in primary macrophages. *J. Exp. Med.* 207: 2081–8.

25. Flynn, J. L., J. Chan, and P. L. Lin. 2011. Macrophages and control of granulomatous inflammation in tuberculosis. *Mucosal Immunol.* 4: 271–8.

26. Schreiber, T., S. Ehlers, L. Heitmann, A. Rausch, J. Mages, P. J. Murray, R. Lang, and C. Hölscher. 2009. Autocrine IL-10 induces hallmarks of alternative activation in macrophages and suppresses antituberculosis effector mechanisms without compromising T cell immunity. *J. Immunol.* 183: 1301–12.

27. Verreck, F. a W., T. de Boer, D. M. L. Langenberg, M. a Hoeve, M. Kramer, E. Vaisberg, R. Kastelein, A. Kolk, R. de Waal-Malefyt, and T. H. M. Ottenhoff. 2004. Human IL-23-producing type 1 macrophages promote but IL-10-producing type 2 macrophages subvert immunity to (myco)bacteria. *Proc. Natl. Acad. Sci. U. S. A.* 101: 4560–5.

28. Wanidworanun, C., and W. Strober. 1993. Predominant role of tumor necrosis factor-alpha in human monocyte IL-10 synthesis. *J. Immunol.* 151: 6853–61.

29. Platzer, C., C. Meisel, K. Vogt, M. Platzer, and H. D. Volk. 1995. Up-regulation of monocytic IL-10 by tumor necrosis factor-alpha and cAMP elevating drugs. *Int. Immunol.* 7: 517–23.

30. Hosokawa, Y., I. Hosokawa, K. Ozaki, H. Nakae, and T. Matsuo. 2009. Cytokines differentially regulate CXCL10 production by interferon-gamma-stimulated or tumor necrosis factor-alpha-stimulated human gingival fibroblasts. *J. Periodontal Res.* 44: 225–31.

31. Ikeda, T., K. Sato, N. Kuwada, T. Matsumura, T. Yamashita, F. Kimura, K. Hatake, K. Ikeda, and K. Motoyoshi. 2002. Interleukin-10 differently regulates monocyte chemoattractant protein-1 gene expression depending on the environment in a human monoblastic cell line, UG3. *J. Leukoc. Biol.* 72: 1198–205.

32. Cheeran, M. C.-J., S. Hu, W. S. Sheng, P. K. Peterson, and J. R. Lokensgard. 2003. CXCL10 production from cytomegalovirus-stimulated microglia is regulated by both human and viral interleukin-10. *J. Virol.* 77: 4502–15.

33. Marfaing-Koka, a, M. Maravic, M. Humbert, P. Galanaud, and D. Emilie. 1996. Contrasting effects of IL-4, IL-10 and corticosteroids on RANTES production by human monocytes. *Int. Immunol.* 8: 1587–94.

34. O'Garra, A., P. Vieira, P. Vieira, and A. E. Goldfeld. 2004. IL-10–producing and naturally occurring CD4+ Tregs: limiting collateral damage. *J. Clin. Invest.* 114: 1–7.

35. Cyktor, J. C., and J. Turner. 2011. Interleukin-10 and immunity against prokaryotic and eukaryotic intracellular pathogens. *Infect. Immun.* 79: 2964–73.

36. Roncarolo, M. G., M. Battaglia, R. Bacchetta, K. Fleischhauer, and M. K. Levings. 2006. Interleukin-10-secreting type 1 regulatory T cells in rodents and humans. *Immunol. Rev.* 212: 28–50.

37. Ray, J. C. J., J. L. Flynn, and D. E. Kirschner. 2009. Synergy between individual TNF-dependent functions determines granuloma performance for controlling Mycobacterium tuberculosis infection. *J. Immunol.* 182: 3706–17.

38. Fallahi-Sichani, M., M. a Schaller, D. E. Kirschner, S. L. Kunkel, and J. J. Linderman. 2010. Identification of key processes that control tumor necrosis factor availability in a tuberculosis granuloma. *PLoS Comput. Biol.* 6: e1000778.

39. Marino, S., D. Sud, H. Plessner, P. L. Lin, J. Chan, J. L. Flynn, and D. E. Kirschner. 2007. Differences in reactivation of tuberculosis induced from anti-TNF treatments are based on bioavailability in granulomatous tissue. *PLoS Comput. Biol.* 3: 1909–24.

40. Imamura, K., D. Spriggs, and D. Kufe. 1987. Expression of tumor necrosis factor receptors on human monocytes and internalization of receptor bound ligand. *J. Immunol.* 139: 2989–92.

41. Pocsik, E., R. Mihalik, F. Ali-Osman, and B. B. Aggarwal. 1994. Cell density-dependent regulation of cell surface expression of two types of human tumor necrosis factor receptors and its effect on cellular response. *J. Cell. Biochem.* 54: 453–64.

42. Van Riemsdijk-Van Overbeeke, I. C., C. C. Baan, C. J. Knoop, E. H. Loonen, R. Zietse, and W. Weimar. 2001. Quantitative flow cytometry shows activation of the TNF-alpha system but not of the IL-2 system at the single cell level in renal replacement therapy. *Nephrol. Dial. Transplant* 16: 1430–5.

43. Nugent, L. J., and R. K. Jain. 1984. Extravascular diffusion in normal and neoplastic tissues. *Cancer Res.* 44: 238–44.

44. Pluen, a, Y. Boucher, S. Ramanujan, T. D. McKee, T. Gohongi, E. di Tomaso, E. B. Brown, Y. Izumi, R. B. Campbell, D. a Berk, and R. K. Jain. 2001. Role of tumor-host interactions in interstitial diffusion of macromolecules: cranial vs. subcutaneous tumors. *Proc. Natl. Acad. Sci. U. S. A.* 98: 4628–33.

45. Newton, R. C., K. a Solomon, M. B. Covington, C. P. Decicco, P. J. Haley, S. M. Friedman, and K. Vaddi. 2001. Biology of TACE inhibition. *Ann. Rheum. Dis.* 60 Suppl 3: iii25–32.

46. Crowe, P. D., B. N. Walter, K. M. Mohler, C. Otten-Evans, R. A. Black, and C. F. Ware. 1995. A metalloprotease inhibitor blocks shedding of the 80-kD TNF receptor and TNF processing in T lymphocytes. *J. Exp. Med.* 181: 1205–10.

47. Solomon, K. A., M. B. Covington, C. P. DeCicco, and R. C. Newton. 1997. The fate of pro-TNF-alpha following inhibition of metalloprotease-dependent processing to soluble TNF-alpha in human monocytes. *J. Immunol.* 159: 4524–31.

48. Cheong, R., A. Bergmann, S. L. Werner, J. Regal, A. Hoffmann, and A. Levchenko. 2006. Transient IkappaB kinase activity mediates temporal NF-kappaB dynamics in response to a wide range of tumor necrosis factor-alpha doses. *J. Biol. Chem.* 281: 2945–50.

49. Grell, M., H. Wajant, G. Zimmermann, and P. Scheurich. 1998. The type 1 receptor (CD120a) is the high-affinity receptor for soluble tumor necrosis factor. *Proc. Natl. Acad. Sci. U. S. A.* 95: 570–5.

50. Pennica, D., V. T. Lam, N. K. Mize, R. F. Weber, M. Lewis, B. M. Fendly, M. T. Lipari, and D. V Goeddel. 1992. Biochemical properties of the 75-kDa tumor necrosis factor receptor. Characterization of ligand binding, internalization, and receptor phosphorylation. *J. Biol. Chem.* 267: 21172–8.

51. Higuchi, M., and B. B. Aggarwal. 1994. TNF induces internalization of the p60 receptor and shedding of the p80 receptor. *J. Immunol.* 152: 3550–8.

52. Bajzer, Z., a C. Myers, and S. Vuk-Pavlović. 1989. Binding, internalization, and intracellular processing of proteins interacting with recycling receptors. A kinetic analysis. *J. Biol. Chem.* 264: 13623–31.

53. Vuk-Pavlović, S., and J. S. Kovach. 1989. Recycling of tumor necrosis factor-alpha receptor in MCF-7 cells. *FASEB J.* 3: 2633–40.

54. Tsujimoto, M., Y. K. Yip, and J. Vilcek. 1985. Tumor necrosis factor: specific binding and internalization in sensitive and resistant cells. *Proc. Natl. Acad. Sci. U. S. A.* 82: 7626–30.

55. Brennan, F. M., P. Green, P. Amjadi, H. J. Robertshaw, M. Alvarez-Iglesias, and M. Takata. 2008. Interleukin-10 regulates TNF-α-converting enzyme (TACE/ADAM17) involving a TIMP3 dependent and independent mechanism. *Eur. J. Immunol.* 38: 1106–17.

56. Balcewicz-Sablinska, M., H. Gan, and H. G. Remold. 1999. Interleukin 10 produced by macrophages inoculated with Mycobacterium avium attenuates mycobacteria-induced apoptosis by reduction of TNF-α activity. *J. Infect. Dis.* 180: 1230–1237.

57. Yoon, S. Il, N. J. Logsdon, F. Sheikh, R. P. Donnelly, and M. R. Walter. 2006. Conformational changes mediate interleukin-10 receptor 2 (IL-10R2) binding to IL-10 and assembly of the signaling complex. *J. Biol. Chem.* 281: 35088–96.

58. Liu, Y., S. H. Wei, a S. Ho, R. de Waal Malefyt, and K. W. Moore. 1994. Expression cloning and characterization of a human IL-10 receptor. *J. Immunol.* 152: 1821–9.

59. Ho, A. S., S. H. Wei, A. L. Mui, A. Miyajima, K. W. Moore, A. S. Ho, S. H. Wei, A. L. Mui, A. Miyajima, and K. W. Moore. 1995. Functional regions of the mouse interleukin-10 receptor cytoplasmic domain . These include : Functional Regions of the Mouse Interleukin-10 Receptor Cytoplasmic Domain. 15.

60. Ding, Y., L. Qin, D. Zamarin, V. Sergei, S. Pestka, K. W. Moore, S. Jonathan, and S. V Kotenko. 2012. Differential IL-10R1 Expression Plays a Critical Role in IL-10-Mediated Immune Regulation. .

61. Tay, S., J. J. Hughey, T. K. Lee, T. Lipniacki, S. R. Quake, and M. W. Covert. 2010. Single-cell NF-kappaB dynamics reveal digital activation and analogue information processing. *Nature* 466: 267–71.

Appendix B

Supplementary Information for Chapter 5

B.1 Supplemental Tables

Table B.1 Changes in ABM Rules From Chapter 3

Previous Rule	New Rule	Reason/References
Non-replicating *Mtb* trapped in caseated compartments can only be killed by hypoxia at a specified death rate.	Additionally, non-replicating *Mtb* trapped in caseated compartments in the Moore neighborhood of an activated macrophage can be killed at a reduced rate of activated macrophage killing ($1/10^{th}$).	Realistically *in-vivo* movement of cells is not constrained to binary (yes/no) decisions (e.g. cell squeezing). Thus, we allow activated macrophages to access compartments in their Moore neighborhood to alleviate artifacts of movement restrictions.
Maximal rates of T cell recruitment are allowed as soon as T cell recruitment is begins.	A time delay now exists such that T cell recruitment rates increase linearly to the maximum rates over the specified time interval.	(2)
Once a compartment becomes caseated due to passing a threshold of death events it stays caseated for the entire simulation.	Activated macrophages have an associated probability of initiating a healing event. If the compartment is marked for healing there is an associated time with the healing process. Once the time interval is passed the compartment changes from caseated to non-caseated.	(3–5)
Regulatory T cells modulate their deactivation capacity based on the relative bound IL-10 and bound TNF molecules on the cells surface.	Now, regulatory T cells have a baseline deactivation capacity. When IL-10 production is deleted from regulatory T cells the deactivation capacity is up regulated by a specified factor.	(6, 7)
Lie-type operator splitting (first order accurate) was employed to separate the coupled reaction/diffusion PDEs into three different problems.	Strang-type splitting (second-order accurate) is now employed to separate the coupled reaction/diffusion PDEs into three different problems.	Increases the accuracy of the splitting technique allowing for larger solution time steps for each of the three different problems.
Each pro-inflammatory T cell was given a probability of activating macrophage STAT1 though IFN-γ at each time step.	Pro-inflammatory T cells are now classified by the ability to secrete IFN-γ and activate STAT1 based on a specified probability when it is born.	Although the previous rule gives correct percentages of T cells secreting IFN-γ at any specific time point the population of IFN-γ secreting T cells changes with every time step when the probability is re-evaluated. Thus, the new rule identifies IFN-γ secreting and non-secreting T cells upon birth and the classification persists over the entire life span of the T cell.
All pro-inflammatory and cytotoxic T cells are capable of producing TNF-α	Pro-inflammatory and cytotoxic T cells are now classified by the ability to secrete TNF-α based on a specified probability when it is born.	(Unpublished data – Personal Communication J. Flynn, University of Pittsburgh)

Table B.2 NHP Data Used to Calibrate *GranSim*

NHP ID	Days Post-Infection of Necropsy	Number of Non-Sterile Lesions	Number of Sterile Lesions
8709	26	9	0
7010	27	35	1
8109	27	5	0
6810	28	18	0
7709	28	16	0
7809	28	11	0
8809	28	16	1
7210	29	22	0
7110	30	8	0
2412	83	13	1
17111	84	16	2
2512	85	21	2
3609	89	7	3
9611	93	12	0
19608	136	7	6
8509	139	6	3
6409	140	4	0
21208	173	10	2
8609	173	16	10
9711	175	10	5
9209	187	5	11
7009	194	4	11
9511	198	3	3
5610	209	2	4
23210	211	26	3
21310	230	22	15
5008	247	4	0
10808	267	2	1
22210	267	9	19
21410	267	13	9
21508	271	3	6
4808	296	1	2

All NHPs were infected with the Erdman strain of *Mycobacterium tuberculosis* except 7010 and 7210 which were infected with barcoded Erdman strains from (9). From (8–11).

Table B.3 Additional ABM Parameters and Changes in Values of ABM Parameters From Chapter 3

Parameter	Parameter Description	Previous Value	New Value
α_{Bi} (per 10 min)	Intracellular Mtb growth rate	1.4×10^{-3}	3×10^{-3}
α_{Be} (per 10 min)	Extracellular Mtb growth rate	7×10^{-4}	1.25×10^{-3}
N_{caseum}	Number of cell deaths required for caseation	15	10
t_{heal} (days)	Healing time of caseated compartment	---	16
τ_{chem} (molecules)	Minimum chemokine concentration threshold	2	1
s_{chem} (molecules)	Saturating chemokine concentration threshold	2000	400
r_{CCL2} (molecules/s)	Full secretion rate of CCL2 by macrophages	4.14	6
r_{CCL5} (molecules/s)	Full secretion rate of CCL5 by macrophages	4.14	6
r_{CXCL9} (molecules/s)	Full secretion rate of CXCL9/10/11 by macrophages	8.28	12
B_{actM}	Number of extracellular Mtb activating NF-κB in a mac	239	200
N_{burst}	Number of intracellular Mtb that leads to M_{ci} bursting	20	15
N_{ak} (per 10 min)	Number of extracellular Mtb killed by M_a	3	5
t_{moveMa} (hour)	Time interval for M_a movement	7.8	2.3
M_{recMax}	Maximum recruitment probability for M_r recruitment	0.09	0.20
$\tau_{recMacTNF}$	TNF threshold for M_r recruitment	0.014	0.05
h_{MacTNF}	Half-saturation of TNF for M_r recruitment	0.5	0.55
P_{heal}	Probability of healing a caseated compartment by M_a	---	0.014
$P_{Fas/FasL}$	Probability of Fas/FasL apoptosis by T_r	0.0095	0.02
$P_{cytKill}$	Probability of T_c killing M_i or M_{ci}	0.0098	0.01
T_{moveM}	Probability of T cell moving to a mac-containing location	0.027	0.07
$P_{IFN\text{-}Tgam}$	Probability of a T_g secreting IFN-γ	---	0.35
$P_{IFN\text{-}Range}$	Range of probability of a T_g secreting IFN-γ	---	0.10
$P_{IFN\text{-}Moore}$	Probability of a T_g activating STAT1 through IFN-γ in its Moore neighborhood	---	0.25
$P_{TNF\text{-}Tcyt}$	Probability of a T_c secreting TNF	---	0.07
$P_{TNF\text{-}Tgam}$	Probability of a T_g secreting TNF	---	0.07
$P_{Deact\text{-}Treg}$	Probability of T_r deactivation of agents	---	0.015
$F_{Deact\text{-}Treg}$	Factor that describes increase in probability of T_r deactivation in the absence of IL-10	---	2.72
$t_{recEnabled}$ (days)	Time T cell recruitment is enabled	---	28
$t_{recDealy}$ (days)	Time delay in maximal T cell recruitment	---	5
$T_{recTgamMax}$	Maximum recruitment probability for T_r recruitment	0.0713	0.096
$\tau_{recTgamTNF}$	TNF threshold for T_r recruitment	0.014	0.1
$h_{TgamTNF}$	Half-saturation of TNF for T_r recruitment	0.3	0.4
$T_{recTcytMax}$	Maximum recruitment probability for T_c recruitment	0.0505	0.08
$\tau_{recTcytTNF}$	TNF threshold for T_c recruitment	0.014	0.1
$h_{TcytTNF}$	Half-saturation of TNF for T_c recruitment	0.3	0.4
$T_{recTregMax}$	Maximum recruitment probability for T_{reg} recruitment	0.0221	0.024
$\tau_{recTcytTNF}$	TNF threshold for T_c recruitment	0.014	0.1
$h_{TcytTNF}$	Half-saturation of TNF for T_c recruitment	0.3	0.4
$k_{NF\kappa B}$ ((#/cell)$^{-1}$s^{-1})	Rate constant for TNF-induced NFκB activation in macrophages	1.41×10^{-8}	1.62×10^{-8}
k_{apopt} ((#/cell)$^{-1}$s^{-1})	Rate constant for TNF-induced apoptosis in all cell types	3.45×10^{-10}	2.22×10^{-9}
$\tau_{NF\kappa B}$ (#/cell)	Cell surface sTNF/TNFR1 threshold for TNF-induced NFκB activation	65	81
τ_{apopt} (#/cell)	Internalized sTNF/TNFR1 threshold for TNF-induced apoptosis	1728	2028
s_{apopt} (#/cell)	Saturation concentration of internalized sTNF/TNFR1 for TNF-induced apoptosis	4022	4691
$s_{NF\kappa B}$	Saturation fraction of sTNF/TNFR1 for TNF-induced NFκB activation	0.43	0.541
$k_{synthMacInf}$ (#/cell.s)	Full synthesis rate of soluble IL10 by infected macrophages	0.061	0.02
$k_{synthMacAct}$ (#/cell.s)	Full synthesis rate of soluble IL10 by activated macrophages	0.41	0.30

Table B.4 Uncertainty and Sensitivity Analysis Partial Rank Correlation Coefficients of IL-10 Parameters – Selected Model Outputs at 200 Days Post-Infection

Model Outputs	D_{IL10}	k_{deg}	K_D	k_{on}	k_t	k_{int}	$IL10R_{Mac}$	$IL10R_{Tcell}$	δ_I	γ_I	$F_{Deact\text{-}Treg}$	$k_{synthMacInf}$	$k_{synthMacAct}$	$h_{synthMacAct}$	$k_{synthTcell}$
TNF-Induced Processes															
Apoptosis/Necrosis – M_r	+	+++		---		+++	---	-		+++	+	---	---	+	-
Apoptosis/Necrosis – M_i		+	+	-		+	--		+		---	---	+		+
Apoptosis/Necrosis – M_{ci}				-			-		+		--	---	+		+
Apoptosis/Necrosis – M_a	+	+++		---		+++	---	-		+++	++	---	---	+	-
Apoptosis/Necrosis – T cells	+	+++		---		+++	---			+++		---	---	+	-
Activation – M_r	+	+++		---		+++	---	-		+++	++	---	-	+	-
Activation – M_i			+						+	-	-	---	+		+
T-Cell Outputs															
CTL Killing		---		+++		---	+++			---		+++	+++		++
Fas/FasL Killing		---		+++		---	+++			---		+++	+++		++
Bacterial Outputs															
Intracellular *Mtb*	-	--		++		---	+++			---		+++	+++	-	++
Extracellular *Mtb*		---		+++		---	+++			---	-	+++	+++		+
CFU per Lesion		---		+++		---	+++			---	-	+++	+++		++
CFU/CEQ		---		+++		---	+++			---		+++	+++		+
Cellular-Level Outputs															
M_r		+++		-		+++	-				+++	---			
M_i	-	--		++		---	+++			---		+++	+++	-	++
M_{ci}	-	---		++		---	+++			---		+++	+++	-	++
M_a		+							-	-	+++		+		
T_g						-	+		--	---	+++	+	+		+
T_c						-	+		--	---	+++	++	+		+
T_r									--	---	+++	+	+		
Tissue-Level Outputs															
Caseous Necrosis		-	-	+		---	+++		--	---	+++	+++	+		+
Lesion Size						-	+		-	---	+++	+++	++		
[TNF-α]		+							-	-	+++				
[IL-10]		---				-			-	---	+++	+++	+++		+++
[Chemokines]						-			-	---	+++	+	+++		

Significant PRCC values are as follows: -/+ $0.005 < p < 0.05$ --/++ $0.0005 < p < 0.005$ ---/+++ $p < 0.0005$
PRCC and significance values calculated from N – 250 simulations with 4 replications each
M_i = Infected Macrophages, M_{ci} = Chronically Infected Macrophages, M_a = Activated Macrophages, M_r = Resting Macrophages, T_g = Pro-inflammatory T cells, T_c = Cytotoxic T cells, T_r = Regulatory T cells
CTL = Cytotoxic, CFU = Colony Forming Units, CEQ = Chromosome Equivalents
Parameters are defined above or in Chapter 3

Table B.5 Uncertainty and Sensitivity Analysis Partial Rank Correlation Coefficients of IL-10 Parameters – Selected Model Outputs at 50 Days Post-Infection

Model Outputs	D_{IL10}	k_{deg}	K_D	k_{on}	k_t	k_{int}	$IL10R_{Mac}$	$IL10R_{Tcell}$	δ_I	γ_I	$F_{Deact\text{-}Treg}$	$k_{synthMacInf}$	$k_{synthMacAct}$	$h_{synthMacAct}$	$k_{synthTcell}$
TNF-Induced Processes															
Apoptosis/Necrosis – M_r	+	+++		---		+++	---			+++		---	---		-
Apoptosis/Necrosis – M_i	+	+		--		+++	---			+++	-	---		+	
Apoptosis/Necrosis – M_{ci}		+		--		+++	--		+		-	---			
Apoptosis/Necrosis – M_a	+	+++		---		+++	---			+++	+	---	---	+	-
Apoptosis/Necrosis – T cells	+	+++		---		+++	---			+++		---	---		-
Activation – M_r	+	+++		---		+++	---			+++	+	---	---		-
Activation – M_i		+	+	-		+++	--			+	-	---			
T-Cell Outputs															
CTL Killing		---		+++		---	+++			---		+++	+		++
Fas/FasL Killing		---		+++		---	+++			---		+++	+		+
Bacterial Outputs															
Intracellular *Mtb*		---		+++		---	+++			---		+++	++		+
Extracellular *Mtb*	-	---		++		---	+++			---		+++	++		+
CFU per Lesion	-	---		+++		---	+++			---		+++	++		+
CFU/CEQ		---		+++		---	+++			---	-	+++	++	-	++
Cellular-Level Outputs															
M_r									+			-		+	
M_i	-	---		++		---	+++			---		+++	++		+
M_{ci}		---		+++		---	+++			---		+++	+		+
M_a		+++		--		+++	---			+++	+++	---	-	+	
T_g									---		+++	+++	-		
T_c									-		+++	+++	-		
T_r											+++	+++	-		
Tissue-Level Outputs															
Caseous Necrosis	+	+++		---		+++	---			+++		---	-	+	-
Lesion Size						--	++			---	+++	+++			
[TNF-α]	+	+++		---		+++	---			+++	++	---	---	+	-
[IL-10]		---		-						-		+++	+++		+++
[Chemokines]			-						-		+++				+

Significant PRCC values are as follows: -/+ 0.005 < p < 0.05 --/++ 0.0005 < p < 0.005 ---/+++ p < 0.0005
PRCC and significance values calculated from N – 250 simulations with 4 replications each
M_i = Infected Macrophages, M_{ci} = Chronically Infected Macrophages, M_a = Activated Macrophages, M_r = Resting Macrophages, T_g = Pro-inflammatory T cells, T_c = Cytotoxic T cells, T_r = Regulatory T cells
CTL = Cytotoxic, CFU = Colony Forming Units, CEQ = Chromosome Equivalents
Parameters are defined above or in Chapter 3

B.2 Supplemental Figures

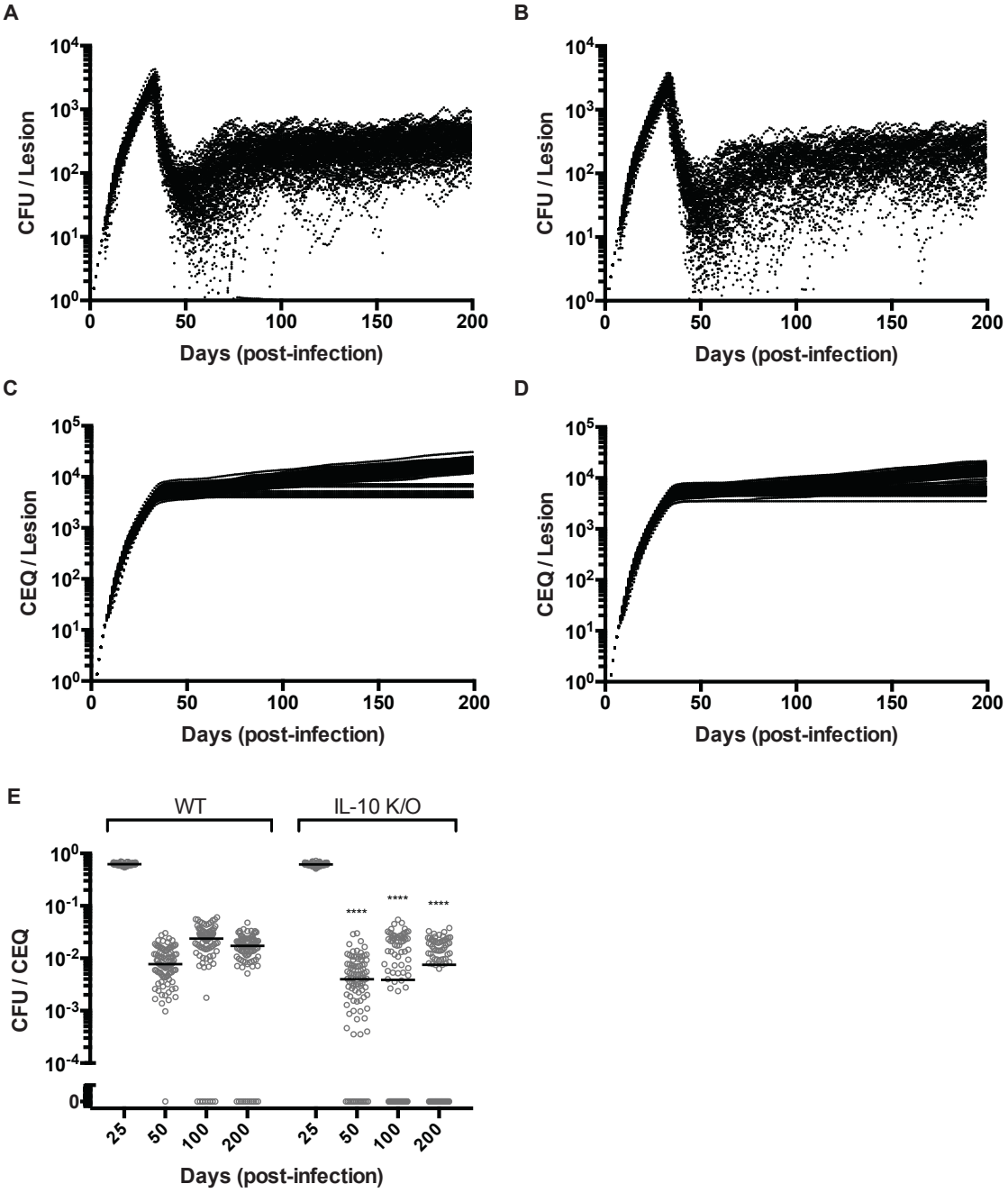

Figure B.1 Virtual IL-10 deletions demonstrate control of the early immune response
A. Simulated temporal CFU data for WT lesions. Dots represent individual lesions at the specified time point. B. Simulated temporal CFU data for IL-10 K/O lesions. Dots represent individual lesions at the specified time point. C. Simulated temporal CEQ data for WT lesions. Individual dots represent individual lesions at the specified time point. D. Simulated temporal CEQ data for IL-10 K/O lesions. Dots represent individual lesions at the specified time point. E. CFU/CEQ for WT and IL-10 K/O lesions, including both sterile and non-sterile lesions. Circles represent individual lesions. Bars indicate median values. For all panels: * $p \leq 0.05$, ** $p \leq 0.01$, *** $p \leq 0.001$, **** $p \leq 0.0001$, N = 100.

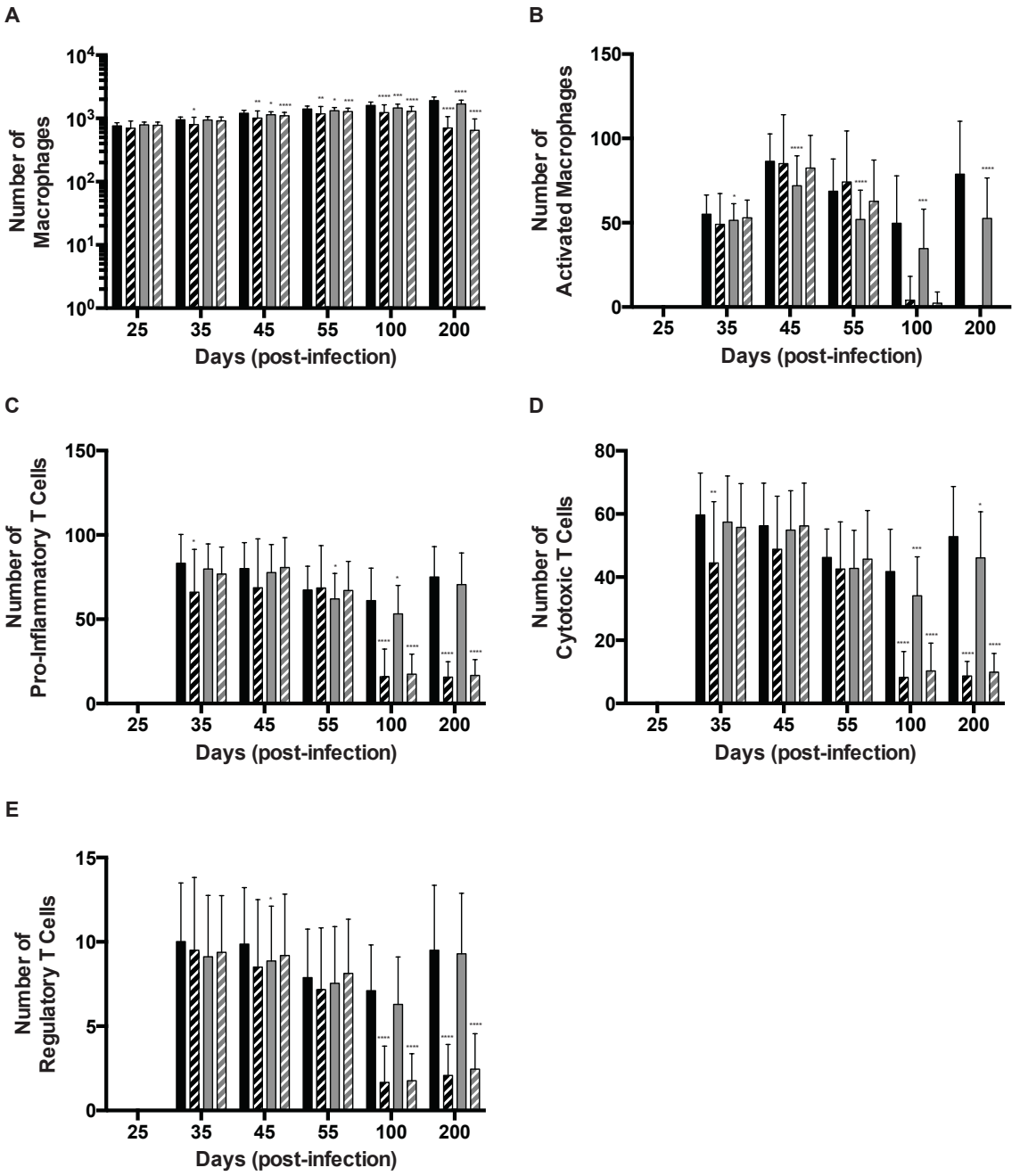

Figure B.2 Virtual IL-10 deletions show limited changes in cellular populations in a lesion
A. Total macrophages. B. Activated macrophages. C. Pro-Inflammatory T cell. D. Cytotoxic T cells. E. Regulatory T cells. Both sterile and non-sterile lesions are included. Non-sterile lesions are displayed as solid bars and sterile lesions are displayed as striped bars. Bars are representative of mean values with error bars showing SD. For all panels: * $p \leq 0.05$, ** $p \leq 0.01$, *** $p \leq 0.001$, **** $p \leq 0.0001$, N = 100.

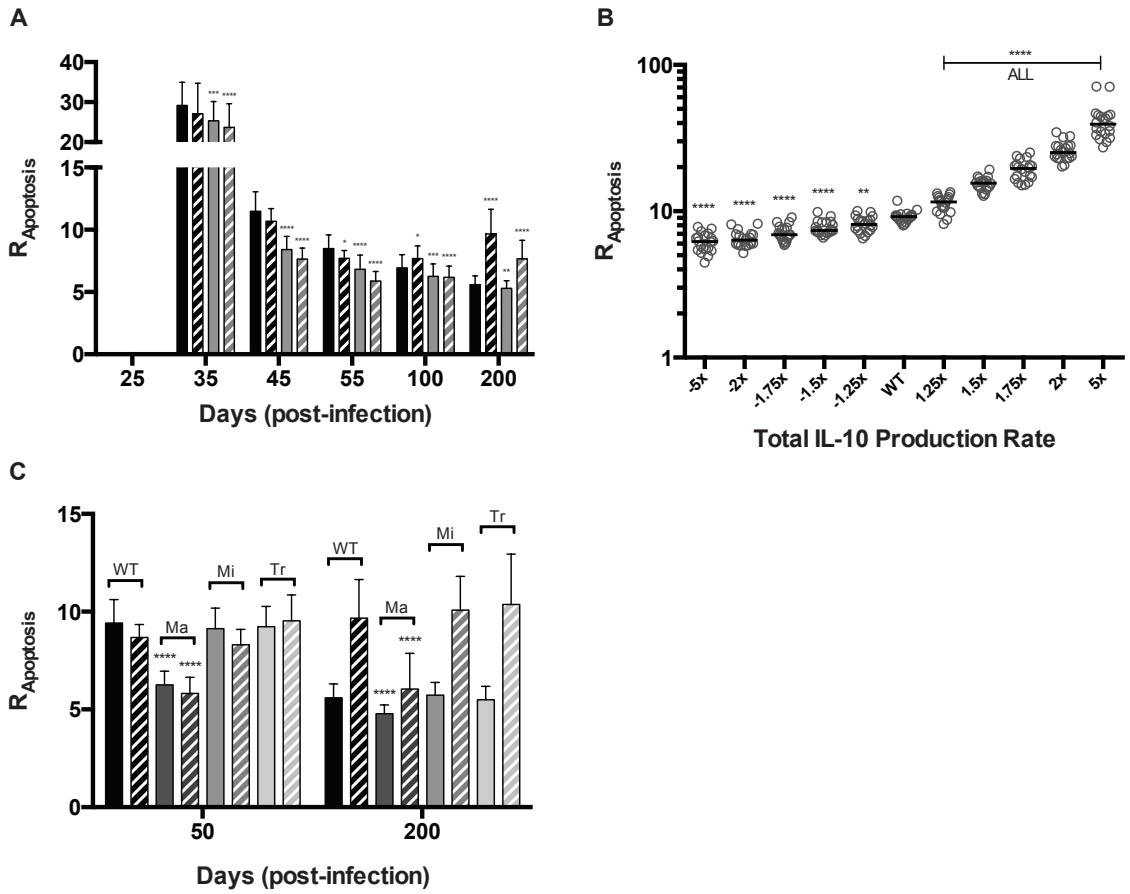

Figure B.3 Ratio of infected macrophage to resting macrophage apoptosis/necrosis for virtual IL-10 experiments

$R_{Apoptosis}$ is defined as the ratio of infected macrophage apoptosis/necrosis to resting macrophage apoptosis/necrosis (12, 13). Thus, it is a metric of 'good' apoptosis to 'bad' apoptosis. A. $R_{Apoptosis}$ for WT (black bars) and IL-10 K/O (grey bars) lesions. Non-sterile lesions are displayed as solid bars and sterile lesions are displayed as striped bars. Bars are representative of mean values with error bars showing SD. B. $R_{Apoptosis}$ for different levels of total IL-10 production (5-fold reduction to 5-fold increase) at 50 days post-infection. Dots represent individual lesions. Lines indicate the median values. C. $R_{Apoptosis}$ for WT, IL-10 K/O, Ma IL-10 K/O, Mi IL-10 K/O, Tr IL-10 K/O lesions at 200 days post-infection. Both sterile and non-sterile lesions are included. Non-sterile lesions are displayed as solid bars and sterile lesions are displayed as striped bars. Bars are representative of mean values with error bars showing SD. For all panels: * $p \leq 0.05$, ** $p \leq 0.01$, *** $p \leq 0.001$, **** $p \leq 0.0001$, N = 100.

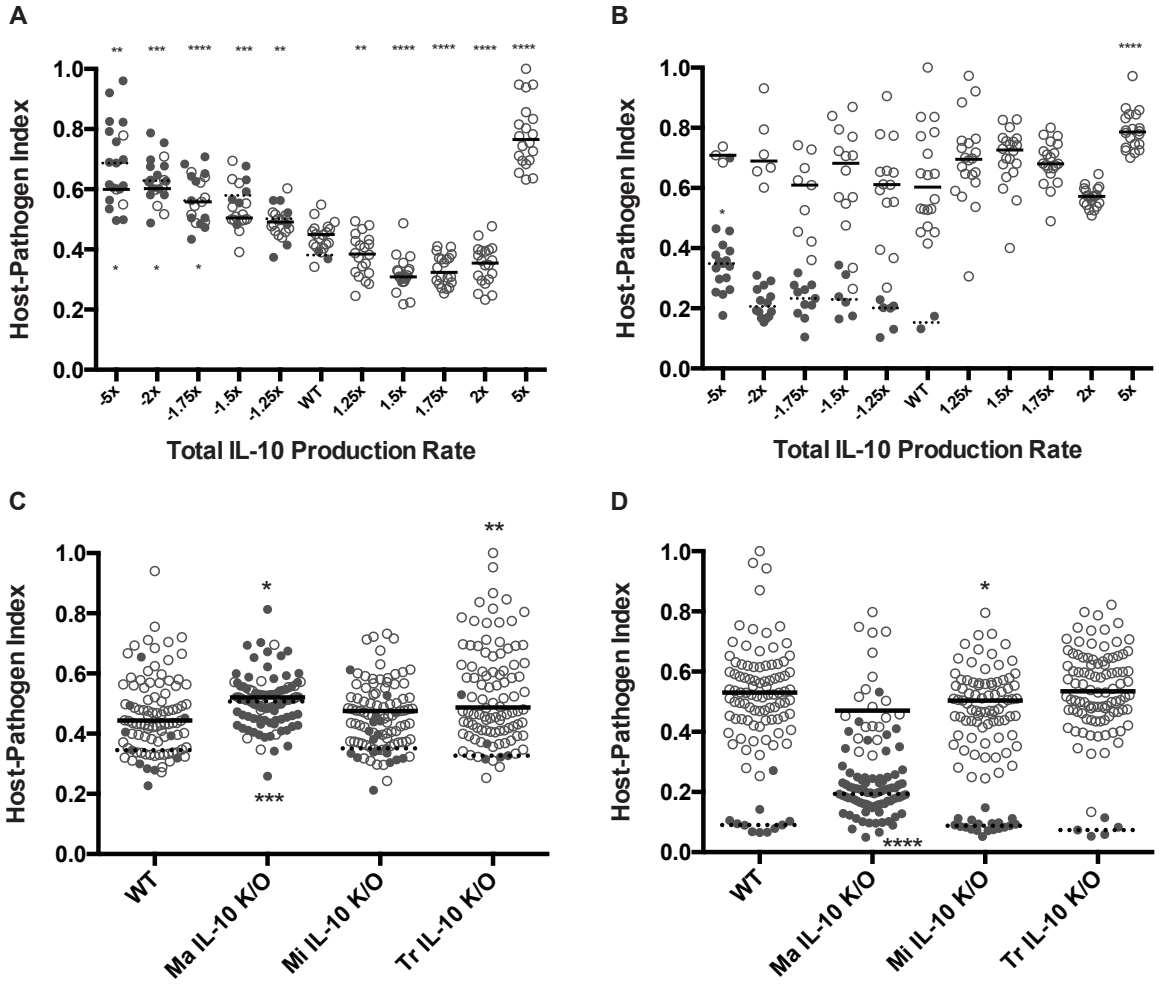

Figure B.4 Modified Host-Pathogen Index for IL-10 virtual transgenic and IL-10 cell specific knockout experiments

The modified Host-Pathogen Index is defined as the scaled measure (between 0 and 1) of lesion function based on the CFU and healthy macrophage apoptosis/necrosis levels (1). Lower values indicate better lesion function. A, B. Host-Pathogen Index for different levels of total IL-10 production (5-fold reduction to 5-fold increase) at 50 and 200 days post-infection, respectively. Dots represent individual lesions. Lines indicate the median values. C, D. Host-Pathogen Index for WT, IL-10 K/O, Ma IL-10 K/O, Mi IL-10 K/O, Tr IL-10 K/O lesions at 50 and 200 days post-infection, respectively. Solid lines indicate the median values for non-sterile lesions. Dotted lines indicate the median values for sterile lesions. Open circles are non-sterile lesions. Closed circles are sterile lesions. For all panels: * $p \leq 0.05$, ** $p \leq 0.01$, *** $p \leq 0.001$, **** $p \leq 0.0001$, N = 100. Significance values above the data points are for non-sterile lesions while significance values below the data points are for sterile lesions.

B.3 References

1. Cilfone, N. A., C. R. Perry, D. E. Kirschner, and J. J. Linderman. 2013. Multi-Scale Modeling Predicts a Balance of Tumor Necrosis Factor-α and Interleukin-10 Controls the Granuloma Environment during Mycobacterium tuberculosis Infection. *PLoS One* 8: e68680.

2. Gong, C., J. T. Mattila, M. Miller, J. L. Flynn, J. J. Linderman, and D. Kirschner. 2013. Predicting lymph node output efficiency using systems biology. *J. Theor. Biol.* 335C: 169–184.

3. Gordon, S. 2003. Alternative activation of macrophages. *Nat. Rev. Immunol.* 3: 23–35.

4. Mantovani, A., A. Sica, S. Sozzani, P. Allavena, A. Vecchi, and M. Locati. 2004. The chemokine system in diverse forms of macrophage activation and polarization. *Trends Immunol.* 25: 677–86.

5. Tolle, L. B., and T. J. Standiford. 2013. Danger-associated molecular patterns (DAMPs) in acute lung injury. *J. Pathol.* 229: 145–56.

6. Rubtsov, Y. P., J. P. Rasmussen, E. Y. Chi, J. Fontenot, L. Castelli, X. Ye, P. Treuting, L. Siewe, A. Roers, W. R. Henderson, W. Muller, and A. Y. Rudensky. 2008. Regulatory T cell-derived interleukin-10 limits inflammation at environmental interfaces. *Immunity* 28: 546–58.

7. Hall, B. M., N. D. Verma, G. T. Tran, and S. J. Hodgkinson. 2011. Distinct regulatory CD4+T cell subsets; differences between naïve and antigen specific T regulatory cells. *Curr. Opin. Immunol.* 23: 641–7.

8. Lin, P. L., M. Rodgers, L. Smith, M. Bigbee, A. Myers, C. Bigbee, I. Chiosea, S. V Capuano, C. Fuhrman, E. Klein, and J. L. Flynn. 2009. Quantitative comparison of active and latent tuberculosis in the cynomolgus macaque model. *Infect. Immun.* 77: 4631–42.

9. Lin, P. L., C. B. Ford, M. T. Coleman, A. J. Myers, R. Gawande, T. Ioerger, J. Sacchettini, S. M. Fortune, and J. L. Flynn. 2014. Sterilization of granulomas is common in active and latent tuberculosis despite within-host variability in bacterial killing. *Nat. Med.* 20: 75–9.

10. Lin, P. L., T. Coleman, J. P. J. Carney, B. J. Lopresti, J. Tomko, D. Fillmore, V. Dartois, C. Scanga, L. J. Frye, C. Janssen, E. Klein, C. E. Barry, and J. L. Flynn. 2013. Radiologic responses in cynomolgous macaques for assessing tuberculosis chemotherapy regimens. *Antimicrob. Agents Chemother.* .

11. Lin, P. L., V. Dartois, P. J. Johnston, C. Janssen, L. Via, M. B. Goodwin, E. Klein, C. E. Barry, and J. L. Flynn. 2012. Metronidazole prevents reactivation of latent Mycobacterium tuberculosis infection in macaques. *Proc. Natl. Acad. Sci. U. S. A.* 109: 14188–93.

12. Fallahi-Sichani, M., M. El-Kebir, S. Marino, D. E. Kirschner, and J. J. Linderman. 2011. Multiscale computational modeling reveals a critical role for TNF-α receptor 1 dynamics in tuberculosis granuloma formation. *J. Immunol.* 186: 3472–83.

13. Fallahi-Sichani, M., D. E. Kirschner, and J. J. Linderman. 2012. NF-κB Signaling Dynamics Play a Key Role in Infection Control in Tuberculosis. *Front. Physiol.* 3: 170.

Appendix C

High Pre-Treatment Bacterial Burden and Sub-Optimal Antibiotic Concentrations Within Granulomas Result in Treatment Failure in TB

The work in Appendix C represents a portion of the submitted manuscript: Pienaar, E., Cilfone, N.A., Lin, P.L., Dartois, V., Mattila, J.T., Butler, R., Flynn, J.L., Kirschner, D.E., Linderman, J.J. High pre-treatment bacterial burden and sub-optimal antibiotic concentrations within granulomas result in treatment failure in TB. (2014).

C.1 Introduction

Despite the availability of anti-TB antibiotics, active TB disease, caused by infection with *Mycobacterium tuberculosis* (*Mtb*), remains a major global health concern (1) with 8.6 million new cases reported in 2012 (2). Worldwide, TB has an 87% treatment success rate in new cases, leaving more than 1 million patients without cure (2). Known obstacles to treatment success (including patient non-compliance, relapse and drug-resistance) are thought be, in part, a result of the unusually long treatment regimens (3, 4). Our goal is to develop a computational approach to improve design of TB drug regimens and development of more efficient anti-TB antibiotics.

Standard therapy for active TB includes an initial combination of 3-4 first-line antibiotics for 2 months followed by another 4-7 months of 2 antibiotics. There are several reasons that such long treatment periods are required, for example the presence of

phenotypically drug-tolerant ‘persister’ bacteria (5–7) and high bacterial loads (8). The complex nature of the site of infection, namely granulomas, further complicates treatment. Granulomas are highly organized immunological structures that develop in response to *Mtb* infection. Multiple granulomas (of various sizes and bacterial burdens) are often present in a single patient, and these granulomas evolve independently of each other over time (9, 10). Granulomas can be caseous (acellular necrotic centers surrounded by macrophages and lymphocyte-rich cuffs), solid cellular (no necrotic cores with densely packed macrophages and T cells (11–13) or fibrotic (healing and long-term granulomas) (14). Granulomas are heterogeneous structures, with different microenvironments (e.g. hypoxic caseous necrotic regions) (15) and bacterial subpopulations (e.g. replicating and non-replicating) (16) developing within. This structural and spatial heterogeneity in granulomas may present a significant obstacle for antibiotics to reach bacteria.

There is a need for shorter regimens with less frequent doses and better treatment outcomes (17–19). True side-by-side comparisons of daily versus intermittent regimens are rare because of limitations in the number of regimens that can feasibly be evaluated in appropriate animal models or clinical trials, in addition to ethical constraints on clinical trials. Computational methods are ideal for such side-by-side comparisons and for testing large numbers of regimens. However, the extent to which regimen changes can improve treatment outcome is limited by the inherent pharmacokinetic and pharmacodynamic properties of current antibiotics.

The first-line antibiotics for TB are isoniazid (INH), rifampin (RIF), pyrazinamide (PZA) and ethambutol (EMB), of which INH and RIF are the focus of this Appendix.

INH is a pro-drug that, upon conversion to its active form, targets mycolic acid production (a component of bacterial cell wall) through inhibition of InhA (a 2-*trans*-enoyl-acyl carrier protein reductase). RIF targets bacterial RNA polymerase, inhibiting transcription. INH has been shown to have good early bactericidal activity but poor sterilizing activity, believed to be due to its high activity against replicating *Mtb*, but low activity against non-replicating *Mtb* (19). RIF has been shown to have good sterilizing activity (20). RIF is effective against hypoxia- or acid-induced non-replicating bacteria (21), but phenotypic tolerance develops in multiple stress-induced non-replicating bacteria (22) or stationary phase *Mtb* (23).

Antibiotic dynamics and bacterial killing within granulomas remain largely un-described and are challenging to evaluate in vivo (24). Investigation into lung antibiotic concentrations first conducted in the 1950s and 1980s (25–27) has recently been revisited using modern techniques that allow visualization of drug distribution within a granuloma (28, 29). Rabbit models of TB show considerable variation in antibiotic concentrations between plasma, tissue and granulomas for four standard TB antibiotics (28). For example, there is preferential accumulation of moxifloxacin (a second-line anti-TB antibiotic) in the cellular cuff relative to the central caseum of necrotic granulomas (29). Other antibiotics such as the nitroimidazoles and clofazimine have been imaged in caseous lesions and exhibit similar heterogeneous intra-lesional distribution with poor penetration into necrotic foci (3). Among the anti-TB drugs that have so far been investigated by MALDI (Matrix-Assisted Laser Desorption/Ionization) imaging, only pyrazinamide penetrates caseum effectively (V. D., unpublished observations). A clinical trial is currently under way to evaluate permeability of several anti-TB antibiotics in

resected lung tissue and granulomas of TB patients (ClinicialTrials.gov NCT00816426). Results point to complex and variable antibiotic distribution within granulomas. Understanding the limiting features of current antibiotics in the context of granulomas can guide the development of new anti-TB antibiotics or modifications of current antibiotics (3).

The technology required to follow antibiotic concentrations and bacterial numbers in a single granuloma over time does not exist. In this Appendix, we use a systems pharmacology approach, integrating experimental data and computational modeling, to address the following questions: What are antibiotic dynamics (distribution and activity) inside a lung granuloma? How does spatial distribution of antibiotics influence treatment outcome? What are host mechanisms contributing to treatment outcome? Can we use currently available antibiotics in optimized regimens to shorten duration of treatment? What modifications could improve efficacy of current anti-TB antibiotic?

C.2 Materials and Methods

Our computational model includes: granuloma formation and function, antibiotic pharmacokinetics, and antibiotic pharmacodynamics (PD). We consider both plasma PK and lung tissue PK (i.e. antibiotic penetration into tissue).

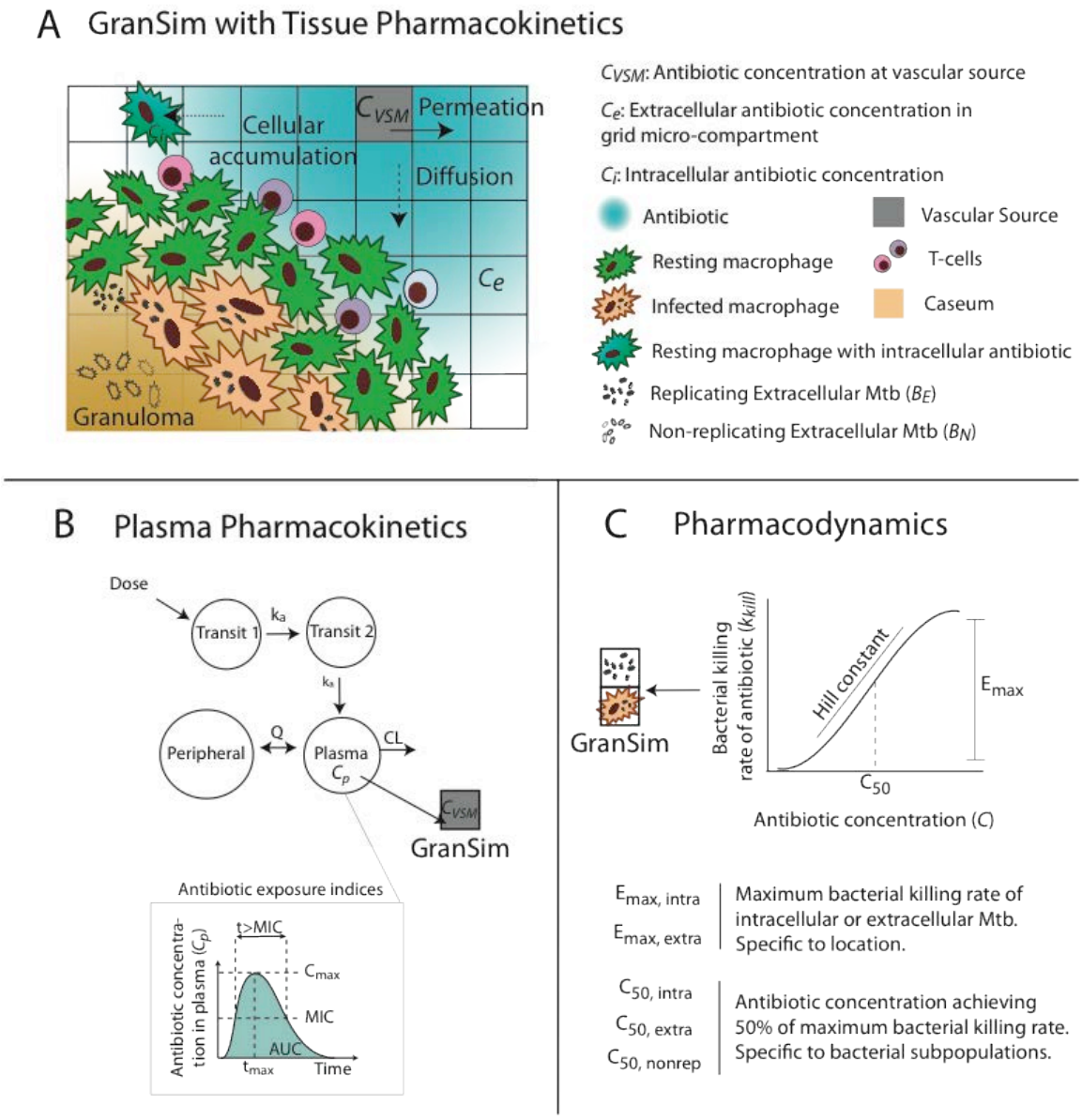

Figure C.1 Pharmacokinetic, granuloma, and pharmacodynamics models of antibiotics
(A) Tissue pharmacokinetics (PK) are added to the existing granuloma model (GranSim) by accounting for antibiotic permeability through vascular walls, diffusion in tissue, uptake by host cells, and degradation by host cells and bacteria. (B) Plasma PK is modeled using two transit compartments, a plasma compartment and a peripheral compartment. The peripheral compartment represents other tissues and organs. Antibiotic doses are added to the first transit compartment. Antibiotic dynamics in the plasma compartment are characterized using the metrics indicated in the bottom panel. (C) Pharmacodynamics are implemented using E_{max} models, defined by maximum activity (E_{max}), concentration where 50% of maximum activity is achieved (C_{50}), and Hill constant (H) describing steepness of the curve. We define PD parameters separately for bacterial subpopulations, since different subpopulations have been shown to have different susceptibilities to INH and RIF (30–32). We define E_{max} and C_{50} for each antibiotic and bacterial subpopulation combination. k_a: absorption rate constant; Q: inter-compartmental clearance rate constant; CL: clearance rate constant from plasma; C_p: plasma antibiotic concentration; C_{max}: maximum concentration; AUC: area under the curve; t_{max}: time after dosing when maximal concentration is reached; *MIC:* minimum inhibitory concentration.

C.2.1 Agent-Based Model of Granuloma Formation and Function

We begin with our existing hybrid multi-scale agent-based model (GranSim) of *Mtb* infection and granuloma formation (see Chapter 3, 4, and 5) (33–36). Briefly, the model encapsulates molecular, cellular and tissue scale characteristics of a granuloma (Figure C.1A). At the tissue scale, the model tracks cellular movement on a 2D grid of micro-compartments based on the chemokine environment, with granuloma formation as an emergent behavior of the system. At the cellular scale, the model tracks individual macrophages and T cells, their states (resting, activated, infected or chronically infected for macrophages; and cytotoxic T cells, regulatory T cells or IFN-γ producing T cells) and interactions. At the molecular level, the model tracks secretion, diffusion, binding and degradation of cytokines and chemokines. A randomly-distributed number of micro-compartments on each grid are designated as vascular source micro-compartments (VSMs). Recruited macrophages and T-cells as well as antibiotics enter the grid exclusively through VSMs.

Bacteria are represented by three subpopulations: intracellular (B_I), replicating extracellular (B_E) and non-replicating extracellular (B_N) (Figure C.1A). B_I can grow, be killed within activated macrophages, or be killed when infected host cells they reside in undergo apoptosis or cytotoxic killing. When B_I reaches a threshold, the infected macrophage irreversibly changes to the 'chronically infected' state that has impaired antibacterial function. When B_I levels reach the carrying capacity of a macrophage, the macrophage bursts and distributes the bacteria in the surrounding grid micro-compartments. B_E can grow or be killed by macrophages in the same micro-compartment or by activated macrophages within its Moore neighborhood. Extracellular growth is

logistic, reaching a defined carrying capacity per micro-compartment. Extracellular bacteria that reside in caseous micro-compartments are labeled 'non-replicating'. However, low levels of metabolic activity remain in these bacteria (37), and therefore we assign a slow growth rate to this sub-population in the model (100-fold lower than B_E).

In this Appendix, we use a larger grid than in Chapters 3, 4, and 5 to better capture physiological granuloma sizes and vascular density. We reduced the complexity in our description of TNF and IL-10 roles (see Chapters 3, 4, and 5) using our tunable resolution approach (see also Chapter 2) (38). In addition, to reduce computational times needed, we implemented spectral methods for solving the partial differential equations describing diffusion (see also Chapter 2) (39, 40).

C.2.2 Plasma PK Model Structure

Plasma PK models for TB antibiotics are available and range in complexity (28, 41–44). We use an established plasma PK model for INH and RIF with two distribution compartments, plasma and peripheral, and two transit compartments shown in Figure C.1B and described by the equations (28):

$$\frac{dC_{t1}}{dt} = -k_a C_{t1} \qquad (Eqn.C.1)$$

$$\frac{dC_{t2}}{dt} = k_a(C_{t1} - C_{t2}) \qquad (Eqn.C.2)$$

$$\frac{dC_{Pe}}{dt} = Q\left({}^{C_P}/_{V_P} - {}^{C_{Pe}}/_{V_{Pe}}\right) \qquad (Eqn.C.3)$$

$$\frac{dC_P}{dt} = k_a C_{t2} - Q\left({}^{C_P}/_{V_P} - {}^{C_{Pe}}/_{V_{Pe}}\right) - CL\,{}^{C_P}/_{V_P} \qquad (Eqn.C.4)$$

C_{t1} and C_{t2} are concentrations of antibiotic in first and second transit compartments, and C_{Pe} and C_P are concentrations in peripheral and plasma compartments (mg/kg). V_{Pe} and V_P are volumes of distribution for peripheral and plasma compartments (L/kg). k_a is the absorption rate constant (h^{-1}), Q is the inter-compartmental clearance rate constant between the plasma and peripheral compartments (L/h•kg) and CL is the clearance rate constant from the plasma compartment (L/h•kg).

To simulate oral dosing, we add new antibiotic doses as a single bolus to any existing concentration in the first transit compartment at designated dosing times, and we assume the plasma concentration is the same for all VSMs on the grid.

C.2.3 Plasma PK Model Calibration

We calibrate plasma PK indices (AUC, C_{max} and t_{max}; Figure C.1B) to those measured for INH and RIF in NHPs (45) by sampling the parameter space for k_a, Q, V_P, V_{Pe} and CL using Latin Hypercube Sampling (46). We simulate 4 daily doses of INH (15 mg/kg) and RIF (20 mg/kg) and measure PK indices for the fourth dose as in (45). Out of 700 parameter combinations we identified 14 combinations that give AUC, C_{max} and t_{max} within one standard deviation of the experimental mean. We then set ranges for each parameter to encompass all values from the set of 14 (Table C.1). Experimental and model outcomes for PK indices are shown in Figure C.2A. We use ranges instead of single values to introduce host-to-host variation in plasma PK. Our parameter ranges agree with known PK differences between INH and RIF. A combination of higher clearance rates, higher peripheral volumes of distribution and higher absorption rates for

INH lead to INH concentrations that peak earlier than RIF and that do not accumulate significantly with repeated dosing, unlike RIF (28, 45, 47–49).

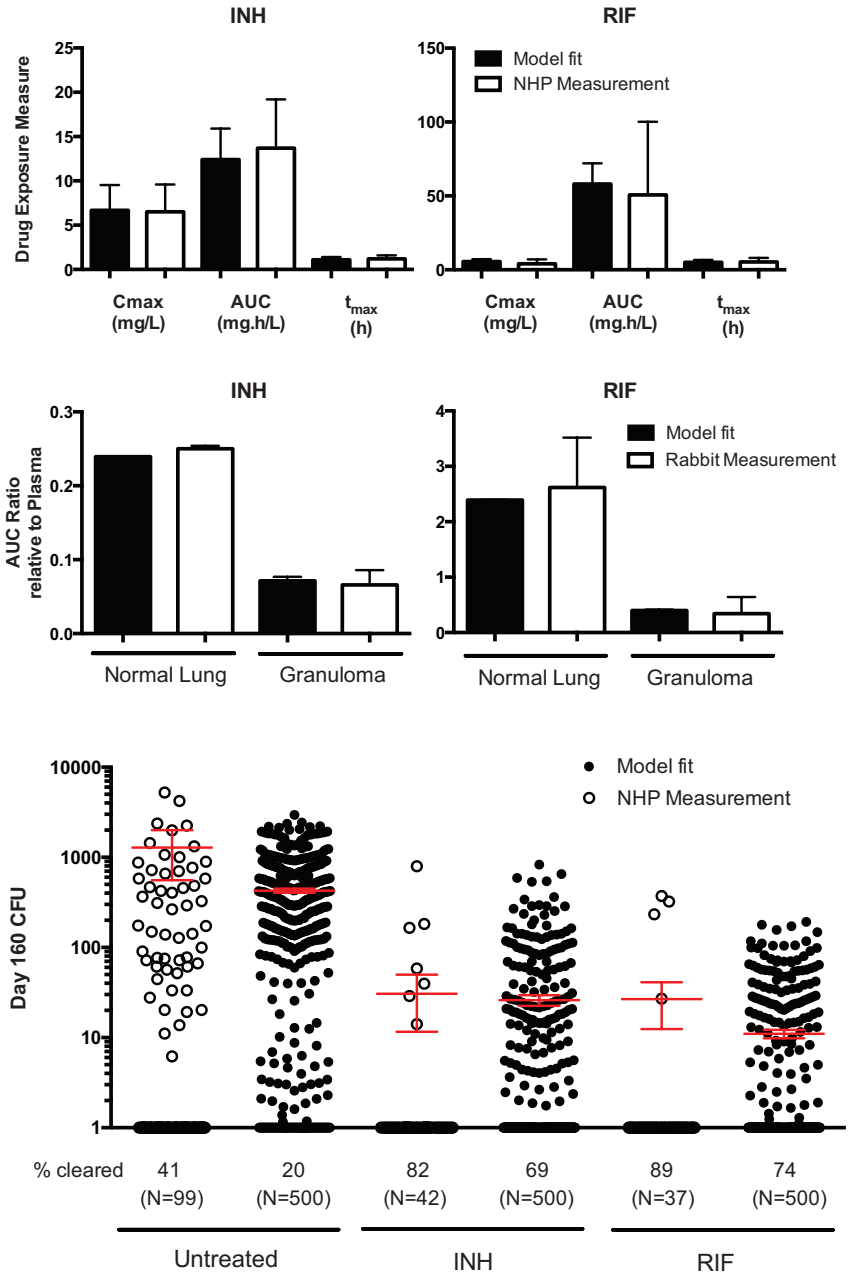

Figure C.2 Model calibration of antibiotic related parameters
Calibration. Our model is calibrated to PK and PD data from rabbits and NHPs for both INH and RIF. (A) Three plasma PK outputs from the model (black bars) match values measured in NHPs (white bars). Bars show means, and error bars show SD (For model fit: N=100; for NHP: N=7). See Table C.1 for parameter ranges used to give variation in model outcomes. (B) Tissue PK parameters are fit (black bars) to give tissue: plasma AUC ratios similar to those measured in rabbit granulomas (white bars). For normal lung, the model fit results from uninfected simulations (N=5). For granuloma values, the model fit measurements are from inside the circumference of granulomas (N=5). Bars show means and error bars show SD. (C) PD

parameters are fit (filled circles) to match measurements from NHPs (open circles). Lines and error bars show mean +/- SEM.

Table C.1 Antibiotic related parameters

Plasma Related PK Parameters [1]				
Parameter Name	**Units**	**INH**	**RIF**	**Reference**
Absorption rate constant (k_a)	h^{-1}	1 - 5	0.2 – 0.8	Fit to (45), Guided by (28, 48, 50)
Intercompartmental clearance rate constant (Q)	L/h•kg	0.025 – 0.2	0.1 – 0.7	Fit to (45), Guided by (28, 48, 50)
Plasma volume of distribution (V_P)	L/kg	0.1 - 2	0.5 – 1.5	Fit to (45), Guided by (28, 48, 50)
Peripheral volume of distribution (V_{Pe})	L/kg	20 - 40	0.1 - 1	Fit to (45), Guided by (28, 48, 50)
Plasma clearance rate constant (CL)	L/h•kg	0.6 – 1.8	0.25 – 0.5	Fit to (45), Guided by (28, 48, 50)
Lung Tissue Related PK Parameters				
Parameter Name	**Units**	**INH**	**RIF**	**Reference**
Degradation rate constant, extracellular ($k_{deg,e}$)	s^{-1}	$5.5x10^{-9}$	$7.5x10^{-8}$	Fit to (28)
Degradation rate constant, intracellular ($k_{deg,i}$)	s^{-1}	$6.4x10^{-3}$	$6.7x10^{-3}$	Fit to (28)
Effective diffusivity (D)	cm^2/s	$1.1x10^{-7}$	$7x10^{-7}$	Fit to (28), Guided by (51)
Cellular accumulation ratio [2] (a)	-	0.35	18	Fit to (28), Guided by (52–55)
Vascular permeability [3] (p)	cm/s	$8.4x10^{-6}$	$1x10^{-5}$	Fit to (28), Guided by (56)
Permeability coefficient [4] (PC)	-	0.25	3.3	(28)
PD Related Parameters				
Parameter Name	**Units**	**INH**	**RIF**	**Reference**
C50 for intracellular *Mtb* ($C_{50,BI}$)	mg/L	0.02	10	(30–32, 57)
C50 for extracellular replicating *Mtb* ($C_{50,BE}$)	mg/L	0.04	1.23	(30–32, 57)
C50 extracellular non-replicating *Mtb* ($C_{50,BN}$)	mg/L	0.5	5	(30–32, 57)
Hill constant for intracellular *Mtb* (H_{BI}) [5]	-	1	0.48	(30–32, 57)
Hill constant for extracellular replicating *Mtb* (H_{BE}) [5]	-	1	0.7	(30–32, 57)
Hill constant for extracellular non-replicating *Mtb* (H_{BN})	-	1	0.7	(30–32, 57)
Max activity intracellular ($E_{max,BI}$)	time $step^{-1}$	0.046	0.069	Fit to (9), Guided by (30, 31)
Max activity extracellular ($E_{max,BE}$)	time $step^{-1}$	0.155	0.296	Fit to (9), Guided by (30, 31)

(1): Plasma PK parameters are given a range of values to account for inter-individual variation
(2): Steady state concentration inside macrophages/concentration outside macrophages
(3): Hill constants describe the steepness of the E_{max} model killing curve (Figure C.1C)

C.2.4 Tissue PK Model Structure

Our model captures spatial distribution of antibiotics in lung tissue by accounting for permeation through the vascular wall, diffusion and degradation within the tissue and penetration into host cells (Figure C.1A) as previously used for modeling anti-TNF therapy (58). Antibiotics can enter or leave through the vascular wall (i.e., at VSMs) depending on the concentration difference between the plasma and lung tissue:

$$C_{VSM}(t + \Delta t) = C_{VSM}(t) + pA_{VSM}\big(PC \cdot C_P(t) - C_{VSM}(t)\big)\Delta t \qquad (Eqn.C.5)$$

where C_{VSM} is antibiotic concentration on the grid at the given VSM (mg/L), p is permeability (cm/s), A_{VSM} is outside area of the grid micro-compartment (cm^2), PC is permeability coefficient (measure of antibiotic sequestration in the tissue) and Δt is time step (s). We assume that adjacent grids to the one under investigation would be similarly vascularized and therefore use insulating boundary conditions for antibiotic diffusion. Because of the small size of the tissue we model (4mm x 4mm), we assume that any contribution from granuloma back to plasma will not significantly affect plasma antibiotic concentrations. The influence of bulk lung tissue on plasma concentrations is captured by the peripheral distribution (at rate constant Q) in the plasma PK model (Figure C.1B).

We assume cellular accumulation of antibiotics is at pseudo-steady state and intracellular (C_i) and extracellular concentrations (C_e) are updated at each time step based on the total amount of antibiotic in the grid micro-compartment where each macrophage is located. C_i and C_e are thus related by:

$$C_e = \frac{A_T}{V_{micro} + aV_{mac}} \qquad (Eqn.C.6)$$

$$C_i = aC_e \qquad (Eqn.C.7)$$

where A_T is the total amount of antibiotic available (intracellular plus extracellular), V_{micro} is the volume of one micro-compartment, V_{mac} is the volume of a macrophage and a is the cellular accumulation ratio (or intracellular partition coefficient). Note: $C_e = C_{VSM}$ at VSMs.

Antibiotics degrade in intracellular and extracellular environments according to

$$\frac{dC_x}{dt} = -k_{deg,x}C_x \qquad (Eqn.C.8)$$

where $k_{deg,x}$ is the degradation rate constant, and C_x is the intracellular or extracellular antibiotic concentration (58).

C.2.5 Tissue PK Model Calibration

We calibrate normal lung tissue and granuloma AUC to that observed in rabbits (28) by sampling GranSim parameter space for $k_{deg,i}$, $k_{deg,e}$, D, a, and p using Latin Hypercube Sampling (46). In order to ensure that plasma PK differences are not influencing our calibration of lung tissue PK, *in these calibration simulations only* we use plasma PK parameters and antibiotic doses (30 mg/kg for INH and 24 mg/kg for RIF) taken from the rabbit model (28). Granulomas were allowed to form for 100 days before antibiotic dosing was started. PK indices were measured after 12 days of treatment (as in (28)). Out of 1000 parameter combinations, parameter values were selected that minimized differences between experimental measurements and model predictions of AUC ratios relative to plasma (Figure C.2B and Table C.1).

Information on antibiotic concentrations in lung tissue and in granulomas is scarce and currently only available for rabbits (28). We assume that antibiotic penetration into lung tissue in rabbit and NHP lungs are similar. The model is flexible to test variations from these values. Furthermore, the rabbit study only measured INH and ignored the active metabolites (because they are transient and reactive and cannot be captured by HPLC/MS analysis). Similarly in the model we only consider pro-drug INH and not its metabolites, though INH metabolism by the bacterium is something the model can be expanded to include in future versions.

Limited data on INH and RIF distribution in the caseum or cavity wall of rabbit granulomas indicate that INH accumulates well in caseum while RIF has higher concentration in the cavity wall (V. Dartois, unpublished observations). While it is difficult to delineate the outline of 'caseum' or 'cavity wall' areas in the simulated granulomas, parameter values from the model calibration are in line with these observations, i.e. low cellular accumulation ratio for INH and high cellular accumulation ratio for RIF.

C.2.6 PD Model Structure

PD parameters have been determined for several TB antibiotics in broth culture, in macrophage culture, and in mice (30, 31, 59). The concentration dependent antibacterial activity is quantified using an E_{max} model (Figure C.1C). Killing rate constants ($k_{kill,x}$) are calculated for each bacterial subpopulation (intracellular, replicating extracellular or non-replicating extracellular) based on local antibiotic concentrations (intra- or extracellular) as in (60):

$$k_{kill,x} = E_{max}^{x} \frac{C_x^H}{C_x^H + C_{50,x}^H} \qquad (Eqn.C.9)$$

where x denotes intracellular or extracellular concentrations or bacterial subpopulations, C is local antibiotic concentration, E_{max} is maximum activity, C_{50} is concentration where 50% of maximum activity is achieved, and H is the Hill constant describing steepness of the curve. Changes in the bacterial subpopulation (B_x) due to growth and killing are expressed as in (61):

$$\frac{dB_x}{dt} = \left(g_x - k_{kill,x}\right)B_x \qquad (Eqn.C.10)$$

where g_x is the growth rate constant for bacterial subpopulation x.

C.2.7 PD Model Calibration

Five hundred simulated granulomas are obtained by varying host parameters that give a distribution of total *Mtb* per granuloma similar to that observed in NHP granulomas at a median of 180 days post infection (d.p.i.) (Figure C.2C) (9). Treatment is initiated in the simulated granulomas at 100 d.p.i. C_{50} and H are estimated from *in vitro* dose response curves for INH and RIF (23, 30, 31, 57) with the caveat that these parameters may not extrapolate to *in vivo* conditions, and that they can vary between strains. E_{max} values are selected that reproduce INH and RIF efficacy in NHPs after 2 months of daily dosing in terms of mean CFU and percentage of granulomas cleared (9). Parameters are given in Table C.1 and the model fitting results are shown in Figure C.2C.

C.2.8 Tunable Resolution

Chapters 3, 4, and 5 focused on understanding the roles of cytokine dynamics (TNF and IL-10) at a molecular scale and how receptor-ligand trafficking events (modeled as a system of non-linear differential equations) influenced infection outcomes (35, 36). Although many TNF and IL-10 events were identified as critical to control of infection, our focus in Appendix C and Chapter 6 was to understand issues that arise during antibiotic treatment at the single granuloma level. Thus, we apply the concept of tunable resolution to our model in order to retain our understanding of the roles of TNF and IL-10 during infection, yet reducing model complexity and computational burden in order to focus on a detailed description of antibiotic treatment (38). Our methods are

motivated by the sensitivity analysis results that we performed in Chapter 3 (36) to identify key model features. Briefly, the system of non-linear ordinary differential equations in Chapter 3 (36) is replaced with the following equations describing the change in soluble TNF and soluble IL-10 concentrations in a compartment containing an agent:

$$\frac{d[sTNF]}{dt} = k'_{sTNF} - k_{cTNF}\left(\frac{[sTNF]}{K_{DT1} * \frac{N_{AV}}{V} + [sTNF]} - \frac{[sTNF]}{K_{DT2} * \frac{N_{AV}}{V} + [sTNF]}\right) \qquad (Eqn.C.11)$$

$$\frac{d[sIL10]}{dt} = k'_{sIL10} - k_{cIL10}\left(\frac{[sIL10]}{K_{DI} * \frac{N_{AV}}{V} + [sIL10]}\right) \qquad (Eqn.C.12)$$

Where k'_{sTNF} and k'_{sIL10} are the apparent secretion rates of TNF and IL-10, k_{cTNF} and k_{cIL10} are the apparent rate constants for consumption (which incorporate estimates for total receptors and any scaling factors for both TNF and IL-10), and K_{DT1}, K_{DT2}, and K_{DI} are affinities for TNFR1, TNFR2, and IL-10R respectively. Each quotient represents the bound fraction of surface receptors assuming a pseudo-steady state.

Additionally, we re-write any probability functions that relied on molecular scale details in terms of soluble TNF and IL-10 concentrations:

$$P_{NF\kappa B} = \begin{cases} 0 & \frac{[sTNF]}{K_{DT1} * \frac{N_{AV}}{V} + [sTNF]} < \tau'_{NF\kappa B} \\ 1 - e^{-k'_{NF\kappa B}\left(\frac{[sTNF]}{K_{DT1} * \frac{N_{AV}}{V} + [sTNF]} - \tau'_{NF\kappa B}\right)\Delta t} & \frac{[sTNF]}{K_{DT1} * \frac{N_{AV}}{V} + [sTNF]} \geq \tau'_{NF\kappa B} \end{cases} \qquad (Eqn.C.13)$$

$$P_{apop} = \begin{cases} 0 & \left(\frac{[sTNF]}{K_{DT1} * \frac{N_{AV}}{V} + [sTNF]}\right) f_{int} < \tau'_{apop} \\ 1 - e^{-k'_{apop}\left(\left(\frac{[sTNF]}{K_{DT1} * \frac{N_{AV}}{V} + [sTNF]}\right) f_{int} - \tau'_{NF\kappa B}\right)\Delta t} & \left(\frac{[sTNF]}{K_{DT1} * \frac{N_{AV}}{V} + [sTNF]}\right) f_{int} \geq \tau'_{apop} \end{cases} \qquad (Eqn.C.14)$$

$k'_{NF\kappa B}$, k'_{apop}, $\tau'_{NF\kappa B}$ and τ'_{apop} are modified rate constants and thresholds for TNF-induced NF-κB activation and apoptosis, respectively, while f_{int} is a partition factor for estimating internalized bound receptors from the pseudo-steady state estimate of surface

bound receptors. These resulting rate constants and parameters can be estimated from their corresponding parameters when the increased molecular scale detail is turned on.

Lastly, inhibition of TNF synthesis by IL-10 is reduced to a simple dose dependent function based on the soluble IL-10 concentration in the compartment.

$$k'_{sTNF} = \frac{1}{1 + e^{\frac{\log[sIL10] + \alpha}{\beta}}} \qquad (Eqn. C.15)$$

Where k'_{sTNF} is the apparent secretion rate of TNF, α is the threshold parameter, and β is the shape parameter. These parameters are calculated directly from results of the system of non-linear differential equations. Tuneable resolution parameter values are given in Table C.2.

Table C.2 Tunable resolution parameters

Parameter	Value	Unit
Apparent TNF consumption rate	0.00077	s^{-1}
Apparent IL-10 consumption rate	0.0004	s^{-1}
Partition factor for estimating internalized bound receptors	11.3	-
Threshold for IL-10 inhibition of TNF secretion	-1.93	-
Shape parameter for IL-10 inhibition of TNF secretion	0.181	-
Apparent TNF secretion rate by macrophages	1.5	Molecules/s
Apparent IL-10 secretion rate by activated macrophages	0.3	Molecules/s
Apparent IL-10 secretion rate by infected macrophages	0.02	Molecules/s
Apparent TNF secretion rate by IFNg producing T-cells	0.15	Molecules/s
Apparent TNF secretion rate by cytotoxic T-cells	0.015	Molecules/s
Apparent IL-10 secretion rate by regulatory T-cells	0.739	Molecules/s
Affinity of TNF for TFNR1	1.9×10^{-11}	M
Affinity of IL-10 for IL-10R	4.56×10^{-10}	M

C.2.9 Spectral Methods for Solving Diffusion Equations

Spectral methods for solving PDEs are a class of collocation methods that analyze the discretized system in a global instead of a local manner (39, 40, 62–64). The solution to

the entire system is assumed by a basis function and time-varying coefficients are determined such that the solution to the system is satisfied. Importantly, spectral methods reduce PDEs into ODEs, thus drastically reducing the computational burden of the numerical approximation (39). For an in depth explanation please refer to Chapter 2 (39). We adapt the basic method for our needs here to allow insulating boundary conditions and apply simple smoothing pre-processing steps to limit errors associated with discontinuous concentration fields (see Chapter 2) (65).

C.2.10 Treatment Regimens

We use the calibrated model to vary dose scheduling according to INH and RIF containing regimens recommended by the Centers for Disease Control and Prevention (66). Selected regimens are outlined in Figure C.3. INH dose size is increased as dose frequency decreases, but RIF dose size is kept constant even when dose frequency changes. We use doses that emulate human exposure levels in NHPs (45). RIF doses are 20 mg/kg. INH doses are 15 mg/kg for daily dosing and 45 mg/kg for twice weekly or thrice weekly dosing. For regimen comparison granulomas that cleared infection prior to 100 d.p.i are excluded from the analysis, leaving 412 (500 – 88) granulomas in the final set.

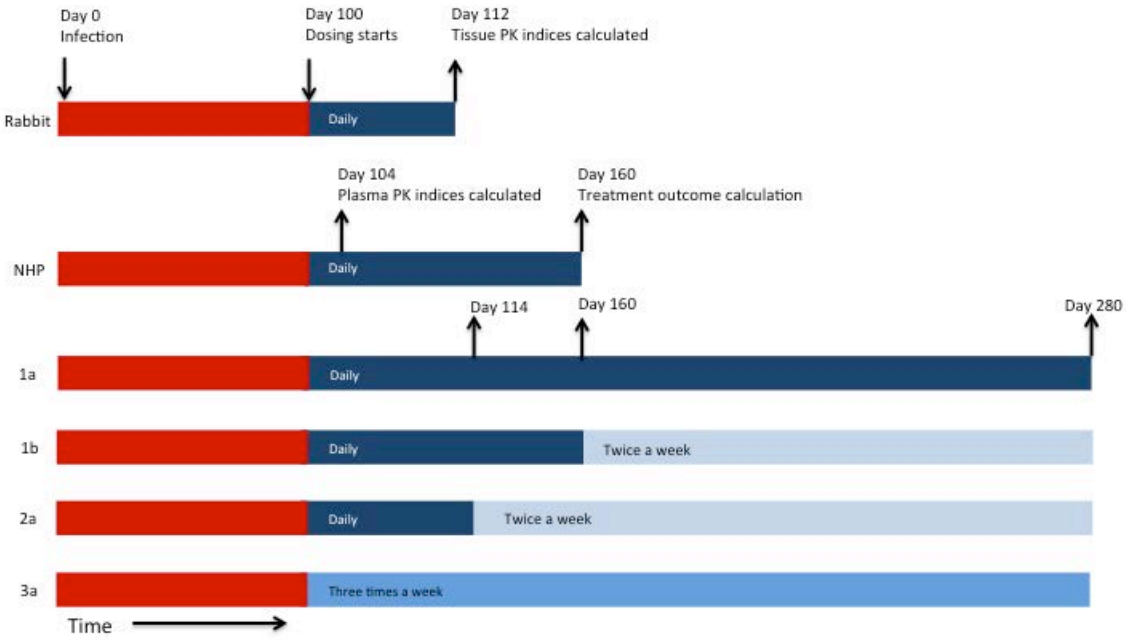

Figure C.3 Simulated treatment regimens
Different treatment regimens are used for model calibration and prediction. The rabbit regimen (28) is used to calibrate tissue PK parameters. The NHP regimen (9, 45) is used to calibrate plasma PK and PD parameters. Regimens 1a, 1b, 2a and 3a are recommended by the CDC/WHO (66) and are implemented with the full calibrated model (Figure C.1) to predict treatment outcomes.

Clinical trials use relapse or recurrence (improvement during treatment followed by relapse once treatment ends), treatment failure (no improvement during treatment), cure (no relapse once treatment ends) or antibiotic resistance as measures of treatment efficacy (18). However, these outcomes are observed at a patient level, while our focus in this Appendix is at a single granuloma level. We define treatment success as elimination of all bacteria from a granuloma (cleared granulomas), and treatment failure as cases where any bacteria remain after treatment (non-cleared granulomas). We evaluate treatment outcome based on (i) CFU after treatment (in non-cleared granulomas), (ii) time to clearance (in cleared granulomas) and (iii) the percentage of granulomas not cleared of infection (%GNC) by the end of the treatment period. For comparing regimens, we define a *treatment outcome index* (TOI) that is an average of the

normalized values of the three treatment outcomes outlined above. Each outcome is normalized to its minimum and maximum over all regimens being compared. The TOI ranges between 0 and 1, with lower values representing "better" outcomes.

C.3 Results

We constructed a model of INH and RIF distribution and action in granulomas and calibrated it to rabbit and NHP PK and PD data (Figure C.2). To our knowledge this is the first PKPD model of antibiotic penetration into granulomas with temporal-spatial resolution. This calibrated model is used to simulate different regimens and make predictions about treatment progression and outcomes. The work in Appendix C has been submitted as part of: Pienaar, E., Cilfone, N.A., Lin, P.L., Dartois, V., Mattila, J.T., Butler, R., Flynn, J.L., Kirschner, D.E., Linderman, J.J. High pre-treatment bacterial burden and sub-optimal antibiotic concentrations within granulomas result in treatment failure in TB. (2014). Outlined below are the important predictions and conclusions from this paper, derived from the model described and constructed in this Appendix.

C.3.1 Mean INH Concentrations in Granulomas Only Exceed C_{50} for Short Periods and Mean RIF Concentrations Do Not Exceed $C_{50,BI}$ or $C_{50,BN}$

Of interest is how antibiotic concentrations, as measured against C_{50}, vary with different treatment regimens. We simulate dosing regimens similar to those recommended by the CDC for treatment of active TB (66) (Figure C.3, regimens 1a, 1b, 2a and 3a). Average antibiotic concentrations per granuloma over seven days for dosing frequencies of seven doses per week (dpw) (regimen 1a, 1b and 2a) or three dpw

(regimen 3a) are shown in Figure C.4. The short half-life of INH in granulomas, due primarily to the high plasma clearance rate constant *CL*, leads to average concentrations below $C_{50,BI}$ and $C_{50,BE}$ for > 80% of the dosing period for 7 dpw and 3 dpw. Peak INH concentrations barely reach $C_{50,BN}$ with the 7 dpw regimen, but do exceed $C_{50,BN}$ for short periods with the 3 dpw regimen, because of the larger dose given at this lower frequency. The longer half-life of RIF in granulomas, due primarily to a lower plasma clearance rate constant *CL*, and high permeability coefficient *PC,* lead to concentrations below $C_{50,BE}$ for only 37% of the 7 dpw dosing period. However, since the dose size for RIF is not increased when the dosing frequency is decreased (as per protocol), reducing frequency to 3 dpw leads to concentrations of RIF below $C_{50,BE}$ for 73% of the dosing period. RIF concentrations never exceed $C_{50,BN}$ or $C_{50,BI}$ inside the granuloma. These suboptimal antibiotic exposures could contribute to treatment failure, in agreement with observations for RIF in patients (67).

C.3.2 Bacterial Regrowth Occurs Between Doses and Is Greater for INH Than RIF

We also are able to track and predict bacterial subpopulation dynamics inside granulomas for the dosing regimens described above. INH treatment leads to a sharp decrease in CFU immediately after dosing (Figure C.4A), followed by bacterial regrowth once antibiotic concentrations drop below $C_{50,BE}$ and $C_{50,BI}$. Outcomes are qualitatively similar for different dosing frequencies; however, longer periods between doses allow more bacterial regrowth for 3 dpw than 7 dpw (Figure C.4B). This occurs despite the larger doses given 3 dpw (45 mg/kg; total 135 mg/kg per week) compared to 7 dpw (15 mg/kg; total 105 mg/kg per week). RIF treatment leads to a more consistent decrease in

total CFU (especially for 7 dpw; Figure C.4C) than INH treatment due to the slower plasma clearance rate constant for RIF as well as the larger Hill constant for INH (Table C.1). Small increases in bacterial numbers are visible at the end of the dosing periods for RIF with the 3 dpw regimen (Figure C.4D).

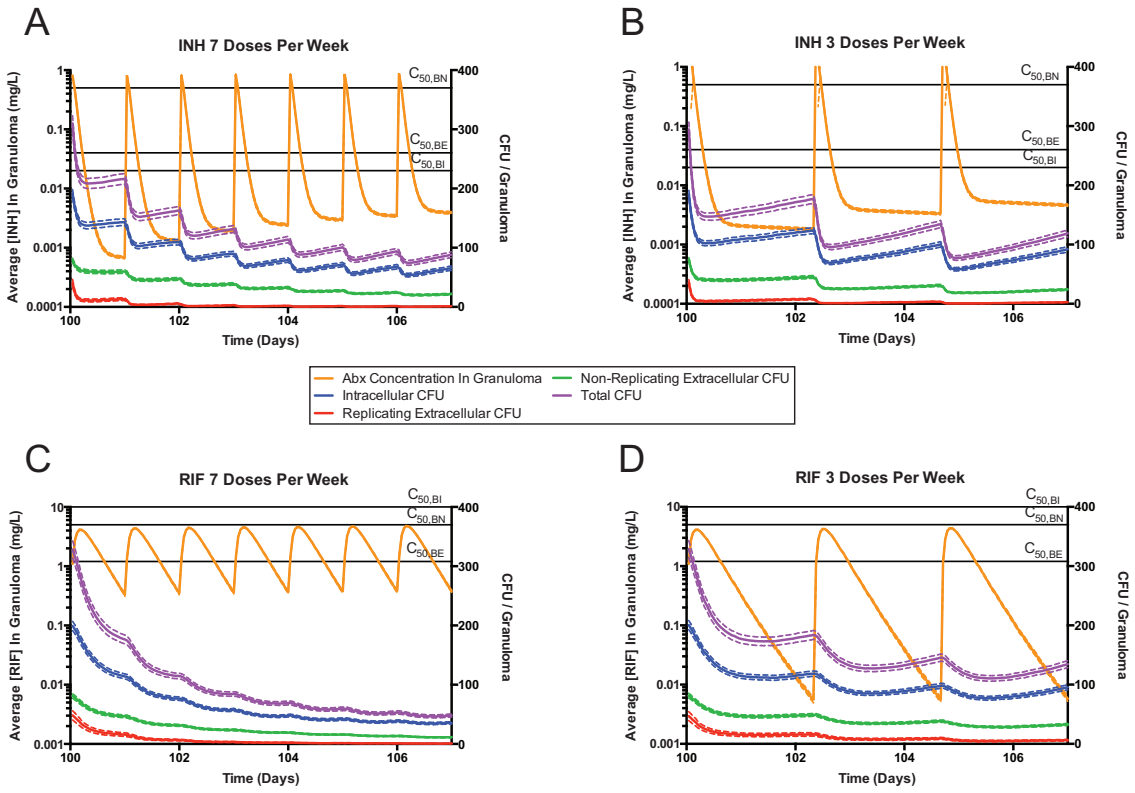

Figure C.4 Average bacterial and antibiotic dynamics in granulomas
INH (A and B) and RIF (C and D) concentrations inside granulomas are plotted on left y-axes; bacterial subpopulations are plotted on right y-axes. Colored solid lines are mean and colored dashed lines are +/- SEM (N=412). Black lines are C50 values for intracellular ($C_{50,BI}$), extracellular ($C_{50,BE}$) and non-replicating ($C_{50,BN}$) bacterial populations.

During the first 7 days of RIF and INH treatment, the proportion of bacteria that are intracellular increases (Figure C.4). This is due to low INH concentrations inside cells and high value of $C_{50,BI}$ for RIF. Furthermore, continued phagocytosis of extracellular bacteria during treatment adds to the protected intracellular population. If we continue the simulation to 280 days, the dominant population starts to change after ~10 days, shifting

from intracellular to non-replicating extracellular (data not shown). The trend is slow, and after 30 days of daily INH or RIF treatment the majority of bacteria are non-replicating extracellular bacteria, i.e. bacteria trapped in hypoxic caseum. Results are similar for INH and RIF and for all dosing regimens. Our results confirm that outcomes of INH and RIF treatment regimens are sensitive to reduced dosing frequencies. The changes in relative bacterial sub-populations over time present a moving target for drug regimens and could lead to changes in treatment efficacy.

C.3.3 Antibiotic Concentration Gradients Form Inside Granulomas

Current technology is beginning to allow observation of the spatial distribution of antibiotics in a granuloma (3). With our computational model, we not only can visualize and track details of the spatial distribution of antibiotics in granulomas, but we can do this over time and calculate the cumulative antibiotic exposure (here calculated as AUC - see Materials and Methods) for all parts of a granuloma. Two sample granulomas that were treated with daily INH or RIF are shown in Figure C.5. Time-lapse movies of drug distributions and treatment progression within these granulomas, as well as high-resolution images that better show cellular level details (such as T-cells and caseation) are available at http://malthus.micro.med.umich.edu/lab/movies/Abx/. Figure C.5A shows a sample solid cellular granuloma of diameter 1.7mm at day 100, when simulated treatment with antibiotics is initiated. Exposure of both INH and RIF during the first week of treatment is significantly lower inside the granuloma than in the surrounding tissue, are well below the 7 day AUC EC_{80} (AUC that achieves 80% of maximum killing) and noticeable gradients form inside the granuloma. RIF has a larger area of suboptimal

exposure than INH. Despite low exposure to both INH and RIF inside the granuloma, CFU is reduced and the granuloma shrinks from 1.7 mm to 1.4 mm diameter by day 160 for both antibiotics. For all simulated granulomas, predicted changes in granuloma size during treatment match NHP data (9) (data not shown). RIF treatment clears bacteria by day 280 while INH treatment does not.

Figure C.5B shows a sample caseous granuloma of diameter 2mm. INH and RIF exposure look qualitatively similar to Figure C.5A; however, the area of suboptimal INH exposure is larger in the granuloma in Figure C.5B. This is a result of the combined effects of larger granuloma size, lower absorption rate constant and higher inter-compartmental and plasma clearance rate constants than the granuloma shown in Figure C.5A. In this case, INH and RIF are less efficient at reducing CFU after 60 days of treatment, and both antibiotics fail to clear bacterial load by day 280. During INH treatment the granuloma size remains at 2mm until the end of treatment, and during RIF treatment the granuloma shrinks to 1.7mm by day 160 but no further. Because INH fails to shrink the granuloma, exposure remains nearly constant over the treatment period while there is a slight improvement in antibiotic exposure for RIF treatment over time.

We can also evaluate the influence of dosing frequency on spatial distributions of antibiotics. For INH, the 3 dpw regimen leads to a smaller area of suboptimal exposure compared to 7 dpw due to the increase in dose (from 15 mg/kg to 45 mg/kg). However, the 2 dpw regimen shows lower penetration into both granulomas. For RIF, intermittent dosing leads to significantly larger areas of suboptimal exposure in granulomas. Taken together, our predictions show that suboptimal INH and RIF exposure exists inside granulomas, especially in areas where bacteria reside, and this contributes to a slow rate

of bacterial clearance. If early treatment can succeed in shrinking granuloma size, antibiotic exposure improves over time and helps clear the bacterial load.

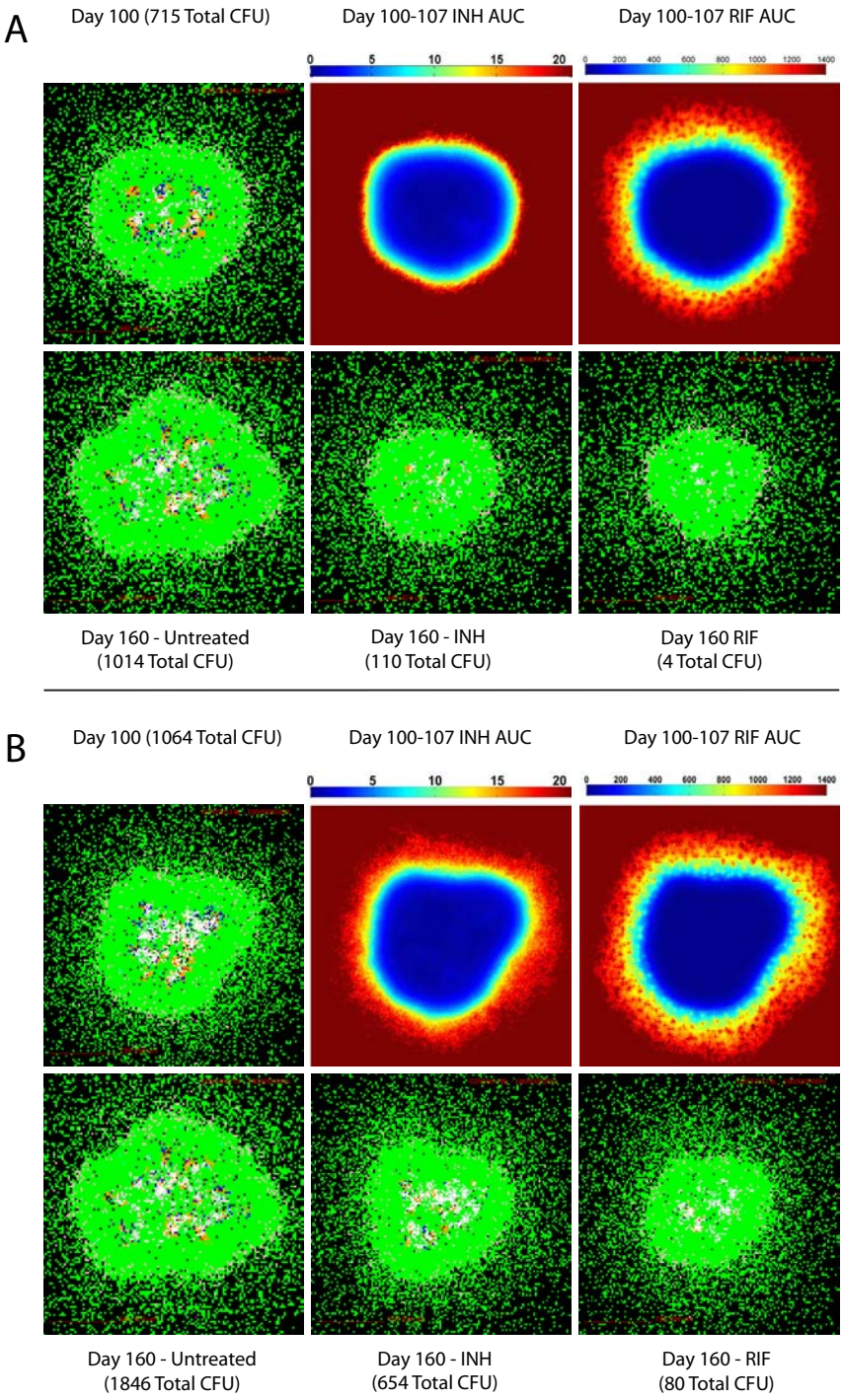

Figure C.5 Snapshots of two representative simulated granulomas
Panels 1,2,4 and 6 show cells in the granuloma: resting macrophages (green), infected macrophages (orange); chronically infected macrophages (red), caseation (white), activated macrophages (blue). A few T cells comprise the lymphocyte cuff around the outside of the macrophages (purple, pink and light blue).

There are a few extracellular *Mtb* (brown). Each granuloma is shown before treatment at 100 d.p.i. (panels A1 and B1) and at 160 d.p.i. when untreated (panels A2 and B2). Panels A4 and B4 show the granulomas after 60 days of daily INH treatment (15 mg/kg) and panels A6 and B6 show the granulomas after 60 days of daily RIF treatment (20 mg/kg). Panels 3 and 5 show cumulative INH and RIF exposure respectively (AUC in mg•h/L) as a function of position within the granuloma during the first week of treatment. Color bars are scaled from 0 mg•h/L to the AUC EC_{80} for each antibiotic (21 mg•h/L for INH and 1400 mg•h/L for RIF). Time-lapse movies of drug distribution and treatment progression, and high-resolution images that better show cellular level details (such as T-cells and caseation) are available at http://malthus.micro.med.umich.edu/lab/movies/Abx/.

C.3.4 Intermittent Dosing Increases Time to Clearance and Percentages of Granulomas Not Cleared for Single Antibiotics

We generated 500 simulated granulomas with treatment regimens as in Figure C.3 (regimens 1a, 1b, 2a and 3a) by initiating treatment at 100 d.p.i for a period of 180 days. We evaluated the outcome of treatment by computing the average time to clearance for those granulomas that do not contain bacteria by day 280 and the percentage of granulomas not cleared by day 280 (Figure C.6). Average time to clearance shows little variation between INH regimens and indicates that the majority of granulomas that cleared with intermittent INH regimens (1b and 2a) were cleared during the initial phase of daily dosing. RIF-3a takes significantly longer to clear infections than RIF-1a. All intermittent regimens had significantly higher %GNC than the corresponding daily regimen ($p < 0.05$; z-test). RIF is less efficient than INH in terms of %GNC in all the intermittent regimens (1b, 2a and 3a), which is expected based on RIF distribution in granulomas for intermittent dosing.

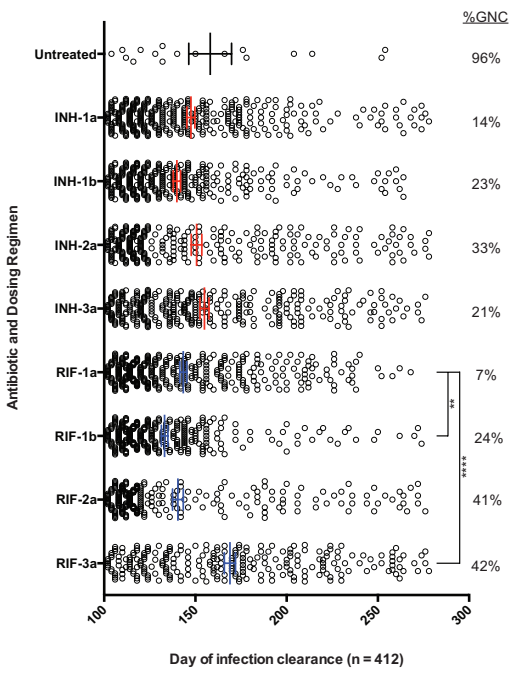

Figure C.6 Treatment outcomes for simulated regimens
Each circle represents one granuloma; only granulomas that cleared between day 100 and 280 (during treatment) are shown. Bars and errors bars show mean +/- SEM of time to clearance for untreated granulomas (black), INH-treated granulomas (red) and RIF-treated granulomas (blue). Numbers on the right show percentage of granulomas not cleared by day 280 for each regimen. (A) Treatment outcomes for single antibiotic therapy show that intermittent regimens clear fewer granulomas than daily regimens. Stars indicate significantly different times to clearance; **: $p<0.005$; ****: $p<0.00005$ (one way ANOVA with Sidak correction for multiple comparisons).

C.4 Discussion

Granulomas, the central feature of *Mtb* infection in human hosts, are heterogeneous both in bacterial populations and microenvironments (68). Thus it is crucial that we understand the distribution and activity of currently available antibiotics within these pathological structures. In this Appendix, we present the first systems pharmacology approach to modeling TB treatment that combines a model of granuloma formation and function and PK and PD dynamics. We characterize the spatial and temporal activity of antibiotics, identify key mechanisms behind antibiotic activity in the dynamic granuloma environment and propose new strategies for improving treatment.

Characterization of antibiotic distribution and activity in granulomas confirms that suboptimal exposure inside granulomas leads to bacterial regrowth between doses and may contribute to long-term treatment requirements for TB. There have been other proposed reasons for the required long-term antibiotic usage in TB, such as protected bacterial subpopulations in a non-replicating state (8) and/or are hiding intracellularly (69). These populations are believed to be protected from INH and RIF activity, respectively. However, our analysis shows that protected subpopulations change over time and that similar subpopulations are protected in both INH- and RIF-treated granulomas. Target bacterial populations change significantly (albeit slowly) during treatment, perhaps requiring a switch in treatment strategies after a few weeks of treatment.

There is clinical evidence for improved patient compliance and effective treatment of active TB with intermittent regimens (70). However, direct comparisons between daily and intermittent regimens are scarce, and existing reports do not agree on the clinical differences between daily and intermittent regimens (71–74). While extrapolation from model results to host level does not directly follow, our findings suggest that daily and intermittent regimens do not have equal clearance percentages on a granuloma level. Given the number of granulomas, an average of 5 in NHPs with latent TB and 13 in NHPs with active TB (10), and high variability between granulomas, it is conceivable that a single patient will have some granulomas with bacterial loads below detection limits after treatment, therefore appearing cured but remaining at risk of relapse.

Finally, we propose possible improvements to TB treatment by exploring alternative dosing regimens and modifications to current antibiotics. A systematic comparison of dose-frequency combinations for INH and RIF indicates that increases in dosing frequency are the most efficient way to improve treatment outcomes, since increasing dose leads to larger increases of cumulative doses. While up to double the current doses of RIF are known to be well-tolerated (75), increases in INH doses are only well-tolerated in patients with fast INH plasma clearance rates (76, 77). It is increasingly appreciated that TB drug levels may have an important impact on treatment outcomes and emergence of drug resistance (24, 78). This is particularly true for the rifamycins as demonstrated in multiple clinical studies of 'high-dose' RIF or rifapentine (75, 79, 80). Alternative strategies to reduce dosing frequency include controlled release drug delivery using micro-particles, explored in Chapter 6 (81, 82).

Clinical trials of antibiotics for TB remain fraught with limitations, specifically the lack of robust outcome measures for demonstrating improvement over current regimens, the difficulty in predicting relapse, the inability to test drugs singly or in unique combinations, cost, and the length of clinical trials. Animal models play an important role in the identification of new and effective regimens, but these studies are also costly, lengthy and require models with human-like pathology, primarily non-human primates. In this Appendix, we provided a complementary approach to predicting efficacy of new drugs and regimens, using a systems biology and pharmacology approach, which will allow a more rapid assessment of drug efficacy at the site of bacterial growth and persistence, the granuloma.

C.5 References

1. McFee, R. B. 2013. Update - pathogens of concern. *Disease-a-month* 59: 437–8.

2. *Global Tuberculosis Report 2013*,. World Health Organization, Geneva ; :1–145.

3. Dartois, V. 2014. The path of anti-tuberculosis drugs: from blood to lesions to mycobacterial cells. *Nat. Rev. Microbiol.* 12: 159–167.

4. WHO. 1999. *What is DOTS? A Guide to Understanding the WHO-recommended TB Control Strategy Known as DOTS*,.

5. Zhang, Y., W. W. Yew, and M. R. Barer. 2012. Targeting persisters for tuberculosis control. *Antimicrob. Agents Chemother.* 56: 2223–30.

6. Gomez, J. E., and J. D. McKinney. 2004. M. tuberculosis persistence, latency, and drug tolerance. *Tuberculosis* 84: 29–44.

7. Ahmad, Z., M. L. Pinn, E. L. Nuermberger, C. A. Peloquin, J. H. Grosset, and P. C. Karakousis. 2010. The potent bactericidal activity of streptomycin in the guinea pig model of tuberculosis ceases due to the presence of persisters. *J. Antimicrob. Chemother.* 65: 2172–5.

8. Connolly, L. E., P. H. Edelstein, and L. Ramakrishnan. 2007. Why is long-term therapy required to cure tuberculosis? *PLoS Med.* 4: e120.

9. Lin, P. L., T. Coleman, J. P. J. Carney, B. J. Lopresti, J. Tomko, D. Fillmore, V. Dartois, C. Scanga, L. J. Frye, C. Janssen, E. Klein, C. E. Barry, and J. L. Flynn. 2013. Radiologic responses in cynomolgous macaques for assessing tuberculosis chemotherapy regimens. *Antimicrob. Agents Chemother.* .

10. Lin, P. L., C. B. Ford, M. T. Coleman, A. J. Myers, R. Gawande, T. Ioerger, J. Sacchettini, S. M. Fortune, and J. L. Flynn. 2014. Sterilization of granulomas is common in active and latent tuberculosis despite within-host variability in bacterial killing. *Nat. Med.* 20: 75–9.

11. Emile, J.-F., N. Patey, F. Altare, S. Lamhamedi, E. Jouanguy, F. Boman, J. Quillard, M. Lecomte-Houcke, O. Verola, J.-F. Mousnier, F. Dijoud, S. Blanche, A. Fischer, N. Brousse, and J.-L. Casanova. 1997. Correlation of granuloma structure with clinical outcome defines two types of idiopathic disseminated BCG infection. *J. Pathol.* 181: 25–30.

12. Ridley, J. M., C. J. Heather, I. Brown, and D. A. Willoughby. 1983. Experimental epithelioid cell granulomas, tubercle formation and immunological competence: an ultrastructural analysis. *J. Pathol.* 141: 97–112.

13. Lin, P. L., S. Pawar, A. Myers, A. Pegu, C. Fuhrman, T. a Reinhart, S. V Capuano, E. Klein, and J. L. Flynn. 2006. Early events in Mycobacterium tuberculosis infection in cynomolgus macaques. *Infect. Immun.* 74: 3790–803.

14. Barry, C. E., H. I. Boshoff, V. Dartois, T. Dick, S. Ehrt, J. Flynn, D. Schnappinger, R. J. Wilkinson, and D. Young. 2009. The spectrum of latent tuberculosis: rethinking the biology and intervention strategies. *Nat Rev Microbiol* 7: 845–55.

15. Via, L. E., P. L. Lin, S. M. Ray, J. Carrillo, S. S. Allen, S. Y. Eum, K. Taylor, E. Klein, U. Manjunatha, J. Gonzales, E. G. Lee, S. K. Park, J. A. Raleigh, S. N. Cho, D. N. McMurray, J. L. Flynn, and C. E. Barry. 2008. Tuberculous granulomas are hypoxic in guinea pigs, rabbits, and nonhuman primates. *Infect. Immun.* 76: 2333–40.

16. Garton, N. J., S. J. Waddell, A. L. Sherratt, S. M. Lee, R. J. Smith, C. Senner, J. Hinds, K. Rajakumar, R. A. Adegbola, G. S. Besra, P. D. Butcher, and M. R. Barer. 2008. Cytological and transcript analyses reveal fat and lazy persister-like bacilli in tuberculous sputum. *PLoS Med.* 5: e75.

17. Saltini, C. 2006. Schedule or Dosage? The Need to Perfect Intermittent Regimens for Tuberculosis. *Am. J. Respir. Crit. Care Med.* 174: 1067–8.

18. Chang, K. C., C. C. Leung, J. Grosset, and W. W. Yew. 2011. Treatment of tuberculosis and optimal dosing schedules. *Thorax* 66: 997–1007.

19. Zumla, A., P. Nahid, and S. T. Cole. 2013. Advances in the development of new tuberculosis drugs and treatment regimens. *Nat. Rev. Drug Discov.* 12: 388–404.

20. Jindani, A., C. J. Doré, and D. a Mitchison. 2003. Bactericidal and sterilizing activities of antituberculosis drugs during the first 14 days. *Am. J. Respir. Crit. Care Med.* 167: 1348–54.

21. Piccaro, G., F. Giannoni, P. Filippini, A. Mustazzolu, and L. Fattorini. 2013. Activities of drug combinations against Mycobacterium tuberculosis grown in aerobic and hypoxic acidic conditions. *Antimicrob. Agents Chemother.* 57: 1428–33.

22. Deb, C., C. M. Lee, V. S. Dubey, J. Daniel, B. Abomoelak, T. D. Sirakova, S. Pawar, L. Rogers, and P. E. Kolattukudy. 2009. A novel in vitro multiple-stress dormancy model for Mycobacterium tuberculosis generates a lipid-loaded, drug-tolerant, dormant pathogen. *PLoS One* 4: e6077.

23. De Steenwinkel, J. E. M., G. J. de Knegt, M. T. ten Kate, A. van Belkum, H. A. Verbrugh, K. Kremer, D. van Soolingen, and I. A. J. M. Bakker-Woudenberg. 2010. Time-kill kinetics of anti-tuberculosis drugs, and emergence of resistance, in relation to metabolic activity of Mycobacterium tuberculosis. *J. Antimicrob. Chemother.* 65: 2582–9.

24. Dartois, V. 2011. Drug forgiveness and interpatient pharmacokinetic variability in tuberculosis. *J. Infect. Dis.* 204: 1827–9.

25. Kislitsyna, N. A. 1985. Comparative assessment of rifampicin and isoniazid penetration into pathological foci of the lungs in tuberculosis patients. *Probl. Tuberk.* 4: 55–57.

26. Kislitsyna, N. A., and N. I. Kotova. 1980. Rifampicin and isoniazid concentration in the blood and resected lungs in tuberculosis with combined use of the preparations. *Probl. Tuberk.* 63–5.

27. Barclay, W. R., R. H. Ebert, G. V Le Roy, R. W. Manthei, and L. J. Roth. 1953. Distribution and excretion of radioactive isoniazid in tuberculous patients. *J. Am. Med. Assoc.* 151: 1384–8.

28. Kjellsson, M. C., L. E. Via, A. Goh, D. Weiner, K. M. Low, S. Kern, G. Pillai, C. E. Barry, and V. Dartois. 2012. Pharmacokinetic evaluation of the penetration of antituberculosis agents in rabbit pulmonary lesions. *Antimicrob. Agents Chemother.* 56: 446–57.

29. Prideaux, B., V. Dartois, D. Staab, D. M. Weiner, A. Goh, L. E. Via, C. E. Barry, and M. Stoeckli. 2011. High-sensitivity MALDI-MRM-MS imaging of moxifloxacin distribution in tuberculosis-infected rabbit lungs and granulomatous lesions. *Anal. Chem.* 83: 2112–8.

30. Jayaram, R., S. Gaonkar, P. Kaur, B. L. Suresh, B. N. Mahesh, R. Jayashree, V. Nandi, S. Bharat, R. K. Shandil, E. Kantharaj, and V. Balasubramanian. 2003. Pharmacokinetics-Pharmacodynamics of Rifampin in an Aerosol Infection Model of Tuberculosis. *Antimicrob. Agents Chemother.* 47: 2118–2124.

31. Jayaram, R., R. K. Shandil, S. Gaonkar, P. Kaur, B. L. Suresh, B. N. Mahesh, R. Jayashree, V. Nandi, S. Bharath, E. Kantharaj, and V. Balasubramanian. 2004. Isoniazid Pharmacokinetics-Pharmacodynamics in an Aerosol Infection Model of Tuberculosis. *Antimicrob. Agents Chemother.* 48: 2951–2957.

32. De Steenwinkel, J. E. M., G. J. de Knegt, M. T. ten Kate, A. van Belkum, H. A. Verbrugh, K. Kremer, D. van Soolingen, and I. A. J. M. Bakker-Woudenberg. 2010. Time-kill kinetics of anti-tuberculosis drugs, and emergence of resistance, in relation to metabolic activity of Mycobacterium tuberculosis. *J. Antimicrob. Chemother.* 65: 2582–9.

33. Ray, J. C. J., J. L. Flynn, and D. E. Kirschner. 2009. Synergy between individual TNF-dependent functions determines granuloma performance for controlling Mycobacterium tuberculosis infection. *J. Immunol.* 182: 3706–17.

34. Segovia-Juarez, J. L., S. Ganguli, and D. Kirschner. 2004. Identifying control mechanisms of granuloma formation during M. tuberculosis infection using an agent-based model. *J. Theor. Biol.* 231: 357–76.

35. Fallahi-Sichani, M., M. El-Kebir, S. Marino, D. E. Kirschner, and J. J. Linderman. 2011. Multiscale computational modeling reveals a critical role for TNF-α receptor 1 dynamics in tuberculosis granuloma formation. *J. Immunol.* 186: 3472–83.

36. Cilfone, N. A., C. R. Perry, D. E. Kirschner, and J. J. Linderman. 2013. Multi-Scale Modeling Predicts a Balance of Tumor Necrosis Factor-α and Interleukin-10 Controls the Granuloma Environment during Mycobacterium tuberculosis Infection. *PLoS One* 8: e68680.

37. Boshoff, H. I., and C. E. Barry. 2005. Tuberculosis - metabolism and respiration in the absence of growth. *Nat Rev Microbiol* 3: 70–80.

38. Kirschner, D. E., C. A. Hunt, S. Marino, M. Fallahi-Sichani, and J. J. Linderman. 2014. Tuneable resolution as a systems biology approach for multi-scale, multi-compartment computational models. *Wiley Interdiscip. Rev. Syst. Biol. Med.* 6: 289–309.

39. Mugler, D. H., and R. A. Scott. 1988. Fast fourier transform method for partial differential equations, case study: The 2-D diffusion equation. *Comput. Math. with Appl.* 16: 221–228.

40. Costa, B. 2004. Spectral Methods for Partial Differential Equations. 6.

41. Egelund, E. F., A. B. Barth, and C. A. Peloquin. 2011. Population pharmacokinetics and its role in anti-tuberculosis drug development and optimization of treatment. *Curr. Pharm. Des.* 17: 2889–99.

42. Reisfeld, B., C. P. Metzler, M. a Lyons, a N. Mayeno, E. J. Brooks, and M. a Degroote. 2012. A physiologically based pharmacokinetic model for capreomycin. *Antimicrob. Agents Chemother.* 56: 926–34.

43. Lyons, M. A., B. Reisfeld, R. S. H. Yang, and A. J. Lenaerts. 2013. A physiologically based pharmacokinetic model of rifampin in mice. *Antimicrob. Agents Chemother.* 57: 1763–71.

44. Goutelle, S., L. Bourguignon, P. H. Maire, M. Van Guilder, J. E. Conte, and R. W. Jelliffe. 2009. Population modeling and Monte Carlo simulation study of the pharmacokinetics and antituberculosis pharmacodynamics of rifampin in lungs. *Antimicrob. Agents Chemother.* 53: 2974–81.

45. Lin, P. L., V. Dartois, P. J. Johnston, C. Janssen, L. Via, M. B. Goodwin, E. Klein, C. E. Barry, and J. L. Flynn. 2012. Metronidazole prevents reactivation of latent

Mycobacterium tuberculosis infection in macaques. *Proc. Natl. Acad. Sci. U. S. A.* 109: 14188–93.

46. Marino, S., I. B. Hogue, C. J. Ray, and D. E. Kirschner. 2008. A methodology for performing global uncertainty and sensitivity analysis in systems biology. *J. Theor. Biol.* 254: 178–96.

47. Peloquin, C. A., G. S. Jaresko, C. L. Yong, A. C. Keung, A. E. Bulpitt, and R. W. Jelliffe. 1997. Population pharmacokinetic modeling of isoniazid, rifampin, and pyrazinamide. *Antimicrob. Agents Chemother.* 41: 2670–9.

48. Wilkins, J. J., R. M. Savic, M. O. Karlsson, G. Langdon, H. McIlleron, G. Pillai, P. J. Smith, and U. S. H. Simonsson. 2008. Population pharmacokinetics of rifampin in pulmonary tuberculosis patients, including a semimechanistic model to describe variable absorption. *Antimicrob. Agents Chemother.* 52: 2138–48.

49. Wilkins, J. J., G. Langdon, H. McIlleron, G. Pillai, P. J. Smith, and U. S. H. Simonsson. 2011. Variability in the population pharmacokinetics of isoniazid in South African tuberculosis patients. *Br. J. Clin. Pharmacol.* 72: 51–62.

50. Wilkins, J. J., G. Langdon, H. McIlleron, G. Pillai, P. J. Smith, and U. S. H. Simonsson. 2011. Variability in the population pharmacokinetics of isoniazid in South African tuberculosis patients. *Br. J. Clin. Pharmacol.* 72: 51–62.

51. Pruijn, F. B., K. Patel, M. P. Hay, W. R. Wilson, and K. O. Hicks. 2008. Prediction of Tumour Tissue Diffusion Coefficients of Hypoxia-Activated Prodrugs from Physicochemical Parameters. *Aust. J. Chem.* 61: 687.

52. Jeena, P. M., W. R. Bishai, J. G. Pasipanodya, and T. Gumbo. 2011. In silico children and the glass mouse model: clinical trial simulations to identify and individualize optimal isoniazid doses in children with tuberculosis. *Antimicrob. Agents Chemother.* 55: 539–45.

53. Mor, N., B. Simon, N. Mezo, and L. Heifets. 1995. Comparison of activities of rifapentine and rifampin against Mycobacterium tuberculosis residing in human macrophages. *Antimicrob Agents Chemother* 39: 2073–7.

54. Ziglam, H. M., D. R. Baldwin, I. Daniels, J. M. Andrews, and R. G. Finch. 2002. Rifampicin concentrations in bronchial mucosa, epithelial lining fluid, alveolar macrophages and serum following a single 600 mg oral dose in patients undergoing fibre-optic bronchoscopy. *J. Antimicrob. Chemother.* 50: 1011–1015.

55. Forsgren, A., and A. Bellahsène. 1985. Antibiotic accumulation in human polymorphonuclear leucocytes and lymphocytes. *Scand. J. Infect. Dis. Suppl.* 44: 16–23.

56. Schmidt, M. M., and K. D. Wittrup. 2009. A modeling analysis of the effects of molecular size and binding affinity on tumor targeting. *Mol. Cancer Ther.* 8: 2861–71.

57. Gumbo, T., A. Louie, W. Liu, D. Brown, P. G. Ambrose, S. M. Bhavnani, and G. L. Drusano. 2007. Isoniazid bactericidal activity and resistance emergence: integrating pharmacodynamics and pharmacogenomics to predict efficacy in different ethnic populations. *Antimicrob. Agents Chemother.* 51: 2329–36.

58. Fallahi-Sichani, M., J. L. Flynn, J. J. Linderman, and D. E. Kirschner. 2012. Differential risk of tuberculosis reactivation among anti-TNF therapies is due to drug binding kinetics and permeability. *J. Immunol.* 188: 3169–78.

59. Shandil, R. K., R. Jayaram, P. Kaur, S. Gaonkar, B. L. Suresh, B. N. Mahesh, R. Jayashree, V. Nandi, S. Bharath, and V. Balasubramanian. 2007. Moxifloxacin, ofloxacin, sparfloxacin, and ciprofloxacin against Mycobacterium tuberculosis: evaluation of in vitro and pharmacodynamic indices that best predict in vivo efficacy. *Antimicrob. Agents Chemother.* 51: 576–82.

60. Bouvier d'Yvoire, M. Y., and P. Maire. 1996. Dosage Regimens of Antibacterials. *Clin. Drug Investig.* 11: 229–239.

61. Regoes, R. R., C. Wiuff, R. M. Zappala, K. N. Garner, F. Baquero, and B. R. Levin. 2004. Pharmacodynamic Functions : a Multiparameter Approach to the Design of Antibiotic Treatment Regimens. *Antimicrob. Agents Chemother.* 48: 3670–3676.

62. Trefethen, L. N. 1996. *Finite Difference and Spectral Methods for Ordinary and Partial Differential Equations*,. Unpublished Text.

63. Fornberg, B. 1996. *A Practical Guide to Pseudospectral Methods*,. WILEY-VCH Verlag.

64. Deen, W. M. 1998. *Analysis of Transport Phenomena*,. OUP USA.

65. Gottlieb, D., and C.-W. Shu. 1997. On the Gibbs Phenomenon and Its Resolution. *SIAM Rev.* 39: 644–668.

66. Blumberg, H. M., W. J. Burman, R. E. Chaisson, C. L. Daley, S. C. Etkind, L. N. Friedman, P. Fujiwara, M. Grzemska, P. C. Hopewell, M. D. Iseman, R. M. Jasmer, V. Koppaka, R. I. Menzies, R. J. O'Brien, R. R. Reves, L. B. Reichman, P. M. Simone, J. R. Starke, and A. A. Vernon. 2003. Treatment of tuberculosis. *Am. J. Respir. Crit. Care Med.* 167: 603–62.

67. Mehta, J. B., H. Shantaveerapa, R. P. Byrd, S. E. Morton, F. Fountain, and T. M. Roy. 2001. Utility of rifampin blood levels in the treatment and follow-up of active pulmonary tuberculosis in patients who were slow to respond to routine directly observed therapy. *Chest* 120: 1520–4.

68. Peloquin, C. 2003. What is the "right" dose of rifampin? *Int. J. Tuberc. lung Dis.* 7: 3–5.

69. Goutelle, S., L. Bourguignon, R. W. Jelliffe, J. E. Conte, and P. Maire. 2011. Mathematical modeling of pulmonary tuberculosis therapy: Insights from a prototype model with rifampin. *J. Theor. Biol.* 282: 80–92.

70. Frieden, T. 2004. *Toman's Tuberculosis: Case detection, treatment and monitoring.*, Second Ed. (T. Frieden, ed). World Health organization, Geneva, Switzerland.

71. Mwandumba, H., and S. Squire. 2001. Fully intermittent dosing with drugs for treating tuberculosis in adults. *Cochrane Database Syst. Rev.* 4.

72. Chang, K. C., C. C. Leung, W. W. Yew, S. L. Chan, and C. M. Tam. 2006. Dosing schedules of 6-month regimens and relapse for pulmonary tuberculosis. *Am. J. Respir. Crit. Care Med.* 174: 1153–8.

73. Menzies, D., A. Benedetti, A. Paydar, I. Martin, S. Royce, M. Pai, A. Vernon, C. Lienhardt, and W. Burman. 2009. Effect of duration and intermittency of rifampin on tuberculosis treatment outcomes: a systematic review and meta-analysis. *PLoS Med.* 6: e1000146.

74. Chang, K. C., C. C. Leung, W. W. Yew, S. C. Ho, and C. M. Tam. 2004. A nested case-control study on treatment-related risk factors for early relapse of tuberculosis. *Am. J. Respir. Crit. Care Med.* 170: 1124–30.

75. Ruslami, R., a R. Ganiem, S. Dian, L. Apriani, T. H. Achmad, A. J. van der Ven, G. Borm, R. E. Aarnoutse, and R. van Crevel. 2013. Intensified regimen containing rifampicin and moxifloxacin for tuberculous meningitis: an open-label, randomised controlled phase 2 trial. *Lancet Infect. Dis.* 13: 27–35.

76. Cho, H.-J., W.-J. Koh, Y.-J. Ryu, C.-S. Ki, M.-H. Nam, J.-W. Kim, and S.-Y. Lee. 2007. Genetic polymorphisms of NAT2 and CYP2E1 associated with antituberculosis drug-induced hepatotoxicity in Korean patients with pulmonary tuberculosis. *Tuberculosis (Edinb).* 87: 551–6.

77. Possuelo, L. G., J. a Castelan, T. C. de Brito, a W. Ribeiro, P. I. Cafrune, P. D. Picon, a R. Santos, R. L. F. Teixeira, T. S. Gregianini, M. H. Hutz, M. L. R. Rossetti, and a Zaha. 2008. Association of slow N-acetyltransferase 2 profile and anti-TB drug-induced hepatotoxicity in patients from Southern Brazil. *Eur. J. Clin. Pharmacol.* 64: 673–81.

78. Srivastava, S., J. G. Pasipanodya, C. Meek, R. Leff, and T. Gumbo. 2011. Multidrug-resistant tuberculosis not due to noncompliance but to between-patient pharmacokinetic variability. *J. Infect. Dis.* 204: 1951–9.

79. Donald, P. R., and a H. Diacon. 2008. The early bactericidal activity of anti-tuberculosis drugs: a literature review. *Tuberculosis (Edinb).* 88 Suppl 1: S75–83.

80. Boeree, M. J., G. Plemper van Balen, and R. A. Aarnoutse. 2011. High-dose rifampicin: how do we proceed? *Int. J. Tuberc. Lung Dis.* 15: 1133.

81. Sosnik, A., A. M. Carcaboso, R. J. Glisoni, M. a Moretton, and D. a Chiappetta. 2010. New old challenges in tuberculosis: potentially effective nanotechnologies in drug delivery. *Adv. Drug Deliv. Rev.* 62: 547–59.

82. Saifullah, B., M. Z. B. Hussein, and S. H. Hussein Al Ali. 2012. Controlled-release approaches towards the chemotherapy of tuberculosis. *Int. J. Nanomedicine* 7: 5451–63.

Appendix D

Supplementary Information for Chapter 6

D.1 Supplemental Text

D.1.1 Methods

D.1.1.1 Inhaled Carrier Model: Granuloma Compartment

Once in the ABM simulation environment carriers move by random walk (Figure 6.1c in Chapter 6) with a time step calculated from an estimated diffusivity of carriers in tissue and mucus and scaled based on carrier size (Stokes-Einstein) (1). Carriers are phagocytosed by macrophages at a probability that is a function of carrier zeta potential (parabolic function), size (Weibull distribution), and surface ligand density (Poisson distribution) and can reside in the intracellular environment for long times (days to weeks) (Figure D.1b-d) (2–5). If a macrophage dies intracellular carriers are dispersed to the extracellular environment in the Moore neighborhood. Carriers degrade in both the extra- and intracellular space, which can occur at differing rates (6). Release of antibiotics from carriers occurs in both the intra- and extracellular space as demonstrated by *in vitro* studies of release kinetics (7–12). We use a description of carrier release kinetics that models both diffusion of antibiotics through the carrier and degradation of the carrier system itself, with time varying boundary conditions (13–15). We assume the carriers are spherical, such that the system is symmetric in the polar and azimuth angles. If the rate of diffusion is faster than the rate of degradation ($D/R^2 >> \delta$) then the carrier release kinetics are diffusion-controlled. If the rate of degradation is faster than the rate of

diffusion ($D/R^2 << \delta$) then the carrier release kinetics are degradation-controlled (Figure 6.1 in Chapter 6) (13–15). We solve the release equations for each carrier using a forward-time-central-space (FTCS) finite difference scheme.

D.1.1.2 Uncertainty and Sensitivity Analysis

We use Latin hypercube sampling (LHS) to simultaneously vary multiple model parameters and sample the parameter space (16). Partial rank correlation coefficients (PRCCs) quantify the effects of varying each parameter on non-linear outputs, where a PRCC of -1 represents a perfect negative correlation and a PRCC of +1 represents a perfect positive correlation. PRCCs are differentiated based on a students t-test to indicate significance ($p < 0.05$, $p < 0.001$, $p < 0.0001$). We generate 200 unique parameter sets for a specific dosing frequency (daily, two-weeks) of inhaled formulations of RIF and INH, each of which are replicated four times, yielding 1000 simulations per dosing frequency. Average values of model outputs (e.g. CFU, AUC, etc.) 14 days post-treatment are used to calculate PRCC and p-values. In addition, we identify parameter combinations describing inhaled formulations that lead to equivalent sterilization capabilities with reduced toxicity compared to daily oral doses. Using these parameter sets and knowledge of parameter PRCCs we design ideal inhaled formulations to test against oral dosing regimens.

D.1.1.3 Computational Platform

Our hybrid multi-scale agent-based model (ABM) of infection and treatment is constructed using the C++ programming language, Boost libraries (distributed under the

Boost Software License), FFTw libraries (distributed under GPL), and the Qt framework for visualization (distributed under GPL). The ABM is cross-platform and can be run with or without visualization software. Data manipulation was carried out in MATLAB R2012a (Natick, MA). Plots and statistical tests were created using GraphPad Prism 6 (La Jolla, CA).

D.1.1.4 Model Analysis

Our work investigates antibiotic efficacy at the single granuloma scale. We first simulate 100 days post-infection, whereby a single macrophage is initially infected and a granuloma emerges by ~4 weeks post-infection. Any granuloma that sterilizes before the onset of treatment at 100 days post-infection is removed from analysis. We subsequently treat with antibiotics for an additional 200 days via the inhaled or oral route at two dosing frequencies: daily or every two-weeks. We define successful treatment as the complete sterilization of all bacteria in a granuloma by 200 days post-treatment initiation. We track average concentrations of antibiotics over time in granulomas, along with concentrations in PK compartments. We calculate cumulative granuloma and peripheral antibiotic exposure (AUC) for 14-day timeframes. Peripheral AUC is a metric of toxicity as the peripheral compartment represents organs such as the liver and kidneys (17). We evaluate hazard ratios (HR) to determine the cumulative risk between inhaled and oral treatments. Uncertainty and sensitivity analysis is used to identify inhaled antibiotic model parameters that have significant effects on model outputs related to treatment efficacy (16).

D.1.2 Results

D.1.2.1 Extended Sensitivity Analysis

For daily dosing of an inhaled formulation of RIF, the antibiotic loading and antibiotic diffusivity in the carrier are strongly negatively correlated with CFU in granulomas and time to granuloma sterilization while strongly positively correlated with granuloma and peripheral AUC (Table 6.1 in Chapter 6), indicating an important role in treatment efficacy. The intra- and extracellular carrier degradation rates (carrier release kinetics) are significantly correlated with both granuloma and peripheral AUC, but with limited effects on CFU and time to sterilization. Clearance of RIF from the peripheral compartment is significantly correlated with reduced granuloma and peripheral AUC, while weakly correlated with increased CFU and time to sterilization (Table 6.1 in Chapter 6). Conversely, dosing every two-weeks with an inhaled formulation of RIF the intra- and extracellular carrier degradation rates (carrier release kinetics) are significantly positively correlated with CFU, while antibiotic loading is still strongly negatively correlated with CFU in granulomas and time to granuloma sterilization. The antibiotic diffusivity of RIF in the carrier increases granuloma AUC yet has limited effects on CFU and time to sterilization.

For daily dosing of an inhaled formulation of INH the antibiotic loading and antibiotic diffusivity (carrier release kinetics) in the carrier are strongly negatively correlated with CFU in granulomas and time to granuloma sterilization, while strongly positively correlated with granuloma and peripheral AUC (Table 6.2 in Chapter 6) indicating an important role in treatment efficacy. The intracellular carrier degradation rate (carrier release kinetics) is strongly correlated with granuloma and peripheral AUC,

CFU, and time to sterilization, while the extracellular carrier degradation rate (carrier release kinetics) is correlated only with granuloma and peripheral AUC. Clearance of INH from the peripheral compartment is strongly correlated with reduced granuloma and peripheral AUC and increased CFU and time to sterilization (Table 6.2 in Chapter 6). Dosing every two-weeks with an inhaled formulation of INH demonstrates that antibiotic diffusivity of INH in the carrier and intracellular carrier degradation rate (carrier release kinetics) are positively correlated with CFU, while antibiotic loading is again significantly negatively correlated with reduced CFU in granulomas and time to granuloma sterilization.

D.2 Supplemental Tables

Table D.1 PK, Granuloma, PD, and Inhaled Carrier Model Parameters

Pharmacokinetic Parameters [1]				
Parameter	**Description**	**INH**	**RIF**	**Reference**
K_a	Absorption Rate Constant (h^{-1})	[0.75 – 1.35]	[0.1 – 0.5]	Fit to (18, 19)
CL_A	Clearance Rate Constant – 2nd Abs Comp. (L/h*kg)	[9.5 – 16]	[0.01 – 0.075]	Fit to (18, 19)
CL_{PE}	Clearance Rate Constant – Peripheral Comp. (L/h*kg)	[0.025 – 0.1]	[0.1 – 1.0]	Fit to (18, 19)
CL_M	Clearance Rate Constant – Macrophage Comp. (L/h*kg)	0.005	0.0053	Fit to (18, 19)
Q_P	Transfer Rate Constant – Plasma to Peripheral (h^{-1})	0.25	0.25	Fit to (18, 19)
Q_L	Transfer Rate Constant – Plasma to Non-Infected Lung (h^{-1})	0.25	0.25	Fit to (18, 19)
V_{PL}	Apparent Volume Distribution – Plasma (L/kg)	0.06	0.06	Fit to (18, 19)
V_{PE}	Apparent Volume Distribution – Periphery (L/kg)	[0.01 – 0.1]	[0.5 – 5]	Fit to (18, 19)
V_L	Apparent Volume Distribution – Non-Infected Lung (L/kg)	0.00875	0.00875	Fit to (18, 19)
PC_L	Partition Coefficient – Non-Infected Lung/Granuloma	0.25	3.3	Fit to (18, 19)
L_L	Total Lung Volume (L)	0.04375	0.04375	(20–24)
L_P	Total Plasma Volume (L)	0.42	0.42	(20–24)
N_M	Number of Macrophages in Non-Infected Lung	2.26×10^{8}	2.26×10^{8}	Estimated
Granuloma and Non-Infected Lung Related Parameters				
Parameter	**Description**	**INH**	**RIF**	
δ_{ext}	Extracellular Degradation Rate Constant (s^{-1})	5.52×10^{-9}	7.5×10^{-8}	Chapter 6
δ_{int}	Intracellular Degradation Rate Constant (s^{-1})	6.4×10^{-3}	6.7×10^{-3}	Chapter 6
D	Apparent Diffusivity in Lung Tissue (cm^2/s)	1.11×10^{-7}	6.96×10^{-7}	Chapter 6
E_M	Equilibrium Partition Coefficient	0.35	17.8	Chapter 6
p	Vascular Permeability (cm/s)	8.42×10^{-6}	8.42×10^{-6}	Chapter 6

L_M	Macrophage Volume (L)	4.85×10^{-12}	4.85×10^{-12}	Chapter 6
L_{Grid}	Micro-Compartment Volume (L)	8×10^{-12}	8×10^{-12}	Chapter 6

Pharmacodynamic Parameters

Parameter	Description	INH	RIF	
$C_{50,BI}$	Intracellular *Mtb* – C50 (mg/L)	0.02	10	Chapter 6
$C_{50,BE}$	Extracellular Replicating *Mtb* – C50 (mg/L)	0.04	1.23	Chapter 6
$C_{50,BN}$	Extracellular Non-Replicating *Mtb* – C50 (mg/L)	0.5	5	Chapter 6
H_{BI}	Intracellular *Mtb* – Hill Constant	1	0.48	Chapter 6
H_{BE}	Extracellular Replicating *Mtb* – Hill Constant	1	0.7	Chapter 6
H_{BN}	Extracellular Non-Replicating *Mtb* – Hill Constant	1	0.7	Chapter 6
$E_{max,BI}$	Intracellular *Mtb* – Max Activity ($timestep^{-1}$)	0.046	0.069	Chapter 6
$E_{max,BE}$	Extracellular *Mtb* – Max Activity ($timestep^{-1}$)	0.155	0.296	Chapter 6

Inhaled Carrier Parameters [(2)]

Parameter	Description	INH	RIF	
T_{Dose}	Total Carrier Dose to Lungs (# of carriers)	1.2×10^{9}	1.2×10^{9}	Fit to (19)
f_D	Dose Fraction to Granuloma Compartment	1.18×10^{-6}	1.18×10^{-6}	Estimated
P_{load}	Inhaled Carrier Drug Loading (mg/carrier)	$[1\times10^{-8} – 5\times10^{-7}]$	$[1\times10^{-9} – 5\times10^{-8}]$	(6, 12, 25–33)
P_{size}	Diameter of Carrier (μm)	[2.0 – 8.0]	[2.0 – 8.0]	(2–5)
$P_{sizeDev}$	Range of Diameter of Carrier (μm)	1.0	1.0	(2–5)
$P_{drugDiff}$	Diffusivity of Drug in Carrier ($\mu m^2/s$)	$[1\times10^{-8} – 5\times10^{-6}]$	$[1\times10^{-8} – 5\times10^{-6}]$	(6, 12, 25–33)
P_{intDeg}	Carrier Intracellular Degradation Rate (s^{-1})	$[5\times10^{-6} – 5\times10^{-5}]$	$[5\times10^{-6} – 5\times10^{-5}]$	(6, 12, 25–33)
P_{extDeg}	Carrier Extracellular Degradation Rate (s^{-1})	$[5\times10^{-6} – 5\times10^{-5}]$	$[5\times10^{-6} – 5\times10^{-5}]$	(6, 12, 25–33)
P_{zeta}	Carrier Zeta Potential (mV)	[-40.0 – 0]	[-40.0 – 0]	(2–5)
P_{diff}	Carrier Apparent Diffusivity in Lung Tissue (cm^2/s)	$[2\times10^{-10} – 1.95\times10^{-9}]$	$[2\times10^{-10} – 1.95\times10^{-9}]$	(1)
M_{uptake}	Macrophage Maximum Carrier Uptake Probability	[0.01 – 0.95]	[0.01 – 0.95]	Estimated
P_{TL}	Density of Targeting Ligand on Carrier (#/carrier)	$[1\times10^{1} – 1\times10^{4}]$	$[1\times10^{1} – 1\times10^{4}]$	(34–37)
M_{TR}	Density of Targeting Receptor on Macrophages (#/cell)	$[1\times10^{1} – 1\times10^{4}]$	$[1\times10^{1} – 1\times10^{4}]$	(34–37)
$K_{D\text{-}TLR}$	Ligand-Receptor Equilibrium Rate Constant (M)	$[1\times10^{-9} – 1\times10^{-7}]$	$[1\times10^{-9} – 1\times10^{-7}]$	(34–37)
k_{TLR}	Poisson – Ligand-Receptor Carrier Uptake Rate (#/cell*s)	$[5\times10^{-4} – 5\times10^{-3}]$	$[5\times10^{-4} – 5\times10^{-3}]$	Estimated
W_{Shape}	Weibull – Carrier Size Uptake Rate – Shape Parameter	1.9	1.9	(2–5)
W_{Scale}	Weibull – Carrier Size Uptake Rate – Scale Parameter	3.5	3.5	(2–5)
W_{Max}	Weibull – Carrier Size Uptake Rate – Max Parameter	0.2372	0.2372	(2–5)
C_{Scale}	Parabolic – Carrier Zeta-Potential Uptake Rate – Scale Parameter	400	400	(2–5)

(1) Ranges given to account for inter-individual variability. These ranges are also used in sensitivity analysis.
(2) Ranges given are used in sensitivity analysis

Table D.2 Agent-Based Model Parameters

Parameter Description	Value(s)
Bacterial carrying capacity of each grid compartment (#)	114.5
Intracellular bacterial growth rate ($timestep^{-1}$)	1.0045
Extracellular bacterial growth rate ($timestep^{-1}$)	1.0025
Rate of death of bacteria trapped in caseated compartments ($timestep^{-1}$)	0.85
Number of host cell deaths causing caseation (#)	9
Time to heal caseation (timesteps)	1467
TNF threshold for causing apoptosis (# of molecules)	1147
Rate of TNF induced apoptosis (s^{-1})	$1.7x10^{-6}$
Minimum chemokine concentration allowing chemotaxis (# of molecules)	0.47
Maximum chemokine concentration allowing chemotaxis (# of molecules)	476
Initial macrophage density (fraction of grid)	0.04
Time steps before a resting macrophage can move (timesteps)	3
Time steps before an activated macrophage can move (timesteps)	19
Time steps before an infected macrophage can move (timesteps)	170
TNF threshold for activating NFkB (# of molecules)	73
Rate of TNF induced NFkB activation (s^{-1})	$1.06x10^{-5}$
Number of bacteria resting macrophage can phagocytose (#)	1
Probability of resting macrophage killing bacteria	0.12
Adjustment for killing probability of resting macrophages with NFkB activated	0.2
Number of extracellular bacteria that can activate NFkB (#)	253
Threshold for intracellular bacteria causing chronically infected macrophages (#)	12
Threshold for intracellular bacteria causing macrophage to burst (#)	23
Number of bacteria activated macrophage can phagocytose (#)	5
Probability of an activated macrophage healing a caseated compartment in its Moore neighborhood	0.0055
Probability of a T-cell moving to the same compartment as a macrophage	0.046
IFNg-producing T-cell probability of inducing Fas/FasL mediated apoptosis	0.035
IFNg-producing T-cell probability of producing TNF	0.045
IFNg-producing T-cell probability of producing IFN	0.35
Cytotoxic T-cell probability of killing a macrophage	0.009
Cytotoxic T-cell probability of killing a macrophage and all of its intracellular bacteria	0.71
Cytotoxic T-cell probability of producing TNF	0.047
Regulatory T-cell probability of deactivating activated macrophage	0.008
Time before maximum recruitment rates are reached (timesteps)	982
Macrophage maximal recruitment probability	0.32
Macrophage chemokine recruitment threshold (# of molecules)	0.86
Macrophage TNF recruitment threshold (# of molecules)	0.011
Macrophage half sat for TNF recruitment (# of molecules)	1.63
Macrophage half sat for chemokine recruitment (# of molecules)	2.16
IFNg-producing T-cell maximal recruitment probability	0.15
IFNg-producing T-cell chemokine recruitment threshold (# of molecules)	0.072

IFNg-producing T-cell TNF recruitment threshold (# of molecules)	1.27
IFNg-producing T-cell half sat for TNF recruitment (# of molecules)	1.34
IFNg-producing T-cell half sat for chemokine recruitment (# of molecules)	1.87
Cytotoxic T-cell maximal recruitment probability	0.12
Cytotoxic T-cell chemokine recruitment threshold (# of molecules)	4.48
Cytotoxic T-cell TNF recruitment threshold (# of molecules)	1.27
Cytotoxic T-cell half sat for TNF recruitment (# of molecules)	1.19
Cytotoxic T-cell half sat for chemokine recruitment (# of molecules)	8.62
Regulatory T-cell maximal recruitment probability	0.029
Regulatory T-cell chemokine recruitment threshold (# of molecules)	2.05
Regulatory T-cell TNF recruitment threshold (# of molecules)	1.63
Regulatory T-cell half sat for TNF recruitment (# of molecules)	2.23
Regulatory T-cell half sat for chemokine recruitment (# of molecules)	1.5

Tuneable Resolution Related Parameters

Parameter Description	**Value(s)**
Apparent TNF consumption rate (s^{-1})	0.00077
Apparent IL-10 consumption rate (s^{-1})	0.0004
Partition factor for estimating internalized bound receptors	11.3
Threshold for IL-10 inhibition of TNF secretion	-1.93
Shape parameter for IL-10 inhibition of TNF secretion	0.181
Apparent TNF secretion rate by macrophages (# of molecules/s)	1.5
Apparent IL-10 secretion rate by activated macrophages (# of molecules/s)	0.3
Apparent IL-10 secretion rate by infected macrophages (# of molecules/s)	0.02
Apparent TNF secretion rate by IFNg producing T-cells (# of molecules/s)	0.15
Apparent TNF secretion rate by cytotoxic T-cells (# of molecules/s)	0.015
Apparent IL-10 secretion rate by regulatory T-cells (# of molecules/s)	0.739
Affinity of TNF for TFNR1 (M)	1.9×10^{-11}
Affinity of IL-10 for IL-10R (M)	4.56×10^{-10}

From (38, 39) and from Chapters 3, 5, and Appendix C

D.3 Supplemental Figures

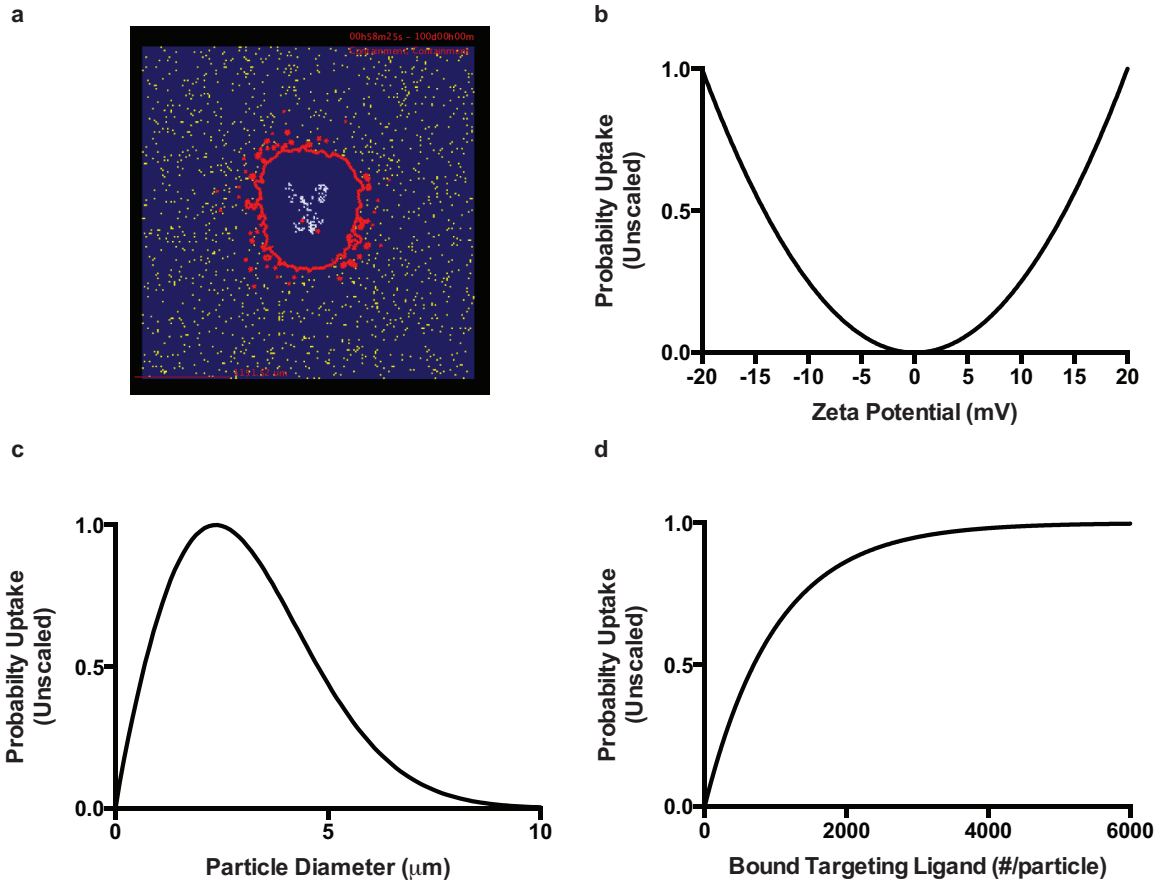

Figure D.1 Inhaled carrier deposition and macrophage uptake functions
(a) Snapshot of the ABM showing an example inhaled dose depositing on the simulation grid. Carriers are denoted as yellow squares and an estimate of the granuloma border is shown in red. **(b)** Unscaled probability function describing the dependence of macrophage uptake on carrier zeta potential (2–4). **(c)** Unscaled probability function describing the dependence of macrophage uptake on carrier diameter (2–4). **(d)** Unscaled probability function describing the dependence of macrophage uptake on carrier targeting-ligand density (2–4).

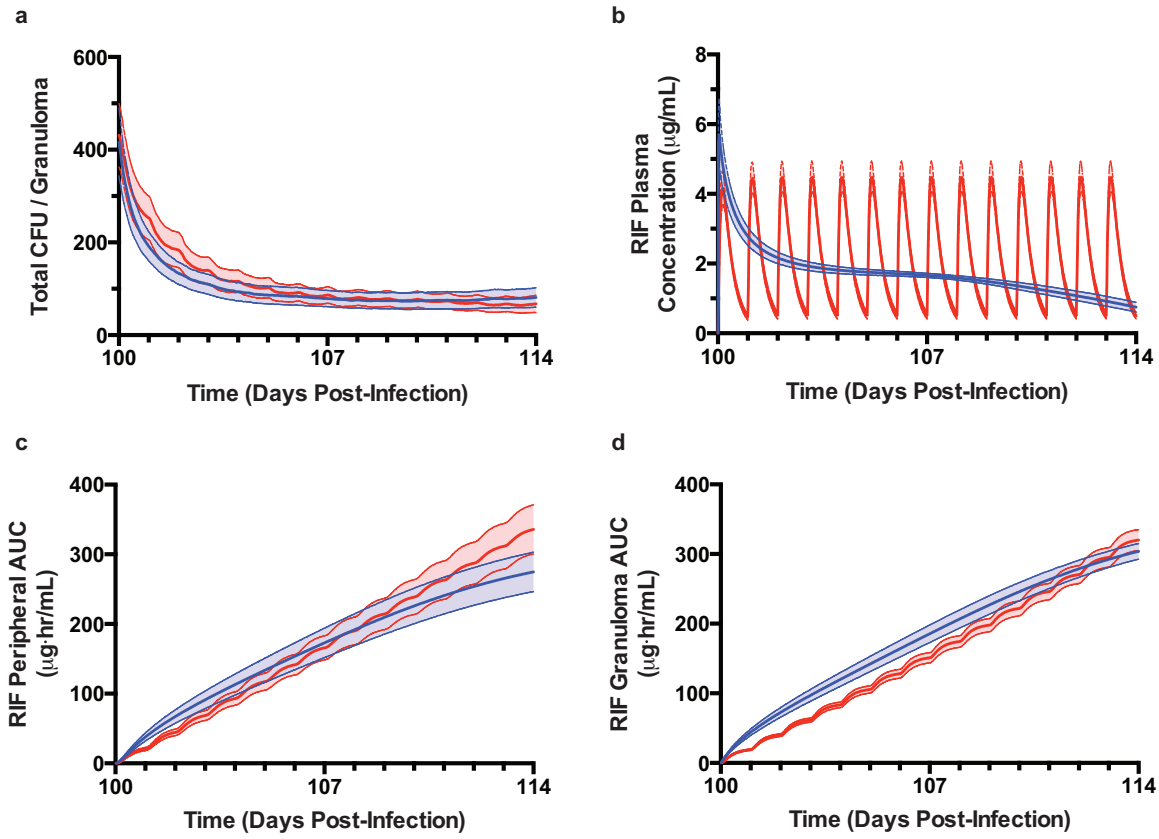

Figure D.2 Comparison of an inhaled RIF formulation given every two-weeks with an oral RIF formulation given daily

(a) Total CFU per granuloma for the first 14-day dosing window. **(b)** Average RIF concentration in the plasma compartment for the first 14-day dosing window. **(c)** Average RIF peripheral AUC for the first 14-day dosing window. **(d)** Average RIF granuloma AUC for the first 14-day dosing window. Red = Oral, Blue = Inhaled. Solid lines indicate average values while dotted lines represent SD. Inhaled (N = 83), Oral (N = 87).

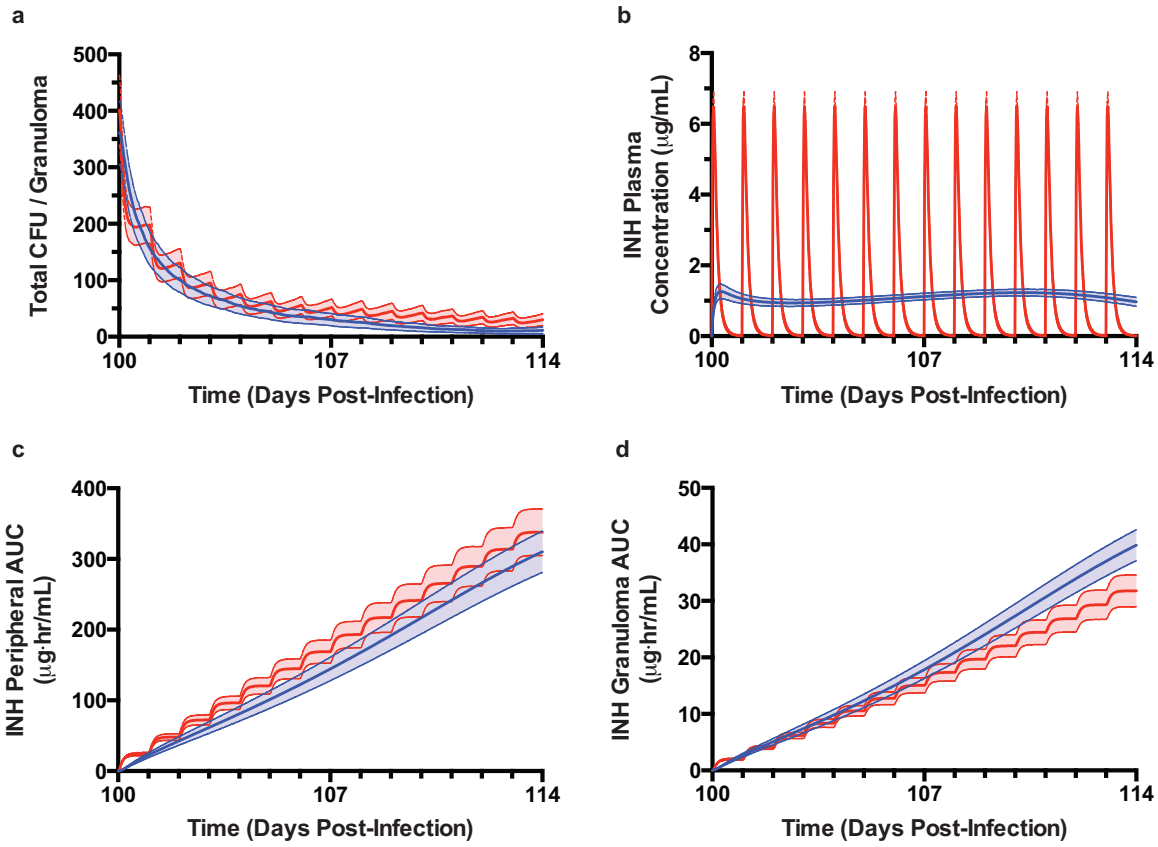

Figure D.3 Comparison of an inhaled INH formulation given every two-weeks with an oral INH formulation given daily
(a) Total CFU per granuloma for the first 14-day dosing window. **(b)** Average INH concentration in the plasma compartment for the first 14-day dosing window. **(c)** Average INH peripheral AUC for the first 14-day dosing window. **(d)** Average INH granuloma AUC for the first 14-day dosing window. Red = Oral, Blue = Inhaled. Solid lines indicate average values while dotted lines represent SD. Inhaled (N = 81), Oral (N = 87).

D.4 References

1. Cu, Y., and W. M. Saltzman. 2010. Controlled surface modification with poly(ethylene)glycol enhances diffusion of PLGA nanoparticles in human cervical mucus. *Mol. Pharm.* 6: 173–81.

2. Tabata, Y., and Y. Ikada. 1988. Effect of the size and surface charge of polymer microspheres on their phagocytosis by macrophage. *Biomaterials* 9: 356–62.

3. Champion, J. a, A. Walker, and S. Mitragotri. 2008. Role of particle size in phagocytosis of polymeric microspheres. *Pharm. Res.* 25: 1815–21.

4. Hasegawa, T., K. Hirota, K. Tomoda, F. Ito, H. Inagawa, C. Kochi, G.-I. Soma, K. Makino, and H. Terada. 2007. Phagocytic activity of alveolar macrophages toward

polystyrene latex microspheres and PLGA microspheres loaded with anti-tuberculosis agent. *Colloids Surf. B. Biointerfaces* 60: 221–8.

5. Kalluru, R., F. Fenaroli, D. Westmoreland, L. Ulanova, A. Maleki, N. Roos, M. Paulsen Madsen, G. Koster, W. Egge-Jacobsen, S. Wilson, H. Roberg-Larsen, G. K. Khuller, A. Singh, B. Nyström, and G. Griffiths. 2013. Poly(lactide-co-glycolide)-rifampicin nanoparticles efficiently clear Mycobacterium bovis BCG infection in macrophages and remain membrane-bound in phago-lysosomes. *J. Cell Sci.* 126: 3043–54.

6. Muttil, P., J. Kaur, K. Kumar, A. B. Yadav, R. Sharma, and A. Misra. 2007. Inhalable microparticles containing large payload of anti-tuberculosis drugs. *Eur. J. Pharm. Sci.* 32: 140–50.

7. Verma, R. K., J. Kaur, K. Kumar, A. B. Yadav, and A. Misra. 2008. Intracellular time course, pharmacokinetics, and biodistribution of isoniazid and rifabutin following pulmonary delivery of inhalable microparticles to mice. *Antimicrob. Agents Chemother.* 52: 3195–201.

8. Hirota, K., T. Hasegawa, H. Hinata, F. Ito, H. Inagawa, C. Kochi, G.-I. Soma, K. Makino, and H. Terada. 2007. Optimum conditions for efficient phagocytosis of rifampicin-loaded PLGA microspheres by alveolar macrophages. *J. Control. Release* 119: 69–76.

9. Parikh, R., S. Dalwadi, P. Aboti, and L. Patel. 2014. Inhaled microparticles of antitubercular antibiotic for in vitro and in vivo alveolar macrophage targeting and activation of phagocytosis. *J. Antibiot. (Tokyo).* 1–8.

10. Yoshida, A., M. Matumoto, H. Hshizume, Y. Oba, T. Tomishige, H. Inagawa, C. Kohchi, M. Hino, F. Ito, K. Tomoda, T. Nakajima, K. Makino, H. Terada, H. Hori, and G.-I. Soma. 2006. Selective delivery of rifampicin incorporated into poly(DL-lactic-co-glycolic) acid microspheres after phagocytotic uptake by alveolar macrophages, and the killing effect against intracellular Mycobacterium bovis Calmette-Guérin. *Microbes Infect.* 8: 2484–91.

11. Zhou, H., Y. Zhang, D. L. Biggs, M. C. Manning, T. W. Randolph, U. Christians, B. M. Hybertson, and K. Ng. 2005. Microparticle-based lung delivery of INH decreases INH metabolism and targets alveolar macrophages. *J. Control. Release* 107: 288–99.

12. Makino, K., T. Nakajima, M. Shikamura, F. Ito, S. Ando, C. Kochi, H. Inagawa, G.-I. Soma, and H. Terada. 2004. Efficient intracellular delivery of rifampicin to alveolar macrophages using rifampicin-loaded PLGA microspheres: effects of molecular weight and composition of PLGA on release of rifampicin. *Colloids Surf. B. Biointerfaces* 36: 35–42.

13. Siepmann, J., and F. Siepmann. 2008. Mathematical modeling of drug delivery. *Int. J. Pharm.* 364: 328–43.

14. Kanjickal, D. G., and S. T. Lopina. 2004. Modeling of drug release from polymeric delivery systems--a review. *Crit. Rev. Ther. Drug Carrier Syst.* 21: 345–86.

15. Arifin, D. Y., L. Y. Lee, and C.-H. Wang. 2006. Mathematical modeling and simulation of drug release from microspheres: Implications to drug delivery systems. *Adv. Drug Deliv. Rev.* 58: 1274–325.

16. Marino, S., I. B. Hogue, C. J. Ray, and D. E. Kirschner. 2008. A methodology for performing global uncertainty and sensitivity analysis in systems biology. *J. Theor. Biol.* 254: 178–96.

17. Kjellsson, M. C., L. E. Via, A. Goh, D. Weiner, K. M. Low, S. Kern, G. Pillai, C. E. Barry, and V. Dartois. 2012. Pharmacokinetic evaluation of the penetration of antituberculosis agents in rabbit pulmonary lesions. *Antimicrob. Agents Chemother.* 56: 446–57.

18. Lin, P. L., V. Dartois, P. J. Johnston, C. Janssen, L. Via, M. B. Goodwin, E. Klein, C. E. Barry, and J. L. Flynn. 2012. Metronidazole prevents reactivation of latent Mycobacterium tuberculosis infection in macaques. *Proc. Natl. Acad. Sci. U. S. A.* 109: 14188–93.

19. Kumar Verma, R., J. K. Mukker, R. S. P. Singh, K. Kumar, P. R. P. Verma, and A. Misra. 2012. Partial biodistribution and pharmacokinetics of isoniazid and rifabutin following pulmonary delivery of inhalable microparticles to rhesus macaques. *Mol. Pharm.* 9: 1011–6.

20. Gerlowski, L. E., and R. K. Jain. 1983. Physiologically based pharmacokinetic modeling: principles and applications. *J. Pharm. Sci.* 72: 1103–27.

21. Armstrong, J. D., E. H. Gluck, R. O. Crapo, H. a Jones, and J. M. Hughes. 1982. Lung tissue volume estimated by simultaneous radiographic and helium dilution methods. *Thorax* 37: 676–9.

22. Nigi, H., and Y. Noguchi. 1967. Circulating blood volume of the Japanese monkey (Macaca fuscata) by means of the dye T-1824. *Primates* 8: 23–28.

23. Ageyama, N., H. Shibata, H. Narita, K. Hanari, A. Kohno, F. Ono, Y. Yoshikawa, and K. Terao. 2001. Specific gravity of whole blood in cynomolgus monkeys (Macaca fascicularis), squirrel monkeys (Saimiri sciureus), and tamarins (Saguinus labiatus) and total blood volume in cynomolgus monkeys. *Contemp. Top. Lab. Anim. Sci.* 40: 33–5.

24. Akabane, T., K. Tabata, K. Kadono, S. Sakuda, S. Terashita, and T. Teramura. 2010. A comparison of pharmacokinetics between humans and monkeys. *Drug Metab. Dispos.* 38: 308–16.

25. Onoshita, T., Y. Shimizu, N. Yamaya, M. Miyazaki, M. Yokoyama, N. Fujiwara, T. Nakajima, K. Makino, H. Terada, and M. Haga. 2010. The behavior of PLGA microspheres containing rifampicin in alveolar macrophages. *Colloids Surf. B. Biointerfaces* 76: 151–7.

26. O'Hara, P., and a J. Hickey. 2000. Respirable PLGA microspheres containing rifampicin for the treatment of tuberculosis: manufacture and characterization. *Pharm. Res.* 17: 955–61.

27. Manca, M. L., G. Loy, M. Zaru, A. M. Fadda, and S. G. Antimisiaris. 2008. Release of rifampicin from chitosan, PLGA and chitosan-coated PLGA microparticles. *Colloids Surf. B. Biointerfaces* 67: 166–70.

28. Coowanitwong, I., V. Arya, P. Kulvanich, and G. Hochhaus. 2008. Slow release formulations of inhaled rifampin. *AAPS J.* 10: 342–8.

29. Durán, N., M. a Alvarenga, E. C. Da Silva, P. S. Melo, and P. D. Marcato. 2008. Microencapsulation of antibiotic rifampicin in poly(3-hydroxybutyrate-co-3-hydroxyvalerate). *Arch. Pharm. Res.* 31: 1509–16.

30. Son, Y.-J., and J. T. McConville. 2012. Preparation of sustained release rifampicin microparticles for inhalation. *J. Pharm. Pharmacol.* 64: 1291–302.

31. Hsu, Y. Y., J. D. Gresser, R. R. Stewart, D. J. Trantolo, C. M. Lyons, G. a Simons, P. R. Gangadharam, and D. L. Wise. 1996. Mechanisms of isoniazid release from poly(d,l-lactide-co-glycolide) matrices prepared by dry-mixing and low density polymeric foam methods. *J. Pharm. Sci.* 85: 706–13.

32. Hsu, Y.-Y., J. D. Gresser, D. J. Trantolo, C. M. Lyons, P. R. J. Gangadharam, and D. L. Wise. 1994. In vitro controlled release of isoniazid from poly (lactide-co-glycolide) matrices. *J. Control. Release* 31: 223–228.

33. Verma, R. K., A. K. Singh, M. Mohan, A. K. Agrawal, and A. Misra. 2011. Inhaled therapies for tuberculosis and the relevance of activation of lung macrophages by particulate drug-delivery systems. *Ther. Deliv.* 2: 753–68.

34. Ghaghada, K. B., J. Saul, J. V Natarajan, R. V Bellamkonda, and A. V Annapragada. 2005. Folate targeting of drug carriers: a mathematical model. *J. Control. Release* 104: 113–28.

35. D'Addio, S. M., S. Baldassano, L. Shi, L. Cheung, D. H. Adamson, M. Bruzek, J. E. Anthony, D. L. Laskin, P. J. Sinko, and R. K. Prud'homme. 2013. Optimization of cell

receptor-specific targeting through multivalent surface decoration of polymeric nanocarriers. *J. Control. Release* 168: 41–9.

36. Ahsan, F., I. P. Rivas, M. A. Khan, and A. I. Torres Suarez. 2002. Targeting to macrophages: role of physicochemical properties of particulate carriers--liposomes and microspheres--on the phagocytosis by macrophages. *J. Control. Release* 79: 29–40.

37. Pacheco, P., D. White, and T. Sulchek. 2013. Effects of microparticle size and Fc density on macrophage phagocytosis. *PLoS One* 8: e60989.

38. Cilfone, N. A., C. R. Perry, D. E. Kirschner, and J. J. Linderman. 2013. Multi-Scale Modeling Predicts a Balance of Tumor Necrosis Factor-α and Interleukin-10 Controls the Granuloma Environment during Mycobacterium tuberculosis Infection. *PLoS One* 8: e68680.

39. Fallahi-Sichani, M., M. El-Kebir, S. Marino, D. E. Kirschner, and J. J. Linderman. 2011. Multiscale computational modeling reveals a critical role for TNF-α receptor 1 dynamics in tuberculosis granuloma formation. *J. Immunol.* 186: 3472–83.